Self-Assembly of Dinuclear Complexes Featuring Aromatic and Aliphatic Walls

by

Kristina Aramantha Stevenson

A thesis submitted to the Department of Chemistry
In conformity with the requirements for
the degree of Master of Science

Queen's University
Kingston, Ontario, Canada
(September, 2013)

Dedicated to my Grandpa

"We cannot direct the wind, but we can adjust the sails"

Abstract

The objective of my MSc thesis is to study the self-assembly process of macrocyclic complexes, as well as the properties that affect the obtained supramolecular architectures. The possibility of substrate recognition within the cavity of these complexes is also of interest. Preparation of three new ligands based on the triazole-pyridine chelating units connected through variable spacer groups, as well as the complexes formed with octahedral metal ions, are described herein.

The first ligand contained a naphthalene spacer region, which was longer than the previously examined xylene spacer. This extension increases the distance between metal ions in the complex, as well as the size of the cavity. More work is required to obtain the unsaturated double-stranded complex, which could potentially bind substrate molecules within its cavity. The triple-stranded saturated complexes with $[Fe(H_2O)_6](BF_4)_2$ and $[Ni(H_2O)_6](BF_4)_2$ both gave insight into the process of self-assembly.

The next two ligands were designed to probe the effect that increasing the length of an aliphatic spacer had on complex self-assembly. Both ethyl and propyl spacer units had been previously studied, so butyl and pentyl spacer groups were the natural next step to analyze. The length of the alkyl spacer was found to be very important in the nature of the obtained complex. As the length of the alkyl chain, and the corresponding flexibility increased, so too did the complexity of the resulting supramolecular architectures.

Acknowledgements

I would first like to express my utmost gratitude and appreciation to my supervisor, Dr. Anne Petitjean. Her enthusiasm and expertise in the area provided me with a wealth of knowledge and the experience was invaluable. The guidance and support I received throughout my Master's degree was second to none and it was truly a pleasure to work and learn from her.

I am grateful for the contributions from the Queen's faculty and staff in the Department of Chemistry. Sincere thanks are given to my committee members, Dr. David Zechel, Dr. Ralph Whitney and Dr. Michael Baird. Your wonderful insights and devotion of time are greatly appreciated. Furthermore, I would like to thank Dr. Ruiyao Wang for his X-ray crystallographic analyses and Dr. Françoise Sauriol for her expertise in NMR spectroscopy.

During my two years working in the Petitjean lab I had the opportunity to work with a number of devoted colleagues, mentors and friends. Dr. Yi Yan, Weiwen, Huan, Caitlin and Mona, your insights and advice were extremely helpful, and I sincerely believe my Master's wouldn't have been as enjoyable without your kind support and friendship.

Most importantly I'd like to thank my family, because without their constant love and support I wouldn't be where I am today. I am extremely fortunate to have such wonderful parents; you've given me everything I could have hoped for. Last, but certainly not least, I owe a huge thanks to my sister Tori. As far as sisters go I'd say I'm pretty lucky. To my mom, dad and Tori, your encouraging words and ongoing support were there when I needed them most, and I could not have made it through my academic career thus far without you.

Statement of Originality

I hereby certify that all of the work described within this thesis is the original work of the author under the supervision of Dr. Anne Petitjean at Queen's University. Exceptions include the X-ray crystallography data, which were collected and solved by Dr. Ruiyao Wang; MS spectroscopy data, which were provided by Dr. Jiaxi Wang and James Wei. Further exceptions include:

Chapter 2: The UV-vis titrations of $[Fe(H_2O)_6](BF_4)_2$/$[Ni(H_2O)_6](BF_4)_2$ into **N1** and corresponding Job plots were performed by Dr. Anne Petitjean.

Chapter 3: The UV-vis titrations of $[Fe(H_2O)_6](BF_4)_2$/$[Ni(H_2O)_6](BF_4)_2$ into **C4** and the corresponding Job plots were performed by Dr. Anne Petitjean. Dr. Petitjean performed the same titration and Job plot experiments with **C5** as well. St

Any published (or unpublished) ideas and/or techniques from the work of others are fully acknowledged in accordance with the standard referencing practices.

Table of Contents

List of Tables

List of Figures

Chapter 1

List of Abbreviations

Ar	Aromatic
Bn	Benzyl
br	Broad
COSY	Correlation spectroscopy
Conc.	Concentration
CuAAC	Copper-catalyzed azide-alkyne cycloaddition
°C	Degree Celsius
d	Doublet
dd	Doublet of doublets
TFA	Trifluoroacetic acid
DMF	Dimethylformamide
DMSO	Dimethylsulfoxide
DCM	Dichloromethane
EDTA	Ethylenediaminetetraacetic acid
ESI	Electrospray ionization
ESI-MS	Electrospray ionization mass spectrometry
EA	Elemental analysis
EI	Electron impact
EtOAc	Ethyl acetate
EtOH	Ethanol
Equiv.	Equivalent
g	Gram
Hz	Hertz
h	Hour(s)
HCl	Hydrochloric acid
HRMS	High resolution mass spectrometry
HPLC	High performance liquid chromatography
HMBC	Heteronuclear multiple bond correlation
HSQC	Heteronuclear single quantum correlation
J	Vicinal coupling constant
K	Kelvin

L	Litre(s)
m	Multiplet
M	Moles per litre
m/z	Mass to charge ration
MeCN	Acetonitrile
mg	Milligram
min	Minute(s)
mL	Millilitre(s)
mmol	Millimole(s)
mol	Mole
MHz	Megahertz
mM	Millimoles per litre
MS	Mass spectrometry
NaASc	Sodium Ascorbate
NMR	Nuclear magnetic resonance
nm	Nanometer
Ph	Phenyl
Py	Pyridine
ppm	Part(s) per million
q	Quartet
quin.	Quintet
Rf	Retention factor
RT	Room temperature
s	Singlet or second(s)
t	Triplet
THF	Tetrahydrofuran
TLC	Thin-layer chromatography
UV	Ultraviolet
δ	Chemical shift
Å	Angstrom
λ	Wavelength

Chapter 1

Introduction

1.1 Self Assembly: A Brief Introduction

In simplest terms, self-assembly is the spontaneous aggregation of an enclosed supramolecular structure, obtained from the combination of molecular subunits.[1] Typically, molecular subunits which are highly symmetrical in nature are utilized, thereby limiting the number of possible side products.[1b, 2] The resulting self-assembled structures are reversible and highly ordered, which is why the phenomenon is extensively employed in coordination chemistry.[2-3]

Despite the appeal of self-assembled supramolecular architectures, obtaining the desired complexes presents some synthetic challenges, including symmetry concerns and unwanted by-products.[4] Techniques have been designed and applied to the self-assembly of coordination complexes, which typically include a combination of structurally rigid ligand component(s) as well as a level of flexibility to obtain the desired architecture.[5] While chemists work to master self-assembly techniques, nature performs tasks of similar complexity with relative ease.[6] Some examples of these self-assembly processes carried out by nature include folding of nucleic acids, DNA recognition, as well as protein folding.[6-7]

The diversity of coordination chemistry and self-assembly provides numerous opportunities for the design of novel supramolecular architectures. A thorough understanding of the self-assembly process is required to synthesize intricate, supramolecular systems from seemingly simple, individual molecular components.[1b] This makes self-assembly extremely powerful and an essential part of a chemist's toolbox.

1.1.1 Hydrogen Bond Directed Self-Assembly

Due to its prevalence in nearly all biological systems, hydrogen bonding has been used extensively in supramolecular self-assembly.[1c, 4, 8] Hydrogen bonds offer both strength and directionality which make them useful in the self-assembly of complex, well-defined architectures.[9] When molecular building blocks are combined, the corresponding complex may selectively assemble, provided the hydrogen bonds are cooperatively used.[8d, 9a] Self-assembly with hydrogen bonds also features directionality and complementarity of the individual subunits.[8b, 9a] There are many examples of supramolecular complexes that self-assemble using hydrogen bonding, such as calixarenes, rotaxanes, helices and a number of cyclic hydrogen bonded structures.[9]

Zafar *et al.* have presented an example where hydrogen bonding controls the formation of discrete molecular architectures through self-assembly.[8b] In their molecular design complementarity between the carboxylic acid and 2-aminopyridine functionalities was exploited (**Figure 1.1**). The two carefully selected components formed a self-assembled architecture through hydrogen bonding interactions, with the nature of the resulting compound dependent on the position of the hydrogen bonding groups.[8b]

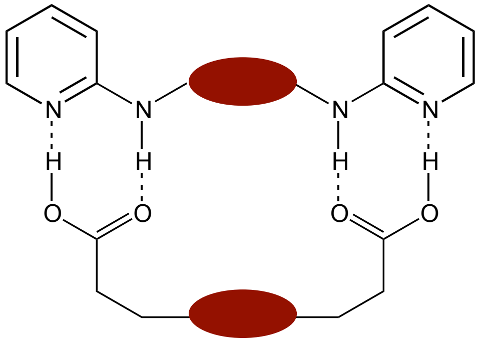

Figure 1.1: A self-assembled architecture formed through hydrogen bonds between bis-carboxylic acid and bis-acylaminopyridine (in acidic solution).[8b]

While hydrogen bonding has provided numerous self-assembled architectures, the incorporation of metal ions into the self-assembly process has redefined the field.

1.1.2 Metal-Directed Self-Assembly

The use of self-assembly to obtain supramolecular architectures containing metal ions has been exploited as an alternative to the previously used organic synthesis.[8a] Syntheses that were typically tedious and low-yielding are now carried out by simply combining metal ions and ligand constituents to obtain a spontaneously self-assembled architecture.[4, 10] Some of the advantages of metal-directed self-assembly include versatile geometry modes, reversibility and moderate to high bond strengths.[1c] Perhaps one of the more important characteristics of this self-assembly process is the labile nature of the metal-ligands bonds, which ensure that self-corrections can occur without too much difficulty.[9b] There are several important examples of these earlier supramolecular complexes that utilize metals in their architectures (**Figure 1.2**). The scope of this self-assembly mode is endless, due to the vast number of chelating ligands and coordination motifs.[1c, 11]

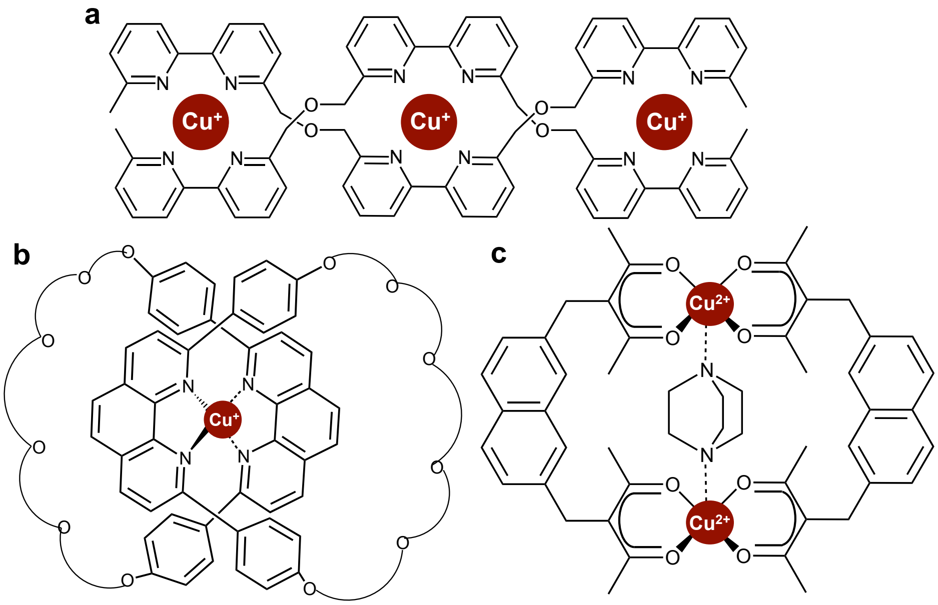

Figure 1.2: Earlier examples of supramolecular complexes:[1c, 12] a) Cu$^+$-chelated double helix (Lehn, 1987), b) Cu$^+$-templated catenane (Sauvage, 1983), c) Metal-linked supramolecular complex (Maverick, 1984).

A more recent example of metal-directed self-assembly was designed by Fujita *et al.* which contained a supramolecular complex with receptor potential. After combining square planar transition metals (right angle directing) with a polydentate ligand, a macrocyclic square was obtained by self-assembly of the molecular components (**Figure 1.3**).[1c] Both Pt^{II} and Pd^{II} metal ions were combined with 4,4-bipyridine, to give the corresponding square macrocycle.[1c] The Pd^{II} complex offered a hydrophobic cavity in water, therefore potentially allowing the recognition of neutral aromatic guest molecules.[1c]

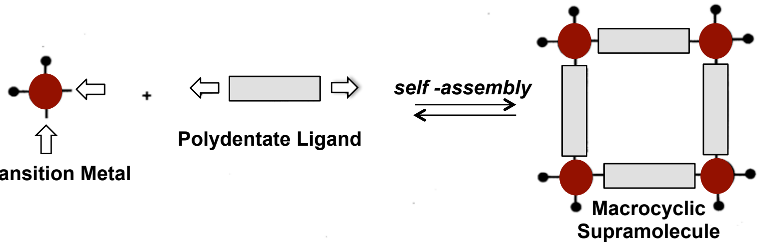

Figure 1.3: Concept of metal-directed self-assembly, using a square-planar transition metal.[1c]

Today, the vast number and type of coordination motifs and multidentate ligands available is taking metal-directed self-assembly to the forefront of supramolecular architectural design.

1.2 Metallomacrocycles

The broadest definition of a macrocycle is one that encompasses any cyclic molecule containing nine or more atoms.[1c] Metallomacrocycles, like macrocycles, are also large cyclic structures, however, one or more of the connections are from a metal ion (**Figure 1.4**).[12]

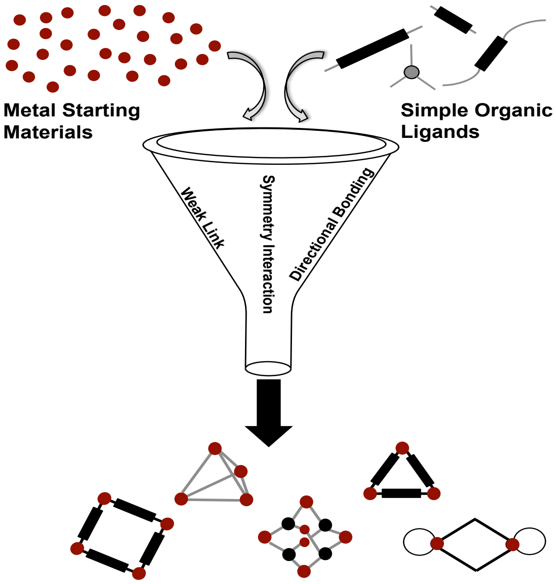

Figure 1.4: Illustrative representation of the components and requirements for metallomacrocyclic complexes.[13]

The product of metal complexation may result in several different complexes, including those that are chiral, achiral, helical, or non-helical in nature.[1a] The resulting supramolecular complex (or metallomacrocycle) and its structural properties are dependent on the structure of the ligand, as well as the metal ion and its coordination geometry.[14] This category is extremely broad and encompasses numerous supramolecular architectures. Some members of the metallomacrocycle family include, but are not limited to, helicates, mesocates, and metalloreceptors.

1.2.1 Directional-Bonding Approach

Directional bonding is an approach to building metallomacrocyclic architectures by systematically choosing the molecular components to obtain the desired supramolecular structure.[13, 15] In this approach, the resulting metal containing complex is obtained from the combination of a metal center, which acts in a highly directional manner, and carefully selected ligands that interact with the metal in a predictable fashion.[13, 15] The previously described "metal-directed self-assembly" approach is inherently similar to this method, with an additional directionality component.

To ensure formation of the desired complex, metal ions with specific coordination geometries (tetrahedral, octahedral and so on) are introduced with carefully designed chelating ligands (**Figure 1.5**). The shape and structure of the complex are therefore pre-determined based on the preferred geometry of the starting metal ions as well as the chelating and linker ligands.[13,15]

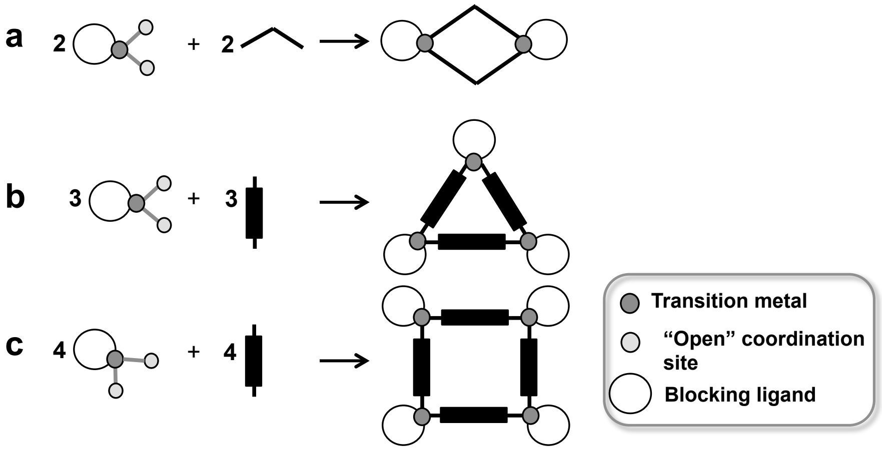

Figure 1.5: Formation of supramolecular structures by the directional-bonding approach. The metal centers have a highly directional effect on the resulting complex geometry: a) Dinuclear macrocycle, b) Supramolecular triangle and c) Supramolecular square.[13]

The directional-bonding approach is a high-yielding synthetic method for obtaining supramolecular architectures with a specified shape and structure. One drawback however, overcome by the following approach, is that the ligands are rigid, which eliminates the possibility of forming a flexible supramolecular architecture.[13]

1.2.2 Symmetry-Interaction Approach

Another approach to obtaining metallomacrocycle complexes is that of the 'symmetry-interaction' approach, which overcomes the rigidity of the previously discussed 'directional-bonding' method.[2, 13, 15] Metals in the absence of coordinating ligands are used in conjunction with multidentate chelating ligands to form a symmetrically designed supramolecular architecture. The nature of the resulting complex is dependent upon the symmetry of the ligands and preferential coordination geometry of the metal ions.[2, 13] In comparison to the directional-bonding approach, there are additional synthetic considerations, including metal ion geometry, ligand orientation, and possible ligand steric interactions.[13] Despite these added challenges many novel architectures have been reported, including tetrahedral,[4] adamantoid,[13] and helical structures[12, 16] (**Figure 1.6**).

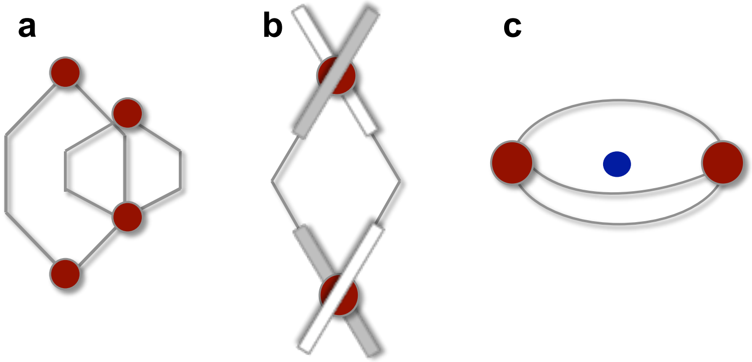

Figure 1.6: Dinuclear structures assembled by the symmetry-interaction approach: a) Catenane b) Double-stranded helicate conformation[16] c) Dinuclear metallacryptand.[13, 17]

As described briefly here, helicate complexes belong to the metallomacrocycle family, and utilize the symmetry-interaction approach of self-assembly. The concept is covered in more detail in the following section.

1.2.3 Helicates and Mesocates

The term *helicate*, derived from the Greek word *helix* and suffix *–ate,* describes complexing between a metal and a ligand.[16] The term "helicate" was first defined in 1987 by Lehn and co-workers as a polymetallic helical complex, or simply a metal-containing helix.[12] Helicates may be further defined as architectures containing one or more covalent organic strands coordinated to a series of ions, wrapped along a helical axis.[18] Helicates are of particular interest due to their wide range of applications in areas such as molecular recognition, which is defined as the discriminatory interaction between two molecular components in a self-assembly process.[12, 18a]

Many examples of helices are present in nature, with the first and perhaps the most common example being DNA. DNA exists as a double helix with complementary bases being held together through hydrogen bonds and hydrophobic effects.[6a, 19] Another example found in nature is collagen, which adopts a triple helical structure and is made up of an array of peptides that adopt an α-helical structure.[20]

The difference between a *helicate* and a *mesocate* is simply the chirality about the metal centers. A *helicate* will have the same chirality at each metal center, whereas a *mesocate* will have opposite (**Figure 1.7**).[18a] More specifically, a dinuclear helicate will have Δ, Δ or Λ, Λ chirality about the metal centers, whereas a mesocate will have Δ, Λ or Λ, Δ.

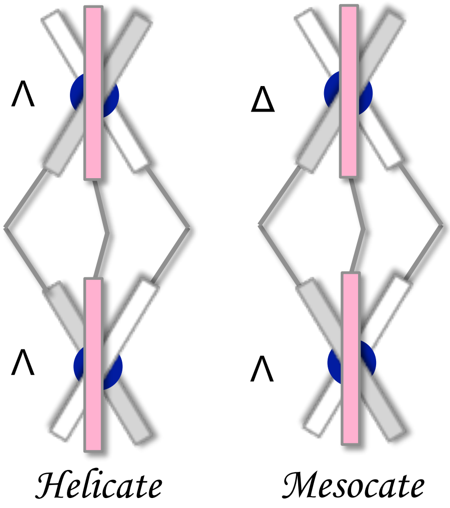

Figure 1.7: Structural representation of a helicate and mesocate and their corresponding chirality assignments with octahedral metal ions.

Outlined below is the method used for assigning chirality based on the chelating ability of the complex, with the tris-chelating complex highlighted below (**Figure 1.8**). In this instance, the direction of the helix is determined from looking down the primary C3 axis. A left-handed helix corresponds to a lambda (Λ) chirality assignment, and a right-handed helix corresponds to a delta (Δ) assignment.[18a]

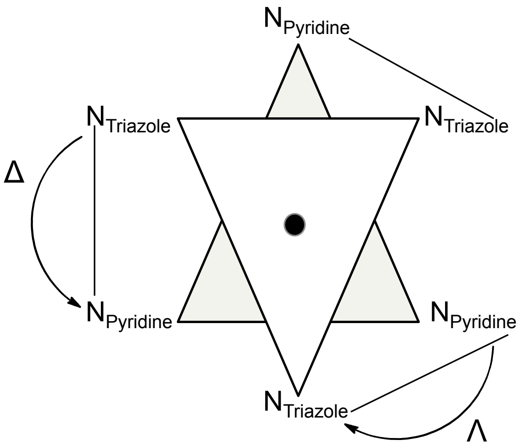

Figure 1.8: Assigning chirality for tris-chelating complexes (octahedral metal ions) The C3 axis of symmetry has been indicated as well as the triazole-pyridine chelating units.[18a]

1.2.4 Helicates vs. Mesocates – The '*Even-Odd*' Principle

Albrecht first introduced the *even-odd* principle, to define a stereochemical preference for supramolecular architectures on the basis of their ligand design.[21] Dinuclear triple-stranded helicates of the general formula [$M_2\mathbf{L}_3$] can be formed from bidentate chelating ligands, which are bound to two octahedral metal ions. The formation of these complexes results in chirality about each of the metal centers, therefore leading to three conceivable coordination complexes. Two enantiomeric helicate complexes are possible (Λ, Λ or Δ, Δ), or a diastereotopic mesocate complex (Λ, Δ) may also be formed based on the relative chirality of the metal centers.[22] There are general properties that typically affect the stereoselectivity, with the two most relevant being: number of methylene groups in the alkyl spacer region and rigidity of the ligand.

With alkyl spacer units, helicates have been shown to preferentially form when there is an even number of methylene groups, whereas mesocates are favoured with an odd number of methylene groups (**Figure 1.9**).[22a] Linear alkyl chains are known to be the most stable when a *zigzag* orientation of alkyl substituents is obtained, which ultimately results in the complexes stereochemical preference. This preference can be further explained in terms of the geometries favoured by the helicate and mesocate complexes, with the macrocycles preferentially forming to maximize their overall stability. Helicates typically form a conformation which resembles an 'S' whereby the ligands are wrapped around the metal centers in a more or less linear fashion.[22a] Mesocates however tend to adopt more of a 'C' type conformation.[22a]

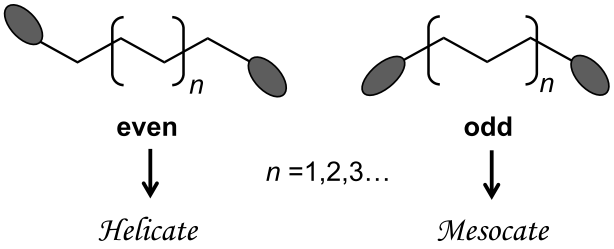

Figure 1.9: Representation of aliphatic ligands and determination of preferred conformation.[22a]

When functionalities other than aliphatic units are used in the spacer region, the stereochemical preference can be determined more simplistically. In these cases, helicates are typically favoured with more rigid spacer groups, for example one that is aromatic.[22] This is a result of the 'C'-type geometry required by the mesocate conformation, which is not favoured on the basis of steric strain.

While metallomacrocycles have a vast number of potential applications, it is more specifically their role as metalloreceptors that is of particular interest for the initial part of my project. Some of the different properties of metalloreceptors as well as their potential applications are described below.

1.3 Metalloreceptors

Metalloreceptors are part of the metallomacrocycle family, but may be further classified by their ability to act as molecular receptors for substrates.[3, 12] There has been tremendous interest in recent years in designing and developing supramolecular systems that are capable of recognizing and binding substrates.[23] There are a wide variety of different molecules that could be recognized and bound inside the cavity of a metalloreceptor, some of which include drug molecules, environmental toxins and reactive molecules.[23b, c, 24]

The motivation and reason for this interest is the role that many of the substrates play in biology, and medicine, among many other fields.

There are many different examples of metalloreceptors in literature, ranging from circular complexes,[20] to squares,[15] cages,[25] and many more. Harding *et al.* have done considerable research on metalloreceptors, with particular attention on the effect that guest molecules have upon incorporation into a metallomacrocycle.

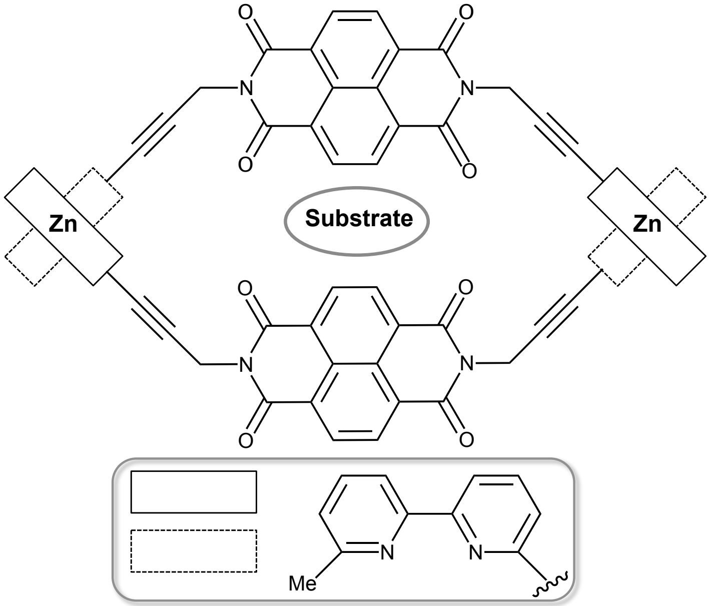

Figure 1.10: Metallomacrocycle formed with two ligands and two Zn^{II} ions in the presence of a substrate molecule. The metallomacrocycle contains pyromellitimide spacers, connected to 6,6'-disubstituted-2,2'-bipyridines through a propynyl linker.[26]

One example includes formation of a metallomacrocycle with various metal ions (Zn^{II}, Cd^{II} or Cu^{I}), which has the capability of recognizing an aromatic substrate molecule within its cavity (**Figure 1.10**). The metallomacrocycle was formed with a [2+2] stoichiometry in the presence of all three metal ions, Zn^{II}, Cd^{II} and Cu^{I} and upon addition of an aromatic substrate molecule all of the complexes were capable of substrate recognition. For the complex with Zn^{II} the presence of the aromatic substrate within the cavity was observed by a color change, indicative of a charge transfer between the spacer and substrate molecules.[26] The results obtained by using Cu^{I} instead of Zn^{II} were comparable, which suggests that the two metal ions are structurally similar.[26] Again, the results for Cd^{II} were comparable to those for Zn^{II}, possibly due to the similar coordination chemistry between the two metal ions.[26] This example highlights the formation of a metallomacrocycle that can also act as a metalloreceptor with specific substrate molecules.

Kruger *et al*. developed an example of a helicate complex capable of binding small anionic guests (**Figure 1.11**). The guest molecules within the cavity of the metalloreceptor interact through hydrogen bonding between the amide proton as well as the bipyridine H_6, as the primary mode of interaction.[23a] Another factor that contributed to substrate binding was the available positive charge, coming from the Fe^{II} metal centers.[23a] Several observations were made in this study. First, the free ligand only interacted very weakly in the presence of an anionic guest molecule. Second, the host complex was selective for chloride anions, with other anions showing little to no changes through NMR spectroscopy titrations. Finally, upon introducing the chloride anions to the metal-ligand complex, it adopts a helical conformation, consistent with a $[(Fe_2(\mathbf{L})_3)(Cl)_2]^{2+}$ stoichiometry (**Figure 1.11b**).

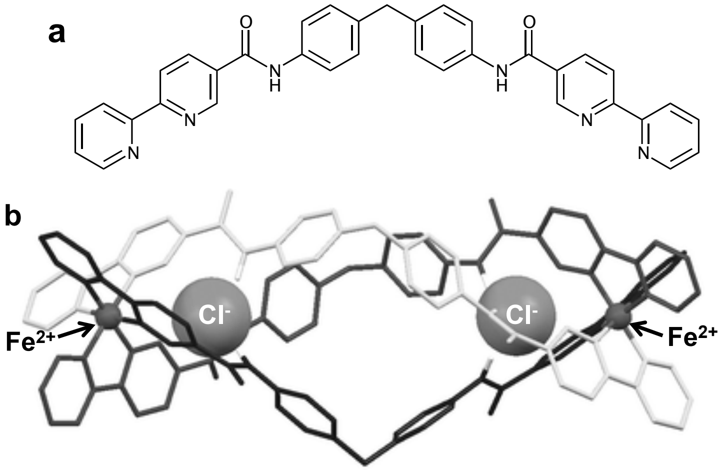

Figure 1.11: a) Structure of the amide-based bis-bipyridine ligand b) Model of the helicate complex with the proposed mode of chloride (Cl^-) binding within the intra-helical cavity.[23a]

The most important characteristics of these metalloreceptors are their selectivity and specificity. The incorporation of metals into the macrocyclic architecture has opened up the opportunity for more robust receptors and recognition of both ionic and neutral guest molecules.[23b, c, 27] Recognition of potential guest molecules is dictated by the size, shape and additional properties of the corresponding metalloreceptors, which in turn results in extraordinary accuracy and controllability.

Using 'click' chemistry (described below), we proposed a ligand design with the end synthetic goal of a metalloreceptor.

1.4 Click Chemistry – An Overview

The term 'click chemistry,' was devised simultaneously in 2002 by Sharpless and Tornøe & Meldal to describe a set of reactions used to rapidly assemble molecules with a specific structure and function from smaller molecular subunits.[28] In order for a reaction to be considered 'click', there are a set of stringent conditions that must be met, meaning the reactions must: "*be modular, be wide in scope, be high yielding, produce only inoffensive by-products, be regioselective, be easy to perform, and use benign solvents that are* *easy to remove*."[28b] Despite the numerous conditions that must be met, click chemistry has been and continues to be, readily utilized, because the reactions are easy to perform, give the anticipated product(s) in high yield, work under several conditions and are tolerant to the nature of the groups being connected to one another.[29] A number of reactions have been identified as 'click' and as such, follow the rigorous reaction conditions outlined above (**Scheme 1.1**). Some examples include, but are not limited to, nucleophilic ring opening reactions, non-aldol carbonyl chemistry, additions to carbon-carbon multiple bonds (oxidative addition and Michael additions of nucleophile-hydrogen reactants) and cycloadditions reactions (1,3-dipolar cycloadditions reactions).[30]

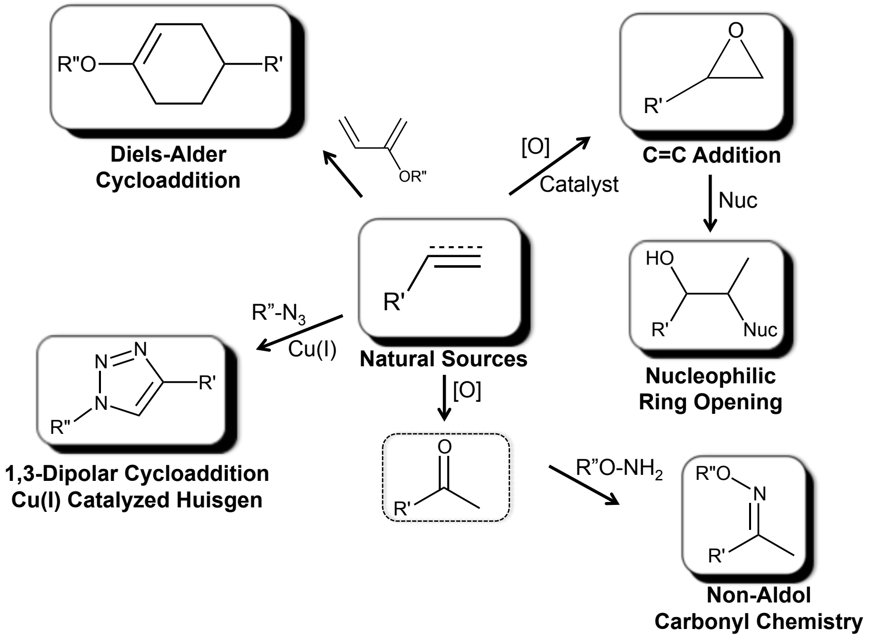

Scheme 1.1: A selection of reactions that fit the 'click' reaction criteria.[30] *Note*: 'Nuc' indicates a nucleophile and [O] corresponds to addition to a C=C bond by oxidative addition.

1.4.1 Copper-Catalyzed Azide-Alkyne Cycloaddition (CuAAC)

The "gold standard" for click chemistry is undoubtedly the Huisgen 1,3-dipolar cycloaddition reaction, which yields exclusively the 1,4-disubstituted-1,2,3-triazole starting from an alkyne and an azide (**Scheme 1.2**).[29-30] Much like all other reactions that have been granted 'click' status, the Huisgen reaction meets all of the rigorous criteria. While the uncatalyzed azide-alkyne cycloaddition (AAC) reaction has been known since 1893 and has been extensively studied, the reaction yielded a mixture of 1,4- and 1,5-disubstituted products and required very high reaction temperatures.[29] The copper-catalyzed cycloaddition reaction eliminated the need for high temperatures, significantly decreased reaction times and solely produced the desired 1,4-disubstituted product.[29, 31, 32]

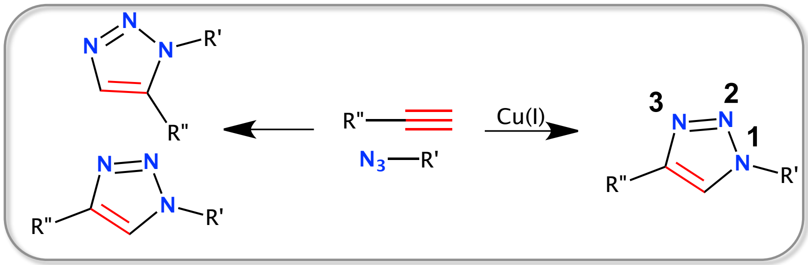

Scheme 1.2: The Cu^I catalyzed Huisgen 'click' reaction resulting in exclusive formation of the 1,4-triazole, while the thermal Huisgen cycloaddition yields a mixture of 1,4 and 1,5-triazole stereoisomers.[30]

Despite its mechanistic complexity, the CuAAC reaction has been readily accepted thanks to its straightforward reaction conditions along with high yields.

1.4.2 'Click-Triazole': Applications

The triazole heterocycle has numerous applications, which is why it has received tremendous attention in recent years. 'Click' triazoles are now seeing use as amide mimics, C-H hydrogen bond donor units, as well as in catalysis, among many others.[32a, 33] The 'click' 1,4-disubstituted-1,2,3-triazole also has the potential to act as a bridging or chelating ligand.[32a] Bridging typically occurs through the N2 or N3 nitrogen, with many examples of this type having been obtained and characterized.[32a, 34]

A study by Crowley *et al.* demonstrated that di-1,2,3-triazole chelating units could be used to generate a self-assembled metallomacrocycle, much like those obtained by using the commonly used dipyridyl chelates (**Figure 1.12**).[35] A family of di-1,4-substituted-1,2,3-triazole ligands were generated by varying the central and peripheral substituents.

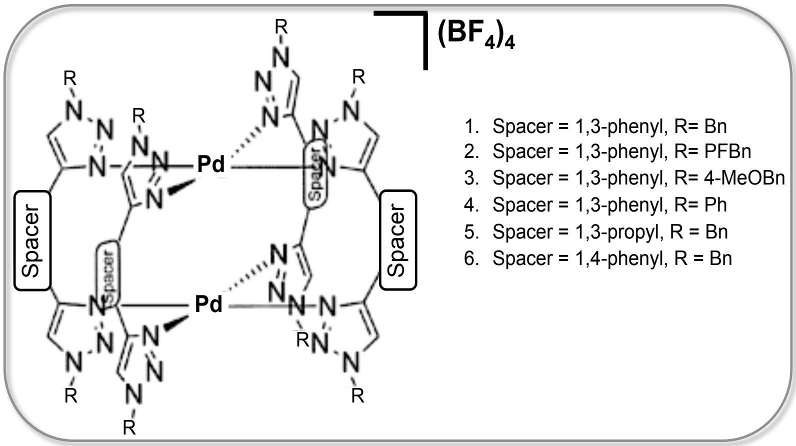

Figure 1.12: Palladium 'click' cage complexes formed from ligands (variable spacer units and peripheral substituents) combined with $[Pd(CH_3CN)_4](BF_4)_2$ in CD_3CN or DMSO-d_6.[35] *Note*: 'R= PFBn' refers to 4-fluorobenzonitrile.

Also of interest were the effects that modifying the spacer and peripheral substituents had on complex formation. Spacer units and substituents with varying geometries and flexibilities and the corresponding ligands (2 equiv.) were combined with $[Pd(CH_3CN)_4](BF_4)_2$ (1 equiv.). In nearly all instances the coordinatively saturated, quadruple stranded helical cage was obtained.[35] When the 1,4-phenyl, rigid aromatic spacer was used with a benzyl (Bn) 'R' group, the saturated complex did not form and a polymeric species was observed instead. This result was attributed to steric interactions between the aromatic spacer units, which made the polymer species more stable than the anticipated cage complex.[35] Overall, it was demonstrated that di-1,4-substituted-1,2,3-triazoles may be used for self-assembly of helicate cages.[35]

1.4.2.1 Triazole-Pyridine: Applications

Triazole-pyridine chelating units are also capable of being employed in the self-assembly of supramolecular architectures. Our group is interested in new bidentate ligands, whereby one of the pyridine functionalities is replaced with triazole, forming a triazole-pyridine chelating unit (**Figure 1.13**).

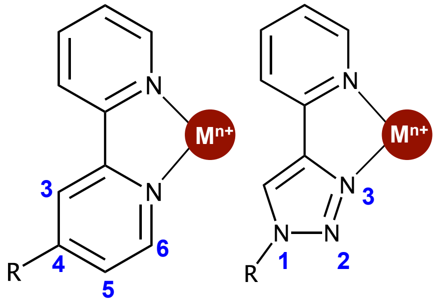

Figure 1.13: Bipyridine and triazole-pyridine chelating units.

Traditional polypyridines, most commonly 2,2-bipyridines, are tedious to synthesize and purify.[33, 36] Comparison of triazole and pyridine structures shows that both are conjugated rings, and contain a nitrogen atom capable of coordinating a metal ion. As a result of these similarities, replacing pyridine with a triazole becomes attractive because of readily available starting materials and easy functionalization through the N1 nitrogen of the triazole. Similar substituent orientation between the traditional 4-substituted-2,2'-bipyridine and triazole-pyridine functionalities further justifies replacement of the bipyridine-chelating unit (**Figure 1.14**).

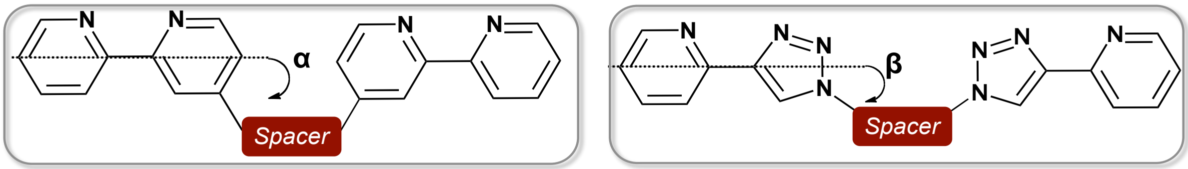

Figure 1.14: Comparison of the substituent orientation and overall structures of the bipyridine and triazole-pyridine chelating units.

1.5 Previously Studied Ligands

The scope of my thesis stems from work that was previously carried out within our lab, whereby a triazole-pyridine chelating unit replaced the traditional 2,2'-bipyridine functionality. The ligand design features two triazole-pyridine chelating units separated by a variable spacer region. Initially synthesized by Crowley, and reproduced by Caroline Melan (4th year student, Jan-Aug 2011) within our group, were the **X1** and **C3** ligands.[34, 37] The **X1** ligand featured a *p*-xylyl spacer region, whereas the **C3** ligand was aliphatic in nature with a propyl spacer (**Figure 1.15**). The ligands were complexed with metal ions of traditional octahedral geometry, Fe^{II} and Ni^{II} in solution and their properties analyzed (Caroline Melan, 4th year student, Jan-Aug 2011).

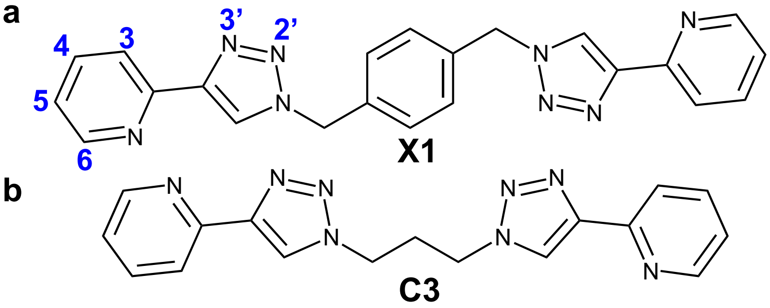

Figure 1.15: Previously synthesized a) **X1** ligand, with a *p*-xylyl spacer region and b) **C3** ligand with a propyl spacer region.[34, 37-38]

1.5.1 Previously Studied X1 Ligand

The **X1** ligand and the complexes formed with Fe^{II} and Ni^{II} were characterized by single crystal X-ray crystallography and UV-vis spectroscopy, and Fe^{II} complexes were also characterized by NMR spectroscopy (Nan Wu, NSERC-USRA summer research student, 2010 assisted by Dr. Olivier Fleischel, and Caroline Melan, 4th year student, Jan-Aug 2011).

The complexes formed with the non-coordinating BF_4^- anion were saturated, with a 2:3 metal-to-ligand ratio, consistent with a $[Fe_2(\mathbf{X1})_3]^{4+}$ stoichiometry. When the complex is considered saturated all of the coordination sites that are available from the metal center are occupied by the ligand. In the unsaturated complex (discussed below) there are available coordination sites that may be occupied by anions, or potentially substrate molecules. The stoichiometry of both the Fe^{II} and Ni^{II} complexes were confirmed by X-ray crystallography. The crystal structures gave further insight into the physical properties of the complexes and showed the Fe^{II} and Ni^{II} complexes were isostructural to one another (**Figure 1.16)**. Also indicated from the X-ray structures were the chiralities of the metal centers, which were identical in both chelating units within the same complex, corresponding to a helicate arrangement. This behaviour may be anticipated based on the *even-odd* rule, with the *p*-xylyl spacer acting as an extended CH_2-CH_2 bridge.[22a] The *even-odd* rule proposed by Albrecht can be applied here, which predicts a mesocate structure for compounds containing spacers with an odd number of carbons.[22a]

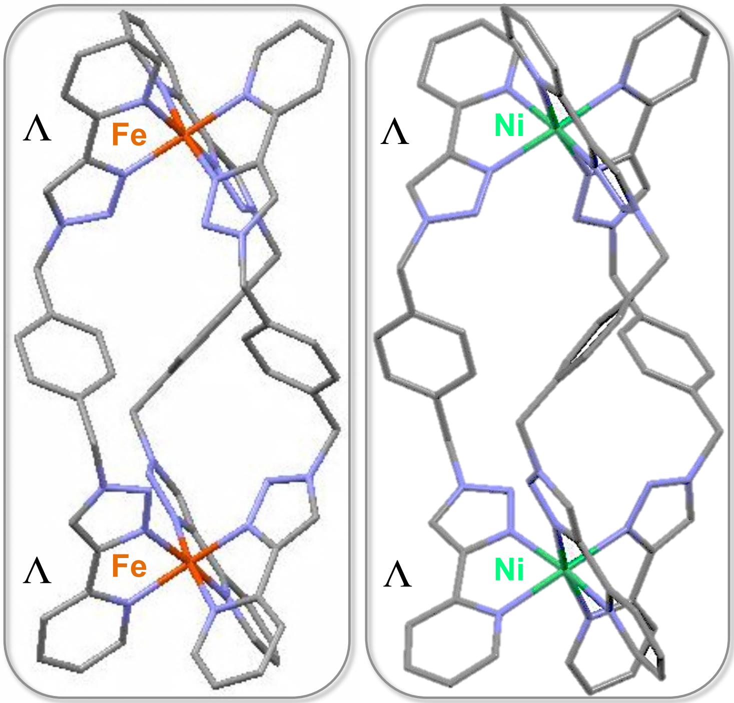

Figure 1.16: Crystal structure of $[Fe_2(\mathbf{X1})_3](BF_4)_4$ and $[Ni_2(\mathbf{X1})_3](BF_4)_4$ with Fe^{II} and Ni^{II} ions indicated, N in purple, and C in grey (H atoms, solvent molecules and counter ions omitted for clarity). Selected bond distances (Å): Fe^{II}-Fe^{II}: 11.391, Fe^{II}-$N_{Triazole}$: 1.939, Fe^{II}-$N_{Pyridine}$: 1.997, Ni^{II}-Ni^{II}: 11.468, Ni^{II}-$N_{Triazole}$: 2.057, Ni^{II}-$N_{Pyridine}$: 2.102.[37-38, 39]

The stoichiometry was also confirmed through UV-vis titration experiments with **X1** and metal ions, Fe^{II} and Ni^{II} in acetonitrile (Caroline Melan, 4th year student, Jan-Aug 2011) (**Figure 1.17**). Both complexes showed a maximum of the absorbance *vs*. $[(n(M^{II}) / n\mathbf{X1}]$ graph at 0.67 (M = Fe^{II} or Ni^{II}), which indicates a stoichiometry of $[Fe_2(\mathbf{X1})_3]^{4+}$ and $[Ni_2(\mathbf{X1})_3]^{4+}$ in the presence of non-coordinating anions. The UV-vis titration data for the $[Fe_2(\mathbf{X1})_3](BF_4)_4$ complex is shown below, and the $[Ni_2(\mathbf{X1})_3](BF_4)_4$ data was consistent, also confirming a 2:3 metal: ligand stoichiometry.

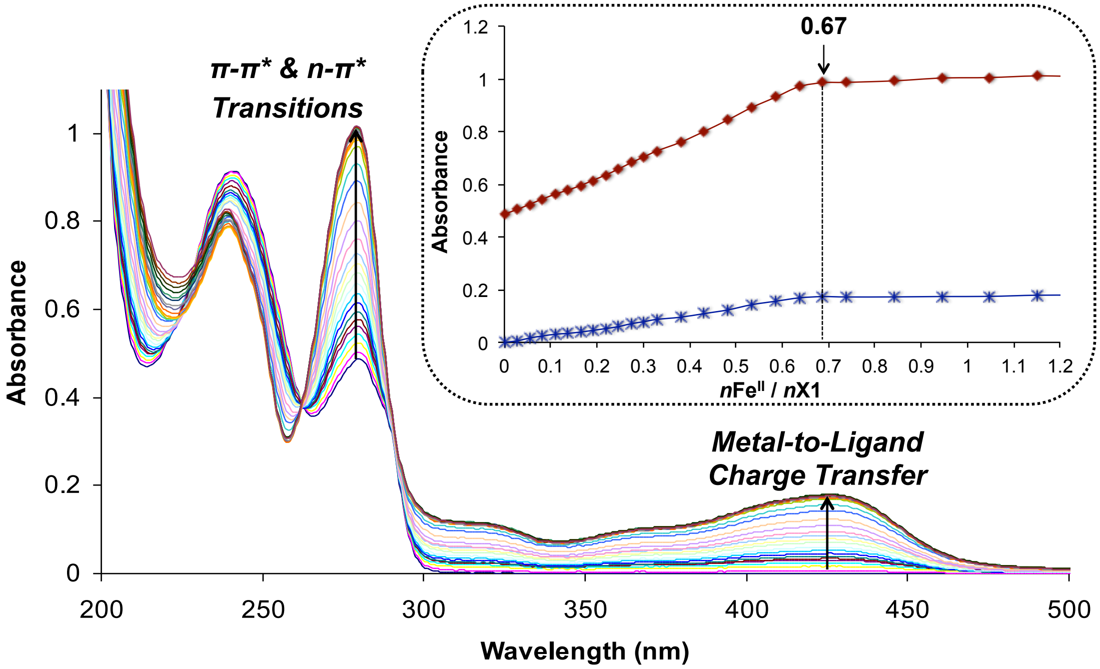

Figure 1.17: UV-vis titration spectrum for **X1** with $[Fe(H_2O)_6](BF_4)_2$ in CH_3CN. *Inset*: Absorbance *vs.* [*n*Fe^{II} / *n***X1**] ratio for peaks at 425 nm and 280 nm. *Note:* '*n*' refers to number of moles.[37, 39]

UV-vis titrations in the presence of a coordinating anion, such as chloride or acetate, were also performed with **X1** and Fe^{II} and Ni^{II} metal ions (Nan Wu, Research summer student, 2010). The complexes that formed were unsaturated and double-stranded in nature (2:2 metal: ligand) in solution (**Figure 1.18**). Unlike the titrations with the BF_4^- anion, which showed a maximum in the absorbance *vs.* [*n*(M^{II}) / *n***X1**] graph at 0.67, the coordinating anions gave a maximum peak around 1.0. This maximum is consistent with the 2: 2, metal: ligand stoichiometry, indicating the unsaturated complex is present in solution. The spectrum below corresponds to the titration with **X1** and $[Ni(H_2O)_4(OAc)_2]$ in methanol and the titration with $[Fe(H_2O)_4Cl_2]$ confirmed the unsaturated complex as well.

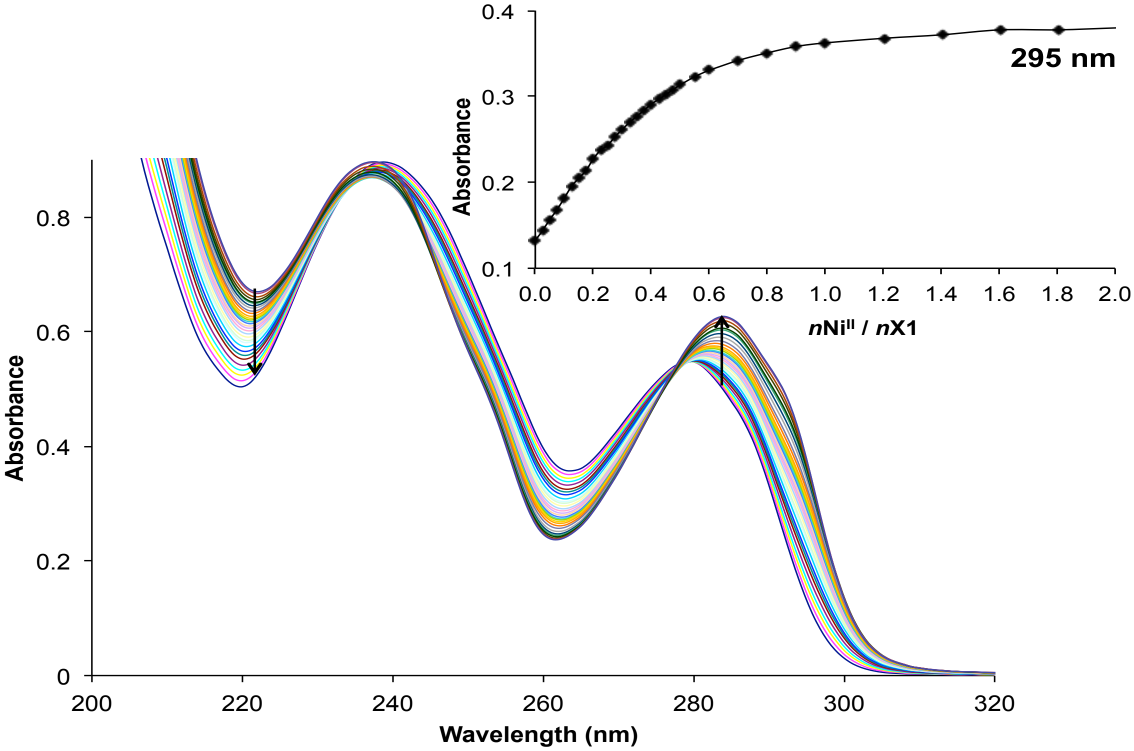

Figure 1.18: UV-vis titration spectrum for **X1** with [Ni(H_2O)$_4$(OAc)$_2$] in CH_3OH. *Inset*: Absorbance *vs.* [*n*Ni^{II} / *n***X1**] ratio for peak at 295 nm (Nan Wu, NSERC-USRA summer research student, 2010).

This result was what prompted the design for my initial ligand, which is discussed in detail in Chapter 2. The unsaturated complex observed with **X1** has available binding sites, whereby potential substrate molecules may be recognized. In this way we were hoping to expand on the knowledge obtained from **X1**, and apply it to a similar ligand with a slightly larger hydrophobic cavity.

1.5.2 Previously Studied C3 Ligand

As with **X1**, **C3** was synthesized and complexed with octahedral metal ions Fe^{II} and Ni^{II}. The obtained complexes were characterized by NMR spectroscopy, UV-vis spectroscopy and X-ray crystallography (Caroline Melan, 4th year student, Jan-Aug 2011). The X-ray crystal structure shown below again indicates that the Fe^{II} and Ni^{II} complexes are isostructural with one another, with identical metal-metal distances (**Figure 1.19**). Unlike **X1** however, the complexes formed with **C3** have opposite chirality at the metal centers, resulting in a *mesocate* structure.[37, 39] The *even-odd* rule, proposed by Albrecht can be applied here, which predict a mesocate structure for compounds containing spacers with an odd number of carbons.[22a]

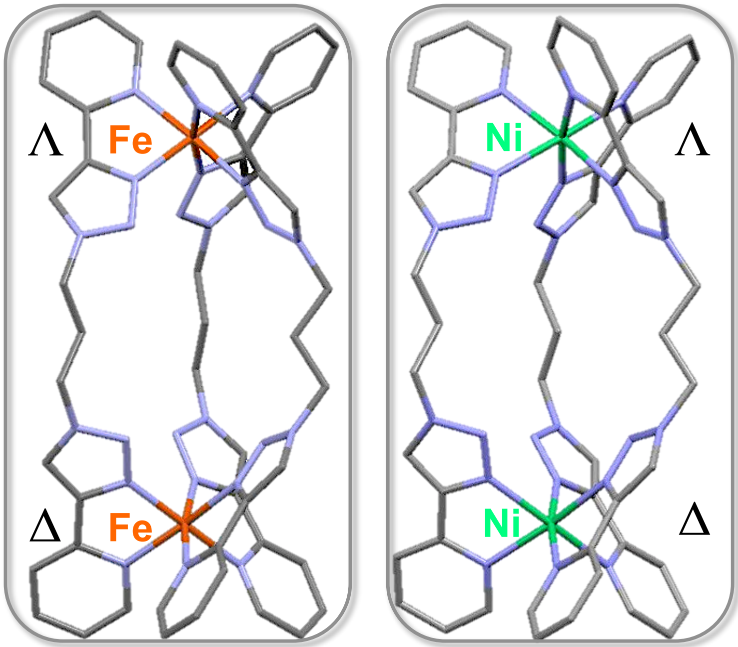

Figure 1.19: Single X-ray crystal structure of $[Fe_2(\mathbf{C3})_3](BF_4)_4$ and $[Ni_2(\mathbf{C3})_3](BF_4)_4$ with Fe^{II} and Ni^{II} ions indicated, N in purple, and C in grey (H atoms, solvent molecules and counter ions omitted for clarity). Selected bond distances (Å): M^{II}-M^{II}: 9.88, Fe^{II}-$N_{Triazole}$: 1.925-1.945, Fe^{II}-$N_{Pyridine}$: 1.995-2.012, Ni^{II}-$N_{Triazole}$: 2.042-2.085, Ni^{II}-$N_{Pyridine}$: 2.100-2.125.[37-38, 39]

UV-vis titration experiments were performed to determine the stoichiometry of the complexes formed between **C3** and $[Fe(H_2O)_6](BF_4)_2$ and $[Ni(H_2O)_6](BF_4)_2$ in solution (Caroline Melan, 4th year student, Jan-Aug 2011) (**Figure 1.20**). Unlike with **X1**, only non-coordinating anions were explored, because the aliphatic spacer region is not overly conducive to substrate recognition.

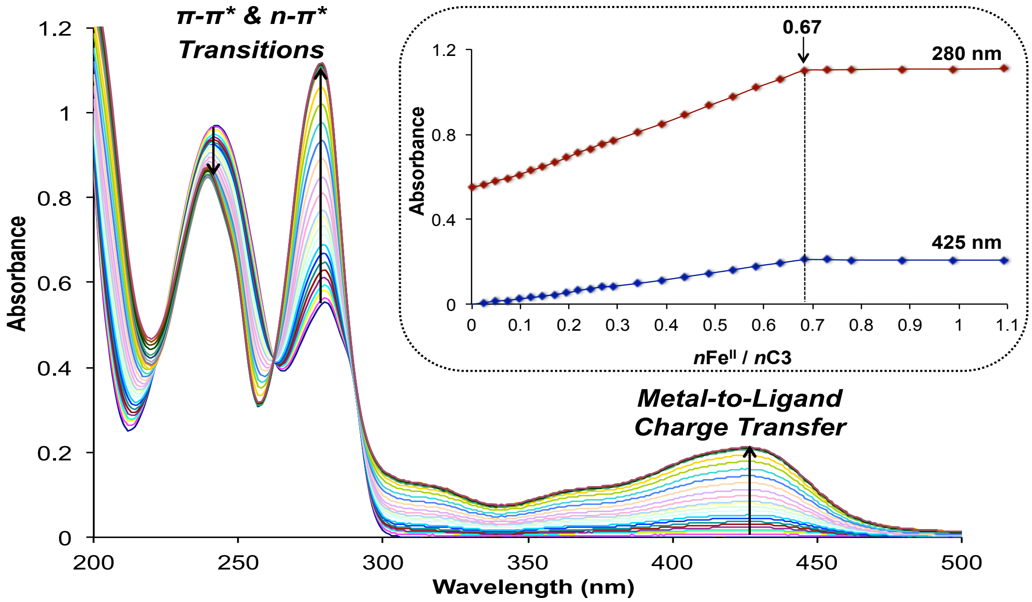

Figure 1.20: UV-vis titration spectrum for **C3** with $[Fe(H_2O)_6](BF_4)_2$ in CH_3CN. *Inset*: Absorbance *vs*. [nFe^{II} / n**C3**] ratio for peaks at 425 nm and 280 nm.[37, 39]

Much like with **X1**, the preferred stoichiometry in solution, with non-coordinating anions is that of the saturated, triple-stranded complex $[Fe_2(\mathbf{C3})_3]^{4+}$. From **Figure 1.20** (*inset*) it can be seen that the maximum value for absorbance *vs*. [nFe^{II} / n**C3**] graph occurs at 0.67, which is consistent with a 2:3 metal: ligand stoichiometry. While the UV-vis titrations with **C3** were quite uneventful, there were magnetism results that were not expected. First, a brief background on the concept of spin crossover is described below.

1.5.2.1 Spin Crossover – A Brief Introduction

There remains ongoing interest in the synthesis and characterization of spin crossover (SCO) materials because of their applications in the molecular memory and sensing industries as well as in visual display devices.[40] An important characteristic that makes SCO materials so appealing in these industries is that they can display *bistability*.[41] This feature allows SCO materials to access two different electronic states at the same temperature.[41]

The phenomenon of spin crossover is related to the molecular architectures and their relationship between the dependence of the ligand field strength on metal-ligand distance and electron-electron repulsion.[42] Spin crossover is indicated by a change in spin state, seen in certain metal complexes when an external perturbation is applied to the system.[43] The most common is a change in temperature, however others include changes in pressure, irradiation as well as an external magnetic field.[43] Spin crossover can occur in d^4-d^7 transition metals, with the Fe^{II} metal ion and d^6 configuration being the most common (**Figure 1.21**).[44]

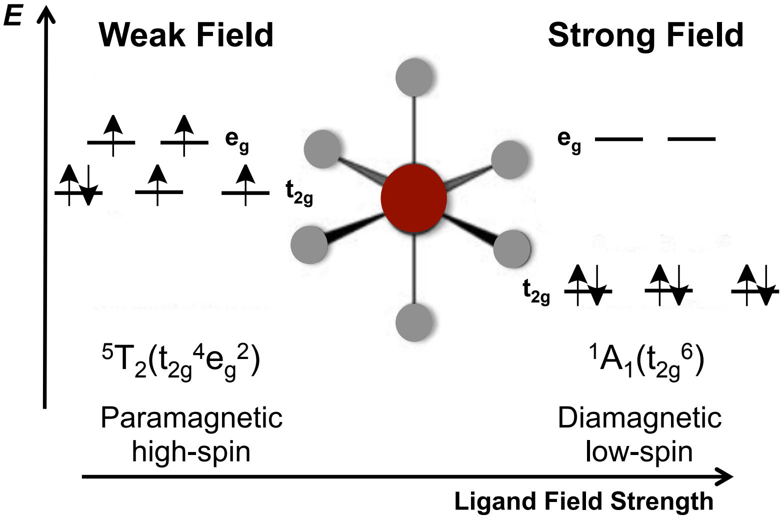

Figure 1.21: Electronic configuration for a d^6 Fe^{II} ion in both the high-spin (HS) and low-spin (LS) states.[44]

1.5.2.2 Previously Studied C3 Magnetism Results

It was observed that the [Fe$_2$(**C3**)$_3$]$^{4+}$ complex displayed spin crossover behaviour at elevated temperatures. In the temperature range of 2.5-300 K a gradual spin transition from low-spin and diamagnetic, to high-spin and paramagnetic, was observed although the full transition was not seen.[39] This was attributed to the fact that the full spin crossover was likely occurring at temperatures higher than those that were examined.[39]

With these results in mind, two more ligands were designed, which will be discussed in detail in Chapter 3. We were interested in probing the effects that aliphatic spacer length had on the resulting complexes and perhaps obtaining other complexes that demonstrated spin crossover behaviour.

1.6 Research Objectives

1.6.1 Synthesis of Aromatic Spacers and Metal Complexes

Our goal was to synthesize new ligands with a naphthalene spacer region capable of recognizing and binding substrates through electrostatic interactions and hydrophobic effects. In these ligands, the traditional 2,2'-bipyridine functionality was replaced with a triazole-pyridine chelating unit. We started by using a naphthalene spacer region to increase the size (length) of the previously synthesized **X1** ligand, which featured a *p*-xylyl spacer (Caroline Melan, 4th year student, Jan-Aug 2011) (**Figure 1.15 a**).[34, 37-38]

We aimed to synthesize two new ligands, both containing a bis-substituted naphthalene spacer, but featuring two different naphthalene substitution patterns. The initial ligand (**N1**) has a 2,6-disubstituted-naphthalene spacer connected through methylene linkers to the triazole pyridine chelating units (**Figure 1.22 a**). The **N2** ligand has a 2,7-disubstituted naphthalene spacer with ester functionalities connecting the spacer to the methylene linkers and two triazole-pyridine chelating units (**Figure 1.22 b**). Compared to **N1**, this ligand is anticipated to have a longer intramolecular metal-metal distance and subsequently a larger cavity for potential substrate molecules.

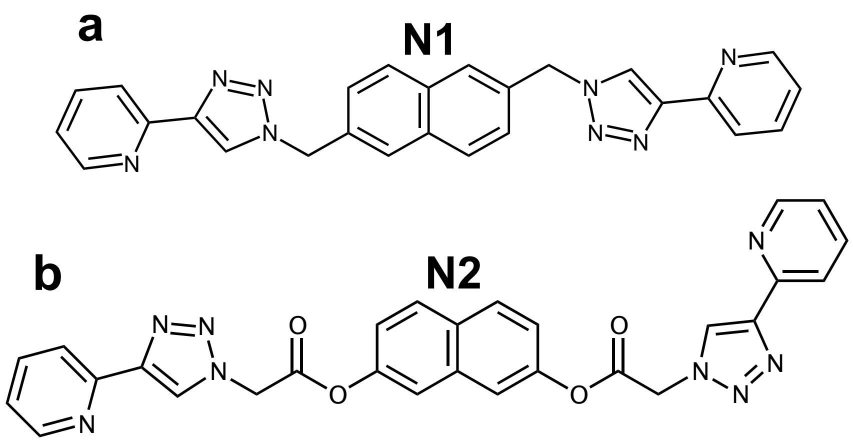

Figure 1.22: Structures of the target ligands with naphthalene spacer regions, varying substitution patterns and functional group connectivity to the triazole-pyridine unit.

After synthesizing the ligands we will complex them with the octahedral metal centers, Fe^{II} and Ni^{II} and study the physical properties of the resulting dinuclear complexes. The **N1** complexes will be examined with both coordinating and non-coordinating anions to observe if there are any variable structural properties observed between the corresponding complexes.

Some features of the desired metallomacrocycles should enable them to potentially accommodate a substrate molecule. In particular, these features include a hydrophobic cavity as well as coordinatively unsaturated sites (if the substrate is a coordinating hydrophobic species). Many different types of substrate molecules may be bound within this cavity, including drug molecules, environmental toxins, or even reactive molecules. We are particularly interested in the encapsulation of medically relevant molecules within the hydrophobic cavity of the spacer region.

1.6.2 Synthesis of Aliphatic Spacers and Metal Complexes

More of a conceptual study was carried out with the ligands containing aliphatic spacers, focusing on how spacer length affects self-assembly properties of the corresponding complexes. We were also interested in probing how the complexes varied when more flexibility was introduced. By varying the spacer length we were hoping to assess the self-assembly modes of the metallomacrocyclic architectures, as well as to tune the metal-metal distances. The ligands were synthesized with increasing spacer length (butyl and pentyl) and complexed with octahedral metal ions Fe^{II} and Ni^{II} (**Figure 1.23**).

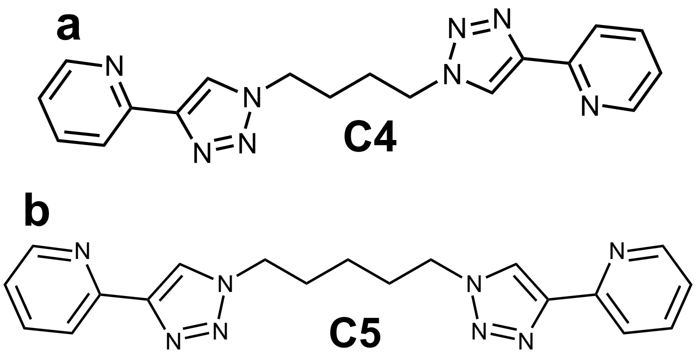

Figure 1.23: Structures of the target ligands with a) butyl and b) pentyl aliphatic spacer regions.

With the characterization of **C3** available, we were hoping to observe some properties of the ligands that may be correlated to the nature of the spacer. Also, since [Fe$_2$(**C3**)$_3$]$^{4+}$ showed spin crossover behaviour, the possibility of similar behaviours in these new complexes will also be probed.

1.7 References

1. (a) van Veggel, F. C. J. M.; Verboom, W.; Reinhoudt, D. N., Metallomacrocycles: Supramolecular Chemistry with Hard and Soft Metal Cations in Action. *Chem. Rev.* **1994**, *94* (2), 279-299; (b) Northrop, B. H.; Zheng, Y.-R.; Chi, K.-W.; Stang, P. J., Self-Organization in Coordination-Driven Self-Assembly. *Acc. Chem. Res.* **2009**, *42* (10), 1554-1563; (c) Fujita, M.; Ogura, K., Supramolecular Self-Assembly of Macrocycles, Catenanes, and Cages through Coordination of Pyridine-Based Ligands to Transition Metals. *Bull. Chem. Soc. Jpn.* **1996**, *69* (6), 1471-1482.
2. Albrecht, M.; Fröhlich, R., Symmetry Driven Self-Assembly of Metallo-Supramolecular Architectures. *Bull. Chem. Soc. Jpn.* **2007**, *80* (5), 797-808.
3. Lehn, J.-M., Supramolecular Chemistry - Scope and Perspectives: Molecules - Supermolecules - Molecular Devices. *Journal of Inclusion Phenom.* **1988**, *6*, 351-396.
4. Seidel, S. R.; Stang, P. J., High-Symmetry Coordination Cages via Self-Assembly. *Acc. Chem. Res.* **2002**, *35*, 972-983.
5. Steel, P. J., Ligand Design in Multimetallic Architectures: Six Lessons Learned. *Acc. Chem. Res.* **2005**, *38*, 243-250.
6. (a) Hannon, M. J., Supramolecular DNA Recognition. *Chem. Soc. Rev.* **2007**, *36*, 280-295; (b) Philp, D.; Stoddart, J. F., Self-Assembly in Natural and Unnatural Systems. *Angew. Chem. Int. Ed. Engl.* **1996**, *35*, 1154-1196.
7. Vendruscolo, M.; Zurdo, J.; MacPhee, C. E.; Dobson, C. M., Protein folding and misfolding: a paradigm of self-assembly and regulation in complex biological systems. *Phil. Trans. R. Soc. Lond. A.* **2003**, *361*, 1205-1222.
8. (a) Leininger, S.; Olenyuk, B.; Stang, P. J., Self-Assembly of Discrete Nanostructures Mediated by Transition Metals. *Chem. Rev.* **2000**, *100*, 853-908; (b) Zafar, A.; Geib, S. J.; Hamuro, Y.; Carr, A. J.; Hamilton, A. D., Hydrogen Bonding Control of Molecular Self-Assembly: Aggregation Behavior of Acylaminopyridine–Carboxylic Acid Derivatives in Solution and the Solid State. *Tetrahedron* **2000**, *56*, 8419-8427; (c) Hamilton, A. D., In *Comprehensive Supramolecular Chemistry*, Lehn, J.-M., Ed. Permagon Press: 1995; Vol. 9; (d) Garcia-Tellado, F.; Geib, S. J.; Goswami, S.; Hamilton, A. D., Molecular recognition in the Solid State: Controlled Assembly of Hydrogen-Bonded Molecular Sheets. *J. Am. Chem. Soc.* **1991**, *113*, 9265-9269.
9. (a) Sijbesma, R. P.; Meijer, E. W., Self-Assembly of Well-Defined Structures by Hydrogen Bonding. *Curr. Opin. Colloid Interface Sci.* **1999**, *4*, 24-32; (b) McMorran, D. A., Ag(I)-Based Tectons for the Construction of Helical and *meso*-Helical Hydrogen-Bonded Coordination Networks. *Inorg. Chem.* **2008**, *47*, 592-601.

10. Fujita, M., Metal-Directed Self-Assembly of Two and Three-Dimensional Synthetic Receptors. *Chem. Soc. Rev.* **1998**, *27*, 417-425.

11. Fochi, F.; Jacopozzi, P.; Wegelius, E.; Rissanen, K.; Cozzini, P.; Marastoni, E.; Fisicaro, E.; Manini, P.; Fokkens, R.; Dalcanale, E., Self-Assembly and Anion Encapsulation Properties of Cavitand-Based Coordination Cages. *J. Am. Chem. Soc.* **2001**, *123*, 7539-7552.

12. Lehn, J.-M.; Rigault, A.; Siegal, J.; Harrowfield, J.; Chevrier, B.; Moras, D., Spontaneous Assembly of Double-Stranded Helicates from Oligobipyridine Ligands and Copper(I) Cations: Structure of an Inorganic Double Helix. *Proc. Natl. Acad. Sci. USA* **1987**, *84* (9), 2565-2569.

13. Holliday, B. J.; Mirkin, C. A., Strategies for the Construction of Supramolecular Compounds through Coordination Chemistry. *Angew. Chem. Int. Ed.* **2001**, *40*, 2022-2043.

14. Bilyk, A.; Harding, M. M.; Turner, P.; Hambley, T. W., Octahedral Non-Helical bis(bisbipyridyl) Metallomacrocycles. *J. Chem. Soc. Dalton Trans.* **1995**, (24), 2549-2553.

15. Stang, P. J.; Cao, D. H.; Chen, K.; Gray, G. M.; Muddiman, D. C.; Smith, R. D., Molecular Architecture via Coordination. *J. Am. Chem. Soc.* **1997**, *119*, 5163-5168.

16. Hannon, M. J.; Childs, L. J., Helices and Helicates: Beautiful Supramolecular Motifs with Emerging Applications. *Supramol. Chemistry* **2004**, *16* (1), 7-22.

17. Saalfrank, R. W.; Dresel, A.; Seitz, V.; Trummer, S.; Hampel, F.; Teichert, M.; Stalke, D.; Stadler, C.; Daub, J.; Schunemann, V.; Trautwein, A. X., Topologic Equivalents of Coronands, Cryptands and Their Inclusion Complexes. *Chem. Eur. J.* **1997**, *3* (12), 2058-2062.

18. (a) Piguet, C.; Bernardinelli, G.; Hopfgartner, G., Helicates as Versatile Supramolecular Complexes. *Chem. Rev.* **1997**, *97*, 2005-2062; (b) Albrecht, M., Supramolecular Templating in the Formation of Helicates. *Top. Curr. Chem.* **2004**, *248*, 105-139.

19. He, Y.; Ye, T.; Su, M.; Zhang, C.; Ribbe, A. E.; Jiang, W.; Mao, C., Hierarchical Self-Assembly of DNA into Symmetric Supramolecular Polyhedra. *Nature* **2008**, *452*, 198-201.

20. Albrecht, M., "Let's Twist Again" - Double-Stranded, Triple-Stranded, and Circular Helicates. *Chem. Rev.* **2001**, *101*, 3457-3497.

21. Albrecht, M.; Kotila, S., Formation of a "*Meso*-Helicate" by Self-Assembly of Three Bis(catecholate) Ligands and Two Titanium(IV) Ions. *Angew. Chem. Int. Ed. Engl.* **1995,** *34*, 2134-2137.

22. (a) Albrecht, M., How Do They Know? Influencing the Relative Stereochemistry of the Complex Units of Dinuclear Triple-Stranded Helicate-Type Complexes. *Chem. Eur. J.* **2000,** *6*, 3485-3489; (b) Xu, J.; Parac, T. N.; Raymond, K. N., *Meso* Myths: What Drives Assembly of Helical *vs*. *Meso*-[M_2L_3] Clusters? *Angew. Chem. Int. Ed.* **1999,** *38*, 2878-2882.

23. (a) Goetz, S.; Kruger, P. E., A New Twist in Anion Binding: Metallo-Helicate Hosts for Anionic Guests. *Dalton Trans.* **2006**, 1277-1284; (b) Wu, B.; Yang, J.; Huang, X.; Li, S.; Jia, C.; Yang, X.-J.; Tang, N.; Janiak, C., Anion binding by metallo-receptors of 5,5'-dicarbamate-2,2'-bipyridine ligands. *Dalton Trans.* **2011**, *40*, 5687-5696; (c) Kumar, A.; Sun, S.-S.; Lees, A. J Directed Assembly Metallocyclic Supramolecular Systems for Molecular Recognition and Chemical Sensing. *Coord. Chem. Rev.* **2008**, *252*, 922-939.
24. Ronconi, L.; Sadler, P. J., Using Coordination Chemistry to Design New Medicines. *Coord. Chem. Rev.* **2007**, *251*, 1633-1648.
25. Lewis, J. E. M.; Gavey, E. L.; Cameron, S. A.; Crowley, J. D., Stimuli-Responsive Pd_2L_4 Metallosupramolecular Cages: Towards Targeted Cisplatin Drug Delivery. *Chem. Sci.* **2012**, *3*, 778-784.
26. Houghton, M. A.; Bilyk, A.; Harding, M. M.; Turner, P.; Hambley, T. W., Effect of Guest Molecules, Metal Ions and Linker Length on the Assembly of Chiral [2+2] Metallomacrocycles: Solution Studies and Crystal Structures. *J. Chem. Soc. Dalton Trans.* **1997**, 2725-2733.
27. Fujita, M., Metal-Directed Self-Assembly of Two and Three-Dimensional Synthetic Receptors. *Chem. Soc. Rev.* **1998**, *27*, 417-425.
28. (a) Tornøe, C. W.; Christensen, C.; Meldal, M., Peptidotriazoles on Solid Phase: [1,2,3] - Triazoles by Regiospecific Copper(I)- Catalyzed 1,3-Dipolar Cycloadditions of Terminal Alkynes to Azides. *J. Org. Chem* **2002**, *67* (9), 3057-3064; (b) Kolb, H. C.; Finn, M. G.; Sharpless, K. B., Click Chemistry: Diverse Chemical Function from a Few Good Reactions. *Angew. Chem. Int. Ed.* **2001**, *40*, 2004-2021.
29. Hein, J. E.; Fokin, V. V., Copper-Catalyzed Azide-Alkyne Cycloaddition (CuAAC) and Beyond: New Reactivity of Copper(I) Acetylides. *Chem. Soc. Rev.* **2010**, *39*, 1302-1315.
30. Moses, J. E.; Moorhouse, A. D., The Growing Applications of Click Chemistry. *Chem. Soc. Rev.* **2007**, *36*, 1249-1262.
31. Himo, F.; Lovell, T.; Hilgraf, R.; Rostovtsev, V.; Noodleman, L.; Sharpless, K. B.; Fokin, V. V., Copper(I)-Catalyzed Synthesis of Azoles. DFT Study Predicts Unprecedented Reactivity and Intermediates. *J. Am. Chem. Soc.* **2005**, *127*, 210-216.
32. (a) Crowley, J. D.; McMorran, D. A., "Click-Triazole" Coordination Chemistry: Exploiting 1,4-Disubstituted-1,2,3-Triazoles as Ligands. *Top. Heterocycl. Chem.* **2012**, *28*, 31-84; (b) Hein, J. E.; Tripp, J. C.; Krasnova, L. B.; Sharpless, K. B.; Fokin, V. V., Copper(I)-Catalyzed Cycloaddition of Organic Azides and 1-Iodoalkynes. *Angew. Chem. Int. Ed.* **2009**, *48*, 8018-8021.
33. Fleischel, O.; Wu, N.; Petitjean, A., Click-triazole: Coordination of 2-(1,2,3-triazol-4-yl)-pyridine to Cations of Traditional Tetrahedral Geometry (Cu(I), Ag(I)). *Chem. Commun.* **2010**, *46*, 8454-8456.

34. Crowley, J. D.; Bandeen, P. H., A multicomponent CuAAC "click" Approach to a Library of Hybrid Polydentate 2-pyridyl-1,2,3-triazole Ligands: New Building Blocks for the Generation of Metallosupramolecular Architectures. *Dalton Trans.* **2010**, *39*, 612-623.

35. Scott, S. O.; Gavey, E. L.; Lind, S. J.; Gordon, K. C.; Crowley, J. D., Self-Assembled Palladium(II) "Click" Cages: Synthesis, Structural Modification and Stability. *Dalton Trans.* **2011**, *40*, 12117-12124.

36. Schubert, U. S.; Hofmeier, H.; Newkome, G. R., Chemistry and Properties of Terpyridine Metal Complexes In *Modern Terpyridine Chemistry* Wiley 2006.

37. Melan, C. F. C. *"Click-helicates": synthesis and characterization of bi-functional ligands based on triazole-pyridine units and the helicate-like structures they form with octahedral metal*; 2011; pp 1-22; 4th year thesis report, Queen's University.

38. (a) Stevenson, K. A.; Melan, C. F. C.; Fleischel, O.; Wang, R.; Petitjean, A., Solid-State Self-Assembly of Triazolylpyridine-Based Helicates and Mesocate: Control of the Metal–Metal Distances. *Cryst. Growth Des.* **2012**, *12*, 5169-5173; (b) Vellas, S. K.; Lewis, J. E. M.; Shankar, M.; Sagatova, A.; Tyndall, J. D. A.; Monk, B. C.; Fitchett, C. M.; Hanton, L. R.; Crowley, J. D., $[Fe_2L_3]^{4+}$ Cylinders Derived from Bis(bidentate) 2-Pyridyl-1,2,3- triazole "Click" Ligands: Synthesis, Structures and Exploration of Biological Activity. *Molecules* **2013**, *18*, 6383-6407.

39. Albrecht, M., How Do They Know? Influencing the Relative chemistry of the Complex Units of Dinuclear Triple-Stranded Helicate-Type Complexes. *Chem. Eur. J.* **2000**, *6*, 3485-3489.

40. Melan, C. F. C.; Wu, N.; Stevenson, K. A.; Fleischel, O.; Wang, R.; Habib, F.; Mosey, N. J.; Guo, H.; Petitjean, A., Click-Triazole: 2-(1,2,3-triazol-4-yl)-pyridine Unit Coordination to Octahedral Cations; Applications to the Self-Assembly of Helicates and Mesocates. Manuscript in preparation, Queen's University: Kingston, 2013.

41. Archer, R. J.; Hawes, C. S.; Jameson, G. N. L.; McKee, V.; Moubaraki, B.; Chilton, N. F.; Murray, K. S.; Scmitt, W.; Kruger, P. E., Partial Spin Crossover Behaviour in a Dinuclear Iron(II) Triple Helicate. *Dalton Trans.* **2011**, *40*, 12368-12373.

42. Amoore, J. J. M.; Neville, S. M.; Moubaraki, B.; Iremonger, S. S.; Murray, K. S.; Letard, J.-F.; Kepert, C. J., Thermal and Light-Induced Spin Crossover in a Guest-Dependent Dinuclear Iron(II) System. *Chem. Eur. J.* **2010**, *16*, 1973-1982.

43. Hauser, A., Ligand Field Theoretical Considerations. *Adv. Polym. Sci.* **2004**, *233*, 49-58.

44. Gutlich, P.; Goodwin, H. A., Spin Crossover - An Overall Perspective. *Top. Curr. Chem.* **2004**, *233*, 1-47.

43. Gutlich, P.; Garcia, Y.; Goodwin, H. A., Spin Crossover Phenomena in Fe(II) Complexes. *Chem. Soc. Rev.* **2000**, *29*, 419-427.

Chapter 2

Ligands Derived From Aromatic Spacers and Their Complexes

2.1 Introduction: Features of Aromatic Spacers

Described herein is the synthesis and characterization of ligands containing a triazole-pyridine chelating unit, as well as a variable aromatic spacer region (**Figure 2.1**). The use of aromatic functionalities in ligand design can introduce many desirable features into supramolecular architectures with metal ions. The triazole-pyridine chelating unit also presents attractive characteristics, and in combination with an aromatic spacer region can give rise to complexes stabilized by numerous interactions. Several of these properties are outlined below, and include inter- and intramolecular interactions, as well as electrostatic and π-interactions.

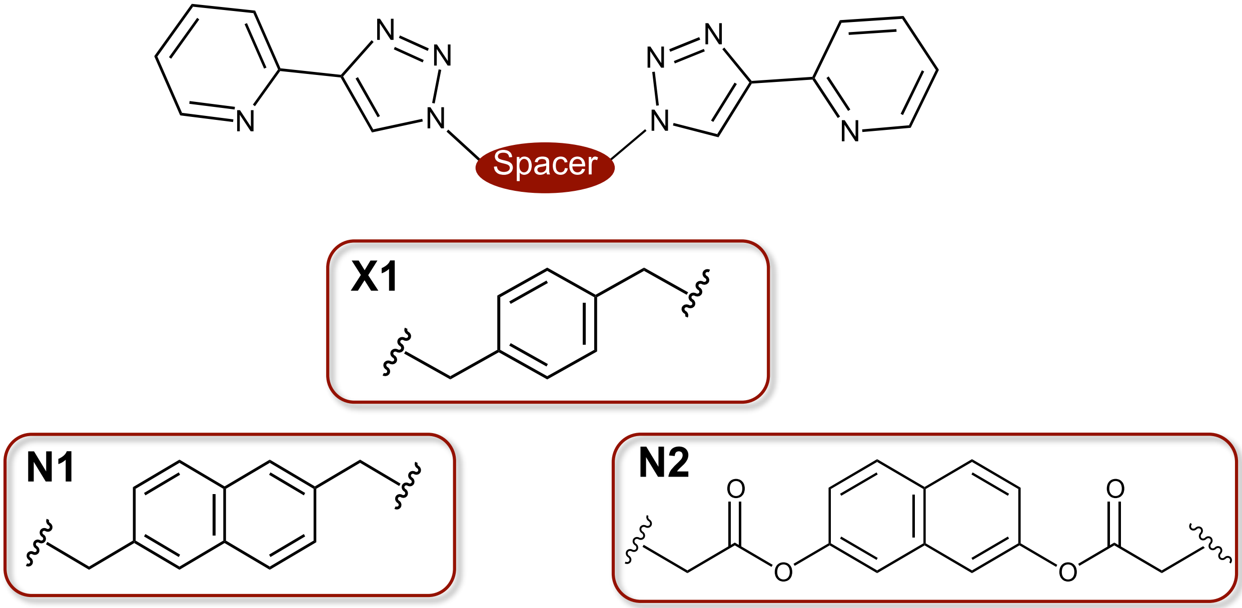

Figure 2.1: Ligand design with triazole-pyridine chelating units and a variable spacer region. Structures include: previously synthesized **X1**,[1] and ligands of interest, **N1** and **N2**.

2.1.1 Increasing Spacer Length - Using Aromatic Functionalities

By manipulating and altering ligand design it is possible to control the self-assembly process as well as properties of the complexes formed with metal ions. An example of this tuneability can be seen in **Figure 2.2**, whereby the initial 4,4'-bipyridine ligand was increased in length. As the length of the ligand was increased the corresponding metal-metal distances also increased upon formation of the metal-ligand complex.[2] For Steel *et al.* the benefits of increasing spacer length included control over the flexibility of their ligands, as well as predictable increases in spacing between the metal centers of the complexes.[2]

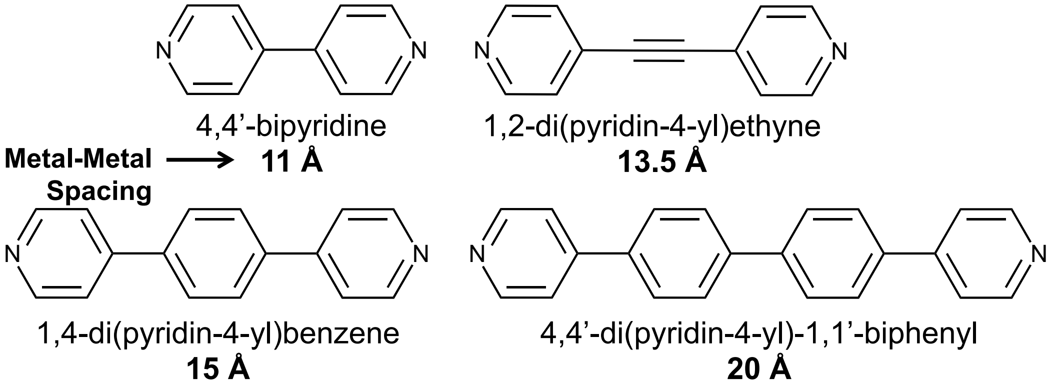

Figure 2.2: The relationship between aromatic spacer length and the resulting metal-metal distances upon complex formation.[2]

As in the example above, upon lengthening the spacer region from xylene to naphthalene we anticipate the metal-metal distance to increase accordingly. The size of the cavity will also increase, which means the resulting complex may have the capability to recognize and encapsulate a greater number of potential substrate molecules.

2.1.2 Variation in Naphthalene Substitution Pattern

By altering substitution on the naphthalene ring, different physical properties may be probed, not only for the free ligand, but for the resulting complexes as well. Hambley *et al.* examined how altering naphthalene substitution affected the physical properties and stoichiometry of the complex that formed with metal ions (specifically Zn^{II}) (**Figure 2.3**).[3] It was observed that both the 2,6- and 2,7-disubstituted naphthalene ligands formed metallomacrocycles, composed of a mixture of both helical and non-helical complexes.[3] The 1,5-disubstituted ligand however formed a 1:1 metal: ligand complex with Zn^{II}, and only at low temperatures, which was attributed to a sterically unfavourable substitution pattern.[3]

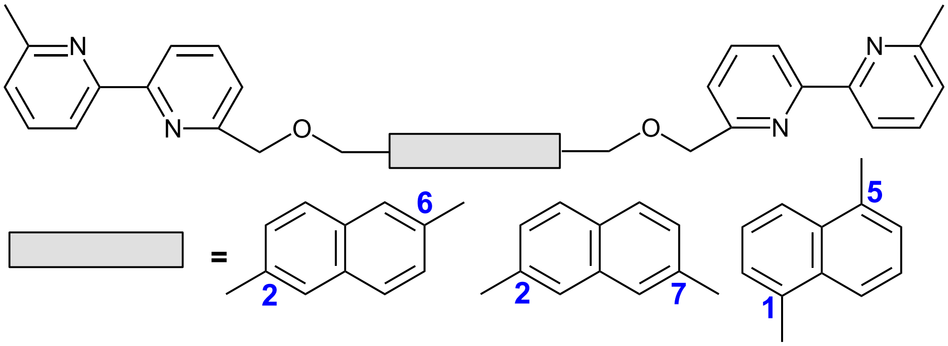

Figure 2.3: Ligand design with 2,2'-bipyridine connected to a variable spacer region through oxapropyl linkers. Naphthalene substitution of the spacer region varied.[3]

This study quite effectively demonstrated that the substitution pattern of naphthalene could have profound effects on the resulting metallomacrocycle. When designing the ligands for my project, these challenges pertaining to naphthalene substitution were certainly taken into consideration.

2.1.3 Previous Ligand: Containing a *p*-xylyl Spacer

The **X1** ligand mentioned herein refers to the ligand with a *p*-xylyl spacer, first synthesized by Crowley *et al.* in 2010[1b] and later reproduced by others (**Figure 2.4**).[4] There are several reasons the 1,2,3-triazolylpyridine chelating unit was chosen, but specifically there are multiple chelating sites, through both the pyridine and triazole nitrogens.[4b]

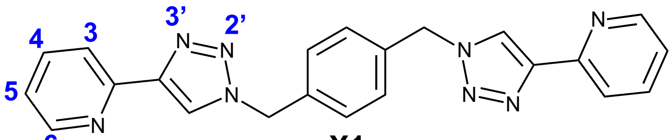

X1

Figure 2.4: Structure of the *para*-substituted **X1** ligand, which has been previously synthesized and characterized.[1b, 4b, c, 5] Atom numbering has been indicated and will be referred to in the corresponding discussion below.

The **X1** ligand was reproduced in our lab and its properties were studied upon complexation with octahedral metal ions, Fe^{II} and Ni^{II} (Nan Wu, NSERC-USRA summer research student, 2010 assisted by Dr. Olivier Fleischel, and Caroline Melan, 4th year student, Jan-Aug 2011). **X1** has been complexed with additional metal ions of varying geometries, including Ag^{I} and Pb^{II}.[1b, 4a] As explained in detail in Chapter 1, the presence of non-coordinating (Caroline Melan) and coordinating anions (Nan Wu) affected the stoichiometry of the **X1** complexes obtained in solution. Use of a non-coordinating anion (tetrafluoroborate) in solution consistently gave the saturated triple-stranded complex with both Fe^{II} and Ni^{II} metal ions.[1a] Coordinating anions however, such as chlorides and acetates, were found to preferentially form a 2:2 stoichiometry (2 metal ions: 2 **X1** ligands) in solution (Nan Wu, NSERC-USRA summer research student).

2.1.4 Ligand Components

The target ligands may be separated into two important components (**Figure 2.5**). First are the 1,2,3-triazolylpyridine chelating units, which offer two coordination sites without being sterically hindered. The two chelating units are connected to a variable spacer region, through a *flexible* methylene linker. The flexibility of the methylene group is important in the self-assembly process, due to the rigidity of the naphthalene spacer region.[2a]

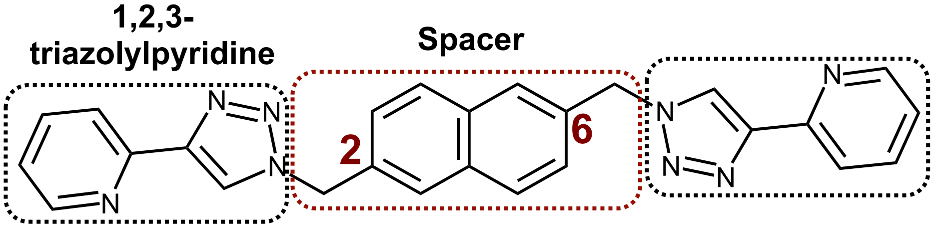

Figure 2.5: Structure of the **N1** ligand illustrating its basic components and naphthalene substitution.

The second component of the spacer is the rigid aromatic core. The ligand that was synthesized (**N1**), and the proposed design for the second (**N2**), have different substitution patterns on the naphthalene ring, with the first being 2,6-disubstituted and the second a 2,7-disubstituted naphthalene.

2.2 Ligand Syntheses

Two different ligands were designed, both containing a naphthalene core (spacer) connected to a triazole-pyridine chelating unit through a flexible linker group. The first ligand, **N1**, contains a 2,6-bis-substituted naphthalene spacer, connected to the chelating units by flexible methylene groups. The **N2** ligand also contains a naphthalene spacer, however it is 2,7-disubstituted, and has an ester functionality connecting it to the triazole-pyridine chelating units through the methylene linkers. Synthesis of **N1** is outlined below and the initial steps towards obtaining **N2** are included, however the final ligand was not obtained.

2.2.1 Synthesis of N1 Ligand

The target molecule **N1** was obtained by first reducing the starting material, naphthalene-2,6-dicarboxylic acid dimethyl ester to 2,6-bis(hydroxymethyl)naphthalene diol **2.1**.[6] Bromination of diol **2.1** afforded the 2,6-bis(bromomethyl)naphthalene product, **2.2**. Dibromide **2.2** was then subjected to the 'click' reaction in a one-pot two-step synthesis. The first step of the 'click reaction' involved formation of the azide, which then underwent the copper-catalyzed azide-alkyne cycloaddition (CuAAC) reaction to form the desired **N1** ligand.

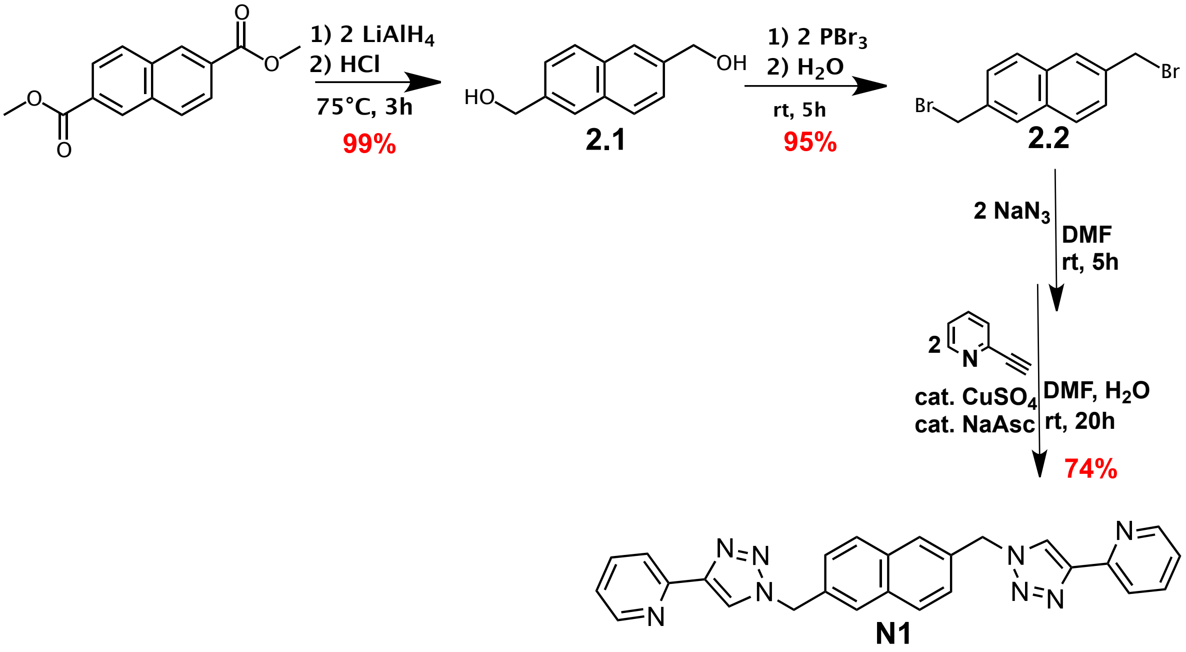

Scheme 2.1: Synthetic route for obtaining the **N1** ligand.[4c]

2.2.1.1 Synthesis of 2,6-bis(hydroxymethyl)naphthalene (2.1) [6]

Following a procedure slightly altered from literature, 1*M* lithium aluminum hydride in tetrahydrofuran solution (2.5 equiv.) was added to the starting material of commercially available naphthalene-2,6-dicarboxylic acid dimethyl ester (1 equiv.).[6a] The reaction was quenched with 5 *N* hydrochloric acid to break apart any aluminum hydroxides. The reduction reaction afforded the diol product (**2.1**) as a white powder in excellent yields, which was used for subsequent steps without further purification.

2.2.1.2 Synthesis of 2,6-bis(bromomethyl)naphthalene (2.2) [6]

Using a procedure slightly modified from literature, the starting material 2,6-bis(hydroxymethyl)naphthalene (**2.1**) was dissolved in anhydrous dichloromethane. To the solution was added phosphorus tribromide (3 equiv.), which was subsequently refluxed for 2 hours at 45 °C. The reaction was extracted with chloroform and water, and the crude product obtained from the organic layer in excellent yield. The crude product was purified by flash column chromatography, giving the desired product (**2.2**) as a white powder.

2.2.1.3 Synthesis of N1 – 'Click Reaction'

The reaction procedure followed a one-pot, two step synthesis, to avoid isolating the product from the first step, a potentially explosive azide. In the initial step, 2,6-bis(bromomethyl)naphthalene (**2.2**) was reacted with sodium azide (3 equiv.), in a S_N2 reaction, which afforded the bis-substituted azide. Without isolating the azide, the next step, the 'click' reaction, was subsequently performed. To the reaction mixture was added water, copper(II) sulfate pentahydrate (0.40 equiv.), sodium ascorbate (0.9 equiv.) and 2-ethynylpyridine (2.15 equiv.) and the solution left to stir at room temperature under argon for 20 h. After 20 h, ammonia, EDTA and water were added and the reaction was left to stir in the air until the solution was green, and the precipitate white. The green color of the solution was an indication that the catalytic Cu^{I} had been converted to Cu^{II} due to the O_2 present when the solution was left to stir in the air. The crude product was purified by recrystallization from 95% ethanol, which gave the desired product as a white powder (**N1**).

2.2.2 Synthesis of [7-[(2-Chloroacetyl)oxy]naphthalen-2-yl 2-chloroacetate]][7] (2.3)

The commercially available 2,7-dihydroxynaphthalene was first recrystallized from toluene and then utilized in the first step of the reaction. Using a method altered slightly from literature, 2,7-dihydroyxynaphthalene (1 equiv.) and 2-chloroacetyl chloride (10 equiv.) were combined under neat conditions. The reaction was refluxed at 100 °C for 4 h under argon with stirring. The reaction was cooled to room temperature and cooled to 0 °C overnight. The resulting grey powder was filtered and washed with cold ethanol, and further purified by column chromatography using 1:0.6 hexanes: ethyl acetate. This afforded the desired product as white, shiny crystals.

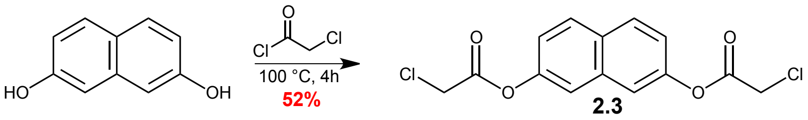

Scheme 2.2: Acylation reaction of 2,7-dihydroxynaphthalene.[7]

The product obtained from the acylation reaction was then supposed to be used for the 'click' reaction to obtain the proposed **N2** ligand. The ester functionality presented some synthetic challenges however, because of its water and pH sensitivity. As a result of these synthetic challenges and time constraints the final **N2** ligand was not obtained. A proposed synthetic scheme may be found in Chapter 5-Conclusions and Future Work.

2.3 Formation of Metallomacrocycles with Octahedral Metal Ions

We were interested in synthesizing and characterizing the complexes that formed between ligands containing a naphthalene spacer and octahedral metal ions, Fe^{II} and Ni^{II}. The complex with **N1** was studied in both the solid and solution states with non-coordinating anions, and in solution with coordinating anions.

2.3.1 Synthesis of $[Fe_2(\mathbf{N1})_3](BF_4)_4$

The iron(II) complex of **N1** was obtained by mixing two equivalents of metal salt, $[Fe(H_2O)_6](BF_4)_2$, with three equivalents of ligand (**N1**) in acetonitrile. This yielded a dark orange solution. Very slow vapour diffusion of diethyl ether led to the formation of bright orange single crystals, which were suitable for X-ray crystallography.

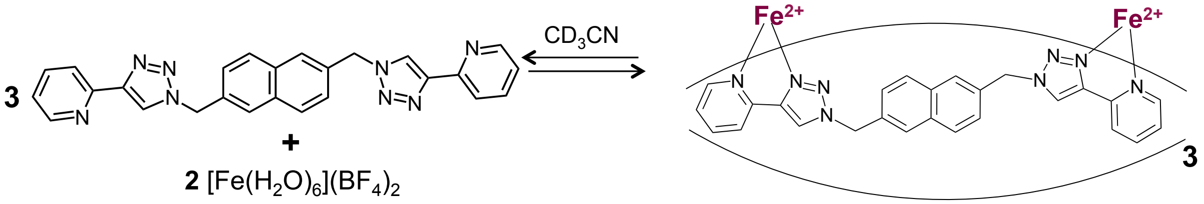

Scheme 2.3: Formation of $[Fe_2(\mathbf{N1})_3](BF_4)_4$ from **N1** and $[Fe(H_2O)_6](BF_4)_2$ in CD_3CN.

2.3.2 Synthesis of $[Ni_2(N1)_3](BF_4)_4$

The nickel(II) complex of **N1** was obtained in an identical fashion, by mixing two equivalents of metal salt, $[Ni(H_2O)_6](BF_4)_2$, with three equivalents of ligand (**N1**) in acetonitrile. This instead yielded a pink solution. Again, very slow vapour diffusion of diethyl ether led to the formation of bright single crystals.

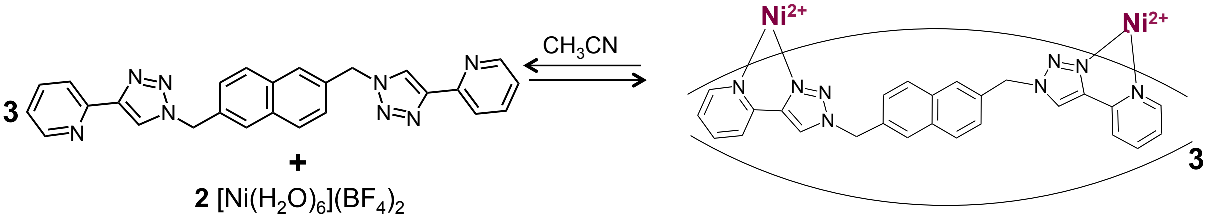

Scheme 2.4: Formation of $[Ni_2(\mathbf{N1})_3](BF_4)_4$ from **N1** and $[Ni(H_2O)_6](BF_4)_2$ in CH_3CN.

2.3.3 Complex Formation of N1 with $[Fe(H_2O)_4Cl_2]$

The coordinating chloride anion, obtained from $[Fe(H_2O)_4Cl_2]$, was complexed with **N1** to observe any structural or stoichiometric changes upon complex formation. The complex was studied by ^1H NMR as well as by UV-vis spectroscopy. For ^1H NMR analysis, two equivalents of $[Fe(H_2O)_4Cl_2]$ were combined with two equivalents of ligand (**N1**) in a 1:1 mixture of $CDCl_3{}^*/CD_3OD$. This mixture of solvents was chosen to accommodate the solubility of both $[Fe(H_2O)_4Cl_2]$ and **N1**. The mixture containing two equivalents of $[Fe(H_2O)_4Cl_2]$, and three equivalents of **N1** was also examined by ^1H NMR spectroscopy. In both instances the resulting solution was a pale orange/yellow in colour. For UV-vis spectroscopy, $[Fe(H_2O)_4Cl_2]$ and ligand solutions were prepared in methanol and aliquots of the Fe^{II} solution were titrated into the **N1** solution until no further changes in absorbance were observed. As Fe^{II} concentration increased, the solution became increasingly yellow in colour, which is consistent with complex formation.

2.3.3.1 Previous Work with Coordinating Anions

Previous work with **X1** (introduced in Chapter 1) demonstrated that the unsaturated double-stranded complex (2:2 metal ion: ligand) was favoured in the presence of a coordinating anion (chloride, or acetate) in solution (Nan Wu, NSERC-USRA summer research student, 2010).[4b] The unsaturated complex was of particular interest because of its available substrate binding sites, as well as the hydrophobic cavity (**Figure 2.6**). Both the available binding sites and the hydrophobic cavity are characteristics that could be exploited to potentially bind a substrate molecule through electrostatic interactions and hydrophobic effects. Given the structural similarities between the **X1** and **N1** ligands, we were hoping to see the same trend with **N1** and a coordinating anion in solution.

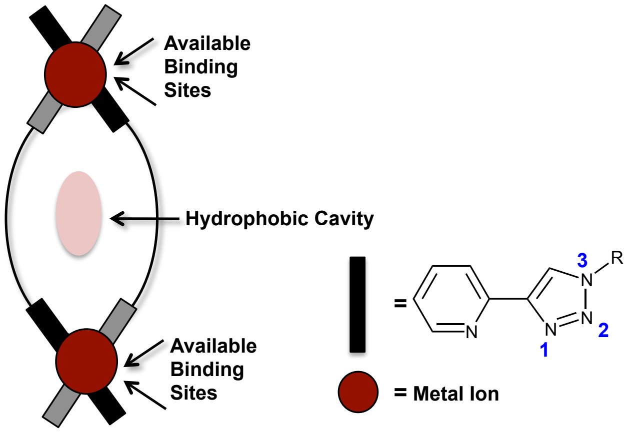

Figure 2.6: Dinuclear double-stranded metal-ligand complex.

2.3.4 Complex Formation of N1 with [Ni(H_2O)$_4$(OAc)$_2$]

As with [Fe(H_2O)$_4$$Cl_2$], [Ni($H_2O$)$_4(OAc)_2$] was complexed with **N1** to observe any structural or stoichiometry changes upon complexation as a result of the coordinating anion. Due to the paramagnetic nature of Ni^{II}, the obtained complex was only studied by UV-vis spectroscopy. Two equivalents of [Ni(H_2O)$_4$(OAc)$_2$] were combined with two equivalents of ligand (**N1**) in methanol, which gave a light pink solution. The goal was to obtain the unsaturated complex with 2:2 [Ni^{II}: **N1**] stoichiometry in solution, which would have available binding sites for a potential substrate.

2.4 Results and Discussion

2.4.1 Characterization of N1 Ligand

The **N1** ligand, which featured a bis-substituted naphthalene spacer unit, was characterized by NMR spectroscopy (^{1}H, ^{13}C, COSY, HSQC and HMBC may be found in **Appendix A**), mass spectrometry, and elemental analysis (see Chapter 4 - *Experimental Section*).

Note: A full description of all instruments and techniques used for all ligands and complexes described herein may be found in Chapter 4.

2.4.1.1 NMR Analysis of N1

NMR spectroscopy was used to confirm that the desired product was synthesized as well as to characterize it (**Figure 2.7**). There were several characteristic signals that helped to confirm that the **N1** ligand was obtained. The diagnostic singlet of the triazole proton was found at 8.1 ppm, which falls into the typical range of 7.5-8.6 ppm.[8] The symmetric nature of the ligand was also reflected in the aromatic signals of the naphthalene group, as three signals corresponded to the appropriate protons (highlighted as a, b and c in **Figure 2.7**).

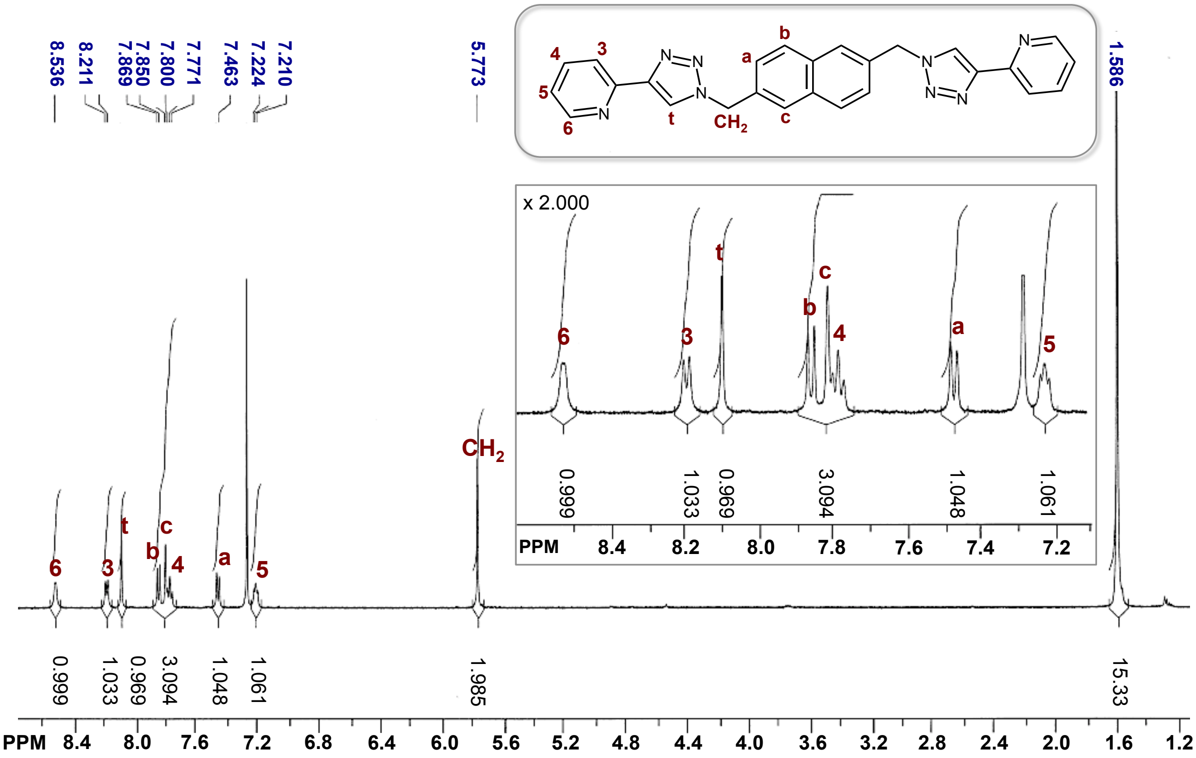

Figure 2.7: ^{1}H NMR spectrum of **N1** ($CDCl_3^*$, 500 MHz, 25 °C).

2.4.1.2 Mass Spectrometry and Elemental Analysis of N1

The electron impact mass spectrum (**Figure 2.8**) further confirmed that the desired ligand was obtained. The molecular peak at m/z 444.18 corresponded to [M^+], as well as the peak at m/z 415.17, which corresponded to [($M-N_2^+$)]. The peak at m/z 154.07 was consistent with $[C_{12}H_{10}]^+$.

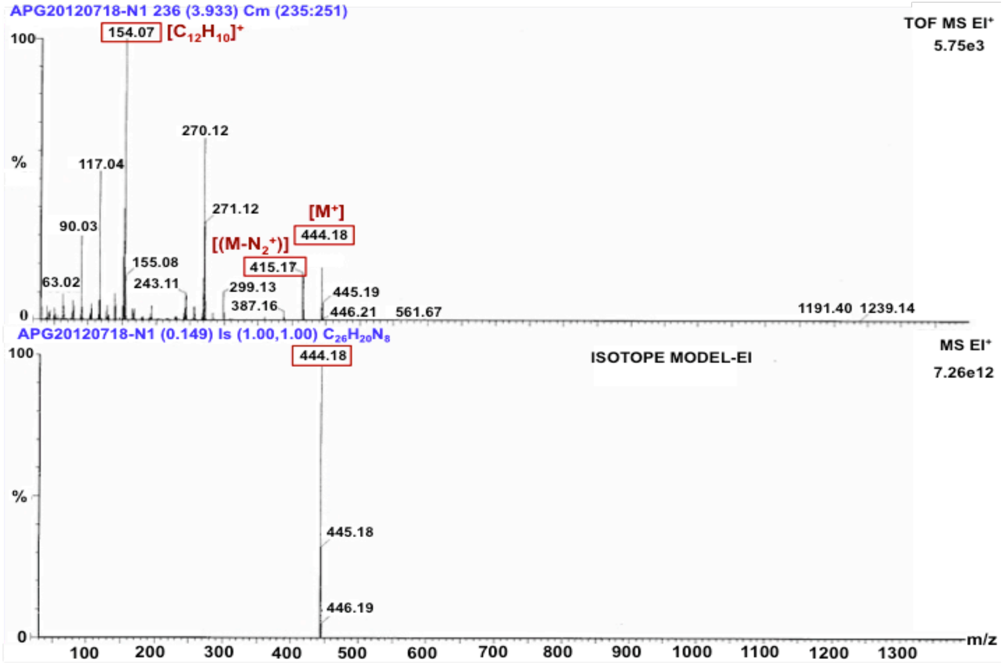

Figure 2.8: EI^+ - mass spectrum of **N1**, with select fragments outlined.

The elemental analysis confirmed the composition of the **N1** ligand, as well as its overall purity (see Chapter 4 - *Experimental Section*). The analysis indicated the presence of a small amount of water (0.25 equivalents) trapped in the crystals. The differences between the experimental and theoretical findings however, still fell within the acceptable range of discrepancies.

2.4.2 Characterization and Analysis of $[Fe_2(N1)_3](BF_4)_4$

The metallomacrocycle formed between **N1** and $[Fe(H_2O)_6](BF_4)_2$ was characterized by NMR spectroscopy (^1H and COSY), single crystal X-ray crystallography as well as by elemental analysis. All of the characterizations were consistent with formation of a dinuclear complex with the general formula $[Fe_2\mathbf{L}_3]^{4+}$. The complex was also further examined by UV-Vis spectroscopy analysis to examine its properties and stoichiometry in the solution state. While mass spectrometry would have further confirmed the formation of a dinuclear triple-stranded structure, previous attempts have been unsuccessful. In the attempts that were made with iron(II) and nickel(II) the corresponding spectra contained only peaks corresponding to the partially dissociated complex, suggesting that the complexes are not stable under MS experimental conditions. Similar difficulties were also seen by Crowley *et al.* with obtaining mass spectrometry spectra of their 'click' complexes.[5]

2.4.2.1 NMR Analysis of $[Fe_2(N1)_3](BF_4)_4$

The seemingly simple ^{1}H NMR spectrum and well resolved peaks obtained for the $[Fe_2(\mathbf{N1})_3](BF_4)_4$ complex are consistent with formation of a single, low-spin species. Compared to the spectrum of the free ligand, the peaks had broadened slightly, however the proton assignments were still extremely clear. Of particular interest were the diastereotopic protons, assigned to the bridging CH_2 groups, which were equivalent in the ^{1}H NMR spectrum of the free ligand. The proton assignments were confirmed by COSY (**Appendix A**).

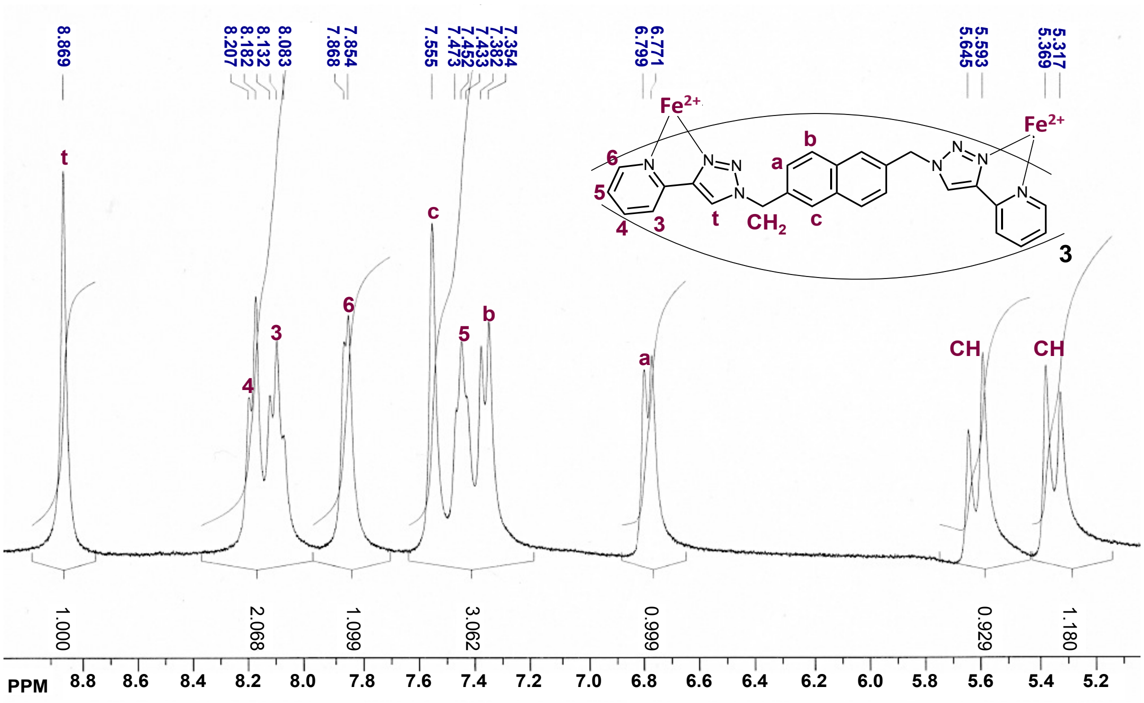

Figure 2.9: ^{1}H NMR spectrum of $[Fe_2(\mathbf{N1})_3](BF_4)_4$ in CD_3CN (300 MHz, 25 °C).

While it was difficult to quantitatively compare the chemical shifts of the free ligand to that of the complex (because different solvents were used) some observations were still made. Upon formation of the complex it was observed that many of the chemical shifts had changed slightly, or become slightly broader than in the free ligand. The changes in chemical shift were attributed to the proton's proximity to the chelating site, and ultimately the Fe^{II} metal ion. It was also expected that some of the protons would show an upfield shift upon formation of the dinuclear complex. These upfield shifts were attributed to the proton's interaction with the π-system of adjacent ligands, ultimately leading to edge-to-face interactions.[9]

2.4.2.2 Single Crystal X-Ray Structure of $[Fe_2(\mathbf{N1})_3](BF_4)_4$

The crystal structure shown in **Figure 2.10** gave insight into many interesting features and physical properties of the metallomacrocyclic complex. The structure and tightness of the self-assembled architecture was reflected in the nature of the spacer region, whether it was aliphatic or aromatic.[4a, 4c, 10] The self-assembly trends observed with previous ligands in the solid state (**C3**, **X1**) may be applied to **N1** with octahedral metal ions, Fe^{II} and Ni^{II}.

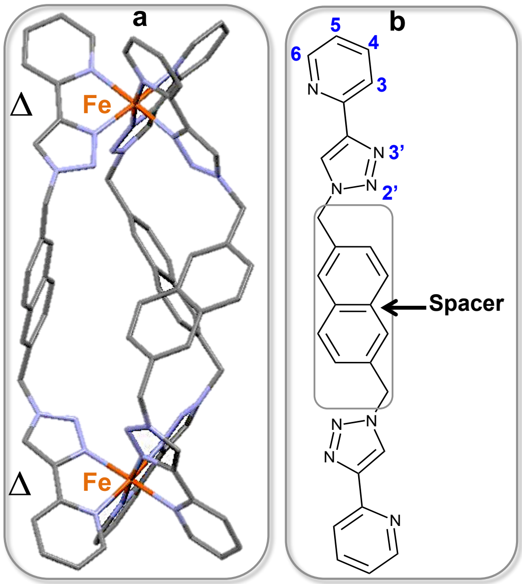

Figure 2.10: a) Single crystal X-ray structure of $[Fe_2(\mathbf{N1})_3](BF_4)_4$ (H atoms, counter-ions (BF_4^-) and solvent molecules (H_2O) omitted for clarity; Fe orange, N blue, and C dark grey). Selected bond distances (Å): Fe^{II}-Fe^{II}: 13.398, Fe^{II}-$N_{Triazole}$: 1.923-1.951, Fe^{II}-$N_{Pyridine}$: 1.978-2.007. b) ChemDraw structure of **N1**, with the spacer region outlined and the triazole-pyridine chelating unit numbered. *Note:* Anions and solvent molecules were extremely disordered.

The structure observed for the $[Fe_2(\mathbf{N1})_3](BF_4)_4$ complex was cylindrical in nature, with both Fe^{II} octahedral coordination centers having the same chirality, which indicated a helicate structure. While it was the Δ, Δ enantiomer indicated above, **N1** formed as a racemic mixture of Δ, Δ and Λ, Λ enantiomers in the solid state. Much like the previous ligand, **X1**, the naphthalene spacer unit of **N1** behaved like an extended CH_2-CH_2 bridge. As a result of this behaviour the *even-odd* rule was applied, which anticipated a helicate structure based on the spacer unit containing an even number of carbons.[11] In the solid state, it was observed that the saturated triple-stranded complex was formed with two metal centers and three ligands. Chelating to the Fe^{II} metal ion occurred through the nitrogen of the pyridine as well as N3' from the triazole. The complex was further stabilized by several electrostatic and π-interactions, which are discussed in detail below.

The X-ray crystal structure was also used to probe potential spin crossover behaviour, by determining whether the complex was in a high- or low-spin state. This information was inferred from the metal-nitrogen coordination distances (Å), from the Fe^{II} metal center to both the triazole (Fe^{II}-$N_{Triazole}$) and pyridine nitrogen's (Fe^{II}-$N_{Pyridine}$).[12] As a general rule of thumb, Fe^{II}-N bond lengths between 1.95-2.00 Å are indicative of a low-spin state and high-spin states typically correspond to Fe^{II}-N bond lengths that are longer, ranging from 2.12-2.18 Å.[12a] From this it can see that the transition from low-spin to high-spin significantly increases the Fe^{II}-N bond lengths of a complex. For the $[Fe_2(\mathbf{N1})_3](BF_4)_4$ complex all of the coordination distances corresponded with a low-spin state, with the Fe^{II}-N distances ranging from 1.92-2.01 Å.

A feature detected in many complexes containing the triazole-pyridine chelating unit, regardless of the nature of the spacer, is that of *head-to-tail dimerization*. This phenomenon has been observed quite frequently with various metal ions (Ag^{I}, Cu^{I}, Pb^{II}) complexed to ligands containing a triazole-pyridine chelate.[1b,4a,4c,13] The concept of dimerization involves π-interactions between the triazole-pyridine chelating units of two adjacent helicate complexes. As a result of the combination of weak interactions a *dimerization box* can be imagined between two complexes. The *dimerization box* (purple box in **Figure 2.11**) is composed of head-to-tail π-π stacking between neighbouring triazole and pyridine groups, hydrogen bonding between pyridine protons and triazole N_2', and finally π-interactions between the pyridine protons and aromatic spacer. Through long range self-assembly, the dimerization box for the **N1** complex can be infinitely extended from the same face of the naphthalene spacer (**Figure 2.11,** *bottom*).

Outlined in **Figure 2.11** (*black line*), is the stacking of the triazole group from one complex with the pyridine of another complex, which are considered face-to face interactions. For the $[Fe_2(\mathbf{N1})_3](BF_4)_4$ complex, the head-to-tail stacking distance between the triazole and pyridine groups ('intermolecular' distance) was 3.50 Å, which was consistent with the distance observed for $[Fe_2(\mathbf{X1})_3](BF_4)_4$ (3.51 Å).[4c] In addition to π-stacking between the triazole-pyridine groups, interactions between the slightly acidic pyridine proton (H_4), and N_2' of the triazole were observed (**Figure 2.11**, *blue lines*). Both face-to-face as well as edge-to-face interactions were observed in **Figure 2.11** (*top*), with the blue and black lines indicating face-to-face interactions, and the red line indicating edge-to-face interactions.

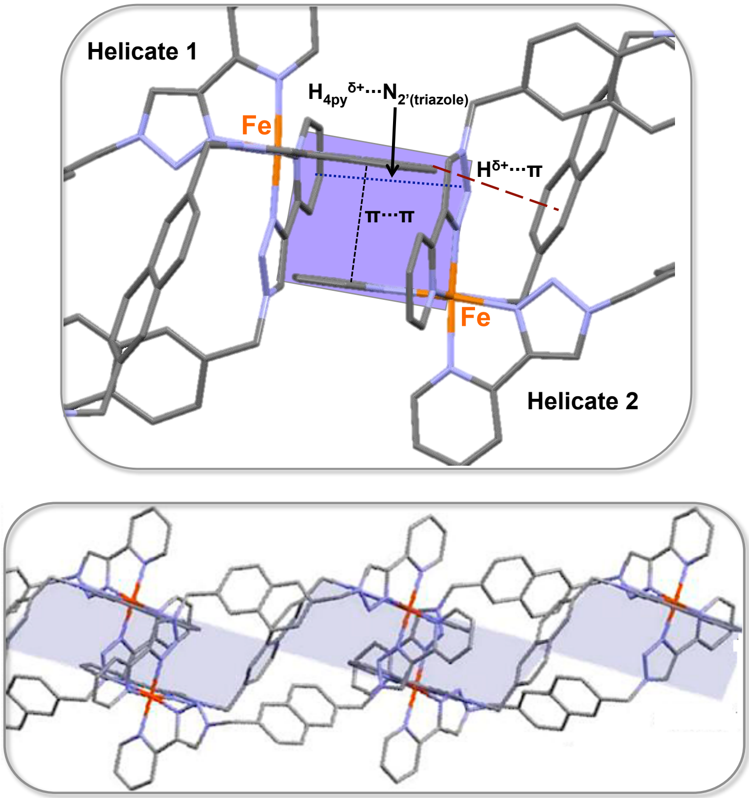

Figure 2.11: '*Head-to-Tail*' *dimerization* of $[Fe_2(\mathbf{N1})_3](BF_4)_4$. *Top*: purple box indicates the *dimerization* box. Black line shows pyridine π-π stacking, blue line shows triazole-pyridine units interactions ($H_{4py}^{\delta+}\cdots N_{2'(triazole)}$), and red line shows interactions between pyridine and naphthalene spacer ($H^{\delta+}\cdots\pi$). *Bottom:* long-range self-assembly and extension of *dimerization* box.

It has been observed that the intermolecular distance may be a reflection of how tight the resulting supramolecular architecture will be. The intermolecular distance is typically related to the rigidity of the spacer region, with a more rigid spacer creating a tighter complex.[4a, 4c, 10] This observation was confirmed by comparing the $H_{4py}^{\delta+\cdots}N_{2'(triazole)}$ 'intermolecular' distances between two stacked helicate complexes for the $[Fe_2(\mathbf{X1})_3](BF_4)_4$ and $[Fe_2(\mathbf{N1})_3](BF_4)_4$ complexes, which were 2.66 Å and 2.57 Å respectively (**Figure 2.11**, *blue line*). As expected, increasing rigidity from xylene to naphthalene (**X1** to **N1**) increased the '*tightness'* of the resulting architecture, which was reflected in a shorter 'intermolecular' distance.[14] As a result of electrostatic interactions, the distances between the two closest metal ions of the stacked helicates (‘intermolecular’) were decreased and therefore brought into closer proximity than the metal ions of a single complex (‘intramolecular’) (**Table 2.1**).

Table 2.1: Metal-metal distances within helicate complexes (‘intramolecular’ distances), and between complexes through head-to-tail stacking (‘intermolecular’ distances).[4c]

Complex	**$[Fe_2(X1)_3](BF_4)_4$**	**$[Fe_2(N1)_3](BF_4)_4$**
‘Intramolecular Distance’ (Å)	11.39	13.40
‘Intermolecular Distance’ (Å)	8.40	8.51

Note: The $[Fe_2($**X1**$)_3](BF_4)_4$ complex and corresponding X-ray crystal data were previously obtained by Caroline Melan (4th year student, Jan-Aug 2011) in our lab.[1a, 4c]

2.4.2.3 Molar Absorptivity Determination of $[Fe_2(N1)_3](BF_4)_4$

The saturated triple-stranded complex was obtained by combining two equivalents of metal salt, ($[Fe(H_2O)_6](BF_4)_2$) and three equivalents of ligand (**N1**) in acetonitrile to yield a dark orange solution. Molar absorptivity values were obtained from the UV-vis spectra of the saturated metal-ligand complex, with prominent peaks occurring at 225 nm, 280 nm and 425 nm. The molar absorptivity values were an indication of how strongly the chemical species absorbed at a specific wavelength (**Figure 2.12**). The peaks in the ultraviolet region, at 225 and 280 nm, were characteristic of ligand based π-π* and n-π* transitions, attributed to the naphthalene spacer. The shoulder occurring around 330 nm and the broad peak highlighted around 425 nm both corresponded to metal-to-ligand charge-transfer (MLCT) transitions. The MLCT transitions were similar to those seen in previous complexes (confirmed by DFT calculations), which were transitions from Fe^{II} metal ions to triazole, and Fe^{II} to pyridine. These obtained MLCT values were observed to be lower than the $[Fe($**2,2’-bpy**$)_3]^{2+}$ (500 nm) counterpart.[9] The two peaks centered at 330 nm and 425 nm indicated complex formation and binding of **N1** with the Fe^{II} metal ions.

While the epsilon values were expected to be independent of concentration, there appeared to be a dependence on concentration (**Figure 2.12**, *inset*), perhaps indicating dissociation of the complex upon dilution.

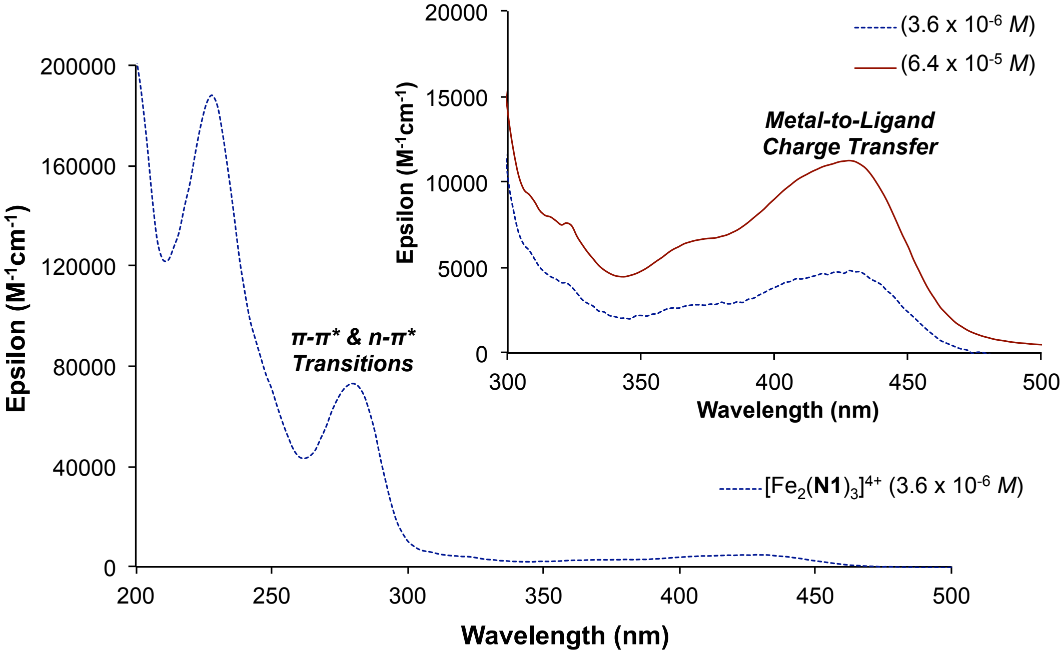

Figure 2.12: UV-vis spectrum of $[Fe_2(\mathbf{N1})_3](BF_4)_4$ in CH_3CN. π-π* / n-π* transitions (225 and 280 nm) and MLCT transitions (425 nm) highlighted

2.4.2.4 UV-vis Titration of N1 with $[Fe(H_2O)_6](BF_4)_2$

Stoichiometry of the Fe^{II}-**N1** complex was determined in solution, by performing a UV-vis titration, whereby aliquots of metal salt, ($[Fe(H_2O)_6](BF_4)_2$) were added to **N1** in acetonitrile. As the concentration of Fe^{II} in solution increased two new bands began to form around 330 nm (shoulder) and 425 nm, both consistent with MLCT transitions and complexation of **N1** with Fe^{II} metal ions.

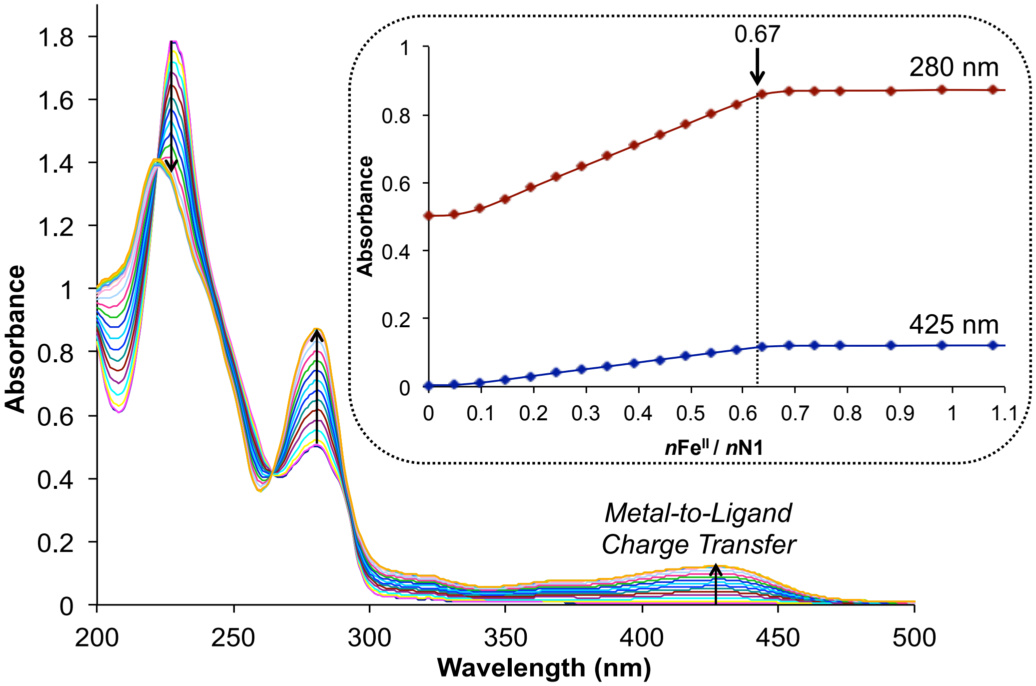

Figure 2.13: UV-vis titration spectrum for **N1** with $[Fe(H_2O)_6](BF_4)_2$ in CH_3CN. *Inset*: Absorbance *vs*. nFe^{II} / n**N1** ratio for peaks corresponding to MLCT transition (425 nm) and π-π*/ n- π* transition (280 nm). *Note:* n mentioned herein refers to the number of moles.[16]

As Fe^{II} concentration increased the solution became a darker yellow and the intensity of the charge-transfer bands (330 nm and 425 nm) also increased. When there was no Fe^{II} present in solution, the peaks at 330 nm and 425 nm were absent, so the enhancement of these peaks with increasing Fe^{II} concentration indicated complex formation. The presence of a sharp, well-defined isosbestic point at 275 nm suggested there was an transformation from starting material to products, both of which are absorbing species. It is likely that the absorbing species in solution are the [Fe$_2$**N1**$_3$]$^{4+}$ complex and free ligand.[15] The transformation of these species was dependent on the concentration of Fe^{II} present in solution. By plotting absorbance of the bands centered at 280 nm and 425 nm as a function of [nFe^{II} / n**N1**], complex stoichiometry was confirmed. From the resulting graph (**Figure 2.13**, *inset*) it was seen that after the addition of about 0.67 equivalents of Fe^{II}, there were no further increases in absorbance, indicating that the complex in solution was of the formula, [Fe$_2$**N1**$_3$]$^{4+}$.

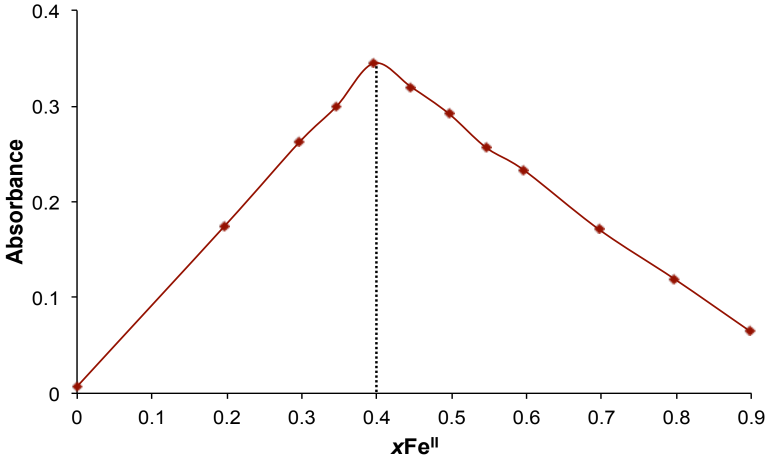

Figure 2.14: Job plot of **N1** with $[Fe(H_2O)_6](BF_4)_2$ in CH_3CN (lines are only connecting the experimental points; no data fitting)[16] *Note:* mentioned herein, x refers to the molar ratio (moles of Fe^{II} / total number of moles).

A Job plot was also performed to confirm the stoichiometry of the complex in solution. Seen in **Figure 2.14**, absorbance was plotted as a function of the molar ratio, determined from the number of moles of Fe^{II}/ the total number of moles. Consistent with the titration data, plotting absorbance *vs*. xFe^{II} showed a maximum at x(Fe^{II}) = 0.40, which indicated formation of the saturated triple-stranded complex under these conditions.

2.4.3 Characterization of $[Ni_2(\mathbf{N1})_3](BF_4)_4$

Unlike the $[Fe_2(\mathbf{N1})_3](BF_4)_4$ complex, the Ni^{II} complex was paramagnetic in nature, meaning that NMR spectroscopic analyses did not assist with characterization. Instead the obtained Ni^{II} complex was studied by UV-vis spectroscopy to investigate the accessibility of potential spin crossover behaviour in the corresponding Fe^{II} complex. While the concept of spin crossover was outside the scope of my thesis, a simple UV-vis experiment gave much information about the possible phenomenon.

Strong metal-to-ligand charge transfer bands typically overlap with the weak *d-d* transitions in Fe^{II} complexes, the absence of a MLCT band made it possible to probe potential spin crossover behaviour from the Ni^{II} electronic spectrum. Unlike Fe^{II}, the d^8 electronic configuration of Ni^{II} forces all of the electrons in the non-bonding orbital (t_{2g}^6) to be paired.[17] With Fe^{II} however, which has a *d*^{6} electronic configuration, multiple orbital arrangements may exist. This variability permits Fe^{II} complexes to potentially display spin crossover behaviour with an external perturbation. While Ni^{II} complexes do not typically display spin crossover behaviour, their *d-d* electronic spectra are quite well understood with regards to ligand field.[17-18] It was for this reason that solution state studies with Ni^{II} were undertaken, and the potential spin crossover behaviours then applied to the corresponding Fe^{II} complexes.

While efforts were made to obtain X-ray crystallography quality crystals, unfortunately all attempts were unsuccessful in obtaining single crystals. As explained in Chapter 1 however, X-ray crystal structures were obtained by Caroline Melan for both the [Fe$_2$(**X1**)$_3$](BF$_4$)$_4$, and [Ni$_2$(**X1**)$_3$](BF$_4$)$_4$ complexes.[1a, 4b] In comparing the Fe^{II} and Ni^{II} crystal structures with **X1**, it was verified that the two were almost completely isostructural, and in both instances resulted in a helicate complex. [1a, 4c] The metal-metal distances, both inter- and intramolecular were essentially equivalent, varying only very slightly (see Chapter 1 for further details).[4b] We can apply these observations to **N1** and extrapolate that the X-ray crystal structure for [Ni$_2$(**N1**)$_3$](BF$_4$)$_4$ would be isostructural to the Fe^{II} complex and share very similar metal-metal distances.

To confirm the intended Ni^{II} complex was made as well as its composition and overall purity, elemental analysis was also performed (see Chapter 4).

2.4.3.1 UV-vis Spectroscopy Analysis of [Ni$_2$(N1)$_3$](BF$_4$)$_4$

To better establish how the complex behaved in solution, a UV-vis titration experiment was performed in acetonitrile to track stoichiometry changes and complex formation. Small increments of [Ni(H$_2$O)$_6$](BF$_4$)$_2$ were titrated into the **N1** solution and analyzed by UV-vis (**Figure 2.15**). Given the similarities between **X1** and **N1**, as well as the presence of a non-coordinating anion, it was expected that a saturated dinuclear complex would form in solution.

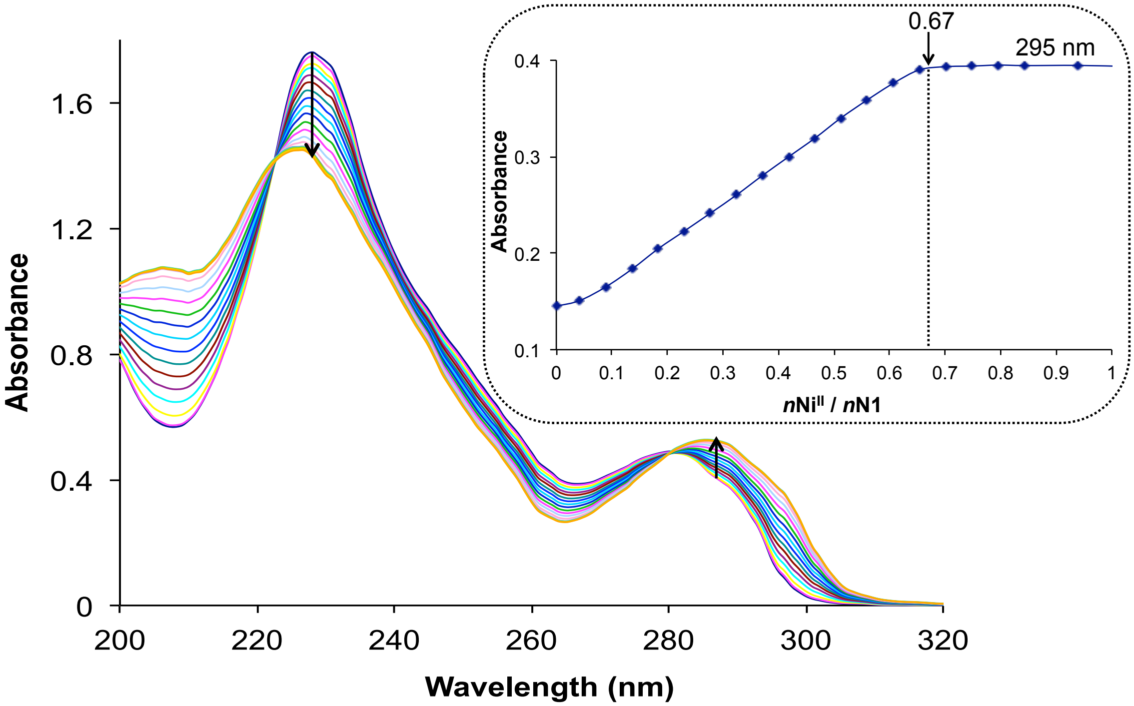

Figure 2.15: UV-vis titration spectrum for **N1** with $[Ni(H_2O)_6](BF_4)_4$ in CH_3CN. *Inset*: Absorbance *vs*. [*n*Ni^{II} / *n***N1**] ratio for peak at 287 nm.[16]

The sharp isosbestic points at 225 nm and 280 nm indicated transformation of the absorbing species, likely free ligand to complex, dependent on the concentration of $[Ni(H_2O)_6](BF_4)_2$ in solution. The graph of absorbance as a function of [*n*Ni^{II} / *n***N1**] (**Figure 2.15**, *inset*) confirmed that the dinuclear complex formed with two Ni^{II} metal ions and three ligands (**N1**). From the shape of the graph it was also inferred that the complex formed with tight binding. This was based on the fact that there was a linear increase in absorbance until 0.67 equivalents of Ni^{II} were added, at which point a horizontal plateau occurred and the absorbance remained constant.

2.4.3.2 Molar Absorptivity Determination of $[Ni_2(N1)_3](BF_4)_4$

UV-vis spectroscopy was used to determine molar absorptivity values for the $[Ni_2(\mathbf{N1})_3](BF_4)_4$ complex at various wavelengths, much like for the $[Fe_2(\mathbf{N1})_3](BF_4)_4$ complex. From the UV-vis spectrum in **Figure**

2.16, the ligand field strength value (wavenumber (cm^{-1})) was obtained and as a result, the accessibility of spin crossover in the corresponding Fe^{II} complex.

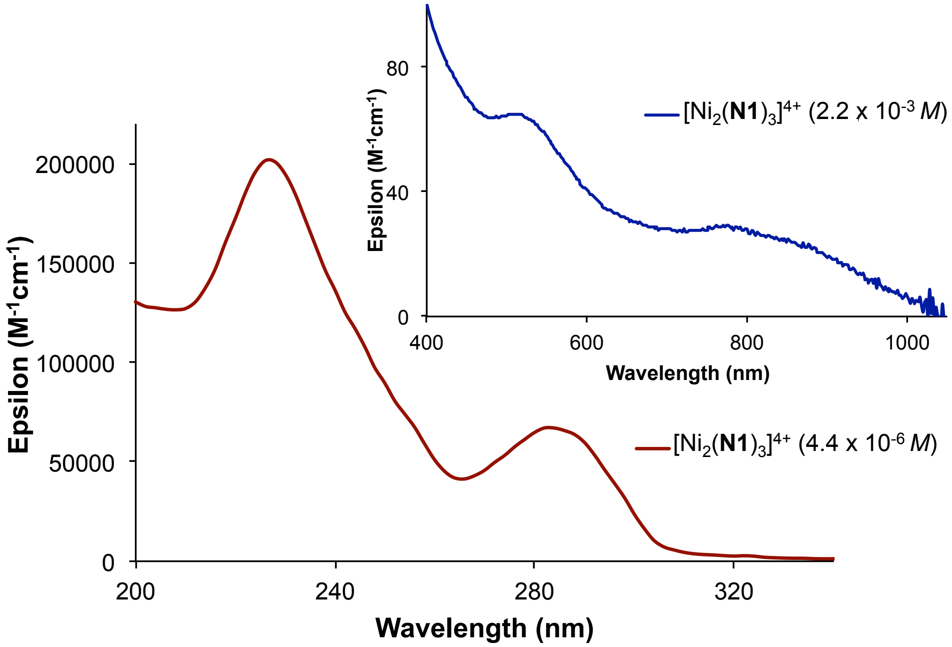

Figure 2.16: UV-vis spectra of $[Ni_2(\mathbf{N1})_3](BF_4)_4$ in CH_3CN.

To determine whether spin crossover was accessible for the Fe^{II} species, the ligand field strength value (10Dq) for the $[Ni_2(\mathbf{N1})_3](BF_4)_4$ complex had to fall between 11,000-12,500 cm^{-1}.[12a] It is within this small range of values that spin crossover may be anticipated for the corresponding Fe^{II} species. The ligand field strength value relates to the *d-d* transitions, which have small intensities (ε values) because they are forbidden.[12a] The ligand field strength value was concluded from the wavenumber (cm^{-1}) that was determined based on the longest wavelength (nm), corresponding to the lowest energy. Based on these characteristics Ni^{II} was useful in determining the ligand field strength value as well as the accessibility of spin crossover. The $[Ni_2(\mathbf{N1})_3](BF_4)_4$ complex was found to have a ligand field strength value of 11,290 cm^{-1}, which was well within the range of values where spin crossover may be accessible for the corresponding Fe^{II} species.

2.4.4 Characterization of N1 with [Fe(H_2O)$_4$Cl$_2$]

2.4.4.1 NMR Analysis of N1 with [Fe(H_2O)$_4$Cl$_2$]

Two mixtures were prepared, each with different stoichiometries and examined by ^{1}H NMR spectroscopy (proton assignments confirmed by COSY; see Chapter 4). The first solution was prepared by mixing two equivalents of [Fe(H_2O)$_4$Cl$_2$], and two equivalents of ligand (**N1**) in a 1:1 mixture of $CDCl_3$*/CD_3OD. This mixture of solvents were chosen because the metal was only sparingly soluble in chloroform and **N1** is minimally soluble in methanol. Based on this, a mixture of solvents was chosen where both metal and ligand were soluble at the desired concentrations. The second solution was prepared in an identical fashion, however the [Fe^{II} : **N1**] ratio was 2:3 instead of 2:2. By preparing and analyzing both mixtures we were hoping to identify any significant spectral changes that may be attributed to formation of the unsaturated 2:2 complex.

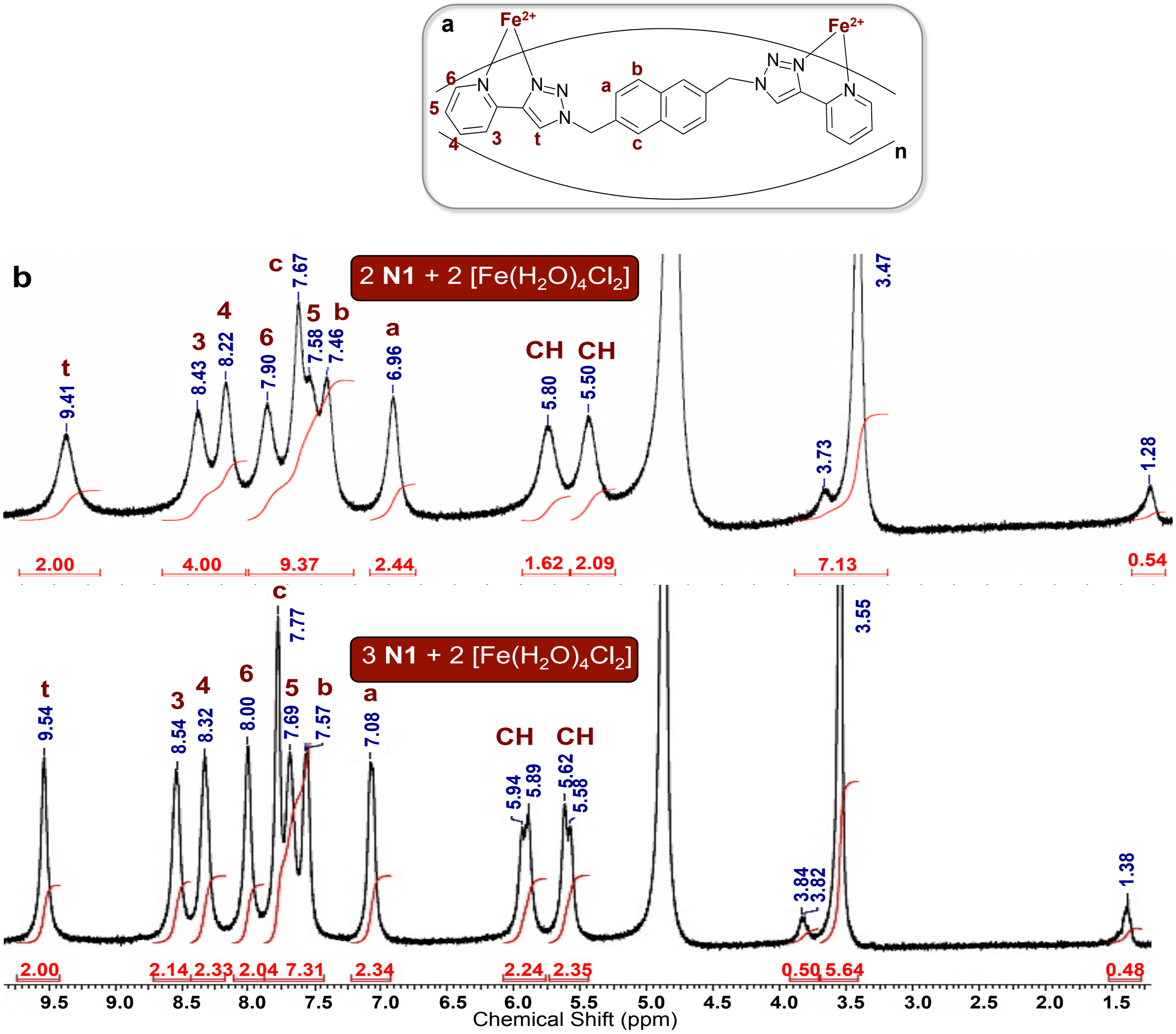

Figure 2.17: a) Structure of the **N1** complex with [Fe(H_2O)$_4$Cl$_2$] and proton numbering *Note*: 'n' refers to the number of ligands b) ^{1}H NMR stack plot of the two mixtures: *Top*: 2 **N1** (5.63 x 10^{-6} *M*) + 2 [Fe(H_2O)$_4$Cl$_2$] (5.63 x 10^{-6} *M*); *Bottom*: 3 **N1** (3.75 x 10^{-6} *M*) + 2 [Fe(H_2O)$_4$Cl$_2$] (3.75 x 10^{-6} *M*); (1:1 $CDCl_3$*/CD_3OD, 300 MHz, 25°C).

From **Figure 2.17** it was observed that by changing the ratio of [Fe(H_2O)$_4$Cl$_2$] to **N1** there was a very minimal change detected by ^{1}H NMR spectroscopy. The 2:2 mixture showed a slight broadening of peaks, as well a minor downfield chemical shift, however these changes were not significant enough to indicate formation of the unsaturated complex. Based on the very similar ^{1}H NMR spectra, it appeared that in both instances it was the triple-stranded complex that formed in solution. Further experiments were conducted to try to force the formation of the unsaturated, double-stranded complex (titration with chloride anions), however these were also unsuccessful.

2.4.4.2 UV-vis Analysis of N1 with [Fe(H_2O)$_4$Cl$_2$]

Previous UV-vis work with **X1** demonstrated that the unsaturated double-stranded complex (**2** metal : **2** ligand) was favoured in solution in the presence of a coordinating anion (chloride, or acetate) (Nan Wu, Research summer student, 2010). It was the unsaturated complex that was of particular interest because of its available binding sites and therefore potential substrate binding capabilities (**Figure 2.6**). Given the similarities between **X1** and **N1**, we were hoping to see the same preference with **N1** for the unsaturated double-stranded complex in solution.

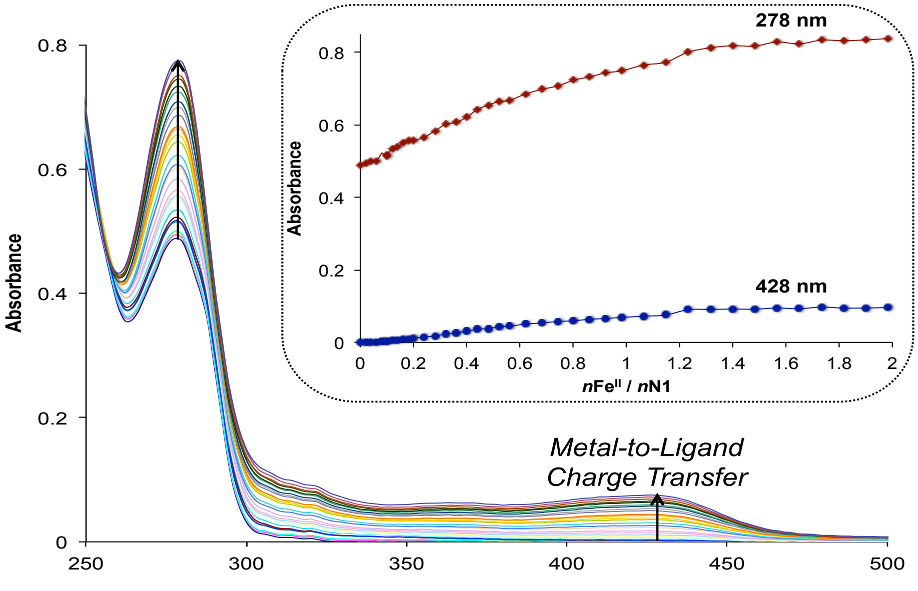

Figure 2.18: UV-Vis titration spectrum for **N1** with [Fe(H_2O)$_4$Cl$_2$] in CH_3OH. *Inset*: Absorbance *vs*. nFe^{II} /n**N1** ratio: peaks corresponding to 280 nm and 428 nm.

The titration gave ambiguous results, with no clear indication of which stoichiometry predominated in solution. There were three prominent peaks in the titration spectrum, which occurred at 430 nm (MLCT transitions), 330 nm (a shoulder) and 278 nm (π-π* and n- π* transitions). When **X1** was complexed with [$Fe(H_2O)_4Cl_2$] there was a clear isosbestic point at 265 nm, whereas with **N1** the isosbestic point was blurred and unclear. The graph of absorbance as a function of [*n*Fe^{II} / *n***N1**] (**Figure 2.18**, *inset*) showed a very gradual increase as the concentration of Fe^{II} increased, which suggested weaker binding than the [Fe_2(**N1**)$_3$](BF_4)$_4$ and [Ni_2(**N1**)$_3$](BF_4)$_4$ complexes. The maximum absorbance also was not very clear, however when [*n*Fe^{II} / *n***N1**] equalled approximately 2.0, the changes in absorbance became extremely subtle. These results were not reproducible however, so information pertaining to the complex stoichiometry could not be concluded.

The UV-vis titrations with [$Fe(H_2O)_4Cl_2$] and **N1** were repeated on several occasions, however each time the results obtained were not consistent and were therefore inconclusive. Shown below is another titration performed with **N1** and the same metal, ([$Fe(H_2O)_4Cl_2$]) in methanol. The data indicated a different result, which was the case for the majority of the UV-vis experiments, and the reason that a concrete stoichiometry determination could not be made.

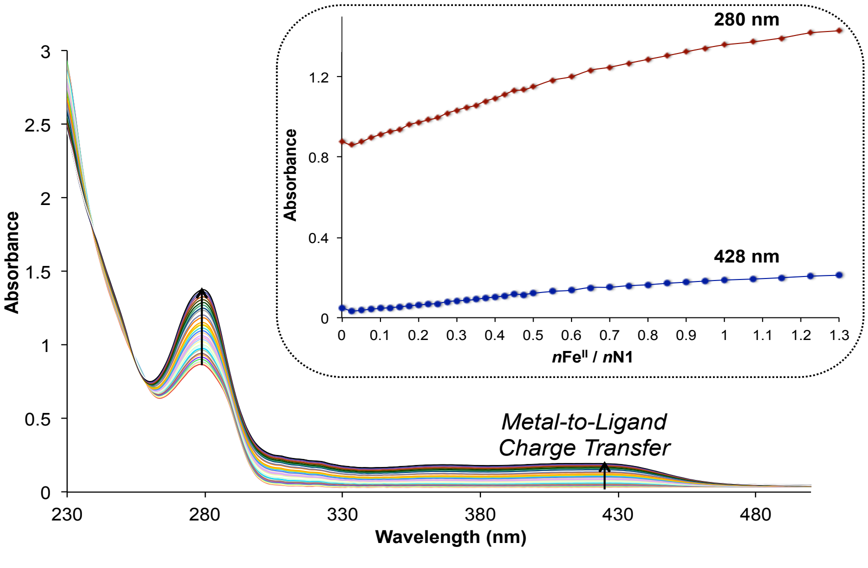

Figure 2.19: UV-vis titration spectrum for **N1** with [$Fe(H_2O)_4Cl_2$] in CH_3OH. *Inset*: Absorbance *vs*. [*n*Fe^{II} / *n***N1**] ratio: peaks corresponding to 280 nm and 428 nm (lines are only connecting the experimental points; no data fitting).

In an attempt to obtain useful information about stoichiometry of the complex in solution, a Job plot was performed in an identical manner to those with a non-coordinating anion (**Figure 2.20**). Much like with the titration data, each Job plot indicated a slightly different stoichiometry in solution, sometimes it was the saturated triple-stranded complex and other times it was the unsaturated double-stranded complex. Initially the Job plot data was plotted as a function of $x\mathrm{Fe}^{\mathrm{II}}$ (molar ratio of $\mathrm{Fe}^{\mathrm{II}}$), which gave an absorbance maximum between 0.4 and 0.5 (**Figure 2.20**). In order to get a more accurate representation of stoichiometry, the data was plotted as a function of [$n\mathrm{Fe}^{\mathrm{II}}$ / n**N1**], which indicated a maximum absorbance around 0.55. Neither method of analyzing the Job plot data provided a consistent stoichiometry and much like the titration data, the experiment was completed on several occasions.

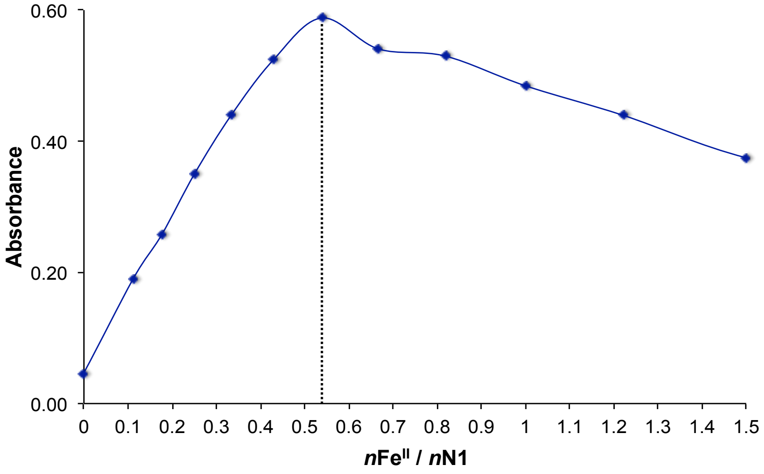

Figure 2.20: Job plot of **N1** with $[\mathrm{Fe(H_2O)_4Cl_2}]$ in $\mathrm{CH_3OH}$ (line is only connecting the experimental points; no data fitting).

Several different experimental techniques were used in an effort to accurately determine the complex stoichiometry that was favoured by **N1** with $[\mathrm{Fe(H_2O)_4Cl_2}]$ in solution. Neither the titration data nor the Job plot data indicated consistent results, with both the 3:2 and 2:2 complexes indicated in solution. To this end, further experiments are required to accurately determine which complex stoichiometry(s) is favoured in solution.

2.4.5 Characterization of N1 with [Ni(H_2O)$_4$(OAc)$_2$]

2.4.5.1 UV-vis Analysis of N1 with [Ni(H_2O)$_4$(OAc)$_2$]

The octahedral metal ion Ni^{II} was examined with **N1**, using the coordinating acetate anion to determine how the complex behaved in solution, much like with **X1**. The paramagnetic nature of Ni^{II} meant analysis of the complex was limited to UV-vis spectroscopy, however useful information was still acquired from this data. As with [Fe(H_2O)$_4$$Cl_2$], it was the unsaturated double-stranded complex that was anticipated in solution, however the UV-vis titration and Job plot analyses did not distinctly support this prediction.

UV-vis titration results showed a slightly blurred isosbestic point at 278 nm and an absorbance maximum at 285 nm (**Figure 2.21**, *inset*). The unclear isosbestic point was also observed with the coordinating chloride anion ([Fe(H_2O)$_4$$Cl_2$]), however with **X1** this was not the case. This variability between isosbestic points is also consistent with the differences in titration results between the two ligands.

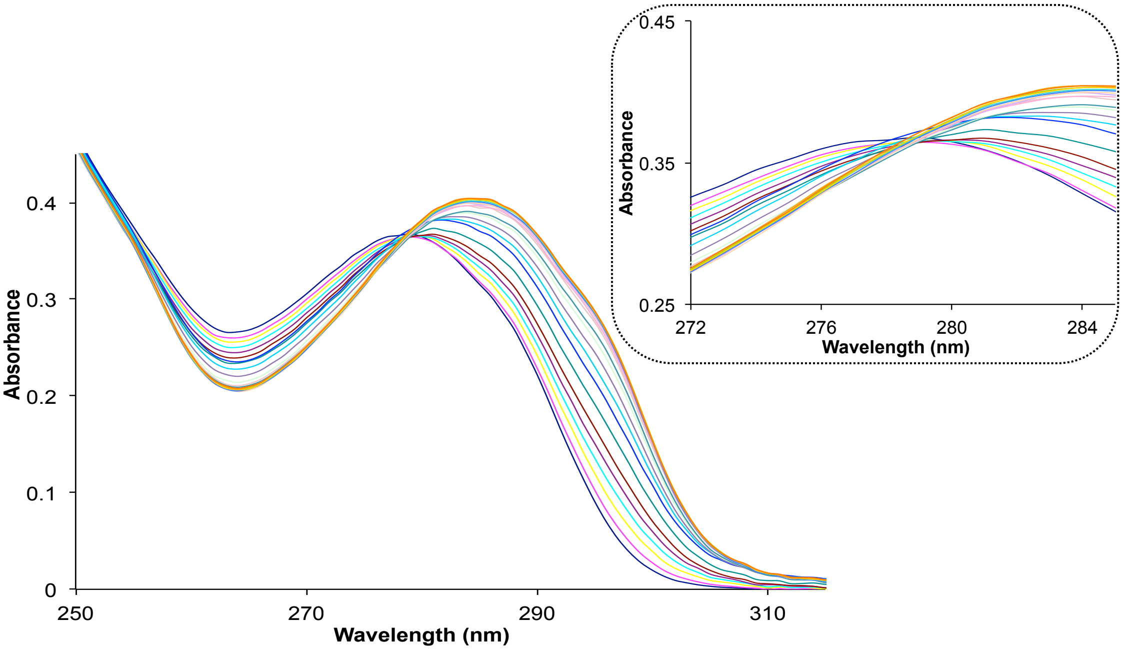

Figure 2.21: UV-Vis titration spectrum for **N1** with [Ni(H_2O)$_4$(OAc)$_2$] in CH_3OH. Full spectrum and zoom (*inset*) on 272-284 nm, showing the isosbestic point (278 nm).

For the graph of absorbance as a function of [nNi^{II} / n**N1**], absorbance at 295 nm was monitored. If the chosen wavelength had been 285 nm, then the change in absorbance would have been insignificant because absorbances are relatively constant at the isosbestic point (278 nm), which evidently was quite close to the maximum absorbance. The graph indicated a Ni^{II} to **N1** mole ratio of about 0.7, suggesting that with [Ni(H_2O)$_4$(OAc)$_2$], **N1** favoured the saturated triple-stranded complex under those conditions.

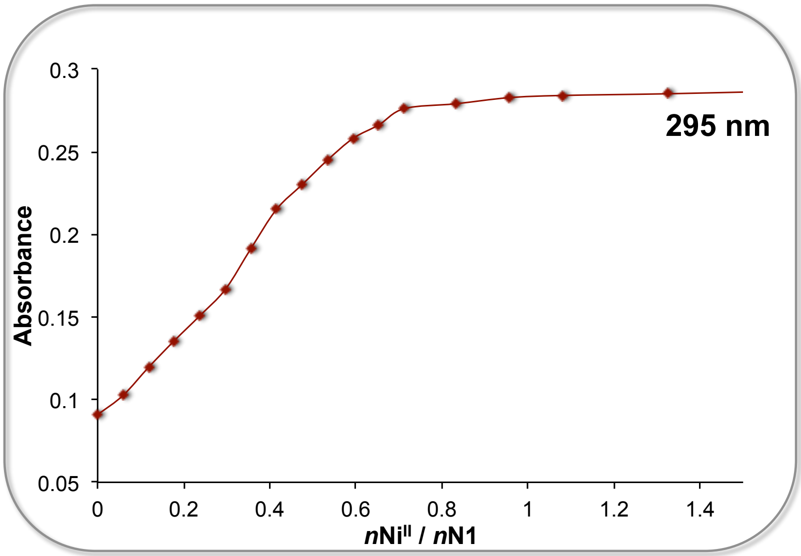

Figure 2.22: Absorbance *vs*. [nNi^{II} / n**N1**] ratio for peak occurring at 295 nm (a line has been added to guide the eye; no data fitting).

The titration data indicated that perhaps it was the triple complex present with those specific reaction conditions in solution and Job plot supported this outcome. From **Figure 2.23** it can be seen that the maximum absorbance value was indicative of the triple-stranded complex and a 3:2 [**N1**: Ni^{II}] binding stoichiometry in solution. While an absorbance maximum was indicated at 1.0, it appeared that the slope of the graph began to level off much before this point. It was also seen that around 3.0 there was another slight increase in absorbance. Both of these findings were attributed to the inconsistencies that were obtained with **N1** and the coordinating anions in solution (with both double- and triple-stranded complexes being observed). As with [Fe(H_2O)$_4$$Cl_2$], an alternative method was used to confirm the stoichiometry obtained from the Job plot (**Appendix B**). Plotting absorbance *vs*. [nNi^{II} / n**N1**] also indicated the saturated complex in solution, supporting the titration data that was obtained.

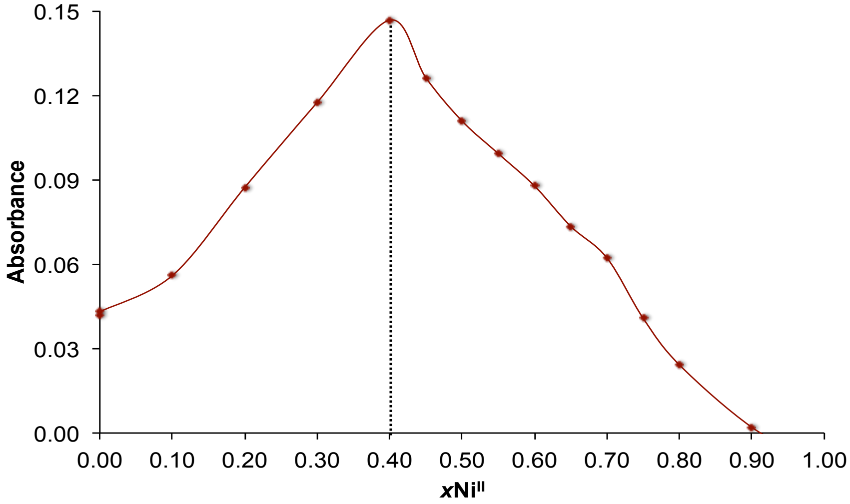

Figure 2.23: Job plot of **N1** with [Ni(H_2O)$_4$(OAc)$_2$] in CH_3OH (line is only connecting the experimental points; no data fitting).

It was a result of this inconsistency between experimental data that inhibited the determination of complex stoichiometry in solution. Compiling all of the obtained data and analyzing it certainly suggested that both the saturated and unsaturated complexes were possible in solution in the presence of coordinating anions. Further work must be done to establish the criteria that favour one stoichiometry over the other.

2.4.6 Towards the N2 Ligand

A second ligand was designed, which would also feature the triazole-pyridine chelating unit. Again naphthalene would be used as the spacer region, however the substitution pattern is varied from **N1** and an ester functionality will be introduced. The naphthalene is 2,7-disubstituted and the ester group will be added between the naphthalene spacer and the methylene linker, which connects to the triazole-pyridine chelating unit. We were hoping to understand how varying naphthalene substitution would affect the self-assembly process of the resulting metallomacrocycle. The ester functionality was introduced to increase the size of the cavity as well as other useful characteristics in the resulting complex. While the synthesis of **N2** was not completed, the intermediate compound was successfully made and compared to literature.

As was outlined in the synthetic scheme above (**Scheme 2.2**), the desired intermediate compound was obtained by an acylation reaction, using neat reaction conditions. Unlike with **N1**, this intermediate molecule (**2.3**) contains a 2,7-disubstituted naphthalene, as well as an ester functionality in addition to the methylene linker. NMR spectroscopy (^{1}H NMR and COSY) as well as mass spectrometry were performed and compared to literature in order to confirm that the desired compound was obtained (**2.3**).[7c,d] The corresponding spectra can be found in **Appendix A**.

Following synthesis of the intermediate compound (**2.3**) the 'click' reaction was intended, however due to time constraints the final **N2** ligand was not synthesized. While the desired ligand was not obtained a synthetic scheme has been proposed and will be explained in Chapter 5 - *Conclusions and Suggestions for Future Work*.

2.5 Conclusions

In summary, a new ligand based on a naphthalene spacer region was synthesized, using the triazole-pyridine chelating unit (with synthesis of the second underway). **N1** was complexed with octahedral metal ions, Fe^{II} and Ni^{II} and properties of the resulting complexes studied. While the initial goal was to potentially utilize **N1** as a metalloreceptor, obtaining the unsaturated double-stranded complex in solution proved to be more complex than originally anticipated. Future work may look into obtaining the unsaturated double-stranded complex and potentially recognizing substrate molecules within the cavity.

Physical properties of the complexes formed between **N1** and octahedral metal ions in the presence of the tetrafluoroborate non-coordinating anion was also explored. Self-assembly properties obtained from previously studied ligands and complexes (specifically **X1**) were used as a template for the newly designed

N1 ligand and the corresponding complexes. **N1** formed complexes that were saturated (triple-stranded), with both metal centers having identical chirality, rendering it a helicate. These properties were anticipated based on the nature of the spacer as well as the non-coordinating BF_4^- anion.

Further work is required to synthesize **N2**. Following synthesis it may be complexed with Fe^{II} and Ni^{II} metal ions, and the corresponding complexes characterized. The obtained complexes may be examined in solid and solution states to determine how the naphthalene substitution pattern and presence of the ester functionality affect the self-assembly process.

2.6 Notes and References

The work described in this chapter includes contributions from the following publication:

Stevenson, K. A.; Melan, C. F. C.; Fleischel, O.; Wang, R.; Petitjean, A., Solid-State Self-Assembly of Triazolylpyridine-Based Helicates and Mesocate: Control of the Metal–Metal Distances. *Cryst. Growth Des.* **2012**, *12*, 5169-5173.

2.7 References

1. (a) Melan, C. F. C. "*Click-helicates": Synthesis and Characterization of Bi-Functional Ligands Based on Triazole-Pyridine Units and the Helicate-Like Structures They Form with Octahedral Metals*. 4th Year Thesis Report, Queen's University: Kinston, 2011; pp 1-22; (b) Crowley, J. D.; Bandeen, P. H., A Multicomponent CuAAC "Click" Approach to a Library of Hybrid Polydentate 2-pyridyl-1,2,3-triazole Ligands: New Building Blocks for the Generation of Metallosupramolecular Architectures. *Dalton Trans.* **2010**, *39*, 612-623.
2. (a) Steel, P. J., Ligand Design in Multimetallic Architectures: Six Lessons Learned. *Acc. Chem. Res.* **2005**, *38*, 243-250; (b) Steel, P. J., Aromatic Nitrogen Heterocycles as Briding Ligands; A Survery. *Coord. Chem. Rev.* **1990**, *106*, 227-265.
3. Bilyk, A.; Harding, M. M.; Turner, P.; Hambley, T. W., Octahedral Non-Helical Bis(bipyridyl) Metallomacrocycles. *J. Chem. Soc. Dalton Trans.* **1995**, 2549-2553.
4. (a) Najar, A. M.; Tidmarsh, I. S.; Ward, M. D., Lead(II) Complexes of Bis- and Tris-Bidentate Compartmental Ligands Based on Pyridyl-Pyrazole and Pyridyl-Triazole Fragments: Coordination Networks and a Discrete Dimeric Box. *CrystEngComm.* **2010**, *12*, 3642-3650; (b) Melan, C. F. C.; Wu, N.; Stevenson, K. A.; Fleischel, O.; Wang, R.; Habib, F.; Mosey, N. J.; Murugesu, M.; Petitjean, A., Click-Triazole: 2-(1,2,3-triazol-4-yl)-pyridine Unit Coordination to Octahedral Cations; Applications to the Self-Assembly of Helicates and Mesocates. Manuscript in preparation, Queen's University: Kingston, 2013; (c) Stevenson, K. A.; Melan, C. F. C.; Fleischel, O.; Wang, R.; Petitjean, A., Solid-State Self-Assembly of Triazolylpyridine-Based Helicates and Mesocate: Control of the Metal–Metal Distances. *Cryst. Growth Des.* **2012**, *12*, 5169-5173.
5. Vellas, S. K.; Lewis, J. E. M.; Shankar, M.; Sagatova, A.; Tyndall, J. D. A.; Monk, B. C.; Fitchett, C. M.; Hanton, L. R.; Crowley, J. D., $[Fe_2L_3]^{4+}$ Cylinders Derived from Bis(bidentate) 2-Pyridyl-1,2,3- triazole "Click" Ligands: Synthesis, Structures and Exploration of Biological Activity. *Molecules* **2013**, *18*, 6383-6407.
6. (a) Rosa, J. C.; Galanakis, D.; Ganellin, C. R.; Dunn, P. M., Synthesis, Molecular Modeling, and K+ Channel-Blocking Activity of Dequalinium Analogues Having Semirigid Linkers. *J. Med. Chem.* **1996**, *39*, 4247-4254; (b) Benito, J. M.; Meldal, M., Bicyclic Organo-Peptides as Selective Carbohydrate Receptors: Design, Solid-phase Synthesis, and on-bead Binding Capability. *QSAR Comb. Sci.* **2004**, *23*, 117-129.
7. (a) Gonda, Z.; Novak, Z., Highly Active Copper-Catalysts for Azide-Alkyne Cycloadditions. *Dalton Trans.* **2010**, *39*, 726-729; (b) Read, M. A.; Wood, A. A.; Harrison, J. R.; Gowan, S. M.; Kelland, L.

R.; Dosanjh, H. S.; Neidle, S., Molecular Modeling Studies on G-Quadruplex Complexes of Telomerase Inhibitors: Structure-Activity Relationships. *J. Med. Chem.* **1999**, *42*, 4538-4546; (c) Suzuki, H.; Padmanabhan, S.; Ogawa, T., Facile Cleavage of Aryl Haloacetates and 2-Chloroethyl Carboxylic Esters with Sodium Telluride. A One-Pot Conversion of Aryl Esters into Aryl Ethers Under Aprotic Conditions. *Chem. Lett.* **1989**, 1017-1020; (d) Resnick, B. M.; West Paterson, N. J. Fungicidal Naphthylene Diesters and Mixtures Thereof 1983.

8. Fleischel, O.; Wu, N.; Petitjean, A., Click-triazole: Coordination of 2-(1,2,3-triazol-4-yl)-pyridine to Cations of Traditional Tetrahedral Geometry (Cu(I), Ag(I)). *Chem. Commun.* **2010**, *46*, 8454-8456.
9. Hawes, C. S.; Fitchett, C. M.; Kruger, P. E., Synthesis of an Fe(II) Dinuclear Triple Helicate from a Novel Bis-(N-pyrazolyl)pyridine Ligand, $[Fe_2L_3]^{4+}$: Solution and Solid-State Studies. *Supramol. Chemistry* **2012**, *24* (8), 553-562.
10. Stevens, J. R.; Plieger, P. G., Anion-Driven Conformation Control and Enhanced Sulfate Binding Utilising Aryl Linked Salicylaldoxime Dicopper Helicates. *Dalton Trans.* **2011**, *40*, 12235-12241.
11. Albrecht, M., How Do They Know? Influencing the Relative Stereochemistry of the Complex Units of Dinuclear Triple-Stranded Helicate-Type Complexes. *Chem. Eur. J.* **2000**, *6*, 3485-3489.
12. (a) Hauser, A., Ligand Field Theoretical Considerations. *Adv. Polym. Sci.* **2004**, *233*, 49-58; (b) Gütlich, P.; Goodwin, H. A., Spin Crossover - An Overall Perspective. *Top. Curr. Chem.* **2004**, *233*, 1-47.
13. Crowley, J. D.; Bandeen, P. H.; Hanton, L. R., A One-Pot Multi-Component CuAAC ‘Click' Approach to Bidentate and Tridentate Pyridyl-1,2,3-triazole Ligands: Synthesis, X-ray Structures and Copper(II) and Silver(I) Complexes. *Polyhedron* **2010**, *29*, 70-83.
14. Yoon, I.; Benitez, D.; Miljanic, O. S.; Zhao, Y.-L.; Tkatchouk, E.; Goddard, W. A.; Stoddart, J. F., Rigidity#Stability Relationship in Interlocked Model Complexes Containing Phenylene-Ethynylene-Based Disubstituted Naphthalene and Benzene. *Cryst. Growth Des.* **2009**, *9* (5), 2300-2309.
15. (a) Cohen, M. D.; Fischer, E., Isobesic Points. *J. Chem. Soc.* **1962**, *588*, 3044-3052; (b) Daly, L. H.; Colthup, N. B.; Wiberley, S. E., *Introduction to Infrared And Raman Spectroscopy* Academic Press 1990.
16. The UV-vis experiments (titrations and Job plots) were performed by Dr. Petitjean, A., Kingston, Spring 2013.
17. (a) Wilson, L. J.; Georges, D.; Hoselton, M. A., Electronic Spectral Study of Some Iron(II) Magnetic Isomers in Solution and a Spectrial-Structural Correlation with Their Nickel(II) Analogs. *Inorg. Chem.* **1975**, *14* (12), 2968-2975; (b) Gütlich, P., Spin Crossover in Iron(II)- Complexes. *Struct. Bond* **1981**, *44*, 83-195.

Chapter 3

Ligands Derived from Aliphatic Spacers and Their Complexes

3.1 Introduction: Previous Aliphatic Spacers

In addition to ligands containing aromatic spacer groups, work within our lab is also interested in multinuclear complexes with aliphatic spacers of varying length. The ligand containing a propyl spacer (**C3**), was first synthesized by Crowley *et al.* in 2010, and reproduced by Petitjean *et al.* in 2011 (**Figure 3.1**).[1] Crowley *et al.* obtained an X-ray crystal structure of the **C3** ligand and observed an *anti*-conformation between pyridine and triazole nitrogen donors.[1a] A coplanar arrangement between pyridine and triazole groups was also observed, with both of these conformations being commonly observed in nitrogen chelating units.[1a, 2] Upon complexing with metal ions the ligand is forced to alter its *anti*-conformation in order to chelate, and therefore must adopt a *syn*-conformation (*anti*-conformation outlined in **Figure 3.1**).

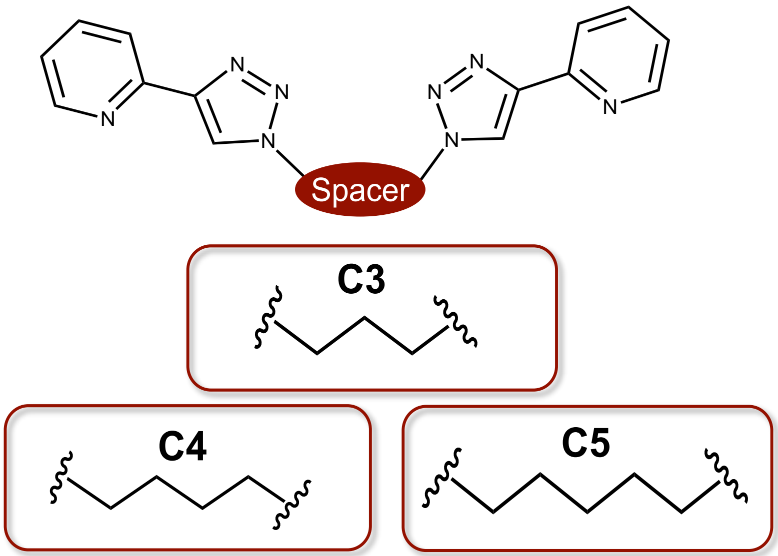

Figure 3.1: Ligand design with triazole-pyridine chelating units and variable spacer region. Structures of aliphatic ligands include: previously synthesized **C3**,[1, 3] and ligands of interest **C4** and **C5**.

The coordination chemistry of **C3** has been previously studied with the labile Ag^{I} metal ion.[1a] In our group, once the ligand was synthesized it was complexed with metal ions of octahedral geometry, Ni^{II} and Fe^{II} and their physical properties examined (Caroline Melan, 4th year student, Jan-Aug 2011).

Compared to the ligands described in Chapter 2 (containing a naphthalene spacer region), the aliphatic spacers offer flexibility, which may affect the self-assembly process as a result. Previous work by Albrecht proposed an *even-odd* rule to assigning complex chirality, based on the number of carbons present in the aliphatic spacer region (explained in detail in Chapter 1).[4] An alkyl spacer unit with an even number of carbons typically corresponds to a helicate conformation, while an odd number of carbons characteristically results in a mesocate structure.[4] With our preliminary ligands this rule may be applied, however as the length of the aliphatic spacer increases, the assignment may not be as clear-cut.

3.1.1 Increasing the Length of the Spacer

As with the ligands in the previous chapter, increasing alkyl spacer alters length alters many physical properties of the ligands as well as the complexes they form with metal ions. It has been previously observed that the length of the spacer connecting the metal centers and the bridging ligands can have a profound effect on the resulting complexes.[5] Increasing the length of the aliphatic spacer also increases the flexibility of the ligand, which may decrease the overall level of control over the self-assembly process.[6] A result of this increased flexibility can be seen in the complex obtained from the pentyl spacer (**C5**), in which the *even-odd* rule may not apply in as concrete a manner as was originally anticipated.[1b]

3.2 Ligand Syntheses: Butyl (C4) and Pentyl (C5) - Alkyl Spacers

Both ligands were obtained from reaction of the commercially available alkyl dihalide to obtain the ‘click’ reaction product. A one pot, two-step synthetic procedure was followed in order to avoid isolating the potentially explosive azide intermediate.[1a] The first step of the ‘click’ reaction involved reacting the alkyl dihalide starting materials (1,4-dibromobutane or 1,5-dibromopentane) with sodium azide, which was then subjected to the ‘click’ reaction without isolation. In both cases the desired ligands were obtained with butyl and pentyl aliphatic spacer regions corresponding to the **C4** (**Figure 3.2**) and **C5** (**Figure 3.3**) ligands respectively.

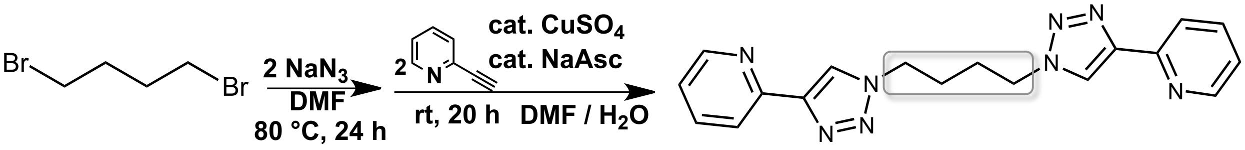

Figure 3.2: Synthetic route for **C4** with the butyl spacer region highlighted.

Unlike with **N1**, both aliphatic ligands required elevated temperatures for the initial step of the reaction, the S_N2 reaction with sodium azide. Crowley *et al.* observed that when this step was carried out at room temperature a mixture of both mono- and bis-substituted products were obtained.[1a] By increasing the temperature to 90 °C a much more complete conversion was observed, obtaining the desired bis-substituted ‘click’ product.[1a] Based on these observations, the initial S_N2 step for both **C4** and **C5** was carried out at 80 °C, which gave the desired products in excellent yields following completion of the reaction.

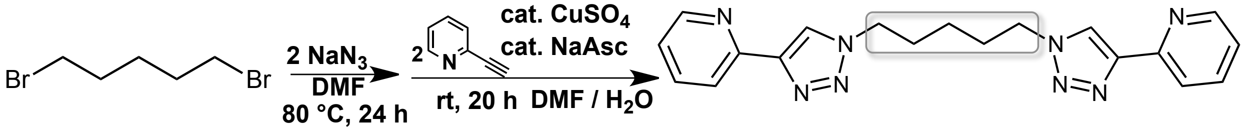

Figure 3.3: Synthetic route for **C5** with the pentyl spacer region highlighted.

C4 and **C5** ligands were chosen because we were specifically interested in how self-assembly of the complexes with octahedral metal ions (Fe^{II} and Ni^{II}) was affected by the increase in aliphatic chain length. We wanted to observe whether the additional flexibility, which was correlated to alkyl chain length, played a role in the nature of the supramolecular architectures that were formed. It was also previously observed that the $[Fe_2($**C3**$)_3](BF_4)_4$ complex displayed spin crossover behaviour, with a transition to high-spin at elevated temperatures.[1b] We were hoping to better understand the properties that influence spin crossover behaviour by studying other complexes with similar structural characteristics.

3.3 Formation of Metallomacrocycles with Octahedral Metal Ions

Much like with the **N1** ligand, we were interested in the complexes that formed between **C4** and **C5** ligands and octahedral metal ions, Fe^{II} and Ni^{II}. The complexes were obtained and studied by NMR spectroscopy (only Fe^{II} complexes), UV-vis spectroscopy and elemental analysis (see Chapter 4). These ligands were only studied with the non-coordinating tetrafluoroborate anion (BF_4^-), as the alkyl spacers are not overly conducive to substrate binding, unlike the naphthalene spacer.

3.3.1 Synthesis of [Fe$_2$(C4)$_3$](BF$_4$)$_4$ and [Fe$_2$(C5)$_3$](BF$_4$)$_4$

The Fe^{II} complexes of both **C4** and **C5** were obtained by mixing two equivalents of metal salt, $[Fe(H_2O)_6](BF_4)_2$, with three equivalents of ligand (**C4** or **C5**) in acetonitrile (**Figure 3.4**). Ethyl acetate was then added to the solution to precipitate out the complex, and the solvent was subsequently removed. Following removal of the solvent, ethyl acetate was added and the solution heated at 30 °C for 2 h to remove any excess ligand remaining in solution. The resulting complexes were collected by vacuum filtration and in both cases yielded a bright orange powder. The complexes were examined by NMR spectroscopy, UV-vis spectroscopy as well as elemental analysis (see Chapter 4).

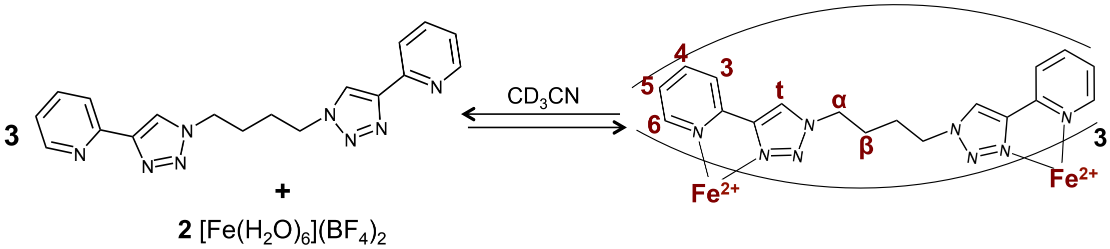

Figure 3.4: Synthetic route for $[Fe_2(\mathbf{C4})_3](BF_4)_4$ in CD_3CN with atom numbering indicated (same route for $[Fe_2(\mathbf{C5})_3](BF_4)_4$: pentyl spacer instead of butyl).

3.3.2 Synthesis of $[Ni_2(C4)_3](BF_4)_4$ and $[Ni_2(C5)_3](BF_4)_4$

In the same way as with the Fe^{II} complexes, the Ni^{II} complexes were obtained by combing two equivalents of metal salt, $[Ni(H_2O)_6](BF_4)_2$, with three equivalents of ligand (**C4** or **C5**) in acetonitrile (**Figure 3.5**). The same procedure was followed and pink powders were obtained for both **C4** and **C5** complexes. The complexes were examined by UV-vis spectroscopy and their molecular composition confirmed by elemental analysis (see Chapter 4).

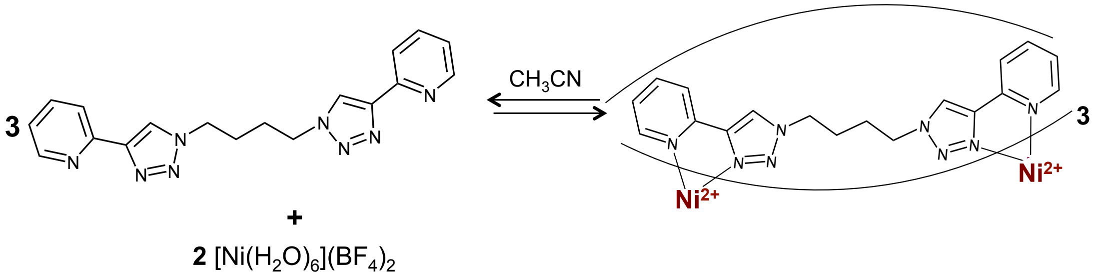

Figure 3.5: Synthetic route for $[Ni_2(\mathbf{C4})_3](BF_4)_4$ in CH_3CN (same route for $[Ni_2(\mathbf{C5})_3](BF_4)_4$: pentyl spacer instead of butyl).

3.4 Results and Discussion

3.4.1 Characterization of C4 Ligand

The **C4** ligand, identified by a butyl spacer region, was obtained and characterized by NMR spectroscopy (^{1}H, ^{13}C, COSY, HSQC and HMBC can be seen in **Appendix A**), mass spectrometry as well as elemental analysis (Chapter 4). We were interested to see the effects, if any, that lengthening the aliphatic spacer region had on self-assembly and complex formation with octahedral metal ions.

Note: A full description of all instruments and techniques used for the ligands and complexes described herein may be found in Chapter 4.

3.4.1.1 NMR Analysis of C4

The ^{1}H NMR spectrum of **C4** gave the anticipated chemical shifts corresponding to the triazole-pyridine chelating unit, as well as the two methylene groups belonging to the butyl spacer region (**Figure 3.6**). As a result of the symmetrical nature of the ligand, only two peaks were assigned to the butyl spacer, indicated by **α** and **β** in the ^{1}H NMR spectrum. The diagnostic triazole singlet was found at 8.16 ppm, which was in the acceptable range of 7.5-8.6 ppm, confirming that the 'click' reaction was successful.[7] To confirm the proton assignments a COSY was performed and analyzed (**Appendix A**).

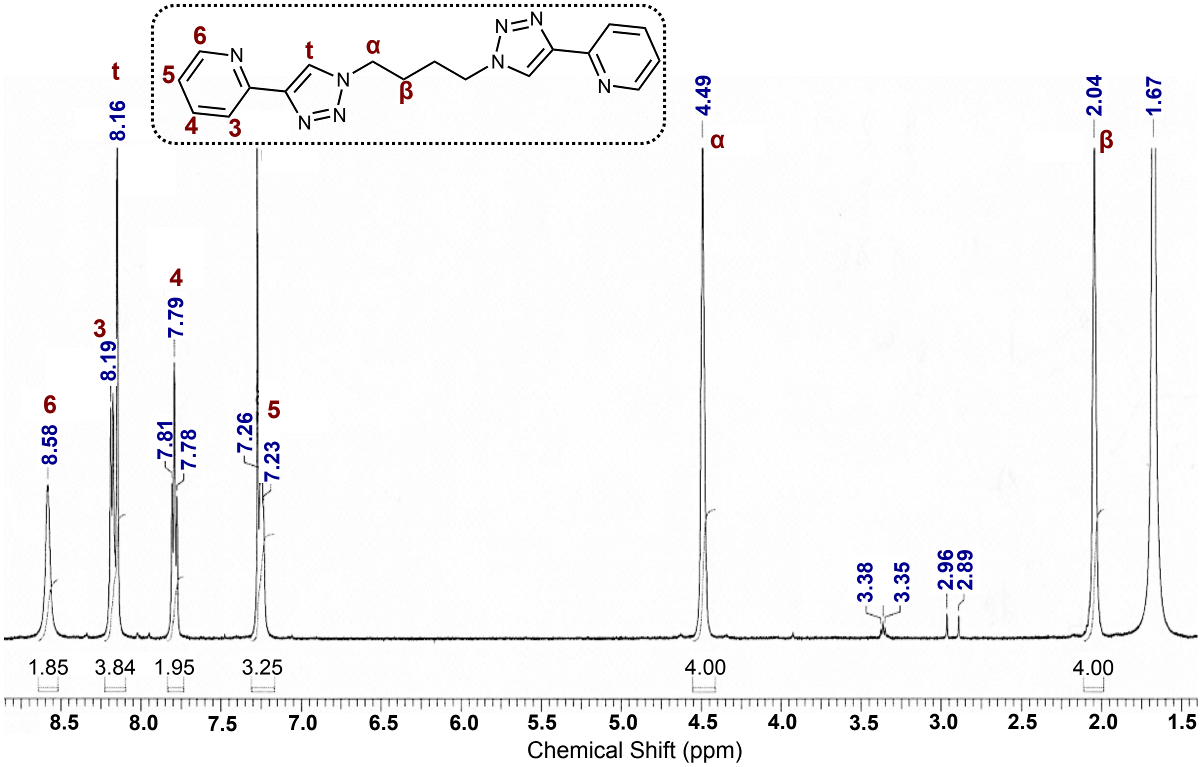

Figure 3.6:^{1}H NMR spectrum of **C4** in $CDCl_3$* (300 MHz, 25°C)

The **C4** ligand was further characterized by ^{13}C NMR, however ligand solubility at high concentrations was poor in all organic solvents. In order to accurately assign all of the carbons, 2D NMR experiments (HSQC and HMBC) were performed, further confirming the structure of the ligand (**Appendix A**).

3.4.1.2 Mass Spectrometry and Elemental Analysis of C4

Mass spectrometry and elemental analysis were analytical methods that were also used for the characterization of **C4**. Electron impact mass spectrometry was utilized to confirm that the desired ligand was obtained based on the theoretical molecular weight (**Figure 3.7**). The molecular ion peak at m/z 346.16 corresponded to [M^+], and another peak to note was seen at m/z 318.16, consistent with [$(M\text{-}N_2^+)$].

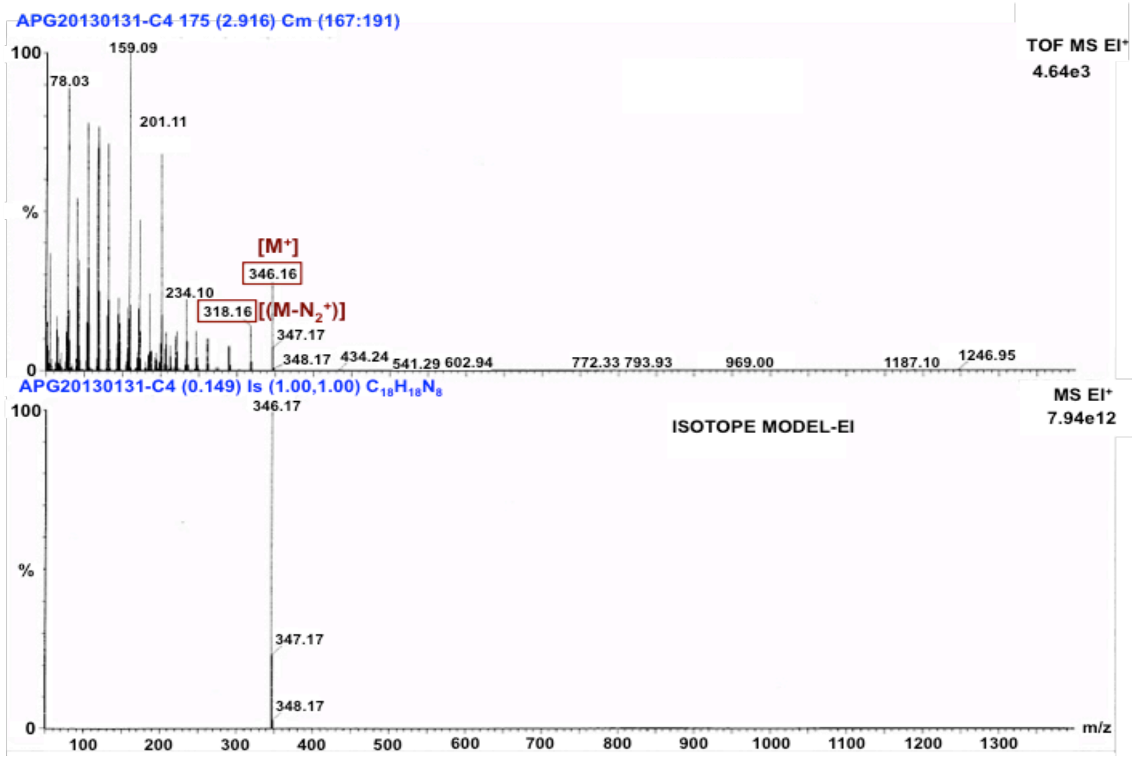

Figure 3.7: EI^+- mass spectrum of **C4** ligand.

Elemental analysis confirmed the overall molecular composition and purity of **C4** (see Chapter 4). Despite extensive efforts to ensure the ligand was extremely pure (recrystallization and column chromatography were both utilized), there were still traces of impurities in the elemental analysis data (0.15 equivalents of H_2O).

3.4.2 Characterization of C5 Ligand

In a similar fashion to **C4**, **C5** was also obtained and characterized by NMR spectroscopy, mass spectrometry as well as elemental analysis. The pentyl spacer region, as compared to the butyl spacer of the **C4** ligand, was used to identify **C5**. Electron impact mass spectrometry confirmed that the correct, pure ligand was obtained and the corresponding spectrum can be found in **Appendix A**. The molecular peak at m/z 360.18 corresponded to the [M^+], which was consistent with the theoretical molecular weight of the ligand. Elemental analysis obtained for **C5** agreed with the experimentally determined values for ligand composition. The ligand appeared to be very pure with no traces of solvent or impurities present in the analysis (see Chapter 4).

3.4.2.1 NMR Analysis of C5

^{1}H NMR spectroscopy was once again used to determine the structure of the obtained ligand. Peaks corresponding to the triazole (H_t) and pyridine (H_3-H_6) groups were identified, in addition to the aliphatic peaks, which were assigned as H_α, H_β and H_γ (**Figure 3.8**). Again the symmetrical nature of the ligand resulted in the two H_α methylene groups being homotopic as well as the two H_β methylene groups. The aliphatic protons closest to the triazole nitrogen were located the further downfield (H_α), with decreasing chemical shifts assigned to H_β and H_γ. This same equivalency was not observed once the ligand was complexed with Fe^{II}, however this will be explained in Section 3.4.4.1 with the corresponding characterization. The proton assignments were confirmed by COSY (**Appendix A**).

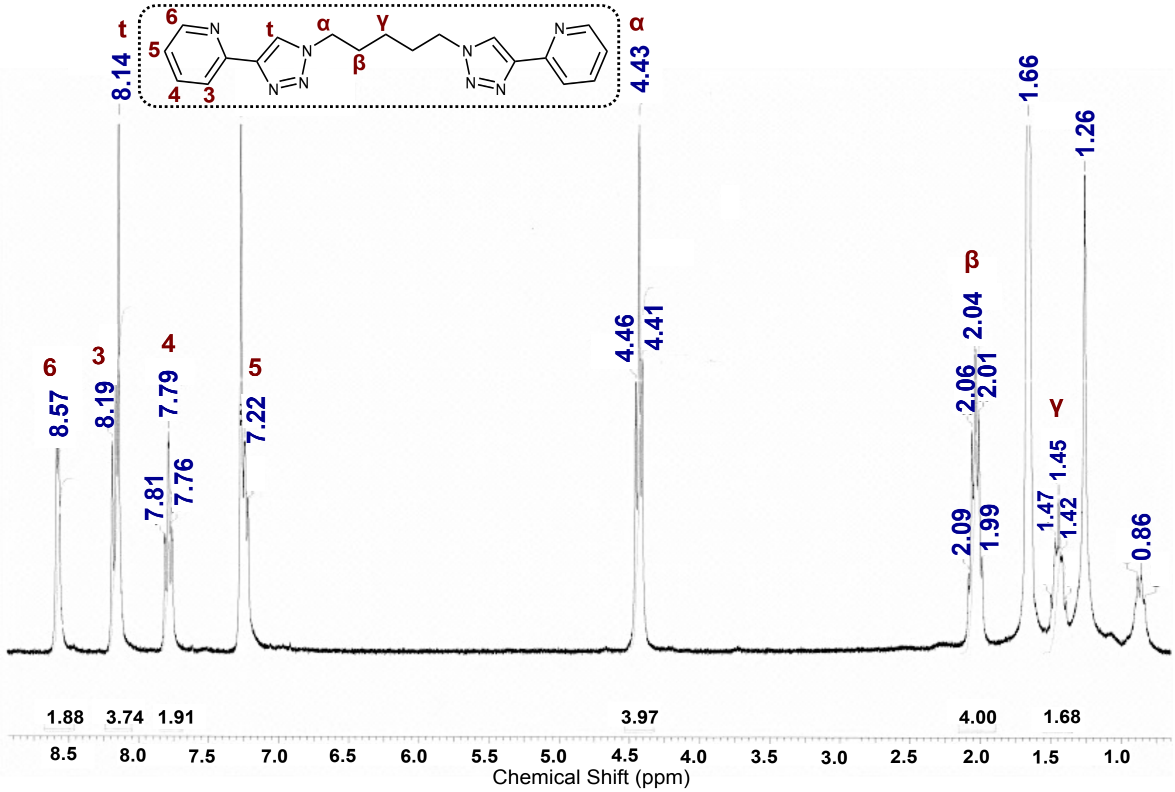

Figure 3.8: ^{1}H NMR spectrum of **C5** in $CDCl_3$* (300 MHz, 25 °C)

C5 was further characterized by ^{13}C, HSQC and HMBC NMR experiments (in addition to the previously discussed ^{1}H and COSY experiments). See **Appendix A** for the corresponding spectra.

3.4.3 Characterization of $[Fe_2(C4)_3](BF_4)_4$

The metallomacrocycle was obtained by combining two equivalents of metal salt, $[Fe(H_2O)_6](BF_4)_2$, with three equivalents of ligand (**C4**) in acetonitrile. The complex was collected as a bright orange powder and examined by NMR spectroscopy (see **Appendix A**), UV-vis spectroscopy as well as elemental analysis (see Chapter 4). Through these experiments various properties were examined, including stoichiometry and assignment of relative chirality at the metal centers based on consistency with the *even-odd* rule.[4] It was anticipated that the saturated triple-stranded complex would form, with a 2:3 [Fe^{II}: **ligand**] stoichiometry, due to the presence of the non-coordinating tetrafluoroborate anion (BF_4^-).

3.4.3.1 NMR Characterization of [Fe$_2$(C4)$_3$](BF$_4$)$_4$

The ^{1}H NMR spectrum of the [Fe$_2$(**C4**)$_3$]$^{4+}$ complex displayed slightly broad and complicated signals compared to the spectrum of the free ligand. There appeared to be a mixture of products, however the expected [Fe$_2$(**C4**)$_3$]$^{4+}$ complex appeared with the highest abundance. Despite the complexity of the ^{1}H NMR spectrum, proton assignments were confirmed by COSY (**Figure 3.10**). Spectra of this nature have been observed in a few other instances and may be attributed to the increased flexibility of the alkyl spacer region.[8] An equilibrium between helicate and mesocate conformations has previously been observed with flexible alkyl spacers in solution, however the ^{1}H NMR spectrum did not support this observation.[4] It was instead speculated that the additional low abundance peaks were a result of polymeric or oligomeric species that had formed in solution.[8] While there may have been additional species present in solution, entropically it was the [Fe$_2$(**C4**)$_3$]$^{4+}$ complex that predominated based on stability.

Application of the *even-odd* rule suggested that there was a conformational preference for a helicate structure to form based on the even number of carbons present in the butyl spacer.[4] While there is a preference for a helicate to form, the aliphatic protons are expected to be diastereotopic regardless of a helicate or mesocate conformation. Based on this the ^{1}H NMR spectrum cannot be used to concretely identify the nature of the species in solution. As will be seen with **C5**, the additional H$_\gamma$ proton is required to distinguish between the two conformations. The peaks belonging to the pyridine and triazole protons were assigned however, and were consistent with the spectrum obtained from the [Fe$_2$(**C3**)$_3$]$^{4+}$ complex.

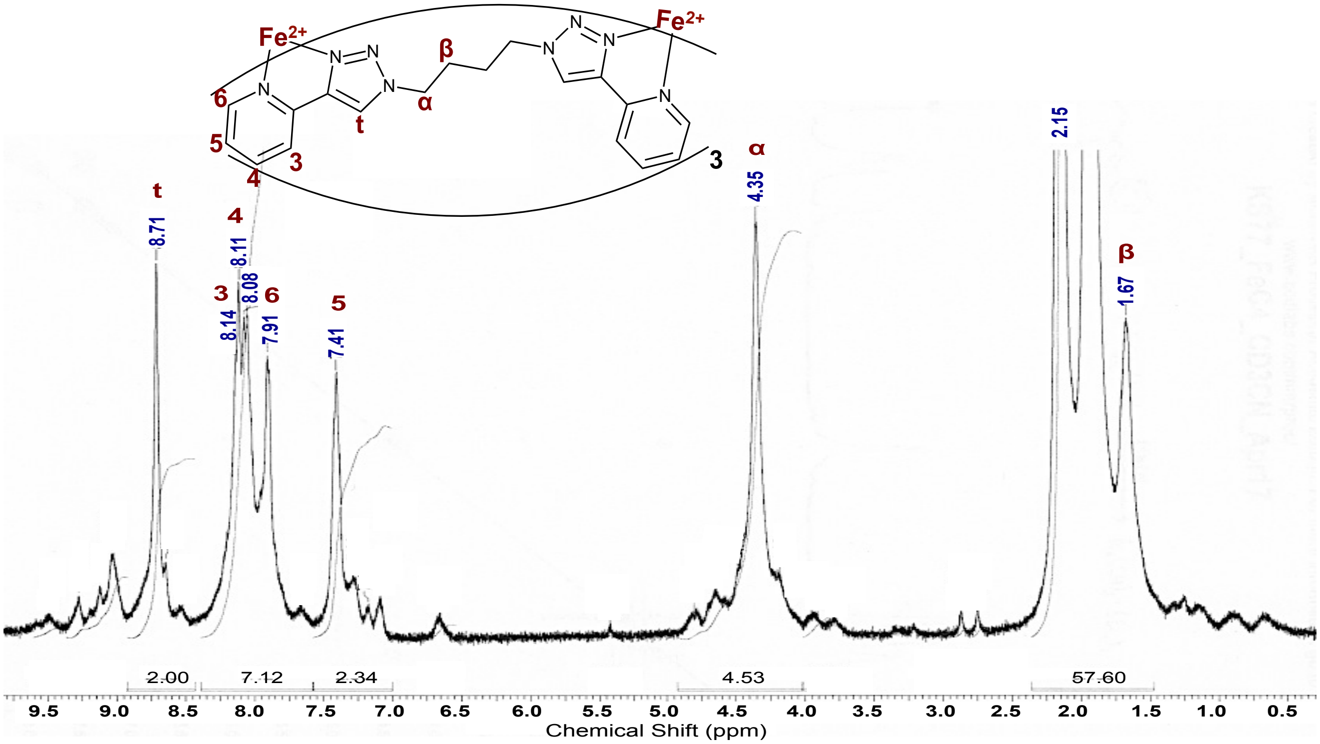

Figure 3.9: ^{1}H NMR spectrum of [Fe_2(**C4**)$_3$](BF_4)$_4$ in $CDCN_3$ (300 MHz, 25°C).

While direct comparison between free ligand (in $CDCl_3$*) and [Fe_2(**C4**)$_3$](BF_4)$_4$ complex (in CD_3CN) could not be made because of solvent discrepancies, useful observations were still made. The ^{1}H NMR spectrum became much more convoluted and difficult to assign upon complexing with Fe^{II}, compared to the free ligand. While a quantitative comparison could not be made, the downfield shift of the triazole proton relative to the free ligand was an indication of complexing with Fe^{II} ions.[8a] The other proton that had a noticeable change in chemical shift upon complexation was H_6, as a result of the close proximity to the chelating pyridine nitrogen.[8a]

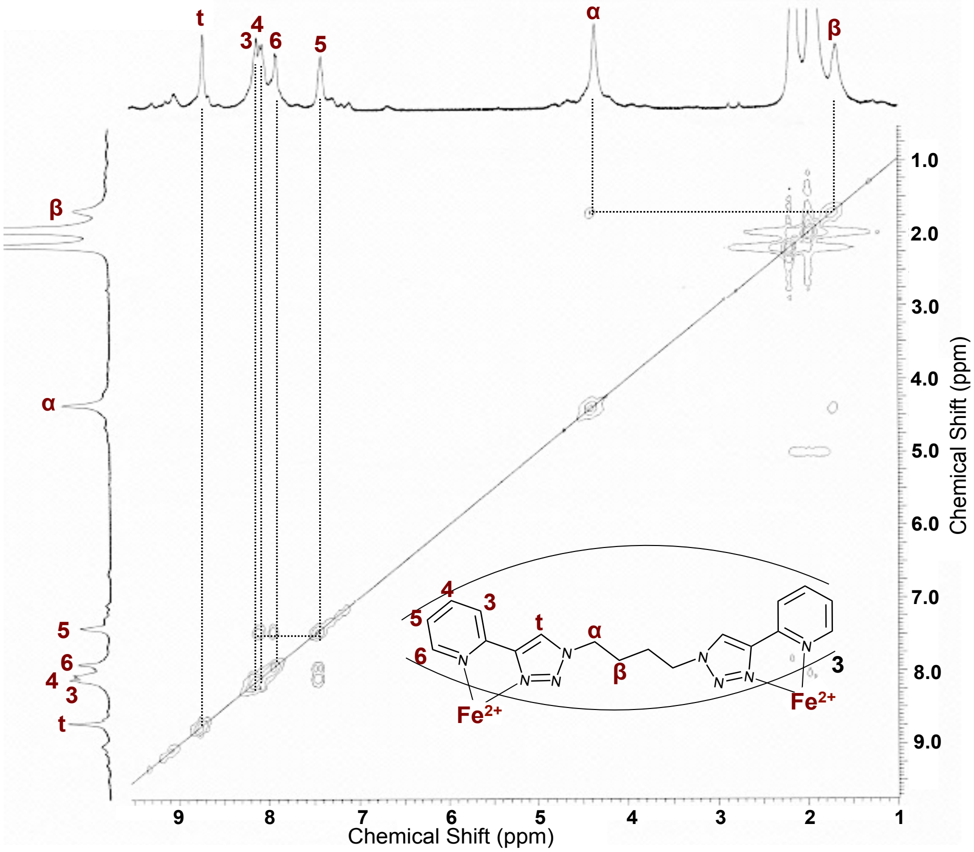

Figure 3.10: ^{1}H-^{1}H COSY spectrum of $[Fe_2(\mathbf{C4})_3](BF_4)_4$ in CD_3CN (300 MHz, 25 °C).

Despite the convoluted ^{1}H NMR spectrum, a COSY experiment made proton assignments much clearer. The COSY spectrum shown in **Figure 3.10** identifies the proton assignments as well as the corresponding proton-proton correlations.

Numerous attempts were made to obtain X-ray quality single crystals, however none were successful. The X-ray crystal structure would have been extremely useful in confirming the stoichiometry of the obtained complex, however the combination of NMR and UV-vis spectroscopy results gave some good insight.

3.4.3.2 UV-vis Titration of C4 with $[Fe(H_2O)_6](BF_4)_2$

By performing a UV-vis titration of $[Fe(H_2O)_6](BF_4)_2$ to **C4**, information was gathered about the physical and structural properties of the complex, including stoichiometry and binding strength. As anticipated, an increase in Fe^{II} concentration correlated with the solution becoming a darker yellow/orange colour. This relationship was consistent with the observed spectrum (**Figure 3.11**), which showed an increase in the peak around 430 nm, corresponding to a metal-to-ligand charge transfer (MLCT) band. The overall spectrum showed four prominent peaks, which occurred at 240 nm, 280 nm, 330 nm (shoulder), and 425 nm.

There was an isosbestic point that occurred around 264 nm, which was indicated transformation from starting materials to products. The absorbing species in solution were likely free **C4** ligand and complex.[9] The transformation was dependent on the concentration of $[Fe(H_2O)_6](BF_4)_2$ present in solution.[9] At the isosbestic point absorbances remained constant, however absorbances on either side changed as the reaction proceeded (increasing amount of $[Fe(H_2O)_6](BF_4)_2$ in solution).[9]

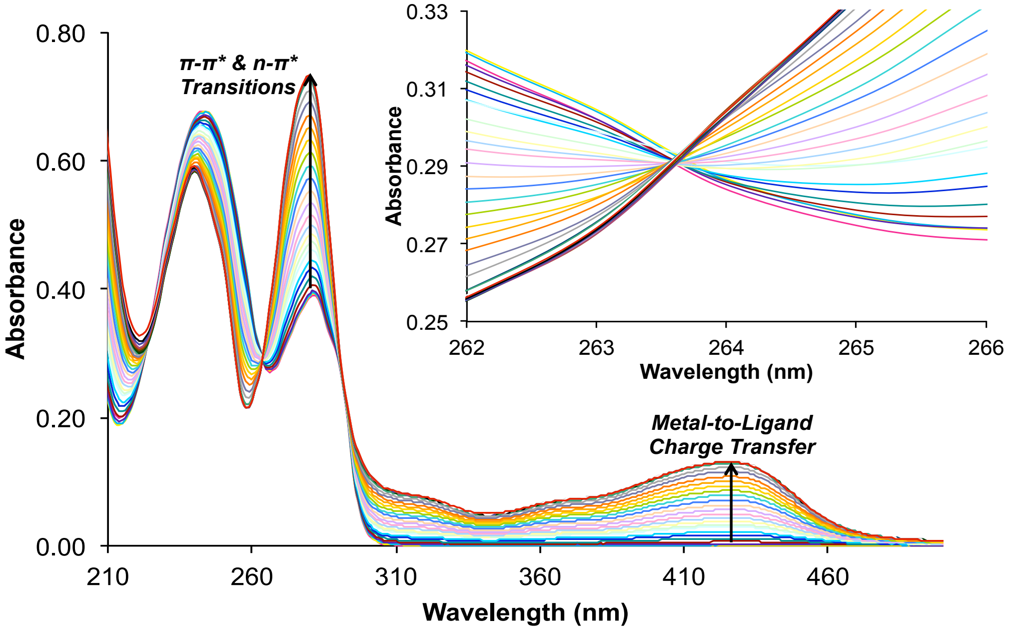

Figure 3.11: UV-vis titration data for $[Fe(H_2O)_6](BF_4)_2$ to **C4** in CH_3CN. Full spectrum and zoom (*inset*) on 260-270 nm, showing the isosbestic point (264 nm).[10]

From the absorbance *vs*. [$n$$Fe^{II}$ / n**C4**] ratio graph it can be seen that a complex formed with two Fe^{II} metal ions and three **C4** ligands, which corresponds to a ratio of 0.67 (**Figure 3.12**). The maximum absorbance at 0.67 was indicative of a complex with the general formula $[Fe_2(\mathbf{L})_3]^{4+}$, which was also consistent with a [2 Fe^{II} : 3 **L**] binding stoichiometry. Another piece of information that was abstracted from the titration data was the relative binding strength of the complex. The shape of the curve indicated that the $[Fe_2(\mathbf{C4})_3]^{4+}$ complex formed with relatively strong binding. This was gathered because when the ratio of [$n$$Fe^{II}$ / n**N1**] reached 0.67 (or two equivalents of Fe^{II} to three equivalents of **C4**) the absorbance reached a plateau and remained constant. A complex that formed with weaker binding would have a much more gradual increase, and the point where absorbance reaches a maximum is not as clear.

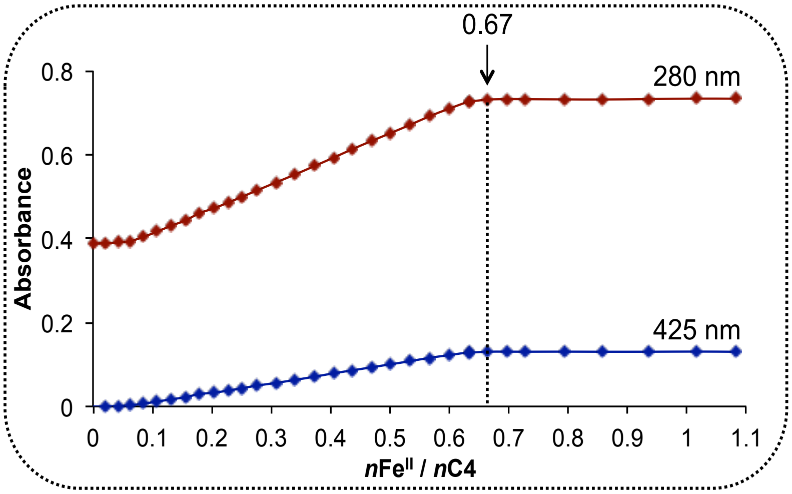

Figure 3.12: Absorbance as a function of [$n$$Fe^{II}$ / n**C4**] ratio for peaks at 425 nm and 280 nm.[10] *Note*: '*n*' mentioned herein refers to number of moles.

To further confirm complex stoichiometry a Job plot was performed with varying solution concentrations (**Figure 3.13**). The Job plot method works on the premise that a series of solutions are prepared, each with an equivalent number of moles of metal ion and ligand.[11] The ratio of moles varies in each solution however, with [n(metal ion) : n(**ligand**)] typically ranging from zero to one.[11a] The Job plot data was analyzed by plotting the absorbance at a specific wavelength as a function of the molar ratio of Fe^{II} ($x$$Fe^{II}$).

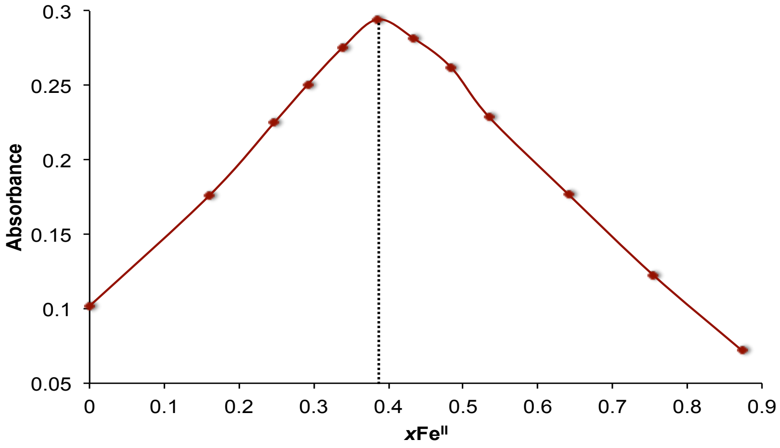

Figure 3.13: Job plot of **C4** with $[Fe(H_2O)_6](BF_4)_2$ in CH_3CN (line is only connecting the experimental points; no data fitting).[10] *Note*: xFe^{II} mentioned herein refers to molar ratio [moles of Fe^{II} / total moles].

The Job plot indicated a very clear absorbance maximum occurring at xFe^{II} = 0.4. Based on this it was confirmed that the species present in solution was the saturated triple-stranded complex, consistent with the formula $[Fe_2(\mathbf{C4})_3]^{4+}$.

3.4.3.3 Molar Absorptivity Analysis of $[Fe_2(C4)_3](BF_4)_4$ and $[Fe_2(C5)_3](BF_4)_4$

Molar absorptivity values for both **C4** and **C5** complexes with $[Fe(H_2O)_6](BF_4)_2$ were determined by UV-vis spectroscopy, which showed how strongly the species absorbed at a given wavelength. To the $[Fe_2(\mathbf{C4})_3](BF_4)_4$ or $[Fe_2(\mathbf{C5})_3](BF_4)_4$ complexes (powder) was added acetonitrile, which both yielded dark orange solutions (*Note*: gentle heating and sonication was required to get a completely homogenous solution). In both cases, as the concentration of Fe^{II} in solution increased, the solutions became darker yellow/orange in color, which also corresponded to an increase in MLCT absorbance. The peaks in the ultraviolet region (230 and 280 nm) were characteristic of π-π* and n-π* transitions, corresponding to promotion of an electron from a π-bonding to anti-bonding orbitals. The metal-to-ligand charge transfer band occurred around 430 nm, which confirmed complexation and coordination of the ligands to Fe^{II} metal ions. The absorption spectrum has been shown in **Figure 3.14**, and the data summarized in **Table 3.1**.

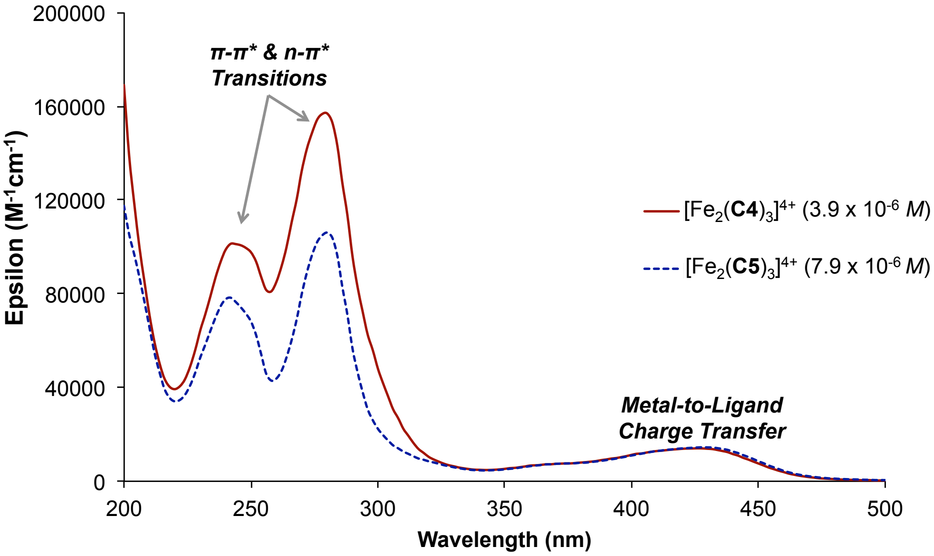

Figure 3.14: UV-vis absorption spectra of $[Fe_2(\mathbf{C4})_3](BF_4)_4$ and $[Fe_2(\mathbf{C5})_3](BF_4)_4$ in CH_3CN.

Similar trends in the UV spectra were observed for both complexes, with maxima occurring at the same wavelengths, 240 nm, 280 nm and 425 nm. When solution concentrations were varied however there were noticeable changes in molar absorptivity values for both complexes. It was expected that the ε values ($M^{-1}cm^{-1}$) were independent of concentration, so such a change indicated that the complex might be dissociating upon dilution. This phenomenon has been seen before however, where as the solutions became increasingly dilute, the complex dissociated into free metal and free ligand.[12]

Table 3.1: Summary of ε ($M^{-1}cm^{-1}$) and log ε values for $[Fe_2(\mathbf{C4})_3](BF_4)_4$ and $[Fe_2(\mathbf{C5})_3](BF_4)_4$ complexes.

Complex	Wavelength (nm)	ε ($M^{-1}cm^{-1}$) [log ε]
$[Fe_2(C4)_3](BF_4)_4$	426	16,114.7 [4.2]
	320	9,465.7 [4.0]
	280	156,931.3 [5.2]
	242	101,284.9 [5.0]
$[Fe_2(C5)_3](BF_4)_4$	430	14,452.9 [4.2]
	280	106,075 [5.0]
	242	78,297.6 [4.9]

3.4.3.4 Models of $[Fe_2(\mathbf{C4})_3]^{4+}$

While we were unable to obtain single crystals suitable for X-ray crystallography, models were predicted using the Advanced Chemistry Development Inc. (ACD/Labs) Software.[13] Both helicate and mesocate structures of the complex formed between **C4** and $[Fe(H_2O)_6](BF_4)_2$ were modelled. NMR spectroscopy, UV-vis spectroscopy and elemental analysis that have been previously explained in detail confirmed that it was the saturated triple-stranded complex favoured in solution with the tetrafluoroborate anion. While these models cannot be interpreted as crystal structures, the structural properties may still be examined and the differences between the helicate and mesocates structures observed (**Figure 3.15**).

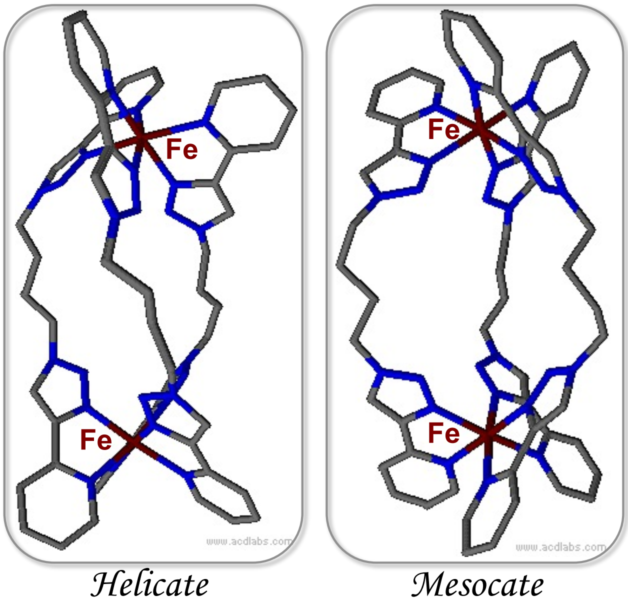

Figure 3.15: Models of $[Fe_2(\mathbf{C4})_3]^{4+}$, with both helicate and mesocate structures represented.[13]

The distance between Fe^{II} metal centers was measured upon energy minimization of the complex. Unlike with an actual X-ray crystal structure, these values cannot be used for any more than a frame of reference and to be very loosely compared to the previously obtained values for $[Fe_2(\mathbf{C3})_3]^{4+}$. The Fe^{II}-Fe^{II} distance for the theoretical $[Fe_2(\mathbf{C4})_3]^{4+}$ complex was found to be 10.4 Å, slightly greater than the experimentally determined value for $[Fe_2(\mathbf{C3})_3]^{4+}$ of 9.88 Å. This slight increase in metal-metal distance can be expected based on the increase in aliphatic chain length, from propyl to butyl.

Based on the *even-odd* rule and the even number of carbons present in the spacer region it was anticipated that the helicate conformation would be favoured by **C4**. With both structures indicated above we can observe the structural differences between the two (**Figure 3.15**). It has been previously indicated that the helicate conformation tends to adopt a 'S' configuration, while the mesocate predominantly conforms to a 'C' configuration on the basis of stability.[4] The explanation for these preferred conformations is based on the number of carbons present in the spacer region, and the preferential *zigzag* orientation of a linear alkyl chain.[4] These conformations are confirmed in the models of $[Fe_2(\mathbf{C4})_3]^{4+}$, which would then suggest formation of the helicate complex as being the most stable.

3.4.4 Characterization of $[Fe_2(C5)_3](BF_4)_4$

In an identical fashion to the $[Fe_2(\mathbf{C4})_3](BF_4)_4$ complex, the **C5** metallomacrocycle was obtained by combining two equivalents of metal salt, $[Fe(H_2O)_6](BF_4)_2$, with three equivalents of ligand (**C5**) in acetonitrile. The complex was collected as a bright orange powder and examined by NMR spectroscopy (see **Appendix A**), UV-vis spectroscopy (see **Appendix B**) as well as elemental analysis (see Chapter 4). These experiments gave some fascinating results, some of which may challenge the previously identified *even-odd* rule.[4] By increasing aliphatic spacer length, the amount of conformational flexibility also increased, which has presented some additional characteristics which were not seen with previous complexes.

3.4.4.1 NMR Characterization of $[Fe_2(C5)_3](BF_4)_4$

From the ^{1}H NMR spectra it became apparent that there was additional complexity associated with the increase in aliphatic spacer length. From the spectrum it appeared that several of the protons had multiple peaks, which suggested that perhaps there were multiple species present in solution (**Figure 3.16**). Similar behaviour has been observed previously, where ligands with flexible spacer regions formed a mixture of complexes in solution, however typically these ligands have heteroatoms connecting the spacer to the chelating units.[1a, 5a, 8a]

Regardless of a helicate or mesocate conformation the protons corresponding to H_α, H_β will be diastereotopic, and it is the H_γ protons that will be used to distinguish between the two different species in solution. Depending on the presence of a helicate or mesocate the splitting pattern for H_γ will be different, and can give insight into the identity of the two species. For the **C5** complex it appeared that there was a 1:2 mixture of species that formed in solution and COSY was used to distinguish between the two.

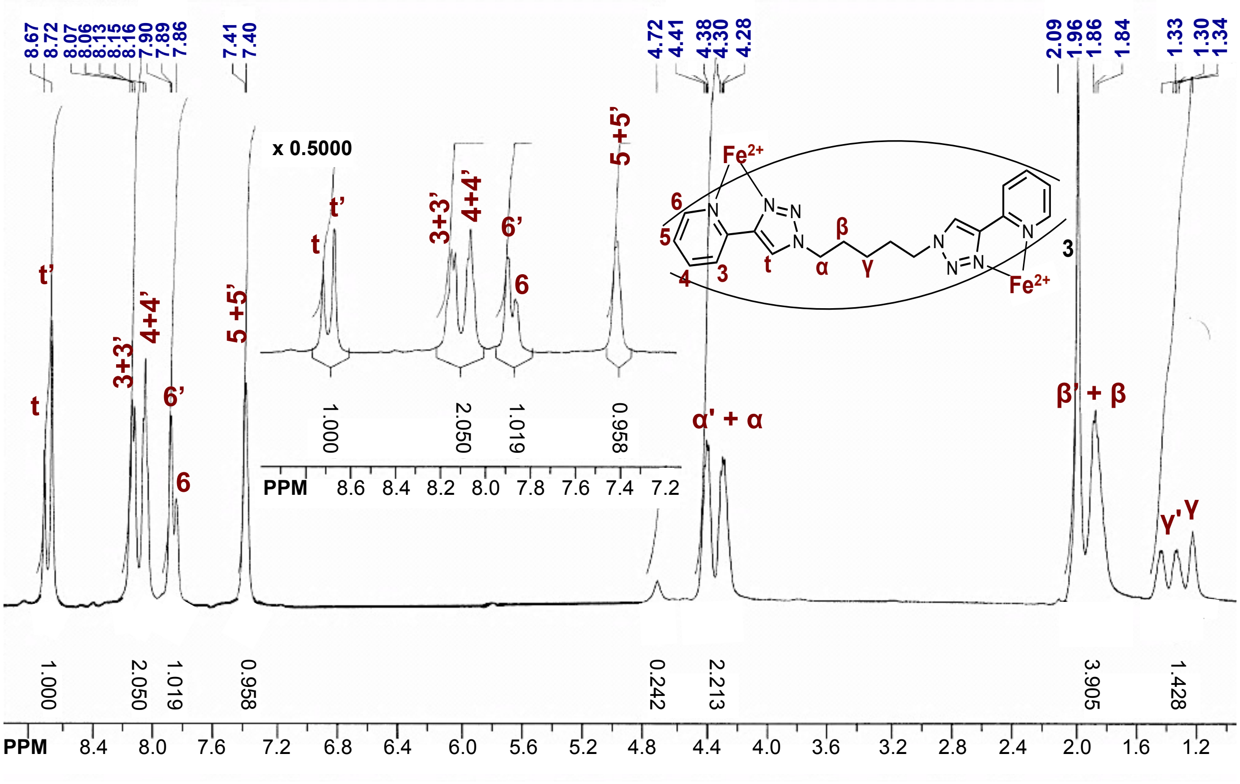

Figure 3.16: ^{1}H NMR spectra of $[Fe_2(\mathbf{C5})_3](BF_4)_4$ in CD_3CN (300 MHz, 25 °C)

The COSY spectrum was ultimately used to distinguish which protons belonged to the mesocate conformation, and which belonged to the helicate (**Figure 3.17**). From the ^{1}H NMR spectrum it was ascertained that not all of the protons had separate peaks, which indicated that the chemical shifts for the two conformations were quite similar. The protons that had clear, separate peaks were those of the aliphatic spacer region, (H_α, H_β and H_γ), as well as H_t and H_6. For the triazole proton and H_6, the appearance of two distinct peaks may be attributed to their proximity to the chelating nitrogens. The H_γ protons appeared as three broad signals, with peaks of similar intensities outlined (**Figure 3.17 a**). As such these protons were used as the starting point to identifying the two different species and shown in **Figure 3.17 b**, a zoom on the aliphatic region made the assignments more clear.

Starting from H_γ the correlation to H_β and H_β' is indicated, showing that there was a slight overlap with the acetonitrile solvent peak. H_γ' however seemed to only have one correlation, presumably to H_β'. From the H_β and H_β' peaks lines were added to show the correlations to H_α and H_α', which suggested that again the two overlapped and could not be distinguished from one another. Based on these correlations and the ratios of the peaks, it appears that there was a 1:2 mixture of helicate to mesocate conformations that formed in solution. While there appeared to be a mixture of both helicate and mesocate present, the predominance of the mesocate conformation agrees with the *even-odd* rule and the odd number of methylene groups in the pentyl spacer. This result was very unique however and it was attributed to the additional flexibility of the aliphatic spacer.

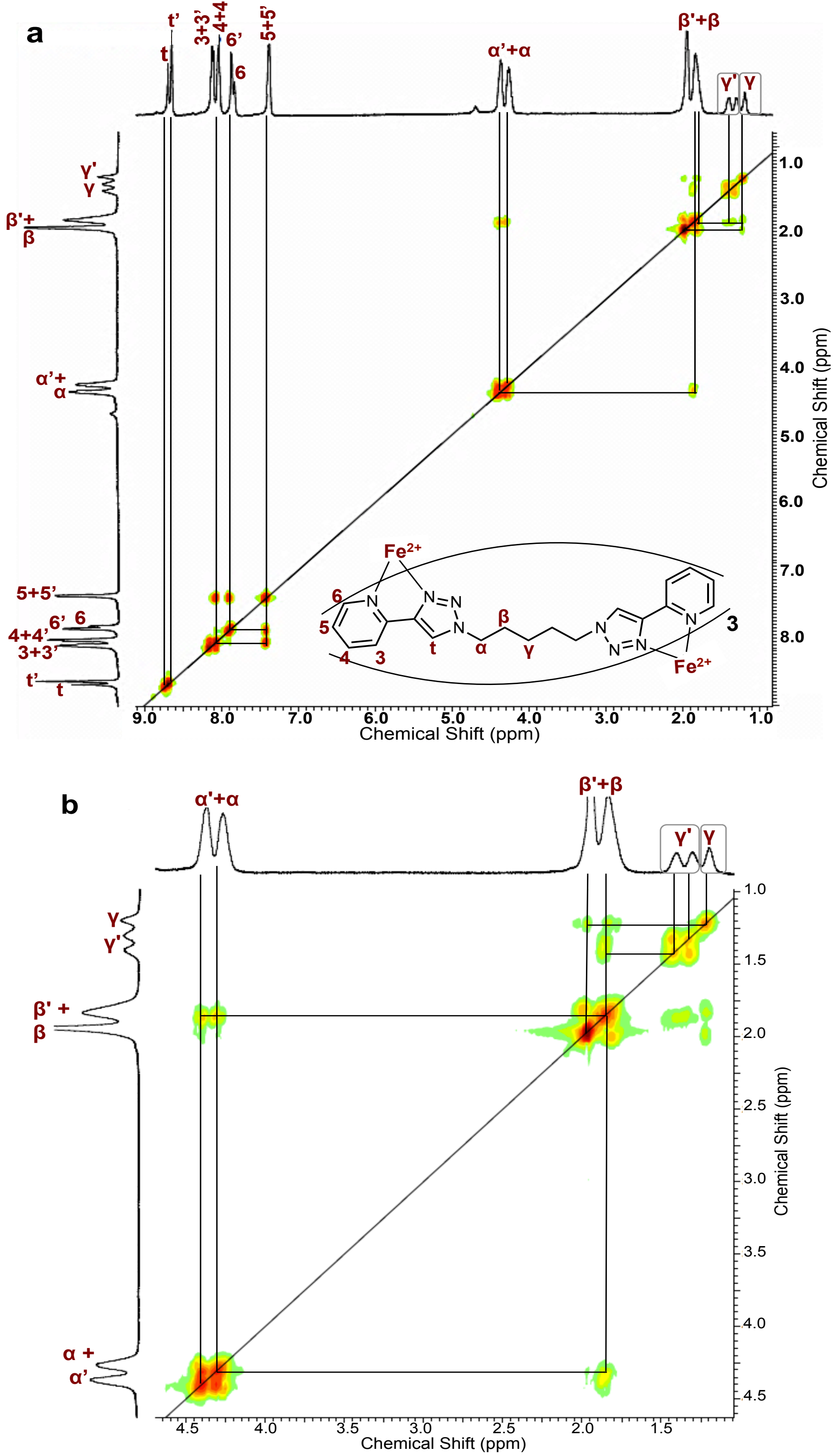

Figure 3.17: a) ^{1}H-^{1}H COSY spectrum of [Fe$_2$(**C5**)$_3$](BF$_4$)$_4$ in CD$_3$CN b) zoom on aliphatic region.

Based on the assignment for the $[Fe_2(\mathbf{C5})_3]^{4+}$ complex by NMR, UV-vis experiments were conducted. We were interested in tracking the complex formation through UV-vis titration experiments, as well as seeing the stoichiometry that was present in solution.

3.4.4.2 UV-vis Titration of $[Fe_2(C5)_3](BF_4)_4$

Stoichiometry of the complex in solution was determined by two different UV-vis analyses, including a titration and a Job plot. Molar absorptivity determinations were also completed in solution and discussed previously in Section 3.4.3.3 (**Figure 3.14**).

The UV-vis titration was performed by adding a small number of aliquots of Fe^{II} to **C5** in acetonitrile (**Figure 3.18**). As the concentration of Fe^{II} increased in solution, the intensity of the peaks at 330 nm and 425 nm also increased, consistent with MLCT transitions. The increase in absorbance of the peak at 425 nm was plotted as a function of the [nFe^{II}: n**C5**] ratio (**Figure 3.18**, *inset*), which gave insight into the complex stoichiometry in solution. It was seen that after about 0.67 equivalents of Fe^{II} had been added the absorbance remained constant, which suggested a 2:3 [Fe^{II}: **C5**] stoichiometry.

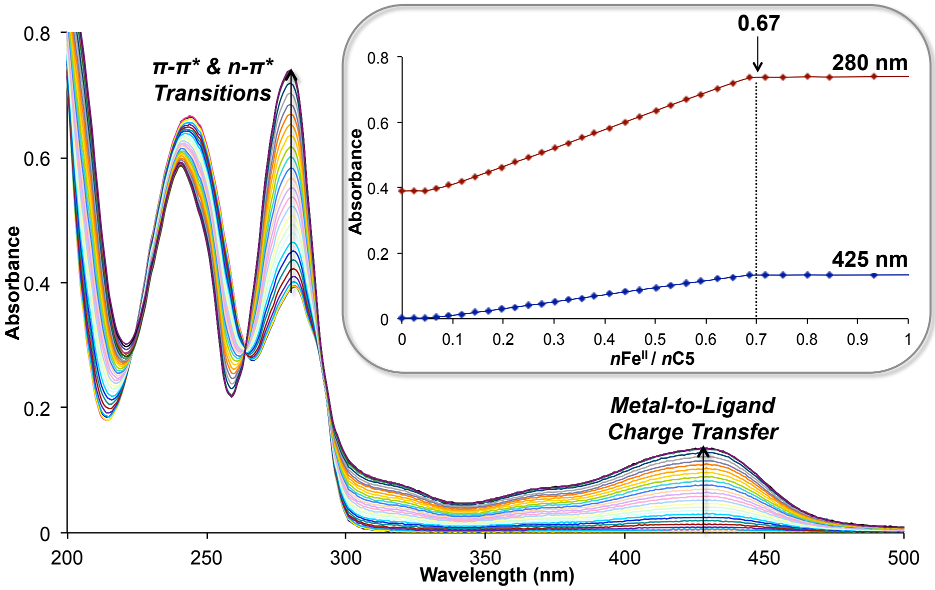

Figure 3.18: UV-vis titration spectrum for **C5** with $[Fe(H_2O)_6](BF_4)_2$ in CH_3CN. *Inset*: Absorbance *vs.* [nFe^{II} / n**C5**] ratio for peaks corresponding to MLCT transitions (425 nm).[10]

Information pertaining to the relative binding strength of the complex was acquired from the titration data as well. The shape of the curve suggested that the complex formed with strong binding because there was a very clear transition, from linear increase in absorbance to a horizontal plateau when $x\mathrm{Fe}^{\mathrm{II}} = 0.67$.

To further assess stoichiometry of the **C5** complex in solution, a Job plot was performed (**Appendix B**). As with the $[\mathrm{Fe}_2(\mathbf{C4})_3]^{4+}$ complex Job plot data was analyzed using two different methods, both of which indicated formation of the saturated triple-stranded complex in solution. The first method used the molar ratio of $\mathrm{Fe}^{\mathrm{II}}$ present in solution at a particular wavelength (410 nm) and plotted as a function of absorbance ($x\mathrm{Fe}^{\mathrm{II}}$). The second method ($n\mathrm{Fe}^{\mathrm{II}}$ / $n\mathbf{C5}$) compared the mole fraction of $\mathrm{Fe}^{\mathrm{II}}$ to the mole fraction of **C5** in solution, which also indicated a maximum value around 0.67 equivalents of $\mathrm{Fe}^{\mathrm{II}}$, consistent with the anticipated $[\mathrm{Fe}_2(\mathbf{C5})_3]^{4+}$ complex in solution.

3.4.4.3 Model of $[\mathrm{Fe}_2(\mathbf{C5})_3]^{4+}$

Despite not being able to obtain an X-ray crystal structure, the structure of the $[\mathrm{Fe}_2(\mathbf{C5})_3]^{4+}$ complex was approximated by modelling both helicate and mesocate conformations of the dinuclear complex in an identical fashion to the $[\mathrm{Fe}_2(\mathbf{C4})_3]^{4+}$ complex (**Figure 3.19**). The $\mathrm{Fe}^{\mathrm{II}}$-$\mathrm{Fe}^{\mathrm{II}}$ distances were again calculated and compared to those obtained for $[\mathrm{Fe}_2(\mathbf{C4})_3]^{4+}$. As expected the metal-metal distances were greater than for **C4**, consistent with increasing the length of the spacer region. There were minor differences between distances of the helicate and mesocate conformations however, with the mesocate distance being slightly longer than the helicate. The mesocate complex had a $\mathrm{Fe}^{\mathrm{II}}$-$\mathrm{Fe}^{\mathrm{II}}$ distance of 12.4 Å, while the helicate conformation was 12.1 Å, however differences such as these have been observed before.[5a]

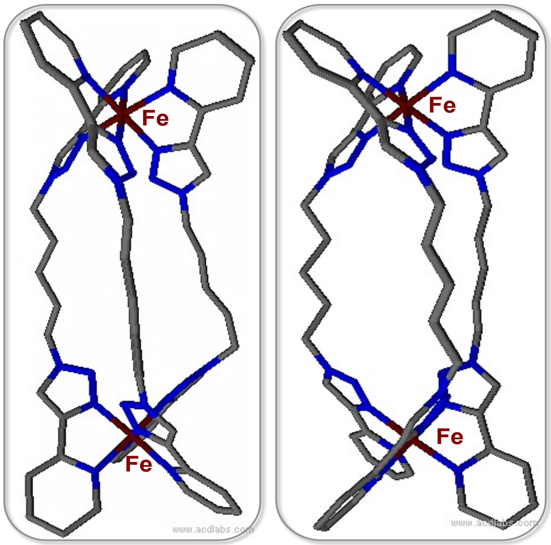

Helicate *Mesocate*

Figure 3.19: Model of $[Fe_2(\mathbf{C5})_3]^{4+}$, with both helicate and mesocate structures represented.[13]

Application of the *even-odd* rule suggested that for **C5** a mesocate structure would be favoured based on the odd number of carbons in the aliphatic spacer unit. This partiality was based on the preferred 'C'-type geometry required in the mesocate conformation. Another factor influencing the nature of the complex is based on the fact that linear aliphatic chains are most stable when a *zigzag* conformation is obeyed.[4, 5a] Based on the 'C' geometry and *zigzag* conformation it was anticipated that the mesocate conformation would be favoured, however flexibility of the pentyl spacer permitted both helicate and mesocate conformations in solution based on the NMR spectroscopy results.

3.4.5 Characterization of $[Ni_2(C4)_3](BF_4)_4$ and $[Ni_2(C5)_3](BF_4)_4$

Nickel(II) complexes with **C4** and **C5** were prepared as outlined in Section 3.3.2 and obtained as bright pink powders, which were used for further analysis. The paramagnetic nature of Ni^{II} made it possible to only examine the complexes by UV-vis experiments and elemental analysis (see Chapter 4). *Note:* Due to their extremely similar properties, **C4** and **C5** complexes with Ni^{II} will be analyzed together.

The absence of a metal-to-ligand charge transfer band with Ni^{II}, made it possible to probe potential spin crossover behaviour in the near-infrared region of the electronic spectrum (between 800-900 nm are of interest).[14] Based on the d^8 electronic configuration, which results in all of the electrons in the non-bonding, t_{2g}^6 orbitals being paired, Ni^{II} is useful for determining ligand field strength values.[14b] Another appealing feature of Ni^{II} is that the *d-d* electronic spectra are quite well understood in terms of ligand field.[14] Based on these reasons, solution state studies with Ni^{II} were undertaken, and potential spin crossover behaviours applied to the corresponding Fe^{II} complexes, which have a very strong charge-transfer band overlapping with the *d-d* transitions of interest.

3.4.5.1 UV-vis Analysis of $[Ni_2(C4)_3](BF_4)_4$ and $[Ni_2(C5)_3](BF_4)_4$

To better establish how the complexes behaved in solution, UV-vis titration experiments were performed in acetonitrile to track stoichiometry changes as well as complex formation. Job plots were also performed for both **C4** and **C5** complexes to further confirm the stoichiometry in solution. Due to the presence of the non-coordinating BF_4^- anion, it was anticipated that the saturated triple-stranded complex would form in solution, with two Ni^{II} metal ions, and three ligands (**C4** or **C5**).

The titration data corresponding to **C4** with $[Ni(H_2O)_6](BF_4)_2]$ in acetonitrile, is shown in **Figure 3.20**. There are two predominant peaks present in the titration spectrum, occurring at 240 and 285 nm, consistent with π-π* and n-π* transitions. There are also two isosbestic points, both of which are in the ultraviolet region of the spectrum, occurring at 235 and 280 nm. As with the Fe^{II} complexes, the isosbestic points indicate a clear transformation from starting materials to products in solution. The absorbing species are likely free ligand (starting material) and complex (product), both of which are dependent on the concentration of $[Ni(H_2O)_6](BF_4)_2$ present in solution. The titration obtained from $[Ni(H_2O)_6](BF_4)_2]$ to **C5** in acetonitrile was also consistent with this finding (**Appendix B**).

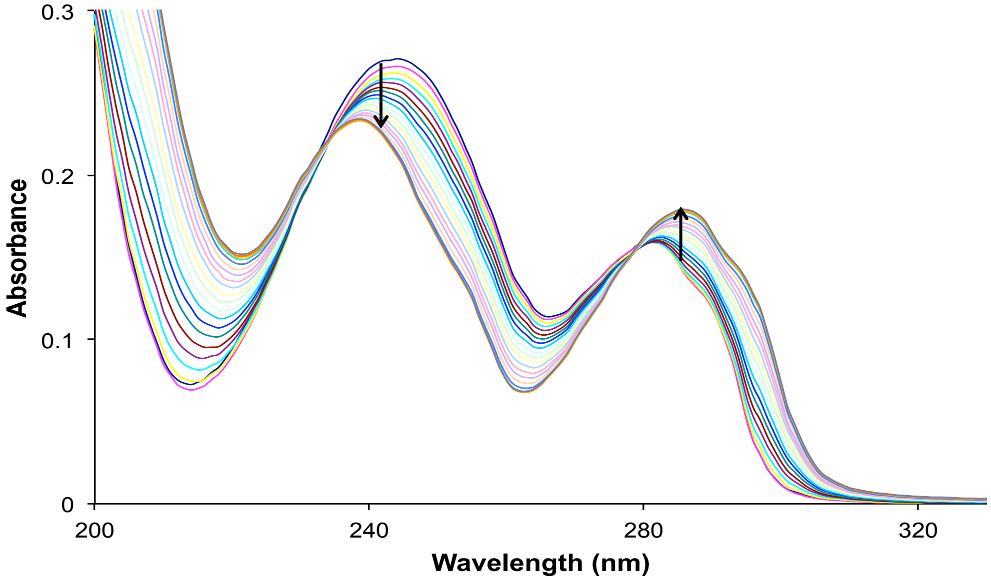

Figure 3.20: UV-vis titration data for $[Ni(H_2O)_6](BF_4)_2$ to **C4** in CH_3CN.[10]

As with the previous complexes, stoichiometry was determined from the titration data by plotting absorbance as a function of the [*n*Ni^{II} to *n***(ligand)**] ratio at various wavelengths (**Figure 3.21**). The changes in absorbance were plotted corresponding to the maximum occurring at 295 nm. The titration spectra for the two complexes showed similar properties, in terms of both isosbestic points and absorbance maxima. For $[Ni_2(\mathbf{C4})_3]^{4+}$ and $[Ni_2(\mathbf{C5})_3]^{4+}$ complexes in the presence of a non-coordinating anion (BF_4^-) the saturated triple-stranded complex was favoured in solution as anticipated.

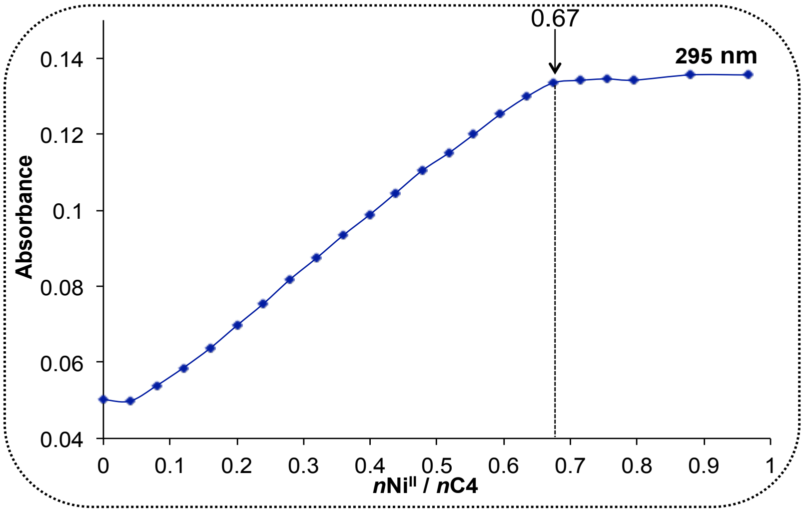

Figure 3.21: Absorbance as a function of [*n*Ni^{II} to *n***C4**] ratio at 295 (line has been added to guide the eye; no data fitting).[10]

Stoichiometry for the **C4** and **C5** complexes was further confirmed by performing Job plots, where the mole fraction of Ni^{II} was varied between zero and one. The Job plot obtained from the $[Ni_2(\mathbf{C4})_3]^{4+}$ complex is shown below (**Figure 3.22**), however the $[Ni_2(\mathbf{C5})_3]^{4+}$ Job plot also confirmed the same stoichiometry (**Appendix B**). The Job plot data was analyzed by plotting absorbance at a specific wavelength as a function of the molar ratio of Ni^{II} (xNi^{II}). Much like with the Fe^{II} complexes, both **C4** and **C5** complexes with Ni^{II} showed a maximum absorbance at xNi^{II} = 0.4. For consistency and to further ensure the stoichiometry determination was accurate a second method was used. The absorbance was plotted as a function of [*n*Ni^{II} / *n*(**ligand**)] which showed a maximum value around 0.67 equivalents of Ni^{II} for both complexes (**Appendix B**). This absorbance maximum was again consistent with the formation of a dinuclear complex with the general formula $[Ni_2(\mathbf{ligand})_3]^{4+}$.

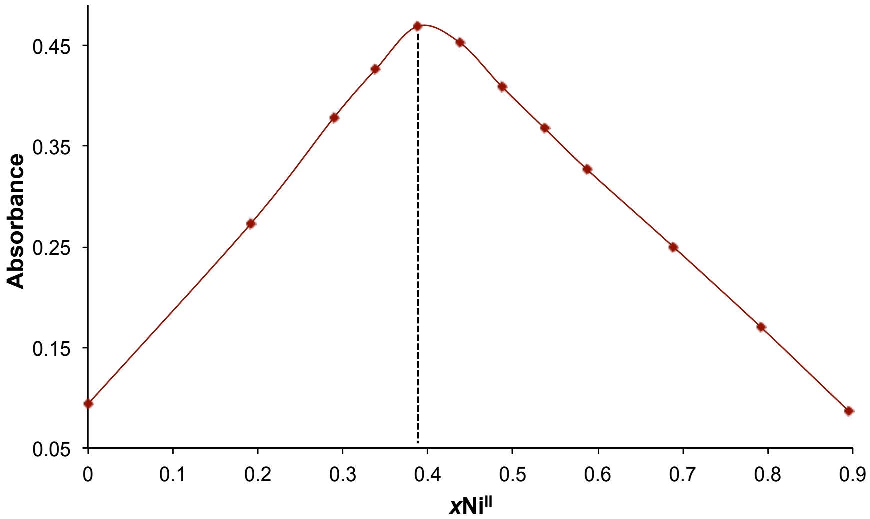

Figure 3.22: Job plot for $[Ni_2(\mathbf{C4})_3](BF_4)_4$ in CH_3CN (line is only connecting the experimental points; no data fitting).[10]

While NMR experiments showed the presence of low abundance peaks, it appeared that the additional flexibility of the aliphatic spacer units did not affect the nature of the complex that formed in solution when analyzed by UV-vis spectroscopy.

3.4.5.2 Molar Absorptivity Values for $[Ni_2(C4)_3](BF_4)_4$ and $[Ni_2(C5)_3](BF_4)_4$

Molar absorptivity values were determined for both $[Ni_2(\mathbf{C4})_3](BF_4)_4$ and $[Ni_2(\mathbf{C5})_3](BF_4)_4$ complexes in acetonitrile with varying solution concentrations. These values gave insight into how strongly the species absorbed at a given wavelength.

As previously stated, Ni^{II} complexes do not have absorbances corresponding to metal-to-ligand charge transfer bands, which makes the information from the weak *d*-*d* transitions accessible. The graph shown in **Figure 3.23** has two peaks in the ultraviolet region, occurring at 240 and 285 nm, which correspond to π-π* and n- π* transitions. There are three peaks occurring in the near infrared region, with one occurring at 520 nm, and two superimposed peaks centered at 850 nm. These peaks were of interest and they corresponded to the forbidden *d*-*d* transitions, based on their very small epsilon (ε) values (**Figure 3.23** *inset*).

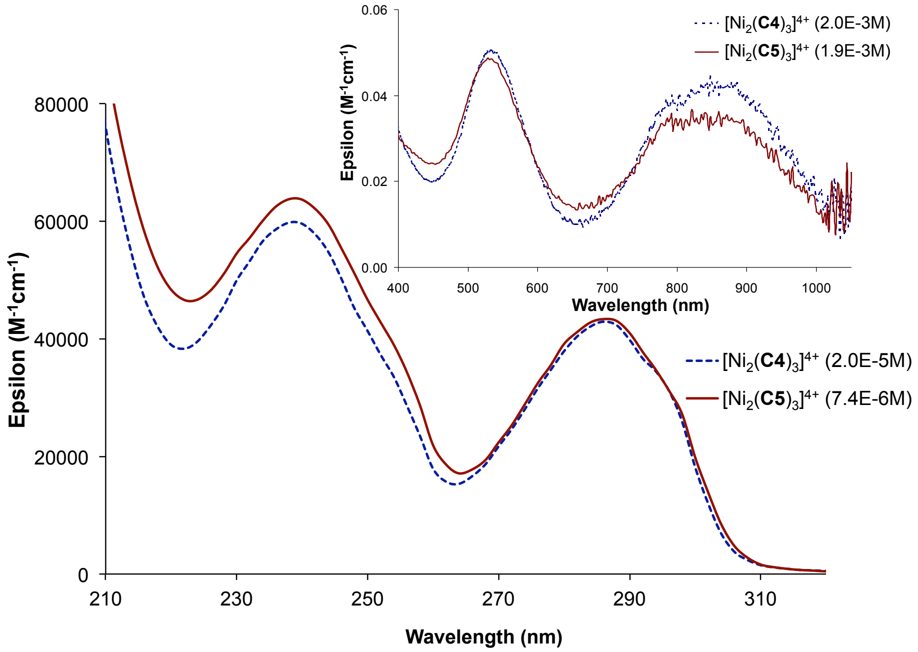

Figure 3.23: Molar absorptivity values in CH_3CN for $[Ni_2(\mathbf{C4})_3](BF_4)_4$ and $[Ni_2(\mathbf{C5})_3](BF_4)_4$.

As described in Chapter 2, in order for spin crossover to be accessible in the corresponding Fe^{II} species, the ligand field strength value (10Dq) for the $[Ni_2(\mathbf{C4})_3]^{4+}$/$[Ni_2(\mathbf{C5})_3]^{4+}$ complexes must fall between 11,000-12,500 cm^{-1}.[15] From the UV-vis data in **Figure 3.23**, the ligand field strength value was determined based on the absorbance maximum that gave the lowest energy. Based on this criterion the longest wavelength would give the lowest energy, which corresponded to 890 nm. The wavenumber (cm^{-1}) was then calculated, which indicated the ligand field strength value was 11,235 cm^{-1}. Based on this, spin crossover was determined to be accessible for the corresponding Fe^{II} complex because the ligand field value was well within the acceptable range.

3.5 Conclusions

In summary, we have successfully studied how an increase in aliphatic spacer length affects complex formation with octahedral metal ions, Fe^{II} and Ni^{II}, which was described in detail within this chapter. **C4** and **C5** ligands as well as their complexes were synthesized and characterized, which were identified by butyl and pentyl spacer regions respectively. NMR spectroscopy analysis for the $[Fe_2(\mathbf{C4})_3]^4$ and $[Fe_2(\mathbf{C5})_3]^{4+}$ complexes indicated that additional flexibility may affect the self-assembly process, resulting in a mixture of species in solution. The results obtained from UV-vis spectroscopy were much more predictable, since the Fe^{II} and Ni^{II} complexes for both **C4** and **C5** favoured the saturated triple-stranded stoichiometry in the presence of a non-coordinating anion. The systematic study of **C4** and **C5** and their corresponding complexes have indicated that perhaps the predictability of the *even-odd* rule is only applicable for short aliphatic spacers.

3.6 References

1. (a) Crowley, J. D.; Bandeen, P. H., A Multicomponent CuAAC "click" Approach to a Library of Hybrid Polydentate 2-pyridyl-1,2,3-triazole Ligands: New Building Blocks for the Generation of Metallosupramolecular Architectures. *Dalton Trans.* **2010**, *39*, 612-623; (b) Melan, C. F. C.; Wu, N.; Stevenson, K. A.; Fleischel, O.; Wang, R.; Habib, F.; Mosey, N. J.; Murugesu, M.; Petitjean, A., Click-Triazole: 2-(1,2,3-triazol-4-yl)-pyridine Unit Coordination to Octahedral Cations; Applications to the Self-Assembly of Helicates and Mesocates. Manuscript in preparation, Queen's University: Kingston, 2013; (c) Melan, C. F. C. *"Click-Helicates": Synthesis and Characterization of Bi-functional Ligands Based on Triazole-Pyridine Units and the Helicate-Like Structures They Form with Octahedral Metals*; 4th Year, Research Project: Queen's University 2011; pp 1-22.
2. (a) McMorran, D. A., Ag(I)-Based Tectons for the Construction of Helical and *meso*-Helical Hydrogen-Bonded Coordination Networks. *Inorg. Chem.* **2008**, *47*, 592-601; (b) Schweinfurth, D.; Hardcastle, K. I.; Bunz, U. H. F., 1,3-Dipolar Cycloaddition of Alkynes to Azides. Construction of Operationally Functional Metal Responsive Fluorophores. *Chem. Commun.* **2008**, 2203-2205; (c) Meudtner, R. M.; Ostermeier, M.; Goddard, R.; Limberg, C.; Hecht, S., Multifunctional "Clickates" as Versatile Extended Heteroaromatic Building Blocks: Efficient Synthesis via Click Chemistry, Conformational Preferences, and Metal Coordination. *Chem. Eur. J.* **2007**, *13*, 9834-9840.
3. Stevenson, K. A.; Melan, C. F. C.; Fleischel, O.; Wang, R.; Petitjean, A., Solid-State Self-Assembly of Triazolylpyridine-Based Helicates and Mesocate: Control of the Metal–Metal Distances. *Cryst. Growth Des.* **2012**, *12*, 5169-5173.
4. Albrecht, M., How Do They Know? Influencing the Relative Stereochemistry of the Complex Units of Dinuclear Triple-Stranded Helicate-Type Complexes. *Chem. Eur. J.* **2000**, *6*, 3485-3489.
5. (a) Xu, J.; Parac, T. N.; Raymond, K. N., *meso* Myths: What Drives Assembly of Helical *vs*. *meso*-[M_2L_3] Clusters? *Angew. Chem. Int. Ed.* **1999**, *38*, 2878-2882; (b) Stevens, J. R.; Plieger, P. G., Anion-Driven Conformation Control and Enhanced Sulfate Binding Utilising Aryl Linked Salicylaldoxime Dicopper Helicates. *Dalton Trans.* **2011**, *40*, 12235-12241; (c) Maeda, T.; Furusho, Y.; Shiro, M.; Takata, T., Self-Assembly of Multinuclear Complexes with Enantiomerically Pure Chiral Binaphthoxy Imine Ligands: Effect of the Alkyl Spacer Connecting Two Binaphthyl Units on the Metal Binding. *Chirality* **2006**, *18*, 691-697.
6. Steel, P. J., Ligand Design in Multimetallic Architectures: Six Lessons Learned. *Acc. Chem. Res.* **2005**, *38*, 243-250.

7. Fleischel, O.; Wu, N.; Petitjean, A., Click-Triazole: Coordination of 2-(1,2,3-triazol-4-yl)-pyridine to Cations of Traditional Tetrahedral Geometry (Cu(I), Ag(I)). *Chem. Commun.* **2010**, *46*, 8454-8456.

8. (a) Vellas, S. K.; Lewis, J. E. M.; Shankar, M.; Sagatova, A.; Tyndall, J. D. A.; Monk, B. C.; Fitchett, C. M.; Hanton, L. R.; Crowley, J. D., $[Fe_2L_3]^{4+}$ Cylinders Derived from Bis(bidentate) 2-Pyridyl-1,2,3- triazole "Click" Ligands: Synthesis, Structures and Exploration of Biological Activity. *Molecules* **2013**, *18*, 6383-6407; (b) Ousaka, N.; Takeyama, Y.; Yashima, E., Dinuclear Metal Complexes Composed of Peptide Chains: Solvent-Induced Switching and Inversion of the Metal-Centered Chirality. *Chem. Sci.* **2012**, *3*, 466-469.

9. (a) Cohen, M. D.; Fischer, E., Isobestic Points. *J. Chem. Soc.* **1962**, *588*, 3044-3052; (b) Daly, L. H.; Colthup, N. B.; Wiberley, S. E., *Introduction to Infrared And Raman Spectroscopy* Academic Press 1990.

10. The UV-vis titration and Job plot data were collected by Dr. Petitjean, A., Kingston, Spring 2013.

11. (a) Velez, S.; Nair, N. G.; Reddy, P., Transition Metal Ion Binding of Carnosine and Histidine: Biologically Relevant Antioxidants. *Colloids Surf., B.* **2008**, *66*, 291-294; (b) Huang, C. Y., Determination of Binding Stoichiometry by the Continuous Variation Method: The Job Plot. *Methods in Enzymology* 1982; pp 509-525.

12. Piguet, C.; Bernardinelli, G.; Hopfgartner, G., Helicates as Versatile Supramolecular Complexes. *Chem. Rev.* **1997**, *97*, 2005-2062.

13. *ACD/3D Viewer,* Academic Version (Queen's University), Advanced Chemistry Development, Inc., http://www.acdlabs.com: Toronto, ON, 2013.

14. (a) Wilson, L. J.; Georges, D.; Hoselton, M. A., Electronic Spectral Study of Some Iron(II) Magnetic Isomers in Solution and a Spectrial-Structural Correlation with Their Nickel(II) Analogs. *Inorg. Chem.* **1975**, *14* (12), 2968-2975; (b) Gütlich, P., Spin Crossover in Iron(II)- Complexes. *Struct. Bond* **1981**, *44*, 83-195.

15. Hauser, A., Ligand Field Theoretical Considerations. *Adv. Polym. Sci.* **2004**, *233*, 49-58.

Chapter 4

Experimental Section

4.1 General Methods

Commercially available compounds were purchased from Alfa Aesar, Aldrich, Strem Chemicals, and VWR. All were used as received with the exception of 2,7-dihydroxynaphthalene, which was re-crystallized in toluene prior to use. Anhydrous dichloromethane and tetrahydrofuran were dried by passing through an activated alumina column according to the manufacturer's instructions (Innovative Technology). Molecular sieves were used to further dry the solvents. Anhydrous DMF was purchased from EMD (DriSolv) and was used as received. All reactions were performed under Argon (Ar) unless otherwise stated. Deuterated solvents (Cambridge Isotopes) were used as received, except for $CDCl_3$ which was sometimes neutralized by passing through a short column of basic alumina (such treated $CDCl_3$ will be signalled below by an asterisk, *i.e.* '$CDCl_3$*'). ^{1}H NMR and ^{13}C NMR analyses were performed using 300 MHz, 400 MHz and 500 MHz Bruker instruments. Peak listings for all NMR spectra are given in ppm and referenced against the residual solvent signal. UV-vis spectra were recorded on both Cary-50 and Cary-300 spectrometers (200-1100 nm). Thin layer chromatography (TLC) analysis was performed on *Merck silica gel* with a pore diameter of 60 Ångstroms. Column chromatography was performed with *Silica-P flash silica gel* with a particle size of 40-63 μm and a pore diameter of 60 Ångstroms. Melting points were recorded on a MEL-TEMP (Laboratory Device, USA) apparatus. X-ray crystallographic data was collected on a Bruker SMART APEX II X-ray diffractometer and processed on a PC using the Bruker AXS Crystal Structure Analysis Package. Mass spectrometry was performed on a Waters/Micromass GC-TOF EI-MS spectrometer or ESI-MS spectrometer. Elemental analyses were conducted at the Elemental Analysis service at the Université de Montréal.

4.2 Experimental Details

4.2.1 2,6-Bis(hydroxymethyl)naphthalene (2.1) [1]

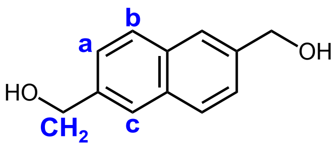

The synthetic method was adapted from literature protocols.[1a,b] Naphthalene-2,6-dicarboxylic acid dimethyl ester (200 mg, 8.20 mmol, 1 equiv.) was dissolved in tetrahydrofuran (45 mL) under argon. To the reaction mixture was added 1 *M* lithium aluminum hydride solution in tetrahydrofuran (21 mL, 21 mmol, 2.5 equiv.) drop-wise. The suspension was refluxed for 3 h at 75 °C with stirring. After cooling to room temperature, aqueous hydrochloric acid (84 mL, 5 N) was added drop-wise with stirring. The resulting homogenous solution was concentrated, and the residue was dissolved in dichloromethane (60 mL) and water (40 mL). The final product precipitated in the aqueous layer, filtered and left to dry in the air. Traces of the product were also found in the organic layer of the extraction. White, powder of the desired product was afforded (1.527 g, 99 %). The physical and spectral data were consistent with those previously reported in literature and the compound was used for the next step without further purification.[1a] δ ^{1}**H** (300 MHz, $CDCl_3$, 25 °C): 7.80 -7.76 (m, 4 H, H_b and H_c), 7.44 (d, ^3J = 7.5 Hz, 2 H, H_a), 4.78 (s, 4 H, CH_2). Mp: 171-174 °C (lit. 170-170.5 °C).[1c]

4.2.2 2,6-Bis(bromomethyl)naphthalene (2.2) [1a, b, 2]

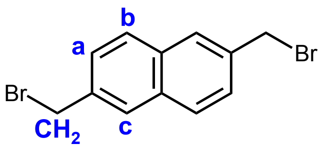

The synthetic method was slightly modified from literature protocols.[1a] 2,6-Bis(hydroxymethyl)naphthalene (153 mg, 8.12 mmol) was dissolved in anhydrous dichloromethane (110 mL) under argon with stirring. Phosphorus tribromide (2.22 mL, 23.4 mmol, 2.88 equiv.) was added drop-wise and the reaction was refluxed at 45 °C with stirring for 2 h. TLC was performed and starting material was still present. Phosphorus tribromide (1.00 mL, 10.5 mmol, 1.30 equiv.) was added and the reaction was left to stir at room temperature overnight. The solution was extracted using water (30 mL) and chloroform (20 mL) and the organic layer was dried over anhydrous sodium sulfate, filtered and concentrated. The crude product was purified by flash column chromatography using dichloromethane as the eluent. This afforded the desired product as a cream powder (2.105 g, 83 %). *δ* ^{1}**H** (300 MHz, $CDCl_3$): 7.83 (br. d, 2 H, H_b), 7.81 (br. d, 2 H, H_c), 7.54 (d, ^{3}J= 8.2 Hz, 2 H, H_a), 4.67 (s, 4 H, CH_2). TLC (SiO_2, CH_2Cl_2); Rf = 0.60. Mp: 180-183 °C (lit.182-184 °C).[2]

4.2.3 [2-{1-[(6-{[4-(Pyridin-2-yl)-1,2,3-triazol-1-yl]methyl}naphthalen-2-yl)methyl]-1,2,3-triazol-4-yl}pyridine]] (N1)[3]

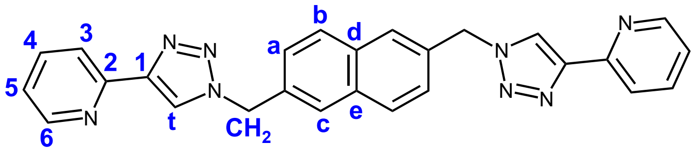

2,6-Bis(bromomethyl)naphthalene (300 mg, 0.95 mmol) was added to dimethylformamide (12 mL) and sodium azide (180 mg, 2.77 mmol, 2.9 equiv.). The solution was stirred under argon at room temperature for 5 h. To the reaction mixture was added, water (3 mL), copper (II) sulfate pentahydrate (95 mg, 0.38 mmol, 0.40 equiv.), sodium ascorbate (170 mg, 0.85 mmol, 0.9 equiv.) and 2-ethynylpyridine (207 µL, 2.04 mmol, 2.15 equiv.). The resulting yellow solution was degassed and left to stir at room temperature under argon for 20 h. The solution was a yellow/orange colour after 20 h; concentrated aqueous ammonia (6 mL), saturated ethylenediaminetetraacetic acid (6 mL) and water (30 mL) were added to the solution and the reaction was left to stir vigorously in the air overnight. The light green suspension was filtered and the white precipitate was washed with water and dried in the air overnight yielding the crude product (0.404 g, 96%). The crude product was recrystallized from 95% ethanol and left to cool overnight. The precipitate was collected through vacuum filtration, and the filtrate placed in the fridge overnight. Another fraction of precipitate was collected. The desired product was afforded, and the powder was cream coloured and fluffy (0.314 g, 74%). The product was further purified by column chromatography using 1:1 dichloromethane: acetone as the eluent. This afforded the desired product as white powder (0.200 g, 47 %). *δ* ^{1}**H** (500 MHz, $CDCl_3$*, 25 °C): 8.52 (d, ^{3}J = 4.1 Hz, 2 H, H_6), 8.19 (d, ^{3}J = 7.8 Hz, 2 H, H_3), 8.09 (s, 2 H, H_t), 7.85 (d, ^{3}J = 8.4 Hz, 2 H, H_b), 7.80 (s, 2 H, H_c), 7.78 (t, $^3J = 7.8$ Hz, 2 H, H_4), 7.46 (d, $^3J = 8.7$ Hz, 2 H, H_a), 7.21 (m, $^3J = 6.8$ Hz, 2 H, H_5), 5.76 (s, 4 H, CH_2). δ ^{13}**C** (125 MHz, $CDCl_3$*, 25 °C): 150.5 (C_6), 149.7 (C_2), 149.2 (C_1), 137.2 (C4), 133.47 (C_d), 133.12 (C_e), 129.62 (C_b), 127.8 (C_c), 126.7 (C_a), 123.3 (C_5), 122.39 (C_t), 120.64 (C_3), 54.7 (CH_2). TLC (SiO_2, 1:1 dichloromethane: acetone); Rf = 0.37. EA: *calc*. for $C_{26}H_{20}N_8 \cdot 0.25\ H_2O$: %C 69.55, %H 4.60, %N 24.96; *found:* %C 69.76, %H 4.50, %N 24.70. MS (EI^+): *calc*. for $C_{26}H_{20}N_8$: 444.18, *found* 444.18 [M^+], 416.17 [$(M-N_2)^+$]. Mp: 233-235 °C.

4.2.4 Metallomacrocycles Formed with Ligands Containing Aromatic Spacer Units

Non-Coordinating Anions

Iron(II) and nickel(II) complexes of **N1** were obtained by mixing 2 equiv. of metal salt, $[Fe(H_2O)_6](BF_4)_2$ and $[Ni(H_2O)_6](BF_4)_2$ (typically, 4.0 x 10^{-5} mol) with 3 equiv. of ligand (**N1**) in a mixture of chloroform and acetonitrile (~5 mL). This yielded dark orange and pink solutions respectively. Very slow vapour diffusion of diethyl ether led to the formation of bright single crystals. *Note*: gentle heating was required to solubilize the reagents. The corresponding UV-vis data can be seen in Chapter 2 and **Appendix B**.

4.2.4.1 $[Fe_2(N1)_3](BF_4)_4$ Complex

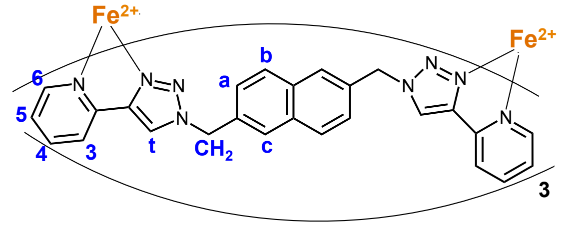

δ ^{1}**H** (300 MHz, CD_3CN, 25 ºC): 8.84 (br s, 2 H, H_t), 8.17 (br d, $^3J = 7.6$ Hz, H_3), 8.08 (br t, $^3J = 7.3$ Hz, H_4), 7.84 (br d, $^3J = 5.4$ Hz, H_6), 7.53 (br s, H_c), 7.43 (br t, $^3J = 8.3$ Hz, H_5), 7.34 (br d, $^3J = 8.2$ Hz, H_b), 6.76 (br d, $^3J = 7.4$ Hz, H_a), 5.59 (d, $^2J = 15.0$ Hz, 2 H, CH'), 5.32 (d, $^2J = 15.4$ Hz, 2 H, CH). UV-vis (CH_3CN; λ_{max} (nm) [$\log_{10}(\varepsilon)$]) 224 [5.2], 278 [4.9], 322 [3.9], 370 [sh; 3.8], 426 [4.0]; EA: *calc.* for $C_{78}H_{60}N_{24}Fe_2B_4F_{16} \cdot 3.6\ H_2O \cdot 1.2\ CHCl_3$: %C 50.2, %H 3.4, %N 17.9; *found:* %C 50.21, %H 3.39, %N 17.90. Details of the crystal structure are given in **Appendix C.**

4.2.4.2 [$Ni_2(N1)_3](BF_4)_4$ Complex

UV-vis (CH_3CN; λ_{max} (nm) [$\log_{10}(\varepsilon)$]) 226 nm [5.3], 284 [4.8], 514 [1.8], 790 [1.4], 850 [1.4]; EA: *calc.* for $C_{78}H_{60}N_{24}Ni_2B_4F_{16}$ • 1.2 $CHCl_3$ • 5.85 H_2O: %C 46.48, %H 3.59, %N 16.42; *found*: %C 46.51, %H 3.63, %N 16.45.

Coordinating Anions

Nickel(II) and iron(II) complexes of **N1** were obtained by mixing 2 equiv. of $[Ni(H_2O)_4(OAc)_2]$ or $[Fe(H_2O)_4Cl_2]$ with 2 equiv. of ligand (**N1**) in methanol. This yielded pink and dark orange solutions respectively. These solutions were tested by UV-vis spectroscopy. The Fe^{II} complex was also examined by NMR spectroscopy, instead using 1:1 $CDCl_3$*/CD_3OD as the solvents. The UV-vis, and titration data, can be seen in **Appendix B**.

4.2.4.3 3 [N1] + 2 [$Fe(H_2O)_4Cl_2$]

δ ^{1}**H** (300 MHz, 1:1 $CDCl_3$*:CD_3OD, 25 ° C): 9.54 (br. s, 2 H, H_t), 8.54 (br. s, 2 H, H_3), 8.32 (br. m, 2 H, H_4), 8.00 (br. m, 2 H, H_6), 7.77 (s, 2 H, H_c), 7.69 (m, 2 H, H_5), 7.56 (m, 2 H, H_b), 7.08 (br. s, 2 H, H_a), 5.92 (d, ^3J = 11.8 Hz, 2 H, CH'), 5.60 (d, ^3J = 11.8 Hz, 2 H, CH).

4.2.5 [2-(1-{4-[4-(Pyridin-2-yl)-1,2,3-triazol-1-yl]butyl}-1,2,3-triazol-4-yl)pyridine]] (C4)

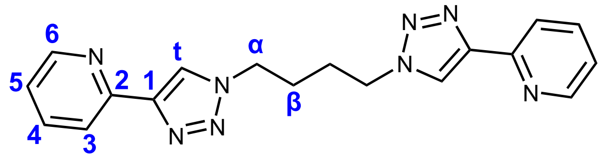

To a stirred solution of 1,4-dibromobutane (180 μL, 1.51 mmol) in dimethylformamide (2.5 mL) was added sodium azide (226 mg, 3.47 mmol, 2.3 equiv.). The white suspension was stirred under argon at 80 °C for 24 h. To the reaction was added: dimethylformamide (0.6 mL), water (0.6 mL), copper (II) sulfate pentahydrate (153 mg, 0.6 mmol, 0.4 equiv.), sodium ascorbate (145 mg, 3.25 mmol, 0.9 equiv.) and 2-ethynylpyridine (330 μL, 3.25 mmol, 2.15 equiv.). The resulting mixture was stirred at room temperature under argon for 20 h. To the mixture was added, concentrated aqueous ammonia (5 mL), saturated aqueous ethylenediaminetetraacetic acid (5 mL) and water (15 mL). The reaction was left to stir vigorously in air until the solution became green and the precipitate white. The solid was filtered, washed with water, air-dried and purified by recrystallization from hot 95% ethanol to give **C4** as a white powder with an overall yield of 92% (0.482 g). A portion of the product was further purified by flash column chromatography using 1:1 dichloromethane: acetone as the eluent. This afforded white powder of the desired final product (0.112 g). δ ^{1}**H** (400 MHz, CDCl$_3$*, 25 °C): 8.58 (br d, ^3J = 5.0 Hz, 2 H, H$_6$), 8.18 (d, ^3J = 7.9 Hz, 2 H, H$_3$), 8.13 (s, 2 H, H$_t$), 7.79 (td, ^3J = 7.5 Hz, ^4J = 1.7 Hz, 2 H, H$_4$), 7.24 (m, 2 H, H$_5$), 4.49 (t, ^3J = 5.6 Hz, 2 H, H$_\alpha$), 2.04 (dt, ^3J = 5.7 Hz, ^4J = 2.9 Hz, 4 H, H$_\beta$). δ ^{13}**C** NMR (125 MHz, CDCl$_3$*, 25 °C): 152.9 (C2), 152.3 (C$_6$), 151.1 (C1), 140.9 (C4), 126.6 (C$_5$), 125.8 (C$_t$), 123.9 (C$_3$), 49.8 (C$_\alpha$), 27.1 (C$_\beta$). TLC (SiO$_2$, 1:2 dichloromethane/acetone); Rf = 0.23. EA: *calc.* for $C_{18}H_{18}N_8$ • 0.15 H_2O: %C 61.93, %H 5.28, %N 32.10; *found*: %C 61.84, %H 5.15, %N 32.28. MS (EI+): *calc.* for $C_{18}H_{18}N_8$: 346.17; *found:* 346.16 [M$^+$], 318.16 [(M-N$_2$)$^+$]. Mp: 223-224 °C.

4.2.6 [2-(1-{5-[4-(Pyridin-2-yl)-1,2,3-triazol-1-yl]pentyl}-1,2,3-triazol-4-yl)pyridine]] (C5)

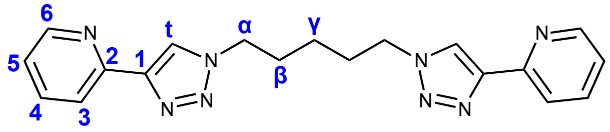

To a stirred solution of 1,5-dibromopentane (180 µL, 1.32 mmol) in dimethylformamide (2.2 mL) was added sodium azide (198 mg, 3.04 mmol, 2.3 equiv.). The mixture was stirred at 80 °C for 24 h. Then were added dimethylformamide (0.5 mL), water (0.5 mL), copper (II) sulfate pentahydrate (132 mg, 0.53 mmol, 0.9 equiv.), sodium ascorbate (236 mg, 1.19 mmol, 0.9 equiv.) and 2-ethynylpyridine (290 µL, 2.84 mmol, 2.15 equiv.). The resulting mixture was stirred at room temperature under argon for 20 h. To the mixture were added a solution of saturated aqueous ethylenediaminetetraacetic acid (4.5 mL), concentrated aqueous ammonia (4.5 mL) and water (15 mL). The resulting suspension was stirred vigorously in air until the solution became dark green and the precipitate white. The solid was filtered, washed with water, air-dried and purified by recrystallization from hot 95% ethanol to give pure **C5** as a white powder with an overall yield of 77% (0.368 g). The product was further purified by flash column chromatography using 0.5:1 dichloromethane: acetone as the eluent. This afforded white powder in 74% yield. δ ^{1}**H** (400 MHz, $CDCl_3$*, 25 °C): 8.58 (d, ^3J = 4.4 Hz, 2 H, H_6), 8.17 (d, ^3J = 7.8 Hz, 2 H, H_3), 8.12 (s, 2 H, H_t), 7.78 (td, ^3J = 7.7 Hz, ^4J = 1.39 Hz, 2 H, H_4), 7.23 (m, 2 H, H_5), 4.43 (t, ^3J = 7.1 Hz, 4 H, H_α), 2.03 (quin., ^3J = 7.4 Hz, 4 H, H_β), 1.45 (m, 2H, H_γ). δ ^{13}**C** NMR (125 MHz, $CDCl_3$*, 25 °C): 150.3 (C_2), 149.3 (C_6), 146.6 (C_1), 136.9 (C4), 122.7 (C_5), 121.6 (C_t), 120.3 (C_3), 50.1 (C_α), 29.6 (C_β), 23.5 (C_γ). TLC (SiO_2, 1:2 dichloromethane/acetone); Rf = 0.32. EA: *calc*. for $C_{19}H_{20}N_8$: %C 63.32, %H 5.59, %N 31.09, *found*: %C 63.34, %H 5.54, %N 31.22. MS (EI+): *calc.* for $C_{19}H_{20}N_8$: 360.18; *found*: 360.18 [M^+], 332.18 [$(M\text{-}N_2)^+$]. Mp: 184-185 °C.

4.2.7 Metallomacrocycles Formed with Ligands Containing Aliphatic Spacer Units

Non-Coordinating Anions

Nickel(II) and iron(II) complexes of **C4** and **C5** were obtained by mixing 2 equiv. of metal salt, $[Ni(H_2O)_6](BF_4)_2$ and $[Fe(H_2O)_6](BF_4)_2$ (typically, 4.0 x 10^{-5} mol) with 3 equiv. of ligand (**C4**/**C5**) in acetonitrile (~5 mL). *Note*: gentle heating was required to solubilize the reagents. This yielded a pink or dark orange solution respectively. Ethyl acetate was then added to the solution to precipitate out the complex (~ 8 mL). The solvent was then removed and 10 mL of ethyl acetate was subsequently added and the solution heated at 30 °C for 2 h to remove any excess ligand that may remain in solution. The resulting complexes were obtained by vacuum filtration and were pink and orange in color respectively. The corresponding UV-vis data can be seen in **Appendix B**.

4.2.7.1 [Fe$_2$(C4)$_3$](BF$_4$)$_4$ Complex

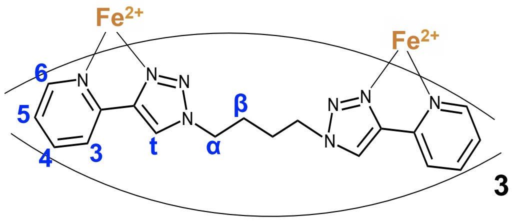

δ ^{1}**H** (300 MHz, CD$_3$CN, 25° C): 8.73 (s, 2 H, H$_t$), 8.13 (m, 2 H, H$_3$), 8.07 (m, 2 H, H$_4$), 7.91 (m, 2 H, H$_6$), 7.42 (br. m, 2 H, H$_5$), 4.37 (br. s, 4 H, H$_\alpha$), 1.72 (br. s, 4 H, H$_\beta$); UV-vis (CH$_3$CN; λ_{max} (nm) [log$_{10}$(ε)]) 240 [4.6], 280 [4.7], 319 [sh; 3.7], 426 [3.9]; EA: *calc.* for $C_{54}H_{54}N_{24}Fe_2B_4F_{16}$ • 5.45 H$_2$O • 0.05 EtOAc: %C 40.67, %H 4.11, %N 21.0; *found:* %C 40.49, %H 3.91, %N 20.80.

4.2.7.2 [Ni$_2$(C4)$_3$](BF$_4$)$_4$ Complex

UV-vis (CH$_3$CN; λ_{max} (nm) [log$_{10}$(ε)]) 238 [4.8], 286 [4.6], 534 [1.4], 858 [1.3]; EA: *calc.* for $C_{54}H_{54}N_{24}Ni_2B_4F_{16}$ • 8.8 H$_2$O • 1.45 EtOAc: %C 40.12, %H 4.68, %N 18.78; *found:* %C 40.04, %H 4.50, %N 18.60.

4.2.7.3 [Fe$_2$(C5)$_3$](BF$_4$)$_4$ Complex

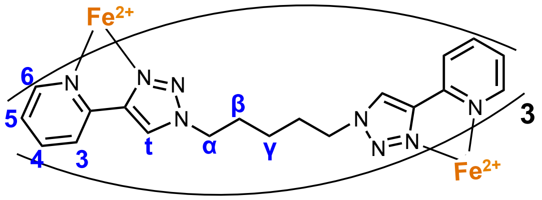

δ ^{1}**H** (500 MHz, CD$_3$CN, 25° C): 8.70 (s, 3 H, H$_t$), 8.65 (s, 3 H, H$_{t'}$), 8.12 (br s, 6 H, H$_{3'}$ and H$_3$), 8.04 (m, 6 H, H$_{4'}$ and H$_4$), 7.87 (d, ^3J = 3.9 Hz, 3 H, H$_{6'}$), 7.84 (d, ^3J = 3.9 Hz, 1 H, H$_6$), 7.38 (d, ^3J = 5.2 Hz, 6 H, H$_{5'}$ and H$_5$), 4.37-4.27 (br. m, 12 H, H$_{\alpha'}$ and H$_\alpha$), 1.83 (br. s, 12 H, H$_\beta$ and H$_{\beta'}$), 1.35 (d, ^3J = 6.7 Hz, 3 H, H$_{\gamma'}$), 1.19 (br. s, 3 H, H$_\gamma$). UV-vis (CH$_3$CN; λ_{max} (nm) [log$_{10}$(ε)]) 240 [4.7], 280 [4.8], 319 [sh; 2.8], 370 [sh; 3.8], 428 [4.1]; EA: *calc.* for $C_{57}H_{60}N_{24}Fe_2B_4F_{16}$ • 4.6 H$_2$O • 0.15 EtOAc: %C 42.28, %H 4.34, %N 20.54; *found:* %C 42.33, %H 4.41, %N 20.62.

4.2.7.4 [$Ni_2(C5)_3](BF_4)_4$ Complex

UV-vis (CH_3CN; λ_{max} (nm) [$\log_{10}(\varepsilon)$]) 238 [4.8], 286 [4.6], 528 [1.4], 842 [1.3]; EA: *calc.* for $C_{57}H_{60}N_{24}Ni_2B_4F_{16}$ • 1.5 H_2O • 1.15 EtOAc: %C 44.19, %H 4.35, %N 20.08; *found*: %C 44.09, %H 4.22, %N 19.95.

4.2.8 [7-[(2-Chloroacetyl)oxy]naphthalen-2-yl 2-chloroacetate]] (2.3) [4]

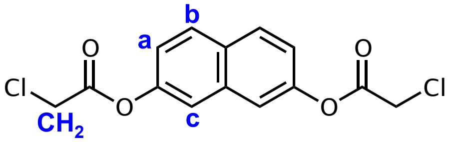

Method A: This method was altered from literature methods.[4] 2,7-Dihydroyxynaphthalene (129 mg, 0.81 mmol) and 2-chloroacetyl chloride (630 µL, 8.1 mmol, 10 equiv.) were combined. The reaction was refluxed at 100 °C for 2 h under argon with stirring. The reaction was cooled to room temperature and cooled to 0 °C overnight. The resulting powder was filtered and washed with ethanol, which gave the desired crude product (96 mg, 38 %). The crude product was further purified by column chromatography using 1:0.6 hexanes: ethyl acetate as the eluent. This afforded the desired product as white, shiny crystals (45mg, 18%). *δ* ^{1}**H** (300 MHz, $CDCl_3$, 25 °C): 7.91 (d, ^3J = 9.2 Hz, 2 H, H_b), 7.61 (d, ^4J = 2.0 Hz, 2 H, H_c), 7.30 (m, 2H, H_a), 4.37 (s, 4 H, CH_2). TLC (SiO_2, 1:0.6 hexanes/ethyl acetate); Rf = 0.12. MS (EI+): *calc.* for $C_{14}H_{10}Cl_2O_4$: 312.00; *found*: 312.00 [M^+].

Method B: This method was adapted slightly from literature protocols.[5] 2,7-Dihydroxynaphthalene (120 mg, 7.5 mmol) and triethylamine (0.50 mL, 15 mmol, 1.9 equiv.) were added to anhydrous dichloromethane (100 mL). To the reaction mixture was added 2-chloroacetyl chloride (0.50 mL, 2.5 equiv.) drop-wise. The reaction was stirred at room temperature under argon for 2 h. The reaction was washed with water, dried over sodium sulfate, filtered and evaporated to give the crude product (1.18 g). The crude product appeared by ^{1}H NMR to be a mixture of the mono and bis-substituted acyl chloride, so further purification was performed to get the desired bis-substituted product. The crude product was purified by column chromatography using 1:0.3 hexanes: ethyl acetate as the eluent. This afforded the desired product as white, shiny crystals (190 mg, 8.1 %). TLC (SiO_2, 1:0.3 Hexanes/EtOAc); Rf = 0.29.

4.3 References

1. (a) Rosa, J. C.; Galanakis, D.; Ganellin, C. R.; Dunn, P. M., Synthesis, Molecular Modeling, and K+ Channel-Blocking Activity of Dequalinium Analogues Having Semirigid Linkers. *J. Med. Chem.* **1996**, *39*, 4247-4254; (b) Benito, J. M.; Meldal, M., Bicyclic Organo-Peptides as Selective Carbohydrate Receptors: Design, Solid-phase Synthesis, and on-bead Binding Capability. *QSAR Comb. Sci.* **2004**, *23*, 117-129; (c) Vanderwerff, W. D. Process for the Preparation of Alkyl-Aromatic Aldehydes from Alkylaromatic Hydrocarbons 3385898, Dec. 21, 1966.
2. Diekmann, J.; Hertler, W. R.; Benson, R. E., Substituted Quinodimethans. VII. Substituent and Structural Effects in Cyano-Substituted Quinodimethans. *J. Org. Chem.* **1963**, *28*, 2719-2724.
3. Crowley, J. D.; Bandeen, P. H., A Multicomponent CuAAC "click" Approach to a Library of Hybrid Polydentate 2-pyridyl-1,2,3-triazole Ligands: New Building Blocks for the Generation of Metallosupramolecular Architectures. *Dalton Trans.* **2010**, *39*, 612-623.
4. (a) Gonda, Z.; Novak, Z., Highly Active Copper-Catalysts for Azide-Alkyne Cycloadditions. *Dalton Trans.* **2010**, *39*, 726-729; (b) Read, M. A.; Wood, A. A.; Harrison, J. R.; Gowan, S. M.; Kelland, L. R.; Dosanjh, H. S.; Neidle, S., Molecular Modeling Studies on G-Quadruplex Complexes of Telomerase Inhibitors: Structure-Activity Relationships. *J. Med. Chem.* **1999**, *42*, 4538-4546.
5. Resnick, B. M.; West Paterson, N. J. Fungicidal Naphthylene Diesters and Mixtures Thereof 1983.

Chapter 5

Conclusions and Perspectives

5.1 Summary and Conclusion

In this work we have prepared three new ligands, each containing two triazole-pyridine chelating units and a variable spacer region. Properties of the ligands as well as the complexes formed with octahedral metal ions have been characterized. We have shown that the length and nature of the spacer unit can be used to tune the metallomacrocycle. As the length of the aliphatic spacer increases, predictability of the self-assembly process has been shown to become slightly more complex.

Two years ago, my MSc research began with synthesis of the **N1** ligand, bearing a naphthalene spacer group. As described in Chapter 2, this ligand design was chosen based on previous studies with **X1**, containing a xylene spacer unit, which connected the two triazole-pyridine chelating units. Solution studies with **X1** had shown interesting properties, which suggested that the unsaturated double-stranded complex was favoured in the presence of coordinating anions (chloride, acetate). With this in mind, **N1** was complexed with octahedral metal ions in the presence of coordinating anions and analyzed in solution, however a similar behaviour was not observed. While the initial goal of using **N1** as a metalloreceptor was not achieved during the course of my project, the complex was still gave insight into self-assembly properties.

The second part of my project, outlined in Chapter 3, involved synthesizing two new ligands that contained varying aliphatic spacer lengths. We were particularly interested in the effect that the length of the aliphatic spacer had on complex self-assembly. Much like with **N1**, it was previous work that inspired the design of the new ligands. As an extension of the previously studied **C3** ligand, came about **C4** and **C5**, which contained butyl, and pentyl spacer regions respectively. As described in Chapter 3, **C4** and **C5** were complexed with octahedral metal ions Fe^{II} and Ni^{II} and characterized in solution. The results suggested that an increase in alkyl length, and as a result the flexibility, greatly affected the complex that was obtained. While the *even-odd* rule had previously been used with great success to assign chirality of the obtained complexes, as the alkyl chain increased (specifically pentyl) these assignments were no longer as concrete. We were able to show that the length of the aliphatic spacer can be used to predict the complex self-assembly process, however as ligand flexibility increases there may be a greater number of factors at play.

5.2 Future Directions

As discussed in Chapter 2, obtaining the unsaturated double-stranded complex with **N1** was much more difficult than anticipated. Further work may be done in solution to determine the reaction conditions that would favour the formation of this stoichiometry. Work may be done to try to force the unsaturated complex to form, such as introducing an excess of the coordinating anion in solution, in the hopes that it would preferentially bind over the ligand.

Synthesis of **N2** may also be performed, with the suggested synthetic scheme outlined below (**Scheme 5.1**). Also, following synthesis of **N2**, the ligand may be complexed with octahedral metal ions Fe^{II} and Ni^{II}, much like with **N1**. The substitution pattern of **N2** and the ester functionality connecting the naphthalene spacer unit to the triazole-pyridine chelating units, are characteristics that would be useful for potentially recognizing a substrate molecule. Based on these characteristics, attempting to obtain the unsaturated double-stranded complex, as was done with **X1**, may be extremely useful with **N2**. Much like **N1** was an extension of **X1**, further work may look into lengthening the spacer region, perhaps looking into anthracene and the complexes that it would form with metal ions.

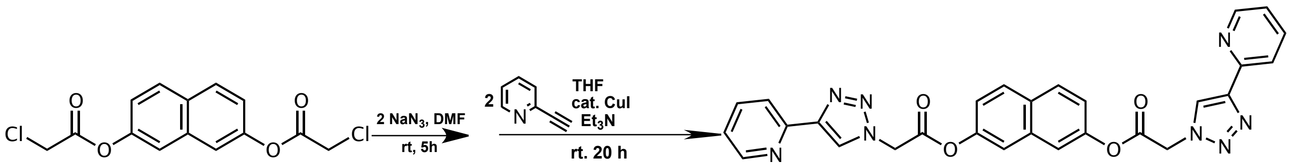

Scheme 5.1: Proposed synthetic scheme for **N2**.

For the **C4** and **C5** complexes, work towards obtaining single crystals suitable for X-ray crystallography would be extremely useful in further characterizing the complexes. Also, extending the aliphatic library, to include longer alkyl chains, may provide useful in probing the extent that aliphatic spacer length affects the self-assembly process.

NMR and MS Spectra

2,6-Bis(hydroxymethyl)naphthalene (2.1)

^{1}H NMR ($CDCl_3$, 300 MHz, 25 °C)

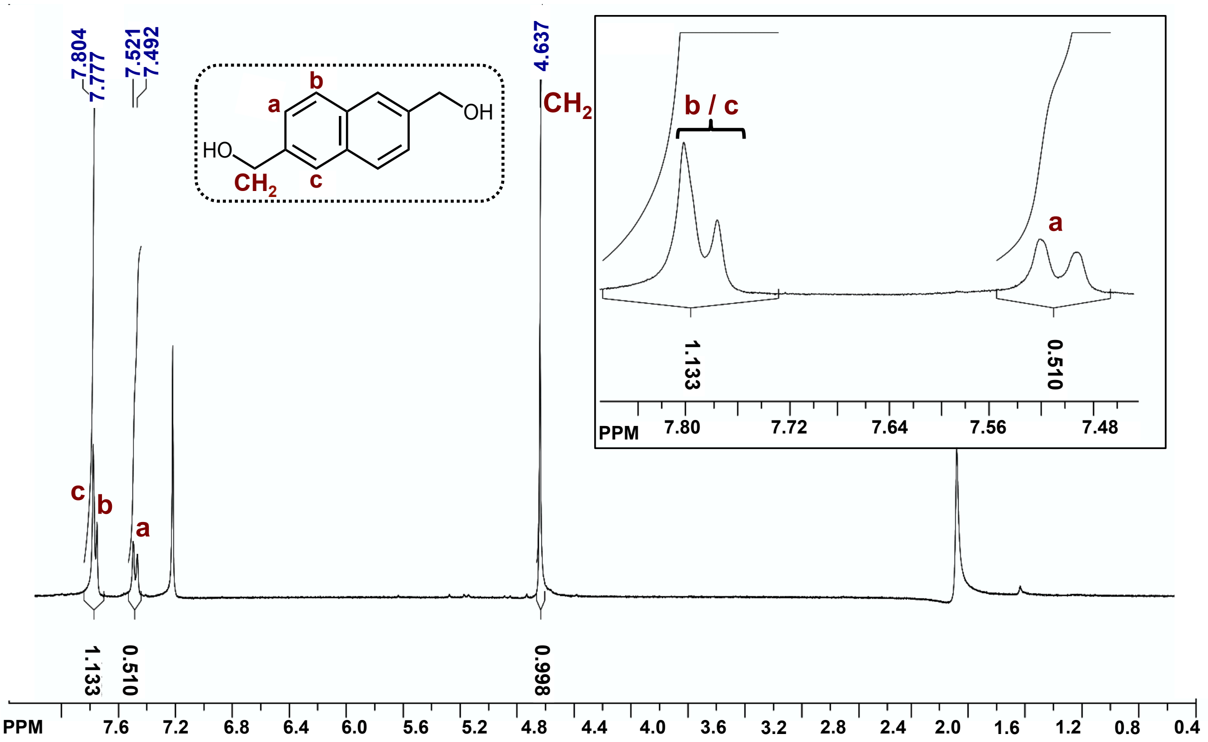

2,6-Bis(bromomethyl)naphthalene (2.2)

^{1}H NMR ($CDCl_3$, 300 MHz, 25 °C)

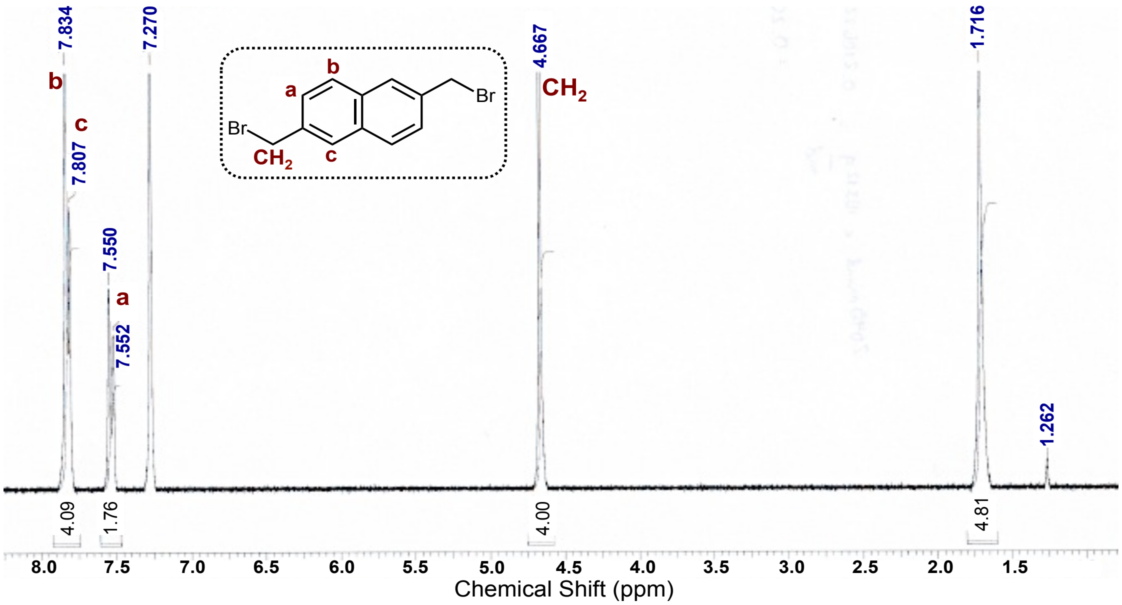

^{1}H - ^{1}H COSY N1 ($CDCl_3$*, 500 MHz, 25 °C)

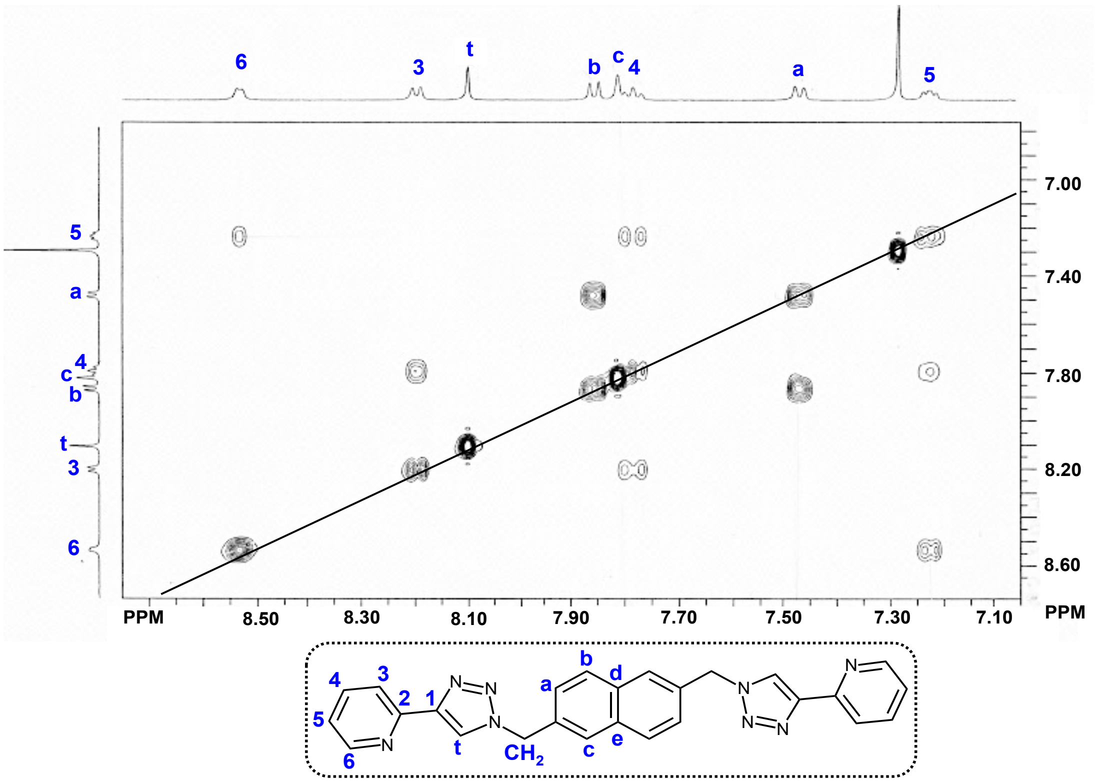

$^{1}H - ^{13}C$ HSQC N1 ($CDCl_3$*, 400 MHz, 25 °C)

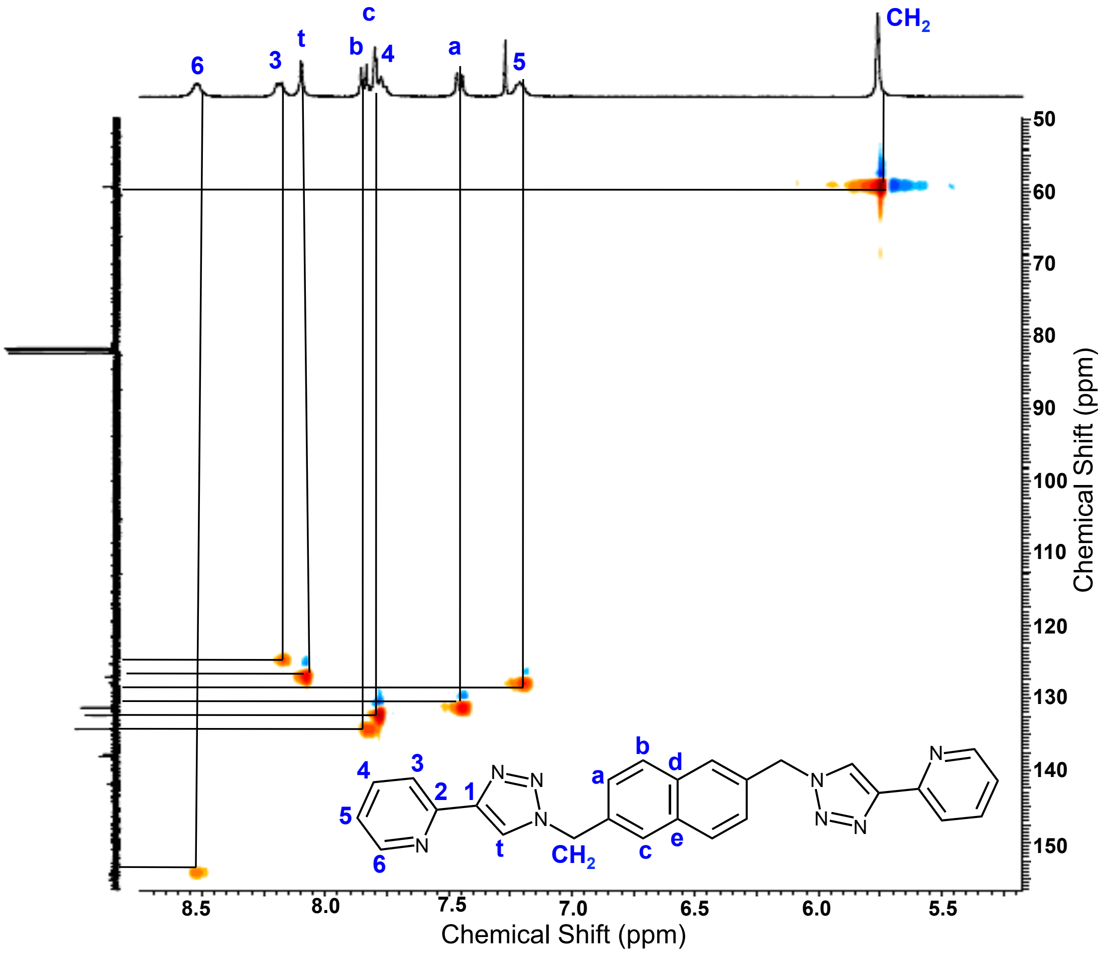

^{1}H – ^{13}C HMBC N1 ($CDCl_3$*, 400 MHz, 25 °C)

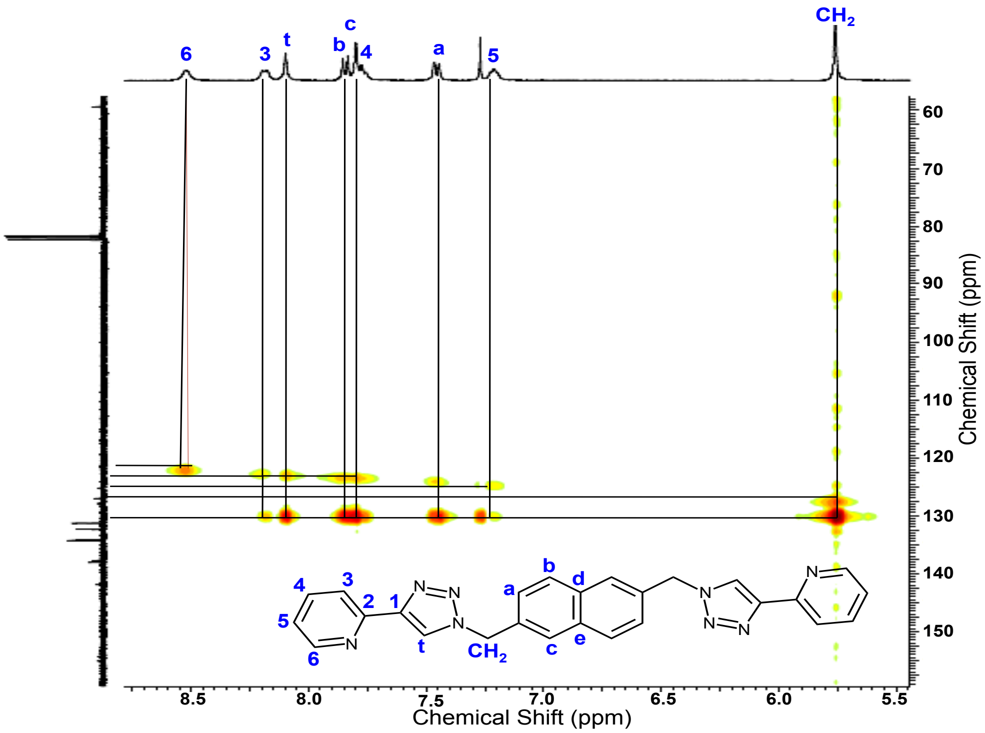

^{13}C NMR N1 ($CDCl_3$*, 125 MHz, 25 °C)

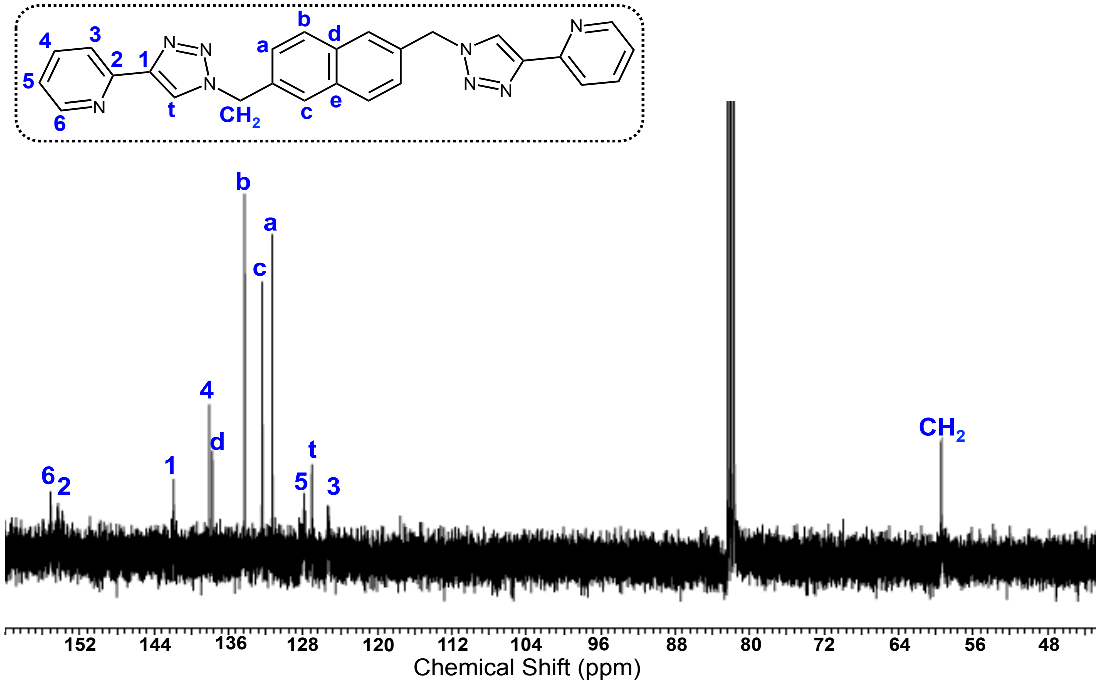

$[Fe_2(N1)_3](BF_4)_4$

^1H – ^1H COSY ($CDCl_3$*, 300 MHz, 25 °C)

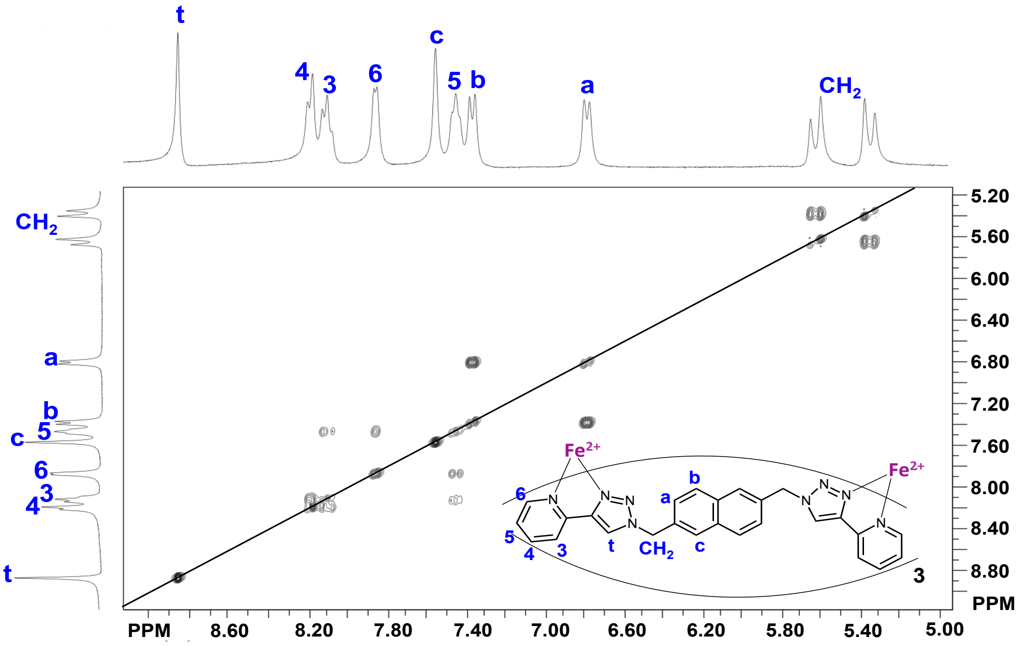

3 N1 + 2 $[Fe(H_2O)_4Cl_2]$

^1H NMR (1:1 $CDCl_3$*: CD_3OD, 300 MHz, 25 °C)

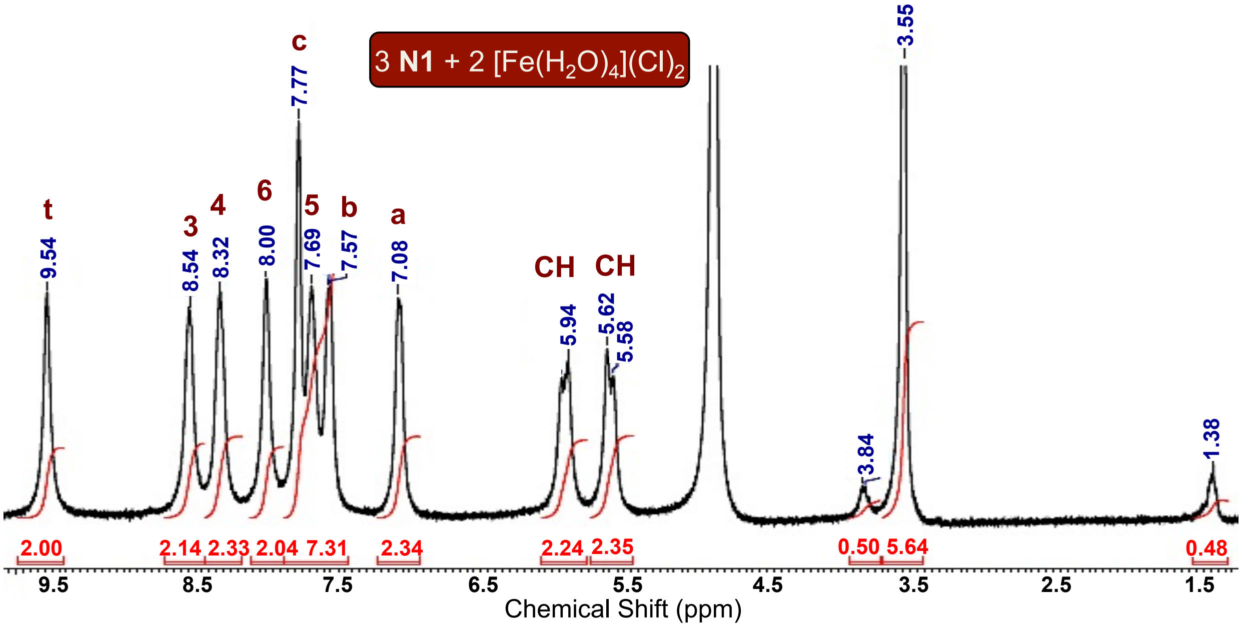

^1H - ^1H COSY (1:1 $CDCl_3$*: CD_3OD, 300 MHz, 25 °C)

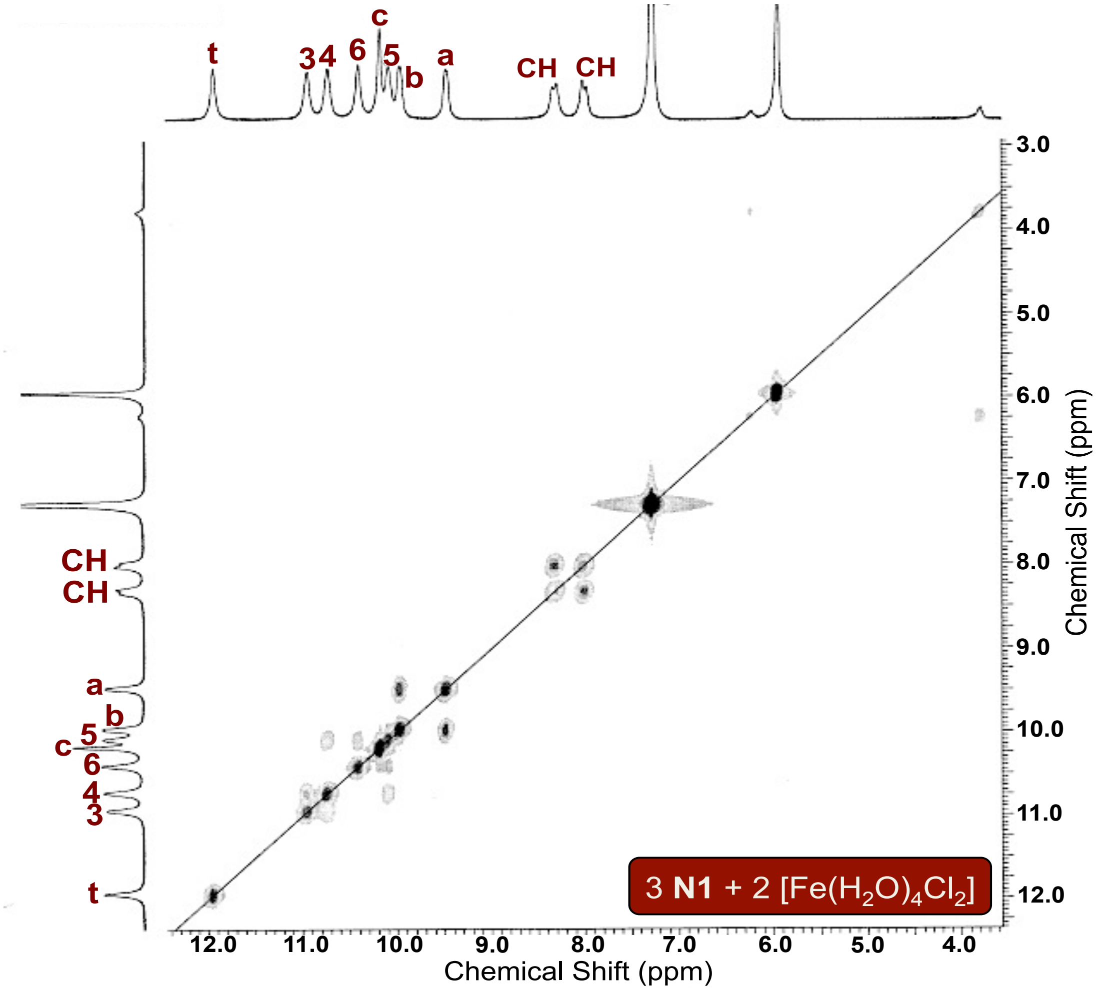

2 N1 + 2 $[Fe(H_2O)_4Cl_2]$

^{1}H NMR (1:1 $CDCl_3$*: CD_3OD, 300 MHz, 25 °C)

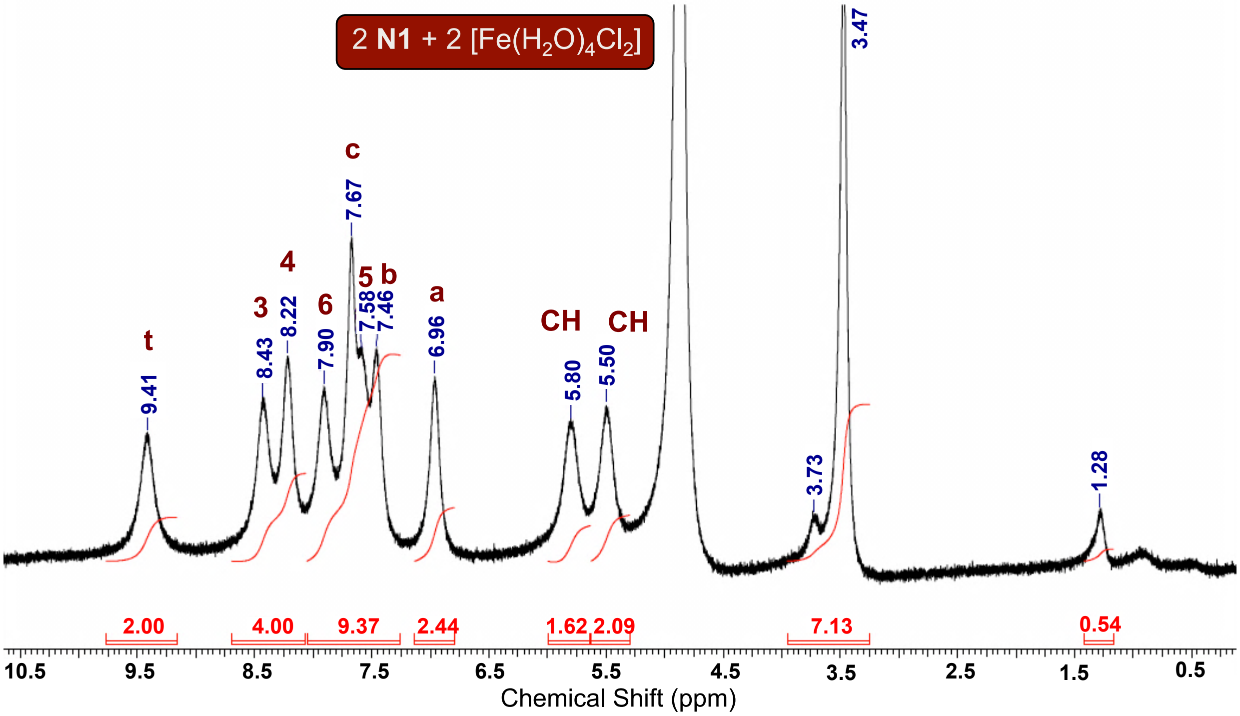

[2-(1-{4-[4-(Pyridin-2-yl)-1,2,3-triazol-1-yl]butyl}-1,2,3-triazol-4-yl)pyridine]] (C4)

^{1}H - ^{1}H COSY (CDCl$_3$*, 500 MHz, 25 °C)

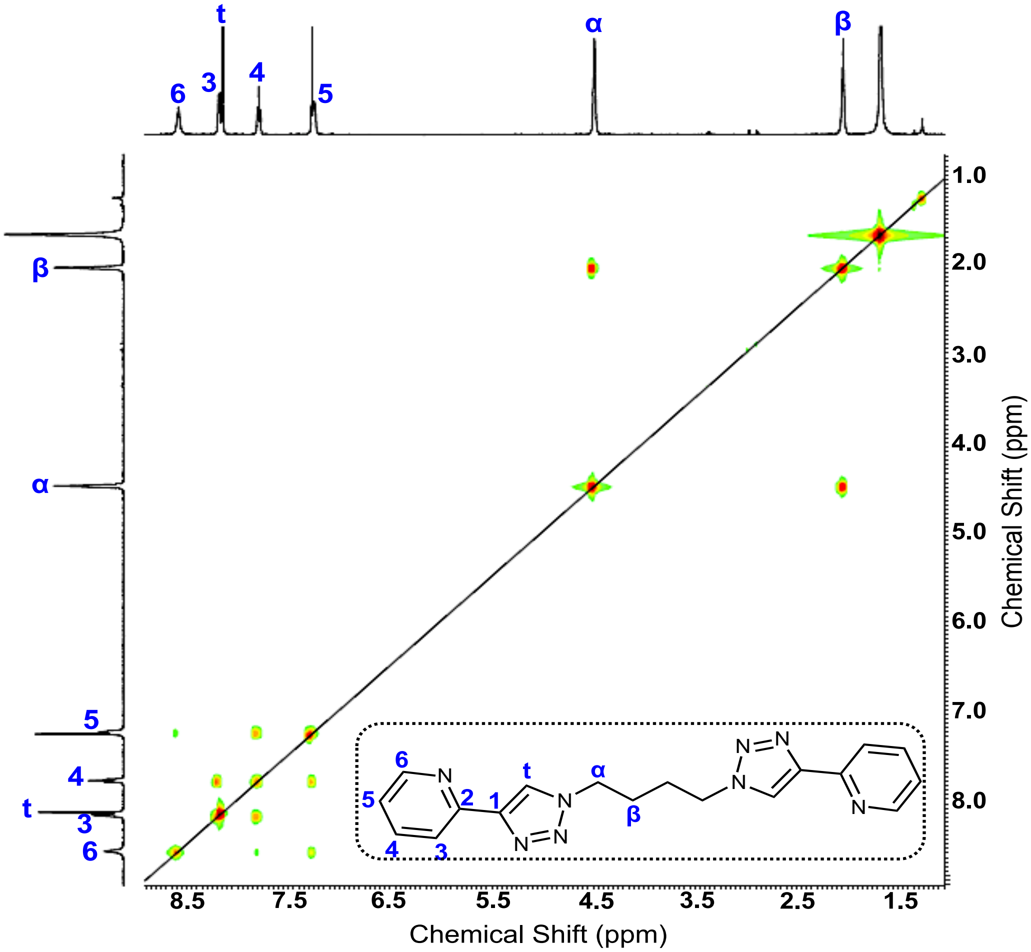

^{13}C NMR C4 (1:1 $CDCl_3$*/CD_3OD, 125 MHz, 25 °C)

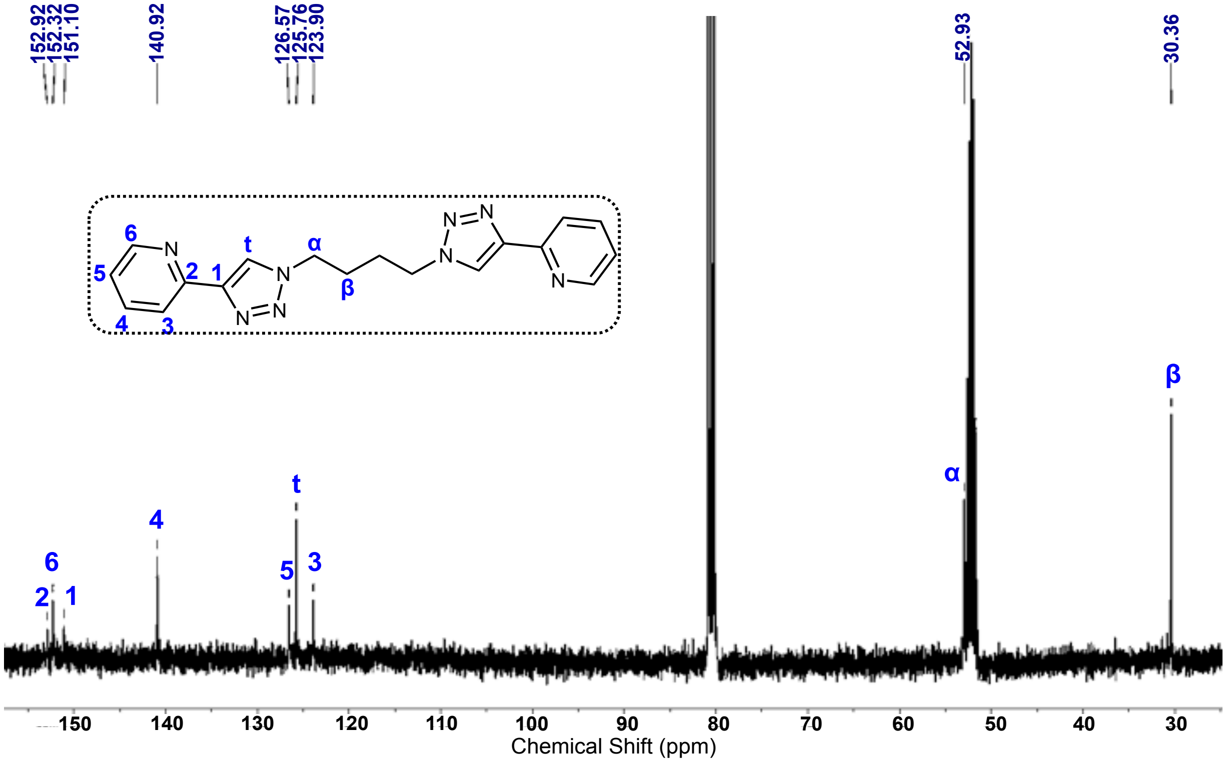

^{1}H - ^{13}C HSQC C4 ($CDCl_3$*, 300 MHz, 25 °C)

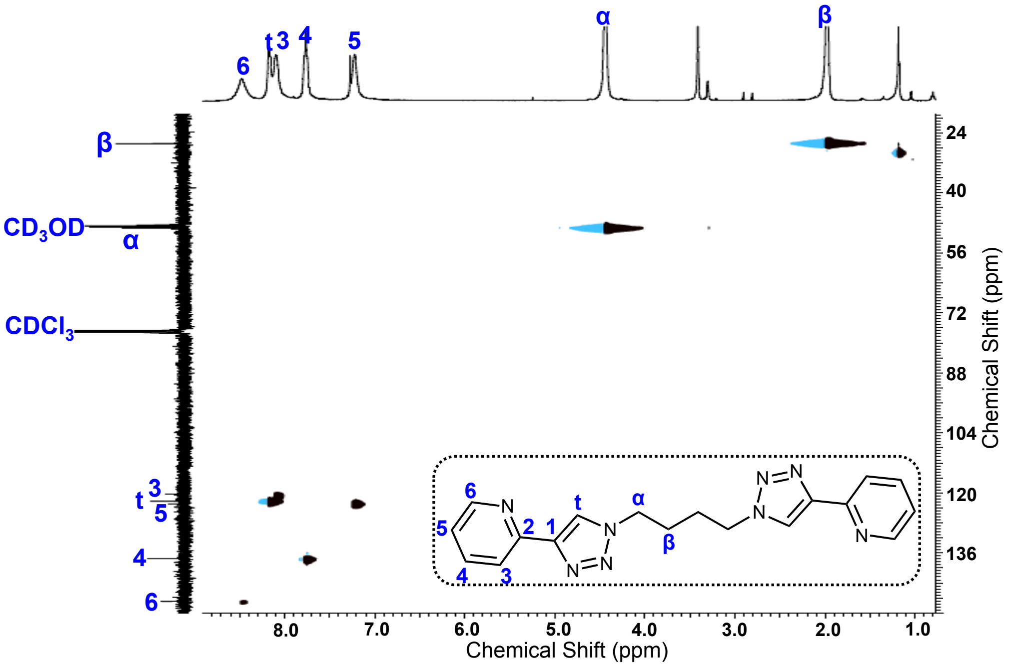

^{1}H - ^{13}C HMBC C4 ($CDCl_3$*, 300 MHz, 25 °C)

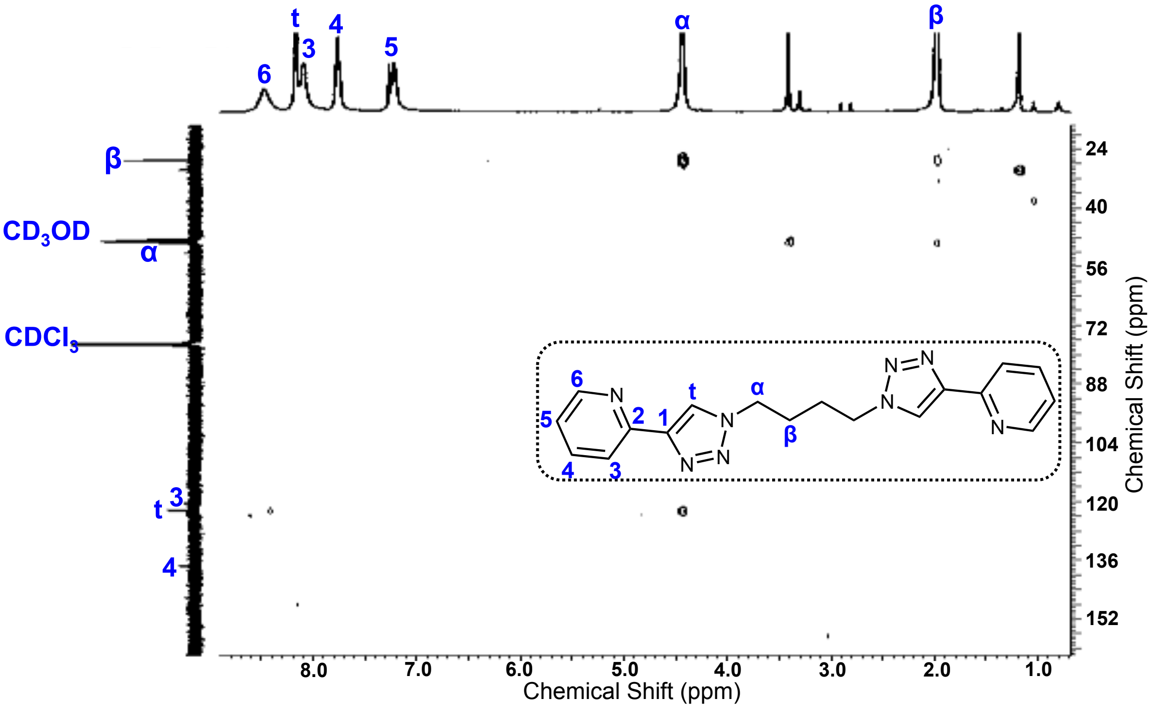

Note: Only those peaks that were readily visible were labeled on the ^{13}C axis for both HSQC and HMBC. For complete carbon peak assignments, please see Chapter 4.

[2-(1-{5-[4-(pyridin-2-yl)-1,2,3-triazol-1-yl]pentyl}-1,2,3-triazol-4-yl)pyridine]] (C5)

^{1}H - ^{1}H COSY (CDCl$_3$*, 300 MHz, 25 °C)

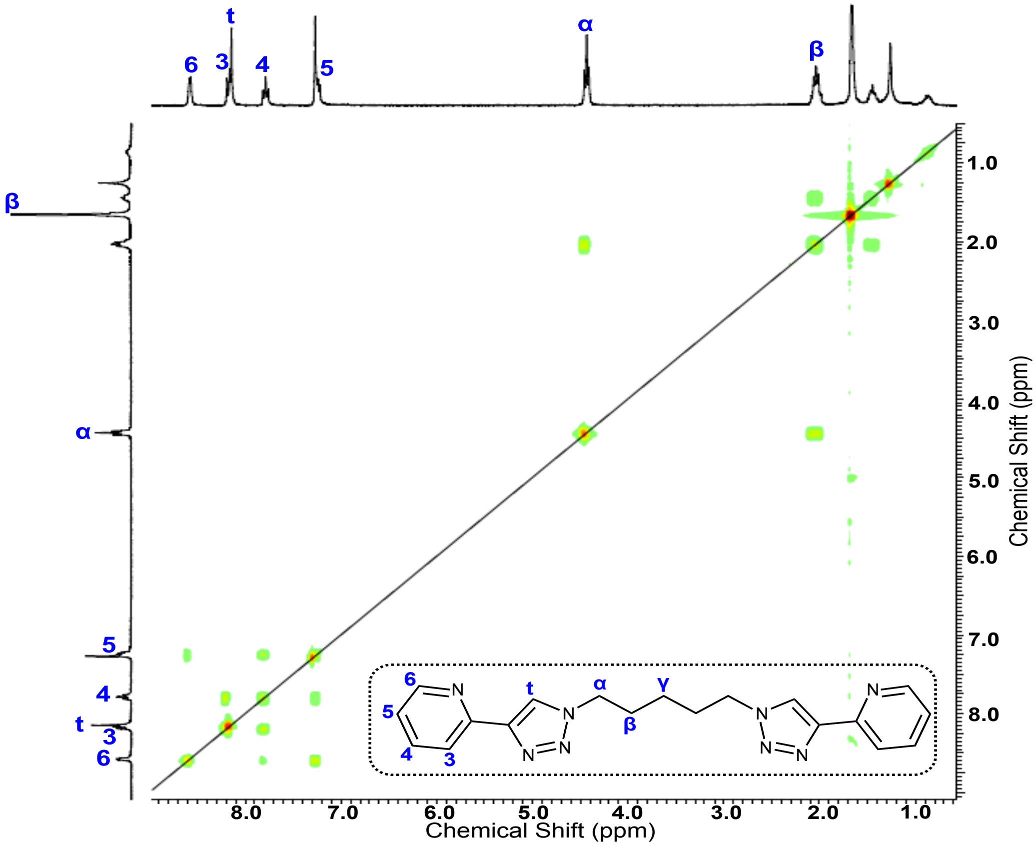

^{13}C NMR C5 ($CDCl_3$*, 125 MHz, 25 °C)

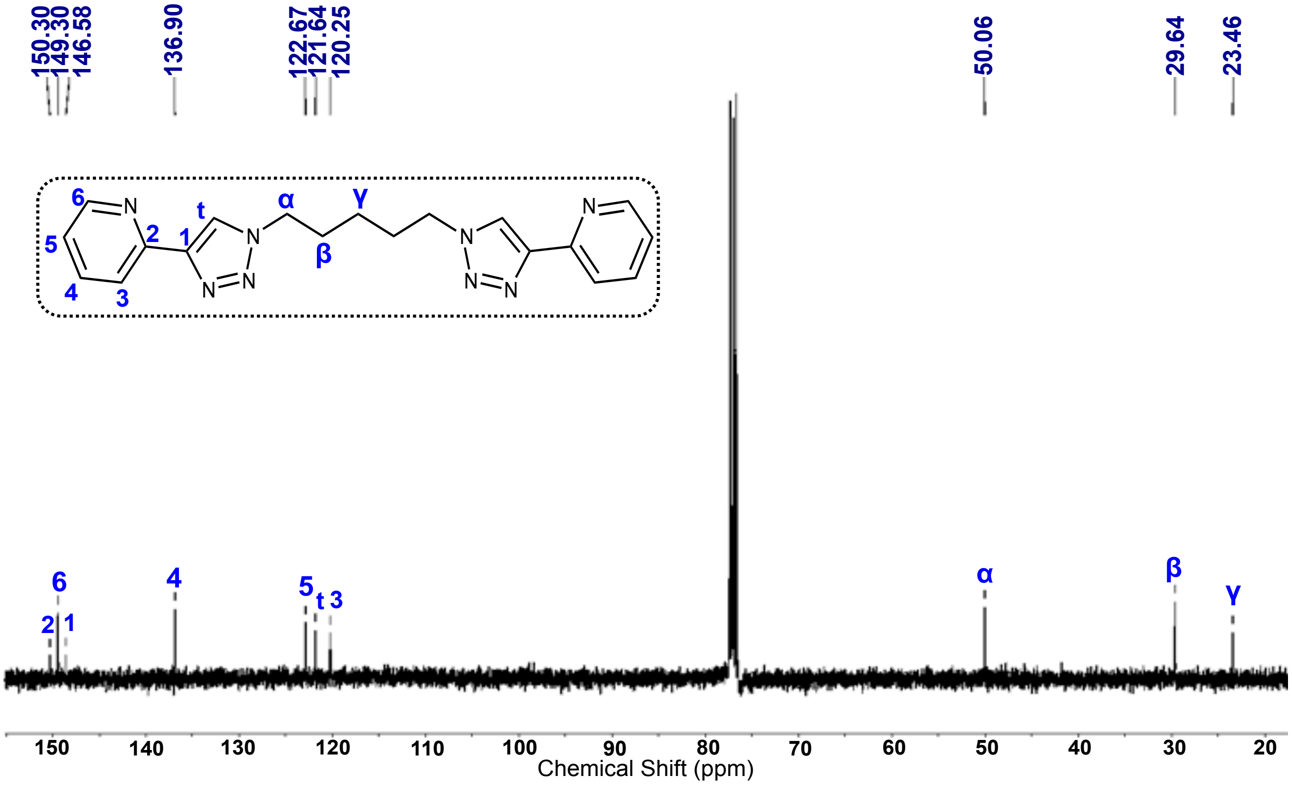

^{1}H - ^{13}C HSQC C5 (CDCl$_3$*, 300 MHz, 25 °C)

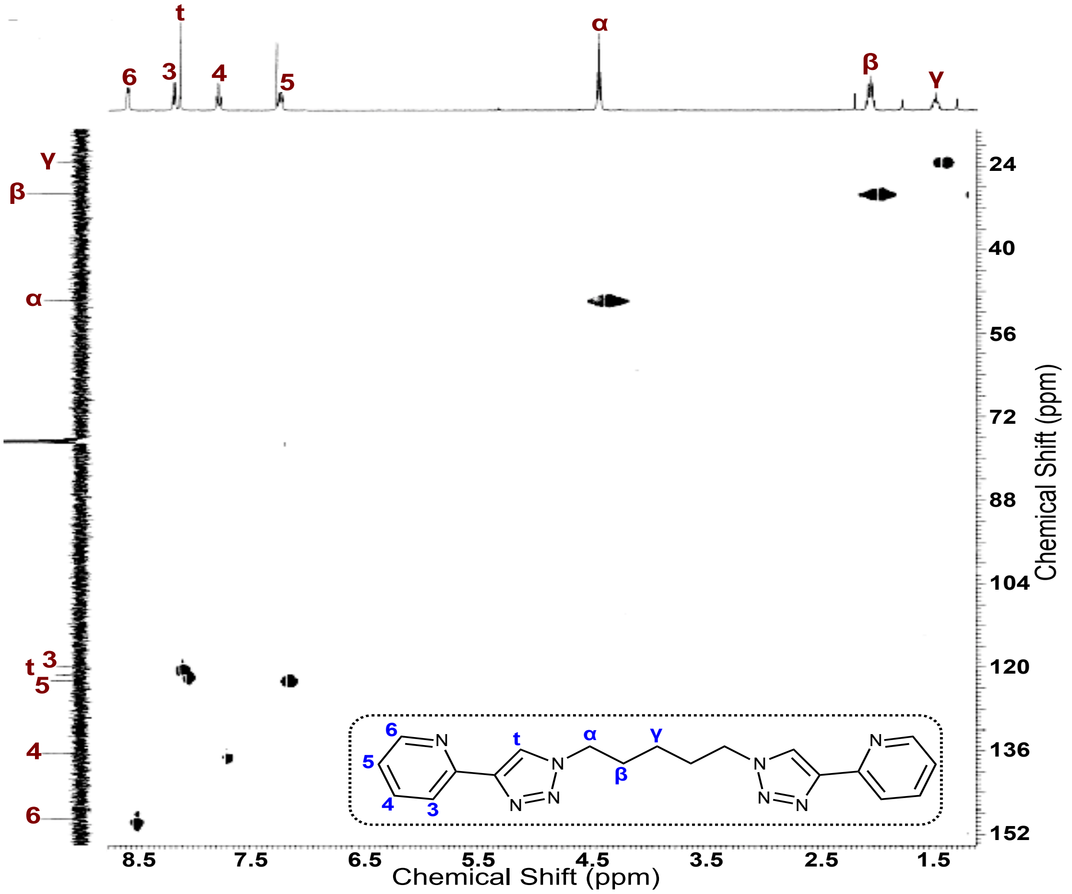

Note: A zoom region of the above spectrum has been included to assist with peak assignments.

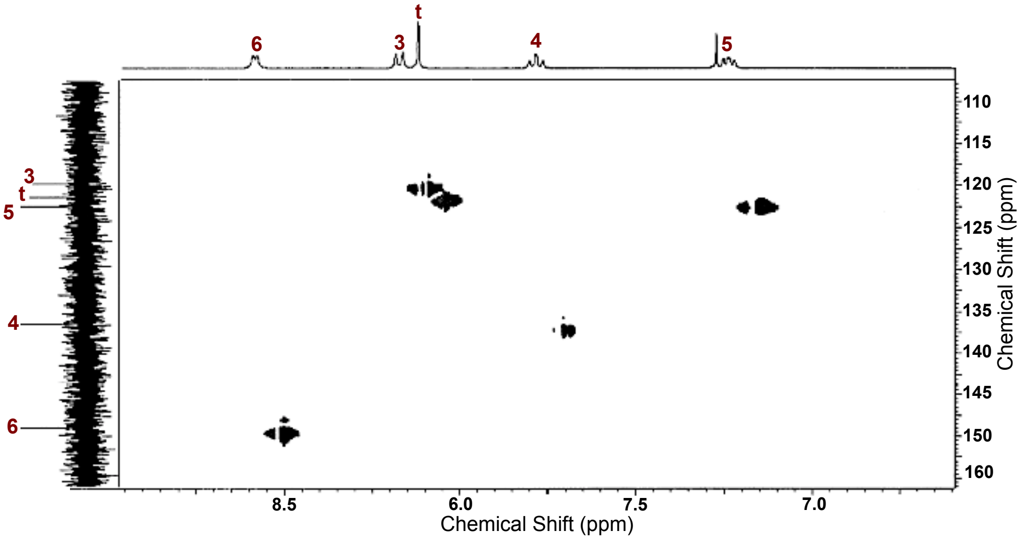

Electron Impact (EI^+) Mass Spectrometry (C5)

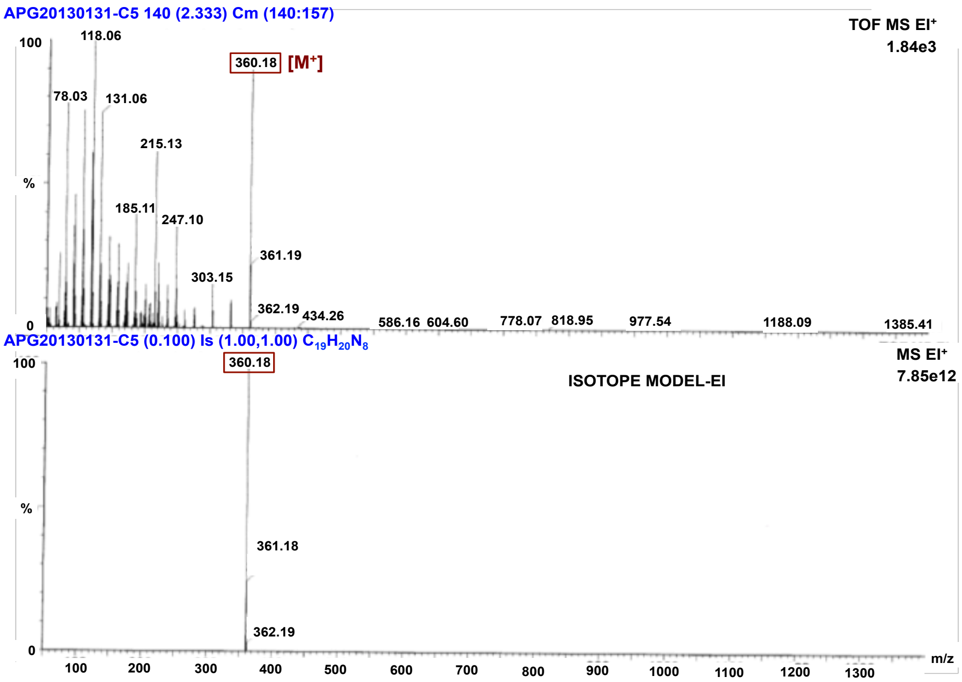

[7-[(2-chloroacetyl)oxy]naphthalen-2-yl 2-chloroacetate]] (2.3)

^{1}H NMR ($CDCl_3$*, 300 MHz, 25 °C)

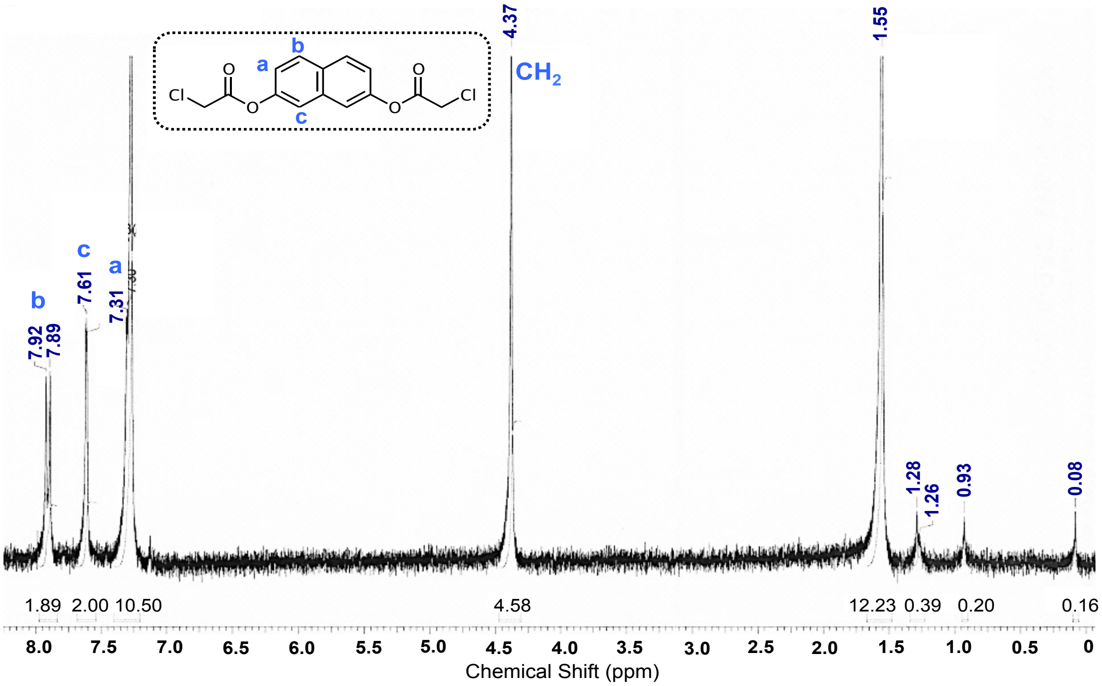

^1H - ^1H COSY ($CDCl_3$*, 300 MHz, 25 °C)

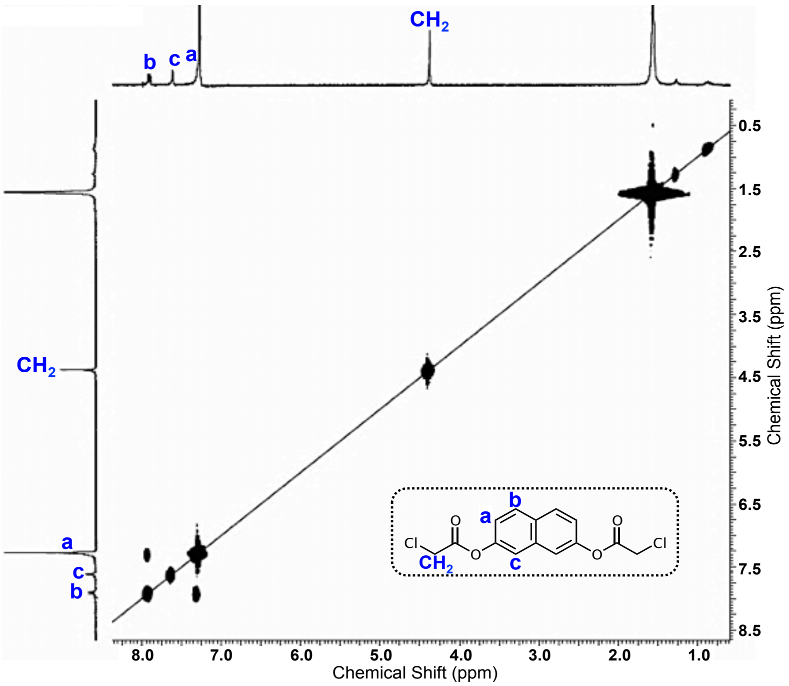

Electron Impact (EI^+) Mass Spectrometry (2.3)

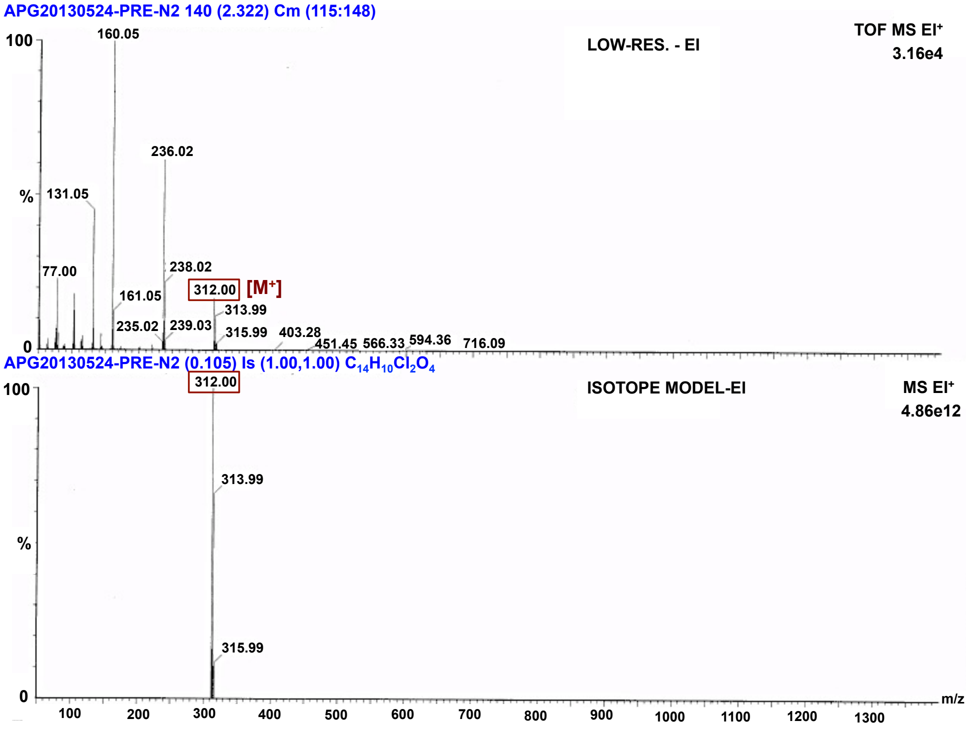

UV-vis Spectra

i. **Job plot for N1 with [$Fe(H_2O)_4Cl_2$].**

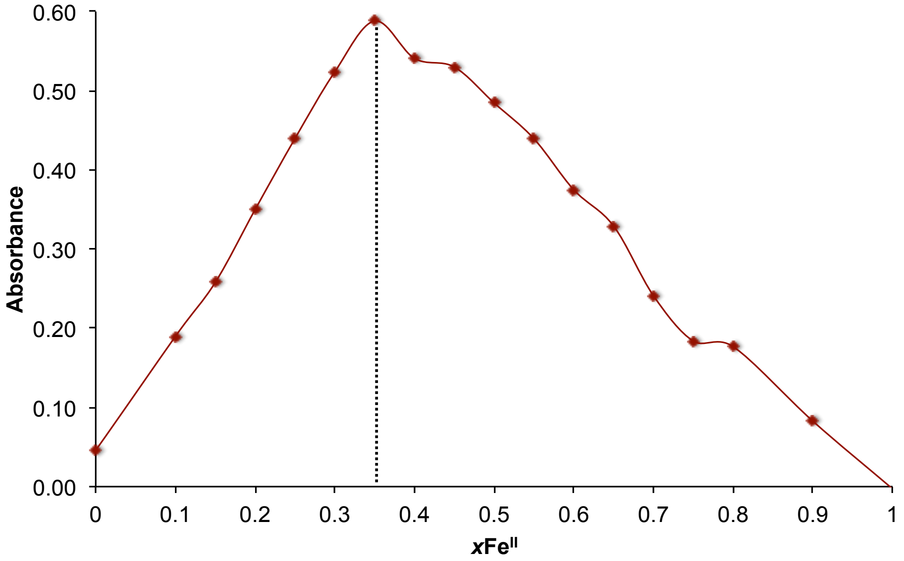

ii. **UV-vis titration for [$Ni(H_2O)_4(OAc)_2$] to N1 in MeOH.**

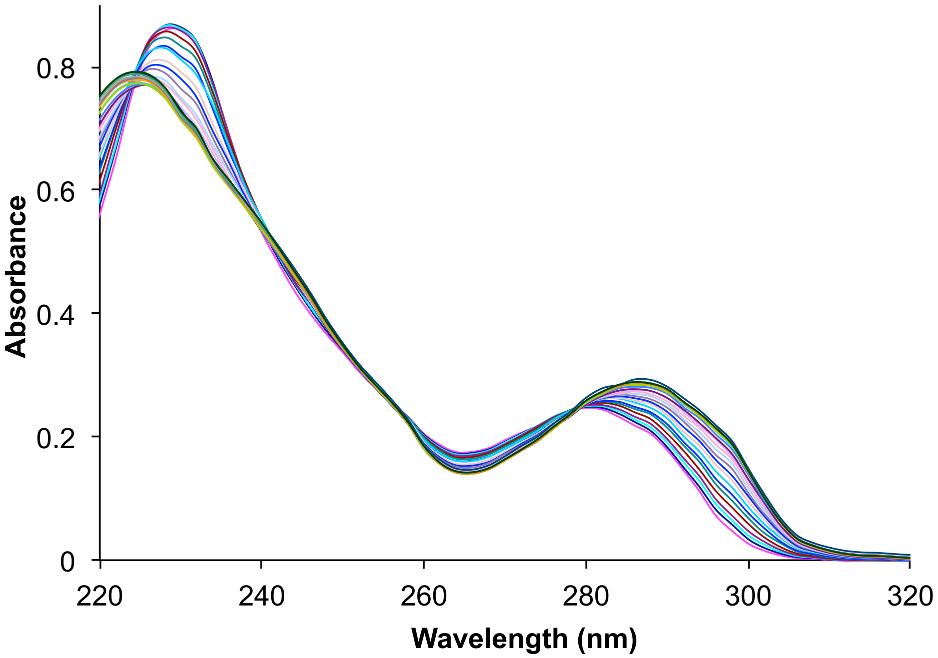

iii. **Absorbance as a function of [nNi^{II} / nN1] ratio at 295 nm with [Ni(H$_2$O)$_4$(OAc)$_2$].**

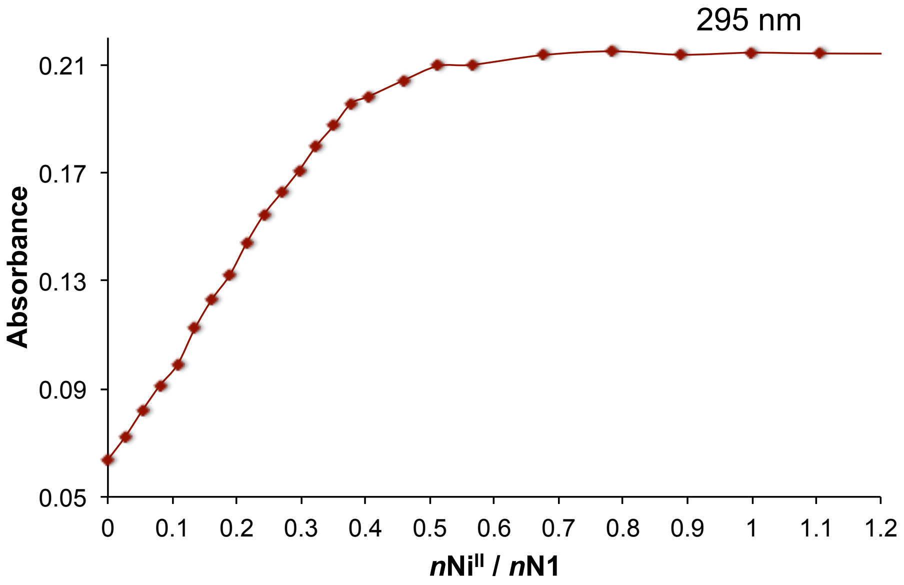

iv. **Job plot for N1 with [Ni(H$_2$O)$_4$(OAc)$_2$].** *Note:* Two methods of analysis have been plotted.

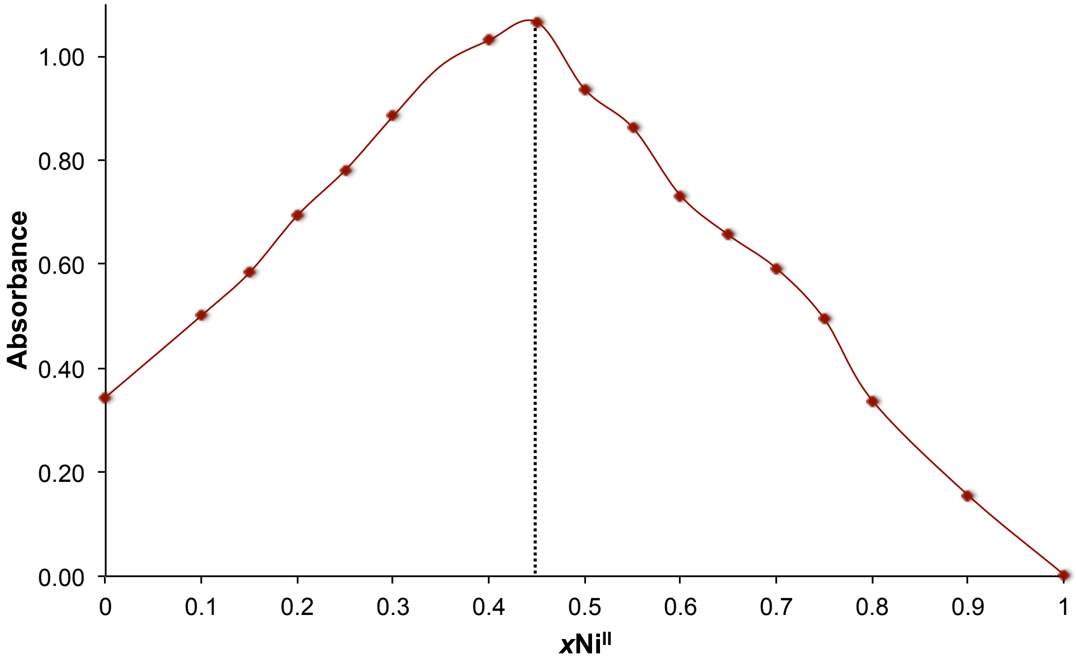

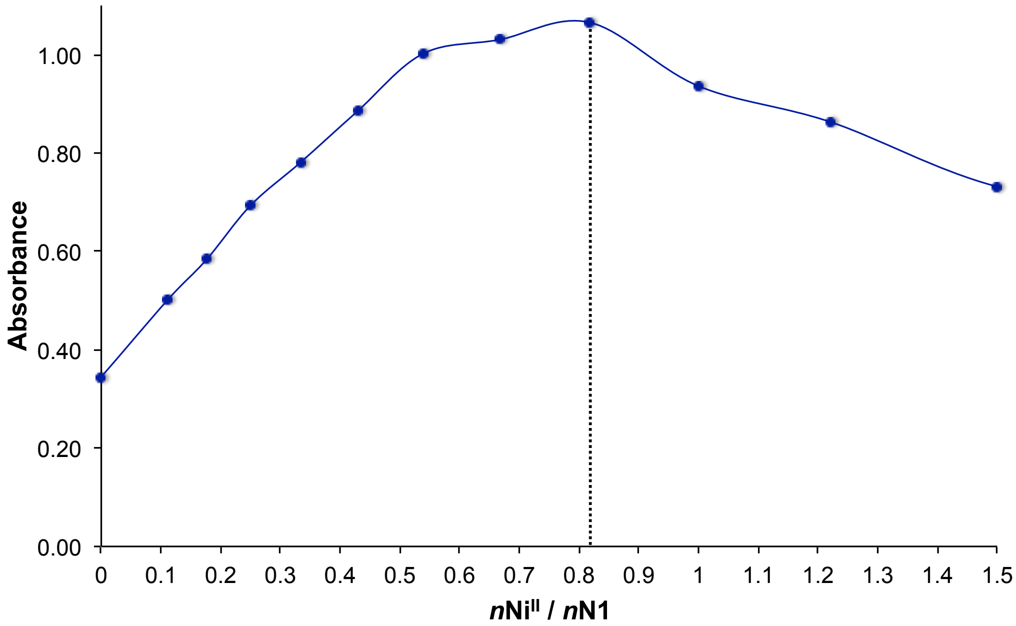

v. Job plot for $[Ni_2(C4)_3](BF_4)_4$ in CH_3CN.

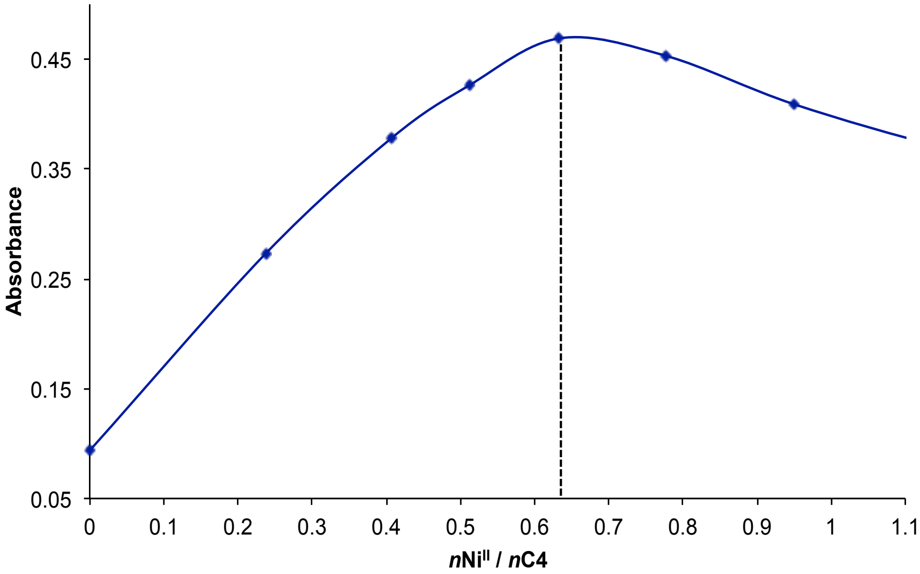

vi. Job plot for $[Fe_2(C5)_3](BF_4)_4$ in CH_3CN. *Note:* Two methods of analysis have been plotted.

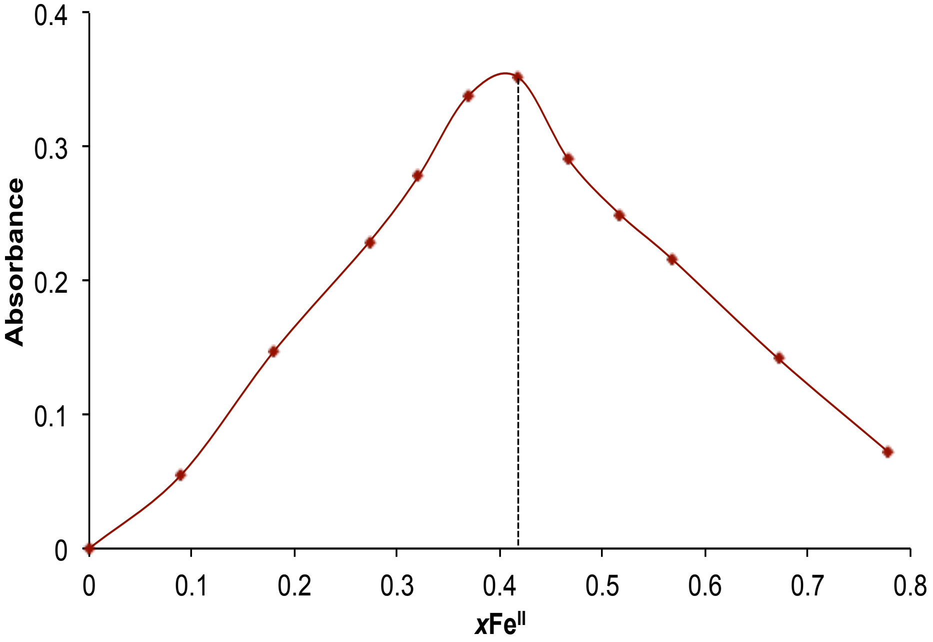

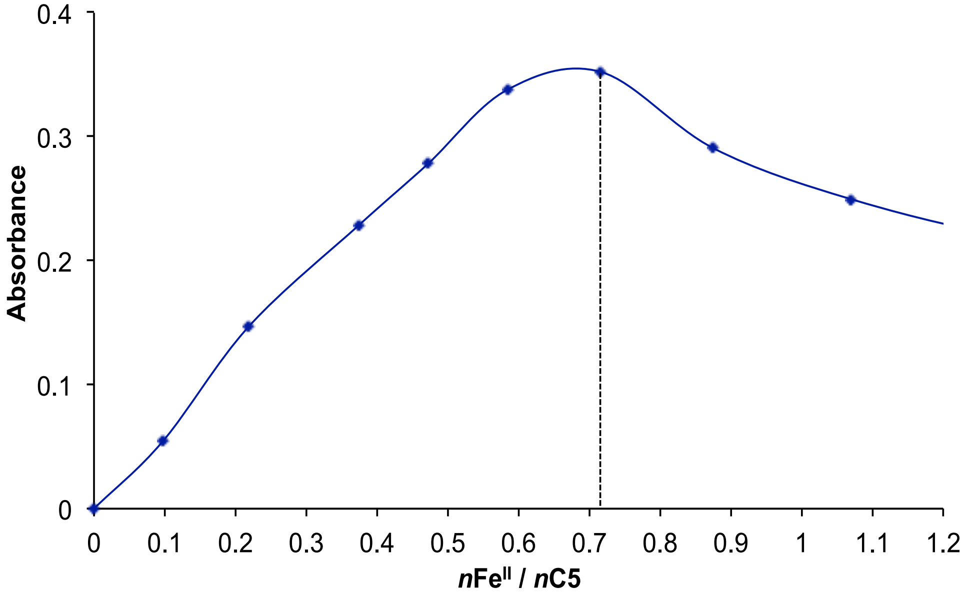

vii. **UV-vis titration for $[Ni(H_2O)_6](BF_4)_2$ to C5 in CH_3CN.**

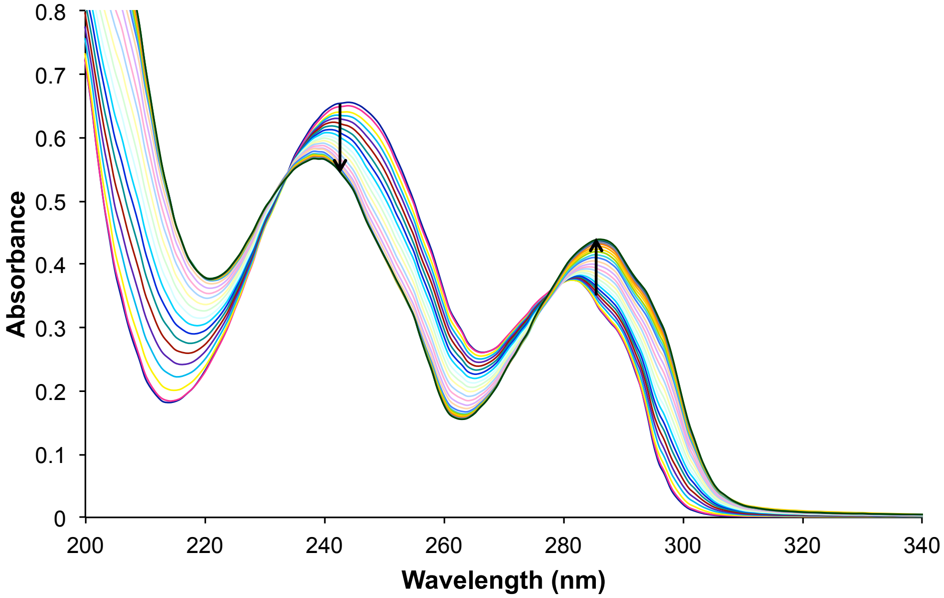

viii. **Absorbance as a function of [*n*Ni^{II} to *n*C5] ratio at 244 nm and 215 nm.**

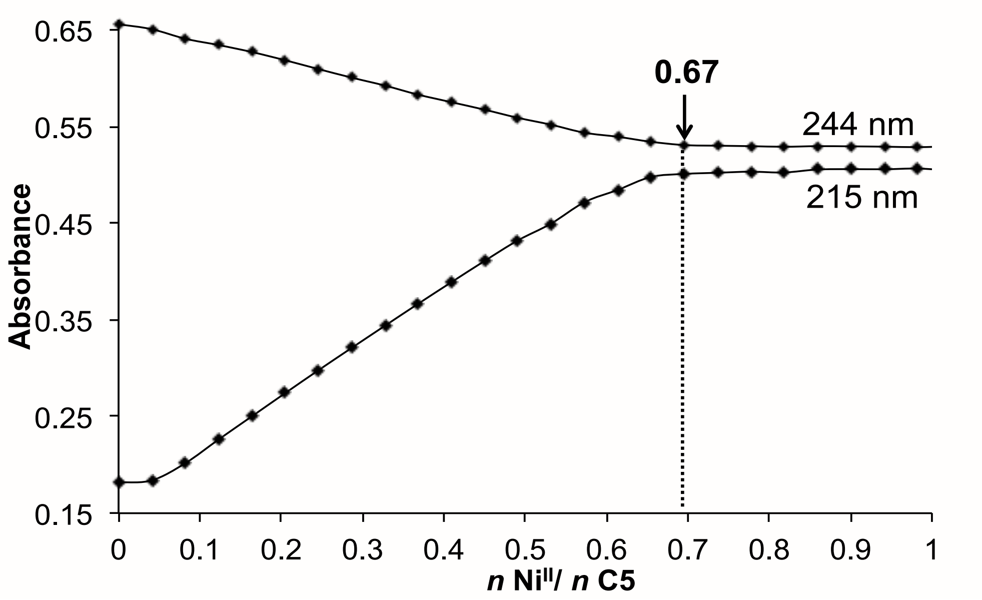

ix. Job plot for [$Ni_2(C5)_3$](BF_4)$_4$ in CH_3CN. *Note*: Two methods of analysis are included.

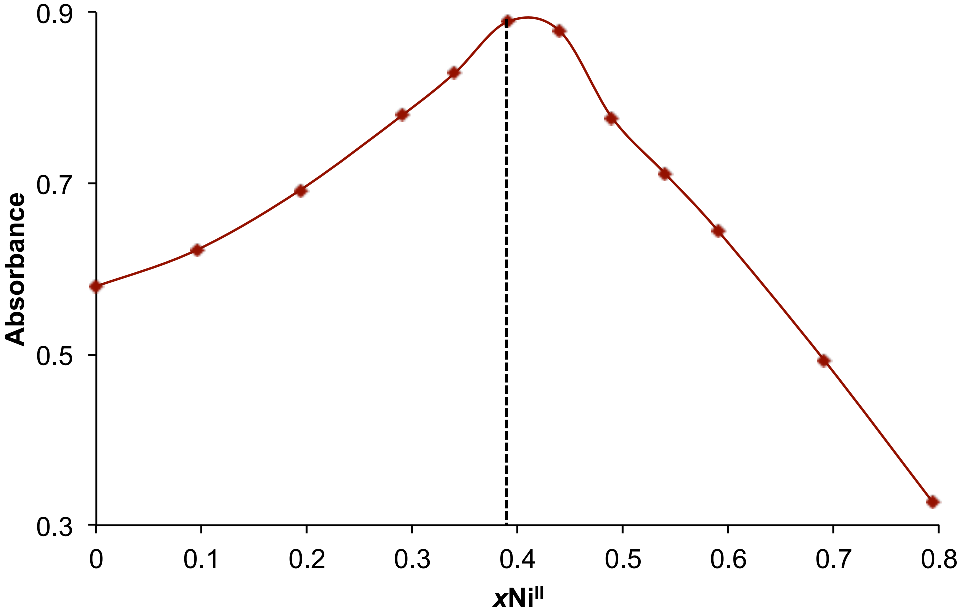

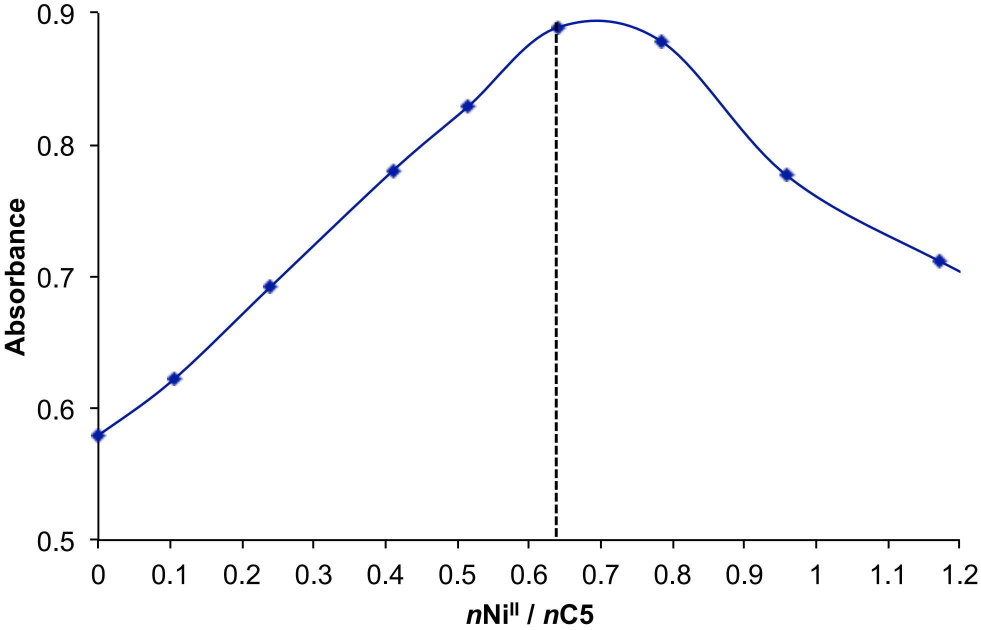

Crystallography Data

$[Fe_2(N1)_3](BF_4)_4 \cdot 2.5\ CH_3CN \cdot 2.5\ Et_2O$ [CCDC: 891128]

A crystal of the compound (dark orange, block-shaped, size 0.20 × 0.20 × 0.15 mm) was mounted on a glass fiber with grease and cooled to -93 °C in a stream of nitrogen gas controlled with Cryostream Controller 700. Data collection was performed on a Bruker SMART APEX II X-ray diffractometer with graphite-monochromated Mo K_α radiation ($\lambda = 0.71073$ Å), operating at 50 kV and 30 mA over 2θ ranges of 2.86 ~ 52.00º. No significant decay was observed during the data collection. Data were processed on a PC using the Bruker AXS Crystal Structure Analysis Package:[1] Data collection: APEX2 (Bruker, 2006); cell refinement: SAINT (Bruker, 2005); data reduction: SAINT (Bruker, 2005); structure solution: XPREP (Bruker, 2005) and SHELXTL (Bruker, 2000); structure refinement: SHELXTL; molecular graphics: SHELXTL; publication materials: SHELXTL. Neutral atom scattering factors were taken from Cromer and Waber.[2] The crystal is monoclinic space group C2/c, based on the systematic absences, *E* statistics and successful refinement of the structure. The structure was solved by direct methods.

Full-matrix least-square refinements minimizing the function $\sum w\ (F_o^2 - F_c^2)^2$ were applied to the compound. All non-hydrogen atoms were refined anisotropically, except two disordered BF_4^- anions. SHELX commands, EADP and SADI were applied to resolve the disorder of the disordered BF_4^- anions. All H atoms were placed in geometrically calculated positions, with C-H = 0.99(CH_2), and 0.95(aryl) Å, and refined as riding atoms, with Uiso(H) = 1.2 UeqC(other C). Difference electron density maps revealed the presence of disordered lattice solvate molecules, CH_3CN and Et_2O, which were ultimately modeled through the use of the SQUEEZE subroutine of the PLATON software suite. PLATON *Reference*: P. v.d. Sluis & A.L. Spek. Acta Cryst. (1990), A46, 194. One big solvent accessible void per lattice were found, comprising a total volume of 5771 A3 and contributing a total of 1231 electrons. The void was thus assigned to 20

CH_3CN and 20 Et_2O, which contribute 20 × (22 + 42) = 1280 electrons, and occupy about 3200 $Å^3$ in space. The larger volume of the void may be a result of the disorder. The contributions have been included in all derived crystal quantities although the precise composition of the lattice solvate is somewhat speculative. Convergence to final $R_1 = 0.0890$ and $wR_2 = 0.2294$ for 9090 ($I>2\sigma(I)$) independent reflections, and $R_1 = 0.1493$ and $wR_2 = 0.2585$ for all 19070 (R(int) = 0.1134) independent reflections, with 1078 parameters and 21 restraints, were achieved.[3] The largest residual peak and hole to be 1.301 and – 0.604 e/$Å^3$, respectively. Crystallographic data, atomic coordinates and equivalent isotropic displacement parameters, bond lengths and angles, anisotropic displacement parameters, hydrogen coordinates and isotropic displacement parameters, and torsion angles are given in **Table C1.1 to C1.6**. The molecular structure and the cell packing are shown in **Figures C1.1 and C1.2**.

[1] Bruker AXS Crystal Structure Analysis Package: Bruker (2000). SHELXTL. Version 6.14. Bruker AXS Inc., Madison, Wisconsin, USA. Bruker (2005). XPREP. Version 2005/2. Bruker AXS Inc., Madison, Wisconsin, USA. Bruker (2005). SAINT. Version 7.23A. Bruker AXS Inc., Madison, Wisconsin, USA. Bruker (2006). APEX2. Version 2.0-2. Bruker AXS Inc., Madison, Wisconsin, USA.

[2] Cromer, D. T.; Waber, J. T. *International Tables for X-ray Crystallography*; Kynoch Press: Birmingham, UK, 1974; Vol. 4, Table 2.2 A.

[3] $R_1 = \sum | |F_o| - |F_c| | / \sum |F_o|$

$$wR_2 = \{\sum [w (Fo^2 - Fc^2)^2] / \sum [w(Fo^2)^2]\}^{1/2}$$

$$(w = 1 / [\sigma^2(Fo^2) + (0.1473P)^2], \text{ where } P = [\mathrm{Max}\ (Fo^2, 0) + 2Fc^2] / 3)$$

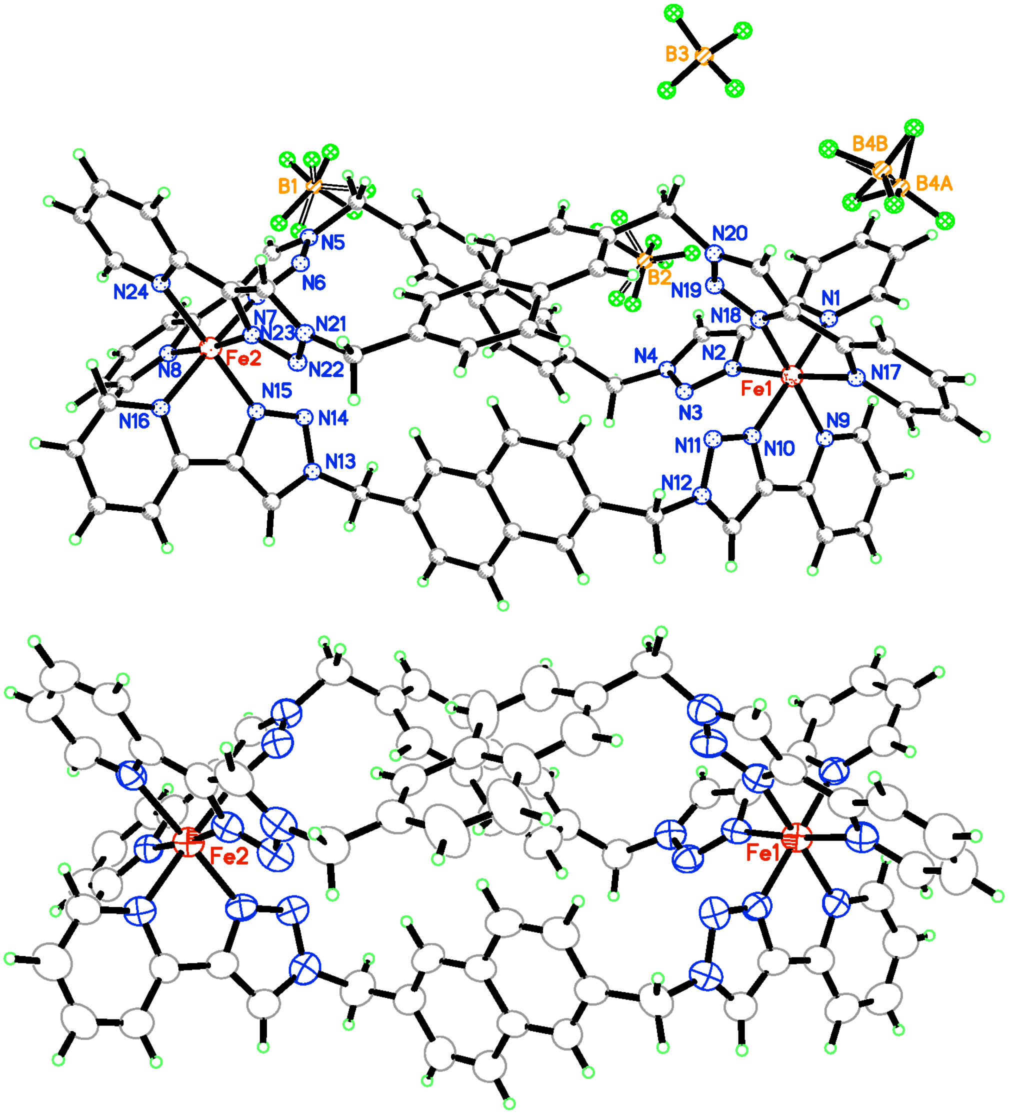

Figure C1.1: *Top*, molecular structure with the BF_4^- anions shown as well as selective atom labels; *Bottom*, Molecular structure (displacement ellipsoids for non-H atoms are shown at the 50% probability level. The solvent molecules and anions are omitted for clarity.

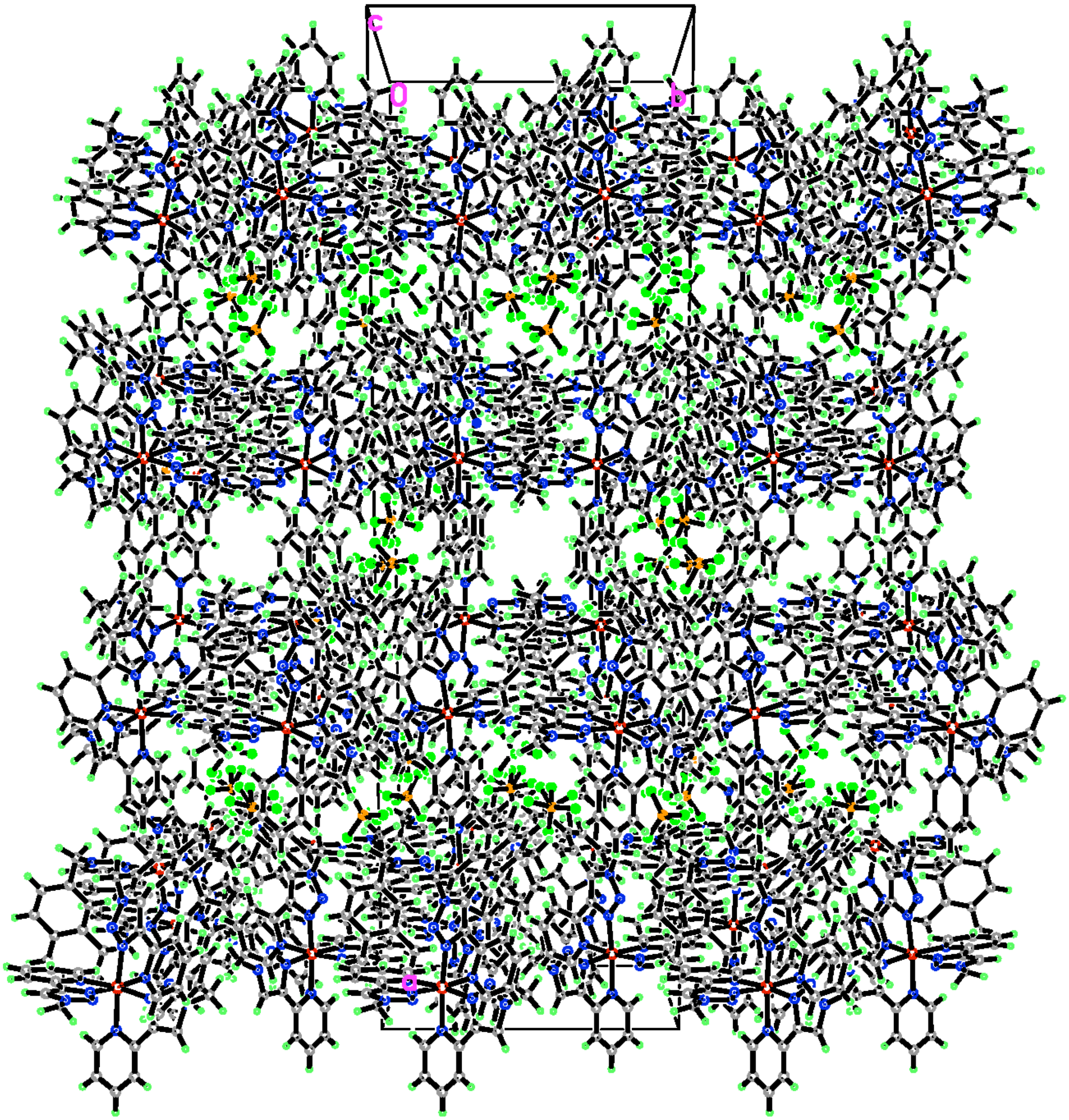

Figure C1.2: Unit cell packing

Table C1.1: Crystal data and structure refinement for ap35a

Identification Code	ap35a	
Empirical Formula	$C_{93}H_{92.50}B_{4}F_{16}Fe_{2}N_{26.50}O_{2.50}$	
Formula Weight	2080.38	
Temperature	180(2) K	
Wavelength	0.71073 Å	
Crystal System	Monoclinic	
Space Group	C2/c	
Unit Cell Dimensions	a = 51.649(3) Å	α = 90°
	b = 14.9251(8) Å	β = 108.648(3)°
	c = 26.5830(15) Å	γ = 90°
Volume	19416.1(19) Å^{3}	
Z	8	
Density (calculated)	1.423 Mg/m^{3}	
Absorption Coefficient	0.394 mm^{-1}	
F(000)	8576	
Crystal Size	0.20 x 0.20 x 0.15 mm^{3}	
Theta Range for Data Collection	1.43 to 26.00°	
Index Ranges	-63<=h<=63, -16<=k<=18, -32<=l<=32	
Reflections Collected	86864	
Independent Reflections	19070 [R(int) = 0.1134]	
Completeness to theta = 26.00°	100.0 %	
Absorption Correction	Multi-scan	
Max. and Min. Transmission	0.9433-0.9254	
Refinement Method	Full-matrix least-squares on F^{2}	
Data / Restraints / Parameters	19070 / 21 / 1078	
Goodness-of-fit on F^{2}	0.929	
Final R indices [I>2sigma(I)]	R1 = 0.0890, wR2 = 0.2294	
R Indices (all data)	R1 = 0.1493, wR2 = 0.2585	
Largest Diff. Peak and Hole	1.301 and -0.604 e.Å^{-3}	

Table C1.2: Atomic coordinates (x 10^4) and equivalent isotropic displacement parameters (Å^2 x 10^3) for ap35a. *Note:* U(eq) is defined as one third of the trace of the orthogonalized U^{ij} tensor.

	x	**y**	**z**	**U(eq)**
Fe(1)	821(1)	7717(1)	4788(1)	40(1)
Fe(2)	1696(1)	7313(1)	10102(1)	39(1)
N(1)	944(1)	6777(3)	4376(2)	40(1)
N(2)	1198(1)	7611(3)	5243(2)	39(1)
N(3)	1349(1)	8011(3)	5679(2)	45(1)
N(4)	1601(1)	7656(3)	5787(2)	45(1)
N(5)	1957(1)	5469(3)	9247(2)	43(1)
N(6)	1742(1)	5925(3)	9307(2)	42(1)
N(7)	1846(1)	6465(3)	9710(2)	37(1)
N(8)	2091(1)	7415(3)	10544(2)	38(1)
N(9)	918(1)	8753(3)	4418(2)	38(1)
N(10)	738(1)	8667(3)	5204(2)	39(1)
N(11)	638(1)	8690(3)	5605(2)	42(1)
N(12)	627(1)	9566(3)	5712(2)	41(1)
N(13)	1807(1)	9345(3)	9189(2)	45(1)
N(14)	1815(1)	8456(3)	9269(2)	42(1)
N(15)	1735(1)	8338(3)	9694(2)	40(1)
N(16)	1581(1)	8254(3)	10509(2)	39(1)
N(17)	430(1)	7715(3)	4328(2)	43(1)
N(18)	685(1)	6803(3)	5154(2)	39(1)
N(19)	798(1)	6262(3)	5551(2)	45(1)
N(20)	590(1)	5787(3)	5619(2)	48(1)
N(21)	904(1)	7067(3)	9199(2)	45(1)
N(22)	1142(1)	7508(3)	9279(2)	46(1)
N(23)	1321(1)	7095(3)	9689(2)	40(1)
N(24)	1619(1)	6290(3)	10522(2)	43(1)
C(1)	795(1)	6357(4)	3942(2)	50(1)

C(2)	893(1)	5675(4)	3712(2)	55(1)
C(3)	1168(1)	5429(4)	3935(2)	52(1)
C(4)	1321(1)	5841(4)	4384(2)	51(1)
C(5)	1209(1)	6516(3)	4594(2)	42(1)
C(6)	1352(1)	7018(4)	5079(2)	46(1)
C(7)	1612(1)	7046(4)	5431(2)	46(1)
C(8)	1815(1)	7940(4)	6270(2)	51(1)
C(9)	1804(1)	7418(4)	6749(2)	48(1)
C(10)	1981(1)	6748(4)	6968(2)	49(1)
C(11)	1966(1)	6257(3)	7408(2)	44(1)
C(12)	2144(1)	5551(4)	7640(2)	54(1)
C(13)	2127(1)	5103(4)	8074(2)	48(1)
C(14)	1928(1)	5345(4)	8308(2)	47(1)
C(15)	1757(1)	6026(4)	8104(2)	55(1)
C(16)	1764(1)	6492(4)	7649(2)	48(1)
C(17)	1584(1)	7197(4)	7416(2)	70(2)
C(18)	1601(1)	7645(4)	6983(3)	68(2)
C(19)	1915(1)	4856(4)	8796(2)	52(1)
C(20)	2194(1)	5708(3)	9613(2)	49(1)
C(21)	2122(1)	6339(3)	9912(2)	40(1)
C(22)	2263(1)	6882(4)	10364(2)	48(1)
C(23)	2545(1)	6898(4)	10616(2)	54(1)
C(24)	2649(1)	7439(4)	11043(2)	60(2)
C(25)	2480(1)	7968(4)	11223(2)	59(2)
C(26)	2200(1)	7932(4)	10953(2)	49(1)
C(27)	1014(1)	8722(4)	4004(2)	51(1)
C(28)	1069(1)	9471(4)	3763(2)	55(1)
C(29)	1041(1)	10301(4)	3966(2)	58(2)
C(30)	945(1)	10356(4)	4396(2)	51(1)
C(31)	888(1)	9570(3)	4616(2)	39(1)
C(32)	786(1)	9504(3)	5059(2)	40(1)

C(33)	714(1)	10095(4)	5397(2)	45(1)
C(34)	537(1)	9826(4)	6171(2)	49(1)
C(35)	764(1)	9684(3)	6687(2)	43(1)
C(36)	946(1)	10353(4)	6902(2)	44(1)
C(37)	1165(1)	10219(3)	7358(2)	40(1)
C(38)	1365(1)	10899(4)	7579(2)	55(1)
C(39)	1588(1)	10732(4)	8016(2)	54(1)
C(40)	1622(1)	9888(4)	8264(2)	47(1)
C(41)	1435(1)	9233(4)	8070(2)	47(1)
C(42)	1207(1)	9375(3)	7617(2)	39(1)
C(43)	1009(1)	8687(4)	7391(2)	52(1)
C(44)	798(1)	8848(4)	6928(2)	52(1)
C(45)	1878(1)	9736(4)	8740(2)	61(2)
C(46)	1718(1)	9799(4)	9549(2)	51(1)
C(47)	1676(1)	9146(3)	9874(2)	45(1)
C(48)	1584(1)	9108(3)	10332(2)	42(1)
C(49)	1505(1)	9846(4)	10566(2)	50(1)
C(50)	1419(1)	9717(4)	10995(2)	58(2)
C(51)	1417(1)	8848(4)	11184(2)	61(2)
C(52)	1495(1)	8152(4)	10935(2)	49(1)
C(53)	317(1)	8216(4)	3895(2)	54(1)
C(54)	38(1)	8220(5)	3636(2)	70(2)
C(55)	-129(1)	7696(5)	3820(3)	71(2)
C(56)	-19(1)	7193(4)	4260(2)	55(1)
C(57)	263(1)	7197(3)	4507(2)	44(1)
C(58)	407(1)	6688(3)	4961(2)	46(1)
C(59)	347(1)	6016(4)	5272(2)	53(1)
C(60)	654(1)	5107(3)	6046(2)	55(1)
C(61)	708(1)	5518(3)	6578(2)	50(1)
C(62)	518(1)	6043(4)	6695(2)	69(2)
C(63)	562(1)	6413(4)	7197(2)	61(2)

C(64)	366(1)	6971(6)	7318(3)	97(3)
C(65)	405(1)	7250(5)	7827(3)	89(2)
C(66)	645(1)	7039(3)	8239(2)	47(1)
C(67)	839(1)	6556(3)	8122(2)	47(1)
C(68)	803(1)	6220(3)	7603(2)	47(1)
C(69)	997(1)	5684(5)	7480(2)	73(2)
C(70)	948(1)	5350(5)	6984(2)	73(2)
C(71)	663(1)	7376(4)	8779(2)	55(1)
C(72)	930(1)	6397(4)	9536(2)	51(1)
C(73)	1200(1)	6416(4)	9855(2)	50(1)
C(74)	1365(1)	5942(3)	10322(2)	46(1)
C(75)	1282(1)	5212(4)	10554(2)	55(2)
C(76)	1456(1)	4853(4)	11000(3)	64(2)
C(77)	1716(1)	5227(4)	11216(2)	63(2)
C(78)	1783(1)	5929(4)	10957(2)	54(1)
B(1)	2774(1)	4418(5)	9255(3)	66(2)
F(1)	2998(1)	3906(3)	9550(2)	85(1)
F(2A)	2759(2)	5111(5)	9605(4)	85(1)
F(3A)	2842(2)	4852(7)	8854(3)	85(1)
F(4A)	2549(2)	3869(6)	9085(4)	85(1)
F(2B)	2740(3)	5246(7)	9405(5)	85(1)
F(3B)	2766(3)	4476(10)	8719(4)	85(1)
F(4B)	2527(2)	4015(8)	9266(5)	85(1)
B(2)	2306(3)	5713(10)	5848(5)	123(4)
F(5)	2070(1)	5589(4)	5410(2)	153(2)
F(6A)	2339(2)	5187(8)	6354(4)	113(4)
F(7A)	2518(3)	5342(10)	5709(5)	137(5)
F(8A)	2282(2)	6510(5)	5985(3)	103(2)
F(6B)	2354(3)	4937(9)	6117(5)	143(5)
F(7B)	2520(2)	5690(8)	5577(4)	105(4)
F(8B)	2419(11)	6410(40)	6130(20)	330(30)

B(3)	783(2)	2619(5)	5668(4)	71(2)
F(9)	1009(1)	3100(3)	5961(2)	102(1)
F(10)	575(1)	3192(3)	5443(2)	107(1)
F(11)	851(1)	2138(2)	5275(2)	89(1)
F(12)	705(1)	2003(3)	5979(2)	102(1)
B(4A)	229(2)	4754(8)	4008(4)	66(3)
F(13)	463(1)	4946(3)	4363(2)	118(2)
F(14)	168(1)	3835(4)	3909(2)	144(2)
F(15A)	211(2)	5251(6)	3582(3)	161(3)
F(16)	6(1)	5056(3)	4176(2)	88(1)
F(15B)	267(6)	4178(18)	4673(10)	169(9)
B(4B)	206(7)	4490(20)	4193(14)	66(3)

Table C1.3: Bond lengths [Å] and angles [°] for ap35a.

Fe(1)-N(10)	1.929(4)	C(5)-C(4)-H(4A)	120.3
Fe(1)-N(18)	1.932(4)	N(1)-C(5)-C(4)	122.6(5)
Fe(1)-N(2)	1.942(4)	N(1)-C(5)-C(6)	112.4(4)
Fe(1)-N(9)	1.982(4)	C(4)-C(5)-C(6)	124.9(5)
Fe(1)-N(17)	1.996(4)	N(2)-C(6)-C(7)	108.0(5)
Fe(1)-N(1)	2.003(4)	N(2)-C(6)-C(5)	115.6(4)
Fe(2)-N(15)	1.923(4)	C(7)-C(6)-C(5)	136.4(5)
Fe(2)-N(23)	1.926(4)	N(4)-C(7)-C(6)	104.7(5)
Fe(2)-N(7)	1.951(4)	N(4)-C(7)-H(7A)	127.7
Fe(2)-N(16)	1.978(4)	C(6)-C(7)-H(7A)	127.7
Fe(2)-N(24)	2.004(4)	N(4)-C(8)-C(9)	111.6(4)
Fe(2)-N(8)	2.007(4)	N(4)-C(8)-H(8A)	109.3
N(1)-C(1)	1.322(6)	C(9)-C(8)-H(8A)	109.3
N(1)-C(5)	1.364(6)	N(4)-C(8)-H(8B)	109.3
N(2)-N(3)	1.316(5)	C(9)-C(8)-H(8B)	109.3

N(2)-C(6)	1.356(6)	H(8A)-C(8)-H(8B)	108.0
N(3)-N(4)	1.347(5)	C(10)-C(9)-C(18)	118.6(5)
N(4)-C(7)	1.328(6)	C(10)-C(9)-C(8)	122.8(5)
N(4)-C(8)	1.463(6)	C(18)-C(9)-C(8)	118.6(5)
N(5)-C(20)	1.344(6)	C(9)-C(10)-C(11)	122.4(5)
N(5)-N(6)	1.353(5)	C(9)-C(10)-H(10A)	118.8
N(5)-C(19)	1.468(6)	C(11)-C(10)-H(10A)	118.8
N(6)-N(7)	1.312(5)	C(12)-C(11)-C(10)	123.8(5)
N(7)-C(21)	1.365(6)	C(12)-C(11)-C(16)	117.1(5)
N(8)-C(26)	1.305(6)	C(10)-C(11)-C(16)	119.1(5)
N(8)-C(22)	1.386(6)	C(13)-C(12)-C(11)	121.9(5)
N(9)-C(27)	1.346(6)	C(13)-C(12)-H(12A)	119.0
N(9)-C(31)	1.355(6)	C(11)-C(12)-H(12A)	119.0
N(10)-N(11)	1.323(5)	C(12)-C(13)-C(14)	120.3(5)
N(10)-C(32)	1.355(6)	C(12)-C(13)-H(13A)	119.8
N(11)-N(12)	1.344(5)	C(14)-C(13)-H(13A)	119.8
N(12)-C(33)	1.329(6)	C(15)-C(14)-C(13)	119.7(5)
N(12)-C(34)	1.489(6)	C(15)-C(14)-C(19)	120.5(5)
N(13)-N(14)	1.342(5)	C(13)-C(14)-C(19)	119.8(5)
N(13)-C(46)	1.369(6)	C(14)-C(15)-C(16)	121.8(5)
N(13)-C(45)	1.477(6)	C(14)-C(15)-H(15A)	119.1
N(14)-N(15)	1.332(5)	C(16)-C(15)-H(15A)	119.1
N(15)-C(47)	1.367(6)	C(15)-C(16)-C(17)	123.7(5)
N(16)-C(52)	1.349(6)	C(15)-C(16)-C(11)	119.0(5)
N(16)-C(48)	1.361(6)	C(17)-C(16)-C(11)	117.3(5)
N(17)-C(53)	1.340(7)	C(18)-C(17)-C(16)	122.0(5)
N(17)-C(57)	1.353(6)	C(18)-C(17)-H(17A)	119.0
N(18)-N(19)	1.309(5)	C(16)-C(17)-H(17A)	119.0
N(18)-C(58)	1.372(6)	C(17)-C(18)-C(9)	120.7(5)
N(19)-N(20)	1.346(5)	C(17)-C(18)-H(18A)	119.7
N(20)-C(59)	1.344(7)	C(9)-C(18)-H(18A)	119.7

N(20)-C(60)	1.481(6)	N(5)-C(19)-C(14)	111.4(4)
N(21)-C(72)	1.321(7)	N(5)-C(19)-H(19A)	109.3
N(21)-N(22)	1.351(5)	C(14)-C(19)-H(19A)	109.3
N(21)-C(71)	1.457(6)	N(5)-C(19)-H(19B)	109.3
N(22)-N(23)	1.332(5)	C(14)-C(19)-H(19B)	109.3
N(23)-C(73)	1.337(6)	H(19A)-C(19)-H(19B)	108.0
N(24)-C(78)	1.311(6)	N(5)-C(20)-C(21)	104.7(4)
N(24)-C(74)	1.351(6)	N(5)-C(20)-H(20A)	127.7
C(1)-C(2)	1.368(7)	C(21)-C(20)-H(20A)	127.7
C(1)-H(1A)	0.9500	C(20)-C(21)-N(7)	108.1(4)
C(2)-C(3)	1.400(7)	C(20)-C(21)-C(22)	136.1(5)
C(2)-H(2A)	0.9500	N(7)-C(21)-C(22)	115.8(4)
C(3)-C(4)	1.352(7)	N(8)-C(22)-C(23)	120.6(5)
C(3)-H(3A)	0.9500	N(8)-C(22)-C(21)	113.8(4)
C(4)-C(5)	1.366(7)	C(23)-C(22)-C(21)	125.6(5)
C(4)-H(4A)	0.9500	C(24)-C(23)-C(22)	119.1(5)
C(5)-C(6)	1.470(7)	C(24)-C(23)-H(23A)	120.4
C(6)-C(7)	1.369(7)	C(22)-C(23)-H(23A)	120.4
C(7)-H(7A)	0.9500	C(23)-C(24)-C(25)	120.7(5)
C(8)-C(9)	1.509(7)	C(23)-C(24)-H(24A)	119.7
C(8)-H(8A)	0.9900	C(25)-C(24)-H(24A)	119.7
C(8)-H(8B)	0.9900	C(24)-C(25)-C(26)	117.8(5)
C(9)-C(10)	1.353(7)	C(24)-C(25)-H(25A)	121.1
C(9)-C(18)	1.422(8)	C(26)-C(25)-H(25A)	121.1
C(10)-C(11)	1.404(7)	N(8)-C(26)-C(25)	123.5(5)
C(10)-H(10A)	0.9500	N(8)-C(26)-H(26A)	118.2
C(11)-C(12)	1.404(7)	C(25)-C(26)-H(26A)	118.2
C(11)-C(16)	1.434(7)	N(9)-C(27)-C(28)	122.8(5)
C(12)-C(13)	1.360(7)	N(9)-C(27)-H(27A)	118.6
C(12)-H(12A)	0.9500	C(28)-C(27)-H(27A)	118.6
C(13)-C(14)	1.405(7)	C(27)-C(28)-C(29)	119.4(5)

C(13)-H(13A)	0.9500
C(14)-C(15)	1.343(7)
C(14)-C(19)	1.510(7)
C(15)-C(16)	1.406(7)
C(15)-H(15A)	0.9500
C(16)-C(17)	1.407(7)
C(17)-C(18)	1.358(8)
C(17)-H(17A)	0.9500
C(18)-H(18A)	0.9500
C(19)-H(19A)	0.9900
C(19)-H(19B)	0.9900
C(20)-C(21)	1.357(7)
C(20)-H(20A)	0.9500
C(21)-C(22)	1.439(7)
C(22)-C(23)	1.393(7)
C(23)-C(24)	1.356(8)
C(23)-H(23A)	0.9500
C(24)-C(25)	1.371(8)
C(24)-H(24A)	0.9500
C(25)-C(26)	1.396(7)
C(25)-H(25A)	0.9500
C(26)-H(26A)	0.9500
C(27)-C(28)	1.363(7)
C(27)-H(27A)	0.9500
C(28)-C(29)	1.377(8)
C(28)-H(28A)	0.9500
C(29)-C(30)	1.387(7)
C(29)-H(29A)	0.9500
C(30)-C(31)	1.382(7)
C(30)-H(30A)	0.9500
C(31)-C(32)	1.441(7)

C(27)-C(28)-H(28A)	120.3
C(29)-C(28)-H(28A)	120.3
C(28)-C(29)-C(30)	119.0(5)
C(28)-C(29)-H(29A)	120.5
C(30)-C(29)-H(29A)	120.5
C(31)-C(30)-C(29)	118.6(5)
C(31)-C(30)-H(30A)	120.7
C(29)-C(30)-H(30A)	120.7
N(9)-C(31)-C(30)	122.3(4)
N(9)-C(31)-C(32)	111.8(4)
C(30)-C(31)-C(32)	125.8(5)
N(10)-C(32)-C(33)	106.7(4)
N(10)-C(32)-C(31)	116.4(4)
C(33)-C(32)-C(31)	136.8(5)
N(12)-C(33)-C(32)	104.2(4)
N(12)-C(33)-H(33A)	127.9
C(32)-C(33)-H(33A)	127.9
N(12)-C(34)-C(35)	110.8(4)
N(12)-C(34)-H(34A)	109.5
C(35)-C(34)-H(34A)	109.5
N(12)-C(34)-H(34B)	109.5
C(35)-C(34)-H(34B)	109.5
H(34A)-C(34)-H(34B)	108.1
C(36)-C(35)-C(44)	119.8(5)
C(36)-C(35)-C(34)	120.6(5)
C(44)-C(35)-C(34)	119.5(5)
C(35)-C(36)-C(37)	121.4(5)
C(35)-C(36)-H(36A)	119.3
C(37)-C(36)-H(36A)	119.3
C(36)-C(37)-C(42)	120.7(5)
C(36)-C(37)-C(38)	122.5(5)

C(32)-C(33)	1.393(7)
C(33)-H(33A)	0.9500
C(34)-C(35)	1.508(7)
C(34)-H(34A)	0.9900
C(34)-H(34B)	0.9900
C(35)-C(36)	1.366(7)
C(35)-C(44)	1.387(7)
C(36)-C(37)	1.380(7)
C(36)-H(36A)	0.9500
C(37)-C(42)	1.420(7)
C(37)-C(38)	1.433(7)
C(38)-C(39)	1.373(7)
C(38)-H(38A)	0.9500
C(39)-C(40)	1.407(7)
C(39)-H(39A)	0.9500
C(40)-C(41)	1.355(7)
C(40)-C(45)	1.527(7)
C(41)-C(42)	1.404(7)
C(41)-H(41A)	0.9500
C(42)-C(43)	1.438(7)
C(43)-C(44)	1.380(7)
C(43)-H(43A)	0.9500
C(44)-H(44A)	0.9500
C(45)-H(45A)	0.9900
C(45)-H(45B)	0.9900
C(46)-C(47)	1.364(7)
C(46)-H(46A)	0.9500
C(47)-C(48)	1.443(7)
C(48)-C(49)	1.390(7)
C(49)-C(50)	1.361(7)
C(49)-H(49A)	0.9500

C(42)-C(37)-C(38)	116.8(5)
C(39)-C(38)-C(37)	121.3(5)
C(39)-C(38)-H(38A)	119.4
C(37)-C(38)-H(38A)	119.4
C(38)-C(39)-C(40)	120.3(5)
C(38)-C(39)-H(39A)	119.9
C(40)-C(39)-H(39A)	119.9
C(41)-C(40)-C(39)	120.0(5)
C(41)-C(40)-C(45)	122.2(5)
C(39)-C(40)-C(45)	117.8(5)
C(40)-C(41)-C(42)	121.2(5)
C(40)-C(41)-H(41A)	119.4
C(42)-C(41)-H(41A)	119.4
C(41)-C(42)-C(37)	120.4(5)
C(41)-C(42)-C(43)	122.7(5)
C(37)-C(42)-C(43)	116.9(5)
C(44)-C(43)-C(42)	120.1(5)
C(44)-C(43)-H(43A)	119.9
C(42)-C(43)-H(43A)	119.9
C(43)-C(44)-C(35)	121.0(5)
C(43)-C(44)-H(44A)	119.5
C(35)-C(44)-H(44A)	119.5
N(13)-C(45)-C(40)	110.7(4)
N(13)-C(45)-H(45A)	109.5
C(40)-C(45)-H(45A)	109.5
N(13)-C(45)-H(45B)	109.5
C(40)-C(45)-H(45B)	109.5
H(45A)-C(45)-H(45B)	108.1
C(47)-C(46)-N(13)	104.2(5)
C(47)-C(46)-H(46A)	127.9
N(13)-C(46)-H(46A)	127.9

C(50)-C(51)	1.393(8)
C(50)-H(50A)	0.9500
C(51)-C(52)	1.361(7)
C(51)-H(51A)	0.9500
C(52)-H(52A)	0.9500
C(53)-C(54)	1.384(7)
C(53)-H(53A)	0.9500
C(54)-C(55)	1.369(9)
C(54)-H(54A)	0.9500
C(55)-C(56)	1.353(8)
C(55)-H(55A)	0.9500
C(56)-C(57)	1.394(7)
C(56)-H(56A)	0.9500
C(57)-C(58)	1.418(7)
C(58)-C(59)	1.396(7)
C(59)-H(59A)	0.9500
C(60)-C(61)	1.484(7)
C(60)-H(60A)	0.9900
C(60)-H(60B)	0.9900
C(61)-C(62)	1.366(8)
C(61)-C(70)	1.383(8)
C(62)-C(63)	1.394(8)
C(62)-H(62A)	0.9500
C(63)-C(68)	1.392(7)
C(63)-C(64)	1.429(8)
C(64)-C(65)	1.367(9)
C(64)-H(64A)	0.9500
C(65)-C(66)	1.400(8)
C(65)-H(65A)	0.9500
C(66)-C(67)	1.350(7)
C(66)-C(71)	1.495(7)

C(46)-C(47)-N(15)	108.1(5)
C(46)-C(47)-C(48)	136.3(5)
N(15)-C(47)-C(48)	115.6(4)
N(16)-C(48)-C(49)	123.3(5)
N(16)-C(48)-C(47)	111.9(4)
C(49)-C(48)-C(47)	124.8(5)
C(50)-C(49)-C(48)	118.9(5)
C(50)-C(49)-H(49A)	120.5
C(48)-C(49)-H(49A)	120.5
C(49)-C(50)-C(51)	118.4(5)
C(49)-C(50)-H(50A)	120.8
C(51)-C(50)-H(50A)	120.8
C(52)-C(51)-C(50)	119.8(5)
C(52)-C(51)-H(51A)	120.1
C(50)-C(51)-H(51A)	120.1
N(16)-C(52)-C(51)	123.4(5)
N(16)-C(52)-H(52A)	118.3
C(51)-C(52)-H(52A)	118.3
N(17)-C(53)-C(54)	121.8(5)
N(17)-C(53)-H(53A)	119.1
C(54)-C(53)-H(53A)	119.1
C(55)-C(54)-C(53)	119.8(6)
C(55)-C(54)-H(54A)	120.1
C(53)-C(54)-H(54A)	120.1
C(56)-C(55)-C(54)	119.1(6)
C(56)-C(55)-H(55A)	120.5
C(54)-C(55)-H(55A)	120.5
C(55)-C(56)-C(57)	119.6(5)
C(55)-C(56)-H(56A)	120.2
C(57)-C(56)-H(56A)	120.2
N(17)-C(57)-C(56)	121.6(5)

C(67)-C(68)	1.423(7)	N(17)-C(57)-C(58)	112.7(4)
C(67)-H(67A)	0.9500	C(56)-C(57)-C(58)	125.6(5)
C(68)-C(69)	1.402(8)	N(18)-C(58)-C(59)	105.8(5)
C(69)-C(70)	1.355(8)	N(18)-C(58)-C(57)	116.8(4)
C(69)-H(69A)	0.9500	C(59)-C(58)-C(57)	137.2(5)
C(70)-H(70A)	0.9500	N(20)-C(59)-C(58)	104.6(5)
C(71)-H(71A)	0.9900	N(20)-C(59)-H(59A)	127.7
C(71)-H(71B)	0.9900	C(58)-C(59)-H(59A)	127.7
C(72)-C(73)	1.379(7)	N(20)-C(60)-C(61)	112.1(4)
C(72)-H(72A)	0.9500	N(20)-C(60)-H(60A)	109.2
C(73)-C(74)	1.448(8)	C(61)-C(60)-H(60A)	109.2
C(74)-C(75)	1.386(7)	N(20)-C(60)-H(60B)	109.2
C(75)-C(76)	1.351(8)	C(61)-C(60)-H(60B)	109.2
C(75)-H(75A)	0.9500	H(60A)-C(60)-H(60B)	107.9
C(76)-C(77)	1.393(8)	C(62)-C(61)-C(70)	117.3(5)
C(76)-H(76A)	0.9500	C(62)-C(61)-C(60)	121.5(5)
C(77)-C(78)	1.359(7)	C(70)-C(61)-C(60)	121.2(5)
C(77)-H(77A)	0.9500	C(61)-C(62)-C(63)	122.2(6)
C(78)-H(78A)	0.9500	C(61)-C(62)-H(62A)	118.9
B(1)-F(2B)	1.326(11)	C(63)-C(62)-H(62A)	118.9
B(1)-F(4A)	1.377(9)	C(68)-C(63)-C(62)	119.7(5)
B(1)-F(3A)	1.385(8)	C(68)-C(63)-C(64)	118.0(5)
B(1)-F(1)	1.395(7)	C(62)-C(63)-C(64)	122.3(6)
B(1)-F(2A)	1.409(9)	C(65)-C(64)-C(63)	120.5(6)
B(1)-F(3B)	1.416(10)	C(65)-C(64)-H(64A)	119.7
B(1)-F(4B)	1.423(11)	C(63)-C(64)-H(64A)	119.7
B(2)-F(8A)	1.263(15)	C(64)-C(65)-C(66)	121.4(6)
B(2)-F(8B)	1.30(5)	C(64)-C(65)-H(65A)	119.3
B(2)-F(6B)	1.342(16)	C(66)-C(65)-H(65A)	119.3
B(2)-F(7A)	1.377(18)	C(67)-C(66)-C(65)	118.4(5)
B(2)-F(5)	1.404(13)	C(67)-C(66)-C(71)	125.3(5)

B(2)-F(7B)	1.500(17)	C(65)-C(66)-C(71)	116.4(5)
B(2)-F(6A)	1.519(17)	C(66)-C(67)-C(68)	122.4(5)
B(3)-F(10)	1.355(9)	C(66)-C(67)-H(67A)	118.8
B(3)-F(9)	1.379(9)	C(68)-C(67)-H(67A)	118.8
B(3)-F(12)	1.379(9)	C(63)-C(68)-C(69)	117.7(5)
B(3)-F(11)	1.400(8)	C(63)-C(68)-C(67)	119.1(5)
B(4A)-B(4B)	0.66(3)	C(69)-C(68)-C(67)	123.2(5)
B(4A)-F(13)	1.307(11)	C(70)-C(69)-C(68)	120.8(6)
B(4A)-F(15A)	1.331(12)	C(70)-C(69)-H(69A)	119.6
B(4A)-F(14)	1.412(12)	C(68)-C(69)-H(69A)	119.6
B(4A)-F(16)	1.434(12)	C(69)-C(70)-C(61)	122.3(6)
B(4A)-F(15B)	1.92(3)	C(69)-C(70)-H(70A)	118.8
F(13)-B(4B)	1.43(3)	C(61)-C(70)-H(70A)	118.8
F(14)-B(4B)	1.22(3)	N(21)-C(71)-C(66)	113.8(4)
F(16)-B(4B)	1.32(3)	N(21)-C(71)-H(71A)	108.8
F(15B)-B(4B)	1.30(4)	C(66)-C(71)-H(71A)	108.8
N(10)-Fe(1)-N(18)	92.72(16)	N(21)-C(71)-H(71B)	108.8
N(10)-Fe(1)-N(2)	93.71(16)	C(66)-C(71)-H(71B)	108.8
N(18)-Fe(1)-N(2)	94.71(16)	H(71A)-C(71)-H(71B)	107.7
N(10)-Fe(1)-N(9)	81.31(16)	N(21)-C(72)-C(73)	105.4(5)
N(18)-Fe(1)-N(9)	172.27(16)	N(21)-C(72)-H(72A)	127.3
N(2)-Fe(1)-N(9)	90.58(16)	C(73)-C(72)-H(72A)	127.3
N(10)-Fe(1)-N(17)	89.23(16)	N(23)-C(73)-C(72)	107.4(5)
N(18)-Fe(1)-N(17)	81.32(17)	N(23)-C(73)-C(74)	116.3(5)
N(2)-Fe(1)-N(17)	175.18(17)	C(72)-C(73)-C(74)	136.0(5)
N(9)-Fe(1)-N(17)	93.64(16)	N(24)-C(74)-C(75)	122.0(5)
N(10)-Fe(1)-N(1)	174.47(16)	N(24)-C(74)-C(73)	112.4(5)
N(18)-Fe(1)-N(1)	90.59(16)	C(75)-C(74)-C(73)	125.6(5)
N(2)-Fe(1)-N(1)	81.60(16)	C(76)-C(75)-C(74)	119.1(6)
N(9)-Fe(1)-N(1)	95.76(16)	C(76)-C(75)-H(75A)	120.5
N(17)-Fe(1)-N(1)	95.65(16)	C(74)-C(75)-H(75A)	120.5

N(15)-Fe(2)-N(23)	94.53(17)	C(75)-C(76)-C(77)	119.1(6)
N(15)-Fe(2)-N(7)	94.81(16)	C(75)-C(76)-H(76A)	120.4
N(23)-Fe(2)-N(7)	94.96(16)	C(77)-C(76)-H(76A)	120.4
N(15)-Fe(2)-N(16)	81.23(17)	C(78)-C(77)-C(76)	117.9(6)
N(23)-Fe(2)-N(16)	90.36(16)	C(78)-C(77)-H(77A)	121.1
N(7)-Fe(2)-N(16)	173.62(16)	C(76)-C(77)-H(77A)	121.1
N(15)-Fe(2)-N(24)	174.32(17)	N(24)-C(78)-C(77)	124.6(6)
N(23)-Fe(2)-N(24)	81.15(17)	N(24)-C(78)-H(78A)	117.7
N(7)-Fe(2)-N(24)	89.26(16)	C(77)-C(78)-H(78A)	117.7
N(16)-Fe(2)-N(24)	95.04(16)	F(2B)-B(1)-F(4A)	118.2(9)
N(15)-Fe(2)-N(8)	90.06(16)	F(2B)-B(1)-F(3A)	83.4(7)
N(23)-Fe(2)-N(8)	174.63(17)	F(4A)-B(1)-F(3A)	114.9(6)
N(7)-Fe(2)-N(8)	81.85(16)	F(2B)-B(1)-F(1)	120.5(8)
N(16)-Fe(2)-N(8)	93.11(16)	F(4A)-B(1)-F(1)	108.6(6)
N(24)-Fe(2)-N(8)	94.45(17)	F(3A)-B(1)-F(1)	108.8(6)
C(1)-N(1)-C(5)	117.3(4)	F(2B)-B(1)-F(2A)	22.8(6)
C(1)-N(1)-Fe(1)	127.7(3)	F(4A)-B(1)-F(2A)	115.7(7)
C(5)-N(1)-Fe(1)	114.9(3)	F(3A)-B(1)-F(2A)	104.2(6)
N(3)-N(2)-C(6)	109.5(4)	F(1)-B(1)-F(2A)	104.1(6)
N(3)-N(2)-Fe(1)	135.1(3)	F(2B)-B(1)-F(3B)	106.3(8)
C(6)-N(2)-Fe(1)	115.4(3)	F(4A)-B(1)-F(3B)	87.3(6)
N(2)-N(3)-N(4)	105.8(4)	F(3A)-B(1)-F(3B)	29.5(5)
C(7)-N(4)-N(3)	112.0(4)	F(1)-B(1)-F(3B)	110.7(6)
C(7)-N(4)-C(8)	129.1(4)	F(2A)-B(1)-F(3B)	128.9(8)
N(3)-N(4)-C(8)	118.8(4)	F(2B)-B(1)-F(4B)	100.4(9)
C(20)-N(5)-N(6)	111.8(4)	F(4A)-B(1)-F(4B)	23.5(5)
C(20)-N(5)-C(19)	128.3(4)	F(3A)-B(1)-F(4B)	131.5(8)
N(6)-N(5)-C(19)	119.8(4)	F(1)-B(1)-F(4B)	110.2(7)
N(7)-N(6)-N(5)	105.6(4)	F(2A)-B(1)-F(4B)	93.3(7)
N(6)-N(7)-C(21)	109.8(4)	F(3B)-B(1)-F(4B)	107.8(8)
N(6)-N(7)-Fe(2)	134.9(3)	F(8A)-B(2)-F(8B)	32(2)

C(21)-N(7)-Fe(2)	115.1(3)	F(8A)-B(2)-F(6B)	132.6(13)
C(26)-N(8)-C(22)	118.2(4)	F(8B)-B(2)-F(6B)	114(3)
C(26)-N(8)-Fe(2)	128.3(3)	F(8A)-B(2)-F(7A)	128.1(14)
C(22)-N(8)-Fe(2)	113.4(3)	F(8B)-B(2)-F(7A)	103(3)
C(27)-N(9)-C(31)	117.7(4)	F(6B)-B(2)-F(7A)	76.7(12)
C(27)-N(9)-Fe(1)	126.7(4)	F(8A)-B(2)-F(5)	102.9(12)
C(31)-N(9)-Fe(1)	115.6(3)	F(8B)-B(2)-F(5)	134(3)
N(11)-N(10)-C(32)	111.1(4)	F(6B)-B(2)-F(5)	107.0(12)
N(11)-N(10)-Fe(1)	134.1(3)	F(7A)-B(2)-F(5)	106.2(12)
C(32)-N(10)-Fe(1)	114.8(3)	F(8A)-B(2)-F(7B)	108.5(11)
N(10)-N(11)-N(12)	104.5(4)	F(8B)-B(2)-F(7B)	92(3)
C(33)-N(12)-N(11)	113.5(4)	F(6B)-B(2)-F(7B)	101.5(13)
C(33)-N(12)-C(34)	128.2(4)	F(7A)-B(2)-F(7B)	24.8(7)
N(11)-N(12)-C(34)	118.3(4)	F(5)-B(2)-F(7B)	100.2(9)
N(14)-N(13)-C(46)	112.2(4)	F(8A)-B(2)-F(6A)	103.0(10)
N(14)-N(13)-C(45)	121.1(4)	F(8B)-B(2)-F(6A)	90(2)
C(46)-N(13)-C(45)	126.7(5)	F(6B)-B(2)-F(6A)	29.8(7)
N(15)-N(14)-N(13)	105.3(4)	F(7A)-B(2)-F(6A)	98.9(12)
N(14)-N(15)-C(47)	110.1(4)	F(5)-B(2)-F(6A)	119.3(11)
N(14)-N(15)-Fe(2)	134.4(3)	F(7B)-B(2)-F(6A)	121.4(12)
C(47)-N(15)-Fe(2)	115.4(3)	F(10)-B(3)-F(9)	109.3(6)
C(52)-N(16)-C(48)	116.1(4)	F(10)-B(3)-F(12)	110.0(6)
C(52)-N(16)-Fe(2)	128.0(4)	F(9)-B(3)-F(12)	111.3(7)
C(48)-N(16)-Fe(2)	115.9(3)	F(10)-B(3)-F(11)	110.4(7)
C(53)-N(17)-C(57)	118.1(4)	F(9)-B(3)-F(11)	108.7(6)
C(53)-N(17)-Fe(1)	127.0(4)	F(12)-B(3)-F(11)	107.1(6)
C(57)-N(17)-Fe(1)	114.7(3)	B(4B)-B(4A)-F(13)	86(3)
N(19)-N(18)-C(58)	111.6(4)	B(4B)-B(4A)-F(15A)	166(4)
N(19)-N(18)-Fe(1)	134.5(3)	F(13)-B(4A)-F(15A)	106.8(10)
C(58)-N(18)-Fe(1)	113.9(3)	B(4B)-B(4A)-F(14)	59(3)
N(18)-N(19)-N(20)	105.2(4)	F(13)-B(4A)-F(14)	116.5(9)

C(59)-N(20)-N(19)	112.7(4)
C(59)-N(20)-C(60)	129.0(5)
N(19)-N(20)-C(60)	118.3(4)
C(72)-N(21)-N(22)	111.8(4)
C(72)-N(21)-C(71)	129.5(5)
N(22)-N(21)-C(71)	118.7(4)
N(23)-N(22)-N(21)	105.1(4)
N(22)-N(23)-C(73)	110.3(4)
N(22)-N(23)-Fe(2)	134.0(3)
C(73)-N(23)-Fe(2)	115.5(4)
C(78)-N(24)-C(74)	117.3(5)
C(78)-N(24)-Fe(2)	128.2(4)
C(74)-N(24)-Fe(2)	114.5(3)
N(1)-C(1)-C(2)	123.2(5)
N(1)-C(1)-H(1A)	118.4
C(2)-C(1)-H(1A)	118.4
C(1)-C(2)-C(3)	118.5(5)
C(1)-C(2)-H(2A)	120.8
C(3)-C(2)-H(2A)	120.8
C(4)-C(3)-C(2)	118.9(5)
C(4)-C(3)-H(3A)	120.5
C(2)-C(3)-H(3A)	120.5
C(3)-C(4)-C(5)	119.3(5)
C(3)-C(4)-H(4A)	120.3
F(15A)-B(4A)-F(14)	115.6(9)
B(4B)-B(4A)-F(16)	67(3)
F(13)-B(4A)-F(16)	110.9(8)
F(15A)-B(4A)-F(16)	104.1(9)
F(14)-B(4A)-F(16)	102.1(8)
B(4B)-B(4A)-F(15B)	18(3)
F(13)-B(4A)-F(15B)	68.5(9)
F(15A)-B(4A)-F(15B)	172.6(12)
F(14)-B(4A)-F(15B)	71.8(10)
F(16)-B(4A)-F(15B)	73.2(10)
B(4A)-F(13)-B(4B)	27.7(14)
B(4B)-F(14)-B(4A)	28.0(17)
B(4B)-F(16)-B(4A)	27.5(15)
B(4B)-F(15B)-B(4A)	9.0(18)
B(4A)-B(4B)-F(14)	93(4)
B(4A)-B(4B)-F(15B)	153(5)
F(14)-B(4B)-F(15B)	105(3)
B(4A)-B(4B)-F(16)	86(4)
F(14)-B(4B)-F(16)	121(3)
F(15B)-B(4B)-F(16)	102(3)
B(4A)-B(4B)-F(13)	66(3)
F(14)-B(4B)-F(13)	122(3)
F(15B)-B(4B)-F(13)	87(2)
F(16)-B(4B)-F(13)	111(3)

Table C1.4: Torsion angles [°] for ap35a

N(10)-Fe(1)-N(1)-C(1)	-150.9(15)
N(18)-Fe(1)-N(1)-C(1)	82.4(4)
N(2)-Fe(1)-N(1)-C(1)	177.1(4)
N(9)-Fe(1)-N(1)-C(1)	-93.2(4)
N(17)-Fe(1)-N(1)-C(1)	1.1(4)
N(10)-Fe(1)-N(1)-C(5)	33.1(18)
N(18)-Fe(1)-N(1)-C(5)	-93.7(3)
N(2)-Fe(1)-N(1)-C(5)	1.0(3)
N(9)-Fe(1)-N(1)-C(5)	90.7(3)
N(17)-Fe(1)-N(1)-C(5)	-175.0(3)
N(10)-Fe(1)-N(2)-N(3)	0.7(5)
N(18)-Fe(1)-N(2)-N(3)	-92.3(4)
N(9)-Fe(1)-N(2)-N(3)	82.0(4)
N(17)-Fe(1)-N(2)-N(3)	-126.8(18)
N(1)-Fe(1)-N(2)-N(3)	177.8(5)
N(10)-Fe(1)-N(2)-C(6)	-176.2(3)
N(18)-Fe(1)-N(2)-C(6)	90.8(4)
N(9)-Fe(1)-N(2)-C(6)	-94.8(4)
N(17)-Fe(1)-N(2)-C(6)	56(2)
N(1)-Fe(1)-N(2)-C(6)	0.9(3)
C(6)-N(2)-N(3)-N(4)	-0.4(5)
Fe(1)-N(2)-N(3)-N(4)	-177.4(3)
N(2)-N(3)-N(4)-C(7)	0.2(5)
N(2)-N(3)-N(4)-C(8)	-177.1(4)
C(20)-N(5)-N(6)-N(7)	0.9(5)
C(19)-N(5)-N(6)-N(7)	-174.7(4)
N(5)-N(6)-N(7)-C(21)	-1.4(5)
N(5)-N(6)-N(7)-Fe(2)	-176.2(3)
N(15)-Fe(2)-N(7)-N(6)	-94.6(4)
N(23)-Fe(2)-N(7)-N(6)	0.4(4)

N(16)-Fe(2)-N(7)-N(6)	-146.0(13)
N(24)-Fe(2)-N(7)-N(6)	81.4(4)
N(8)-Fe(2)-N(7)-N(6)	176.0(4)
N(15)-Fe(2)-N(7)-C(21)	90.8(3)
N(23)-Fe(2)-N(7)-C(21)	-174.2(3)
N(16)-Fe(2)-N(7)-C(21)	39.4(16)
N(24)-Fe(2)-N(7)-C(21)	-93.2(3)
N(8)-Fe(2)-N(7)-C(21)	1.4(3)
N(15)-Fe(2)-N(8)-C(26)	83.1(4)
N(23)-Fe(2)-N(8)-C(26)	-128.3(16)
N(7)-Fe(2)-N(8)-C(26)	177.9(4)
N(16)-Fe(2)-N(8)-C(26)	1.8(4)
N(24)-Fe(2)-N(8)-C(26)	-93.5(4)
N(15)-Fe(2)-N(8)-C(22)	-94.2(3)
N(23)-Fe(2)-N(8)-C(22)	54.4(18)
N(7)-Fe(2)-N(8)-C(22)	0.6(3)
N(16)-Fe(2)-N(8)-C(22)	-175.5(3)
N(24)-Fe(2)-N(8)-C(22)	89.2(3)
N(10)-Fe(1)-N(9)-C(27)	179.6(4)
N(18)-Fe(1)-N(9)-C(27)	-140.8(11)
N(2)-Fe(1)-N(9)-C(27)	85.9(4)
N(17)-Fe(1)-N(9)-C(27)	-91.8(4)
N(1)-Fe(1)-N(9)-C(27)	4.3(4)
N(10)-Fe(1)-N(9)-C(31)	1.0(3)
N(18)-Fe(1)-N(9)-C(31)	40.7(13)
N(2)-Fe(1)-N(9)-C(31)	-92.6(3)
N(17)-Fe(1)-N(9)-C(31)	89.7(3)
N(1)-Fe(1)-N(9)-C(31)	-174.2(3)
N(18)-Fe(1)-N(10)-N(11)	2.9(4)
N(2)-Fe(1)-N(10)-N(11)	-92.0(4)
N(9)-Fe(1)-N(10)-N(11)	177.9(4)

N(17)-Fe(1)-N(10)-N(11)	84.1(4)
N(1)-Fe(1)-N(10)-N(11)	-123.8(16)
N(18)-Fe(1)-N(10)-C(32)	-176.0(3)
N(2)-Fe(1)-N(10)-C(32)	89.0(3)
N(9)-Fe(1)-N(10)-C(32)	-1.0(3)
N(17)-Fe(1)-N(10)-C(32)	-94.8(3)
N(1)-Fe(1)-N(10)-C(32)	57.3(18)
C(32)-N(10)-N(11)-N(12)	-0.3(5)
Fe(1)-N(10)-N(11)-N(12)	-179.2(3)
N(10)-N(11)-N(12)-C(33)	0.0(5)
N(10)-N(11)-N(12)-C(34)	-176.4(4)
C(46)-N(13)-N(14)-N(15)	-1.1(5)
C(45)-N(13)-N(14)-N(15)	-178.8(4)
N(13)-N(14)-N(15)-C(47)	0.3(5)
N(13)-N(14)-N(15)-Fe(2)	-177.5(3)
N(23)-Fe(2)-N(15)-N(14)	-91.1(4)
N(7)-Fe(2)-N(15)-N(14)	4.3(4)
N(16)-Fe(2)-N(15)-N(14)	179.2(4)
N(24)-Fe(2)-N(15)-N(14)	-131.4(16)
N(8)-Fe(2)-N(15)-N(14)	86.1(4)
N(23)-Fe(2)-N(15)-C(47)	91.2(3)
N(7)-Fe(2)-N(15)-C(47)	-173.4(3)
N(16)-Fe(2)-N(15)-C(47)	1.5(3)
N(24)-Fe(2)-N(15)-C(47)	50.9(18)
N(8)-Fe(2)-N(15)-C(47)	-91.6(3)
N(15)-Fe(2)-N(16)-C(52)	178.3(4)
N(23)-Fe(2)-N(16)-C(52)	83.7(4)
N(7)-Fe(2)-N(16)-C(52)	-129.7(14)
N(24)-Fe(2)-N(16)-C(52)	2.6(4)
N(8)-Fe(2)-N(16)-C(52)	-92.2(4)
N(15)-Fe(2)-N(16)-C(48)	-0.6(3)

N(23)-Fe(2)-N(16)-C(48)	-95.1(3)
N(7)-Fe(2)-N(16)-C(48)	51.4(16)
N(24)-Fe(2)-N(16)-C(48)	-176.3(3)
N(8)-Fe(2)-N(16)-C(48)	89.0(3)
N(10)-Fe(1)-N(17)-C(53)	88.2(4)
N(18)-Fe(1)-N(17)-C(53)	-178.9(4)
N(2)-Fe(1)-N(17)-C(53)	-144.2(18)
N(9)-Fe(1)-N(17)-C(53)	7.0(4)
N(1)-Fe(1)-N(17)-C(53)	-89.2(4)
N(10)-Fe(1)-N(17)-C(57)	-86.2(4)
N(18)-Fe(1)-N(17)-C(57)	6.7(3)
N(2)-Fe(1)-N(17)-C(57)	41(2)
N(9)-Fe(1)-N(17)-C(57)	-167.4(3)
N(1)-Fe(1)-N(17)-C(57)	96.4(3)
N(10)-Fe(1)-N(18)-N(19)	-96.6(4)
N(2)-Fe(1)-N(18)-N(19)	-2.7(4)
N(9)-Fe(1)-N(18)-N(19)	-135.8(11)
N(17)-Fe(1)-N(18)-N(19)	174.6(4)
N(1)-Fe(1)-N(18)-N(19)	78.9(4)
N(10)-Fe(1)-N(18)-C(58)	83.1(3)
N(2)-Fe(1)-N(18)-C(58)	177.1(3)
N(9)-Fe(1)-N(18)-C(58)	44.0(13)
N(17)-Fe(1)-N(18)-C(58)	-5.7(3)
N(1)-Fe(1)-N(18)-C(58)	-101.3(3)
C(58)-N(18)-N(19)-N(20)	-0.2(5)
Fe(1)-N(18)-N(19)-N(20)	179.6(3)
N(18)-N(19)-N(20)-C(59)	0.0(5)
N(18)-N(19)-N(20)-C(60)	-179.9(4)
C(72)-N(21)-N(22)-N(23)	-0.8(5)
C(71)-N(21)-N(22)-N(23)	178.4(4)
N(21)-N(22)-N(23)-C(73)	0.7(5)

N(21)-N(22)-N(23)-Fe(2)	-175.1(3)
N(15)-Fe(2)-N(23)-N(22)	-2.1(4)
N(7)-Fe(2)-N(23)-N(22)	-97.4(4)
N(16)-Fe(2)-N(23)-N(22)	79.1(4)
N(24)-Fe(2)-N(23)-N(22)	174.1(4)
N(8)-Fe(2)-N(23)-N(22)	-150.7(15)
N(15)-Fe(2)-N(23)-C(73)	-177.8(3)
N(7)-Fe(2)-N(23)-C(73)	87.0(4)
N(16)-Fe(2)-N(23)-C(73)	-96.5(4)
N(24)-Fe(2)-N(23)-C(73)	-1.5(3)
N(8)-Fe(2)-N(23)-C(73)	33.7(18)
N(15)-Fe(2)-N(24)-C(78)	-137.2(16)
N(23)-Fe(2)-N(24)-C(78)	-178.0(4)
N(7)-Fe(2)-N(24)-C(78)	86.9(4)
N(16)-Fe(2)-N(24)-C(78)	-88.4(4)
N(8)-Fe(2)-N(24)-C(78)	5.1(4)
N(15)-Fe(2)-N(24)-C(74)	42.9(18)
N(23)-Fe(2)-N(24)-C(74)	2.2(3)
N(7)-Fe(2)-N(24)-C(74)	-93.0(3)
N(16)-Fe(2)-N(24)-C(74)	91.7(3)
N(8)-Fe(2)-N(24)-C(74)	-174.7(3)
C(5)-N(1)-C(1)-C(2)	1.0(7)
Fe(1)-N(1)-C(1)-C(2)	-175.0(4)
N(1)-C(1)-C(2)-C(3)	-2.2(8)
C(1)-C(2)-C(3)-C(4)	3.3(8)
C(2)-C(3)-C(4)-C(5)	-3.2(8)
C(1)-N(1)-C(5)-C(4)	-0.9(7)
Fe(1)-N(1)-C(5)-C(4)	175.6(4)
C(1)-N(1)-C(5)-C(6)	-179.0(4)
Fe(1)-N(1)-C(5)-C(6)	-2.5(5)
C(3)-C(4)-C(5)-N(1)	2.1(8)

C(3)-C(4)-C(5)-C(6)	179.9(5)
N(3)-N(2)-C(6)-C(7)	0.4(6)
Fe(1)-N(2)-C(6)-C(7)	178.1(3)
N(3)-N(2)-C(6)-C(5)	179.8(4)
Fe(1)-N(2)-C(6)-C(5)	-2.5(5)
N(1)-C(5)-C(6)-N(2)	3.3(6)
C(4)-C(5)-C(6)-N(2)	-174.8(5)
N(1)-C(5)-C(6)-C(7)	-177.5(5)
C(4)-C(5)-C(6)-C(7)	4.4(9)
N(3)-N(4)-C(7)-C(6)	0.1(5)
C(8)-N(4)-C(7)-C(6)	177.0(5)
N(2)-C(6)-C(7)-N(4)	-0.3(5)
C(5)-C(6)-C(7)-N(4)	-179.5(5)
C(7)-N(4)-C(8)-C(9)	-93.0(6)
N(3)-N(4)-C(8)-C(9)	83.8(6)
N(4)-C(8)-C(9)-C(10)	103.4(6)
N(4)-C(8)-C(9)-C(18)	-77.3(6)
C(18)-C(9)-C(10)-C(11)	1.8(8)
C(8)-C(9)-C(10)-C(11)	-178.9(5)
C(9)-C(10)-C(11)-C(12)	179.1(5)
C(9)-C(10)-C(11)-C(16)	-2.5(8)
C(10)-C(11)-C(12)-C(13)	178.7(5)
C(16)-C(11)-C(12)-C(13)	0.3(8)
C(11)-C(12)-C(13)-C(14)	-0.8(8)
C(12)-C(13)-C(14)-C(15)	-0.4(8)
C(12)-C(13)-C(14)-C(19)	-178.6(5)
C(13)-C(14)-C(15)-C(16)	2.1(9)
C(19)-C(14)-C(15)-C(16)	-179.8(5)
C(14)-C(15)-C(16)-C(17)	178.7(6)
C(14)-C(15)-C(16)-C(11)	-2.5(8)
C(12)-C(11)-C(16)-C(15)	1.3(8)

C(10)-C(11)-C(16)-C(15)	-177.2(5)
C(12)-C(11)-C(16)-C(17)	-179.8(5)
C(10)-C(11)-C(16)-C(17)	1.7(8)
C(15)-C(16)-C(17)-C(18)	178.5(6)
C(11)-C(16)-C(17)-C(18)	-0.3(9)
C(16)-C(17)-C(18)-C(9)	-0.4(11)
C(10)-C(9)-C(18)-C(17)	-0.3(9)
C(8)-C(9)-C(18)-C(17)	-179.7(6)
C(20)-N(5)-C(19)-C(14)	-89.0(6)
N(6)-N(5)-C(19)-C(14)	85.8(5)
C(15)-C(14)-C(19)-N(5)	-58.3(7)
C(13)-C(14)-C(19)-N(5)	119.8(5)
N(6)-N(5)-C(20)-C(21)	0.0(6)
C(19)-N(5)-C(20)-C(21)	175.1(4)
N(5)-C(20)-C(21)-N(7)	-0.8(5)
N(5)-C(20)-C(21)-C(22)	179.9(5)
N(6)-N(7)-C(21)-C(20)	1.4(5)
Fe(2)-N(7)-C(21)-C(20)	177.3(3)
N(6)-N(7)-C(21)-C(22)	-179.2(4)
Fe(2)-N(7)-C(21)-C(22)	-3.2(5)
C(26)-N(8)-C(22)-C(23)	0.2(7)
Fe(2)-N(8)-C(22)-C(23)	177.8(4)
C(26)-N(8)-C(22)-C(21)	180.0(4)
Fe(2)-N(8)-C(22)-C(21)	-2.4(5)
C(20)-C(21)-C(22)-N(8)	-177.1(5)
N(7)-C(21)-C(22)-N(8)	3.7(6)
C(20)-C(21)-C(22)-C(23)	2.7(10)
N(7)-C(21)-C(22)-C(23)	-176.6(5)
N(8)-C(22)-C(23)-C(24)	0.4(8)
C(21)-C(22)-C(23)-C(24)	-179.3(5)
C(22)-C(23)-C(24)-C(25)	-0.5(9)

C(23)-C(24)-C(25)-C(26)	0.0(9)
C(22)-N(8)-C(26)-C(25)	-0.8(8)
Fe(2)-N(8)-C(26)-C(25)	-178.0(4)
C(24)-C(25)-C(26)-N(8)	0.7(9)
C(31)-N(9)-C(27)-C(28)	-3.3(7)
Fe(1)-N(9)-C(27)-C(28)	178.2(4)
N(9)-C(27)-C(28)-C(29)	3.9(8)
C(27)-C(28)-C(29)-C(30)	-3.3(8)
C(28)-C(29)-C(30)-C(31)	2.2(8)
C(27)-N(9)-C(31)-C(30)	2.1(7)
Fe(1)-N(9)-C(31)-C(30)	-179.2(4)
C(27)-N(9)-C(31)-C(32)	-179.5(4)
Fe(1)-N(9)-C(31)-C(32)	-0.9(5)
C(29)-C(30)-C(31)-N(9)	-1.7(8)
C(29)-C(30)-C(31)-C(32)	-179.8(5)
N(11)-N(10)-C(32)-C(33)	0.5(5)
Fe(1)-N(10)-C(32)-C(33)	179.6(3)
N(11)-N(10)-C(32)-C(31)	-178.4(4)
Fe(1)-N(10)-C(32)-C(31)	0.8(5)
N(9)-C(31)-C(32)-N(10)	0.1(6)
C(30)-C(31)-C(32)-N(10)	178.3(4)
N(9)-C(31)-C(32)-C(33)	-178.3(5)
C(30)-C(31)-C(32)-C(33)	-0.1(9)
N(11)-N(12)-C(33)-C(32)	0.3(5)
C(34)-N(12)-C(33)-C(32)	176.2(4)
N(10)-C(32)-C(33)-N(12)	-0.5(5)
C(31)-C(32)-C(33)-N(12)	178.0(5)
C(33)-N(12)-C(34)-C(35)	-99.0(6)
N(11)-N(12)-C(34)-C(35)	76.8(5)
N(12)-C(34)-C(35)-C(36)	90.1(5)
N(12)-C(34)-C(35)-C(44)	-86.1(6)

C(44)-C(35)-C(36)-C(37)	0.1(7)
C(34)-C(35)-C(36)-C(37)	-176.2(4)
C(35)-C(36)-C(37)-C(42)	0.0(7)
C(35)-C(36)-C(37)-C(38)	177.4(5)
C(36)-C(37)-C(38)-C(39)	-176.4(5)
C(42)-C(37)-C(38)-C(39)	1.1(7)
C(37)-C(38)-C(39)-C(40)	-1.4(8)
C(38)-C(39)-C(40)-C(41)	0.4(8)
C(38)-C(39)-C(40)-C(45)	178.6(5)
C(39)-C(40)-C(41)-C(42)	1.0(8)
C(45)-C(40)-C(41)-C(42)	-177.1(5)
C(40)-C(41)-C(42)-C(37)	-1.4(7)
C(40)-C(41)-C(42)-C(43)	178.0(5)
C(36)-C(37)-C(42)-C(41)	177.8(4)
C(38)-C(37)-C(42)-C(41)	0.3(7)
C(36)-C(37)-C(42)-C(43)	-1.6(7)
C(38)-C(37)-C(42)-C(43)	-179.1(4)
C(41)-C(42)-C(43)-C(44)	-176.3(5)
C(37)-C(42)-C(43)-C(44)	3.2(7)
C(42)-C(43)-C(44)-C(35)	-3.2(8)
C(36)-C(35)-C(44)-C(43)	1.5(8)
C(34)-C(35)-C(44)-C(43)	177.8(5)
N(14)-N(13)-C(45)-C(40)	95.0(6)
C(46)-N(13)-C(45)-C(40)	-82.3(6)
C(41)-C(40)-C(45)-N(13)	-51.0(7)
C(39)-C(40)-C(45)-N(13)	130.9(5)
N(14)-N(13)-C(46)-C(47)	1.5(5)
C(45)-N(13)-C(46)-C(47)	179.1(5)
N(13)-C(46)-C(47)-N(15)	-1.2(5)
N(13)-C(46)-C(47)-C(48)	-179.8(6)
N(14)-N(15)-C(47)-C(46)	0.6(6)

Fe(2)-N(15)-C(47)-C(46)	178.9(3)
N(14)-N(15)-C(47)-C(48)	179.5(4)
Fe(2)-N(15)-C(47)-C(48)	-2.2(5)
C(52)-N(16)-C(48)-C(49)	-0.1(7)
Fe(2)-N(16)-C(48)-C(49)	178.8(4)
C(52)-N(16)-C(48)-C(47)	-179.4(4)
Fe(2)-N(16)-C(48)-C(47)	-0.4(5)
C(46)-C(47)-C(48)-N(16)	-179.8(6)
N(15)-C(47)-C(48)-N(16)	1.7(6)
C(46)-C(47)-C(48)-C(49)	0.9(10)
N(15)-C(47)-C(48)-C(49)	-177.6(5)
N(16)-C(48)-C(49)-C(50)	0.2(8)
C(47)-C(48)-C(49)-C(50)	179.3(5)
C(48)-C(49)-C(50)-C(51)	0.4(8)
C(49)-C(50)-C(51)-C(52)	-1.0(9)
C(48)-N(16)-C(52)-C(51)	-0.5(7)
Fe(2)-N(16)-C(52)-C(51)	-179.3(4)
C(50)-C(51)-C(52)-N(16)	1.0(9)
C(57)-N(17)-C(53)-C(54)	0.6(8)
Fe(1)-N(17)-C(53)-C(54)	-173.6(4)
N(17)-C(53)-C(54)-C(55)	-0.6(9)
C(53)-C(54)-C(55)-C(56)	1.3(10)
C(54)-C(55)-C(56)-C(57)	-2.0(9)
C(53)-N(17)-C(57)-C(56)	-1.3(7)
Fe(1)-N(17)-C(57)-C(56)	173.6(4)
C(53)-N(17)-C(57)-C(58)	178.9(4)
Fe(1)-N(17)-C(57)-C(58)	-6.2(5)
C(55)-C(56)-C(57)-N(17)	2.0(8)
C(55)-C(56)-C(57)-C(58)	-178.2(5)
N(19)-N(18)-C(58)-C(59)	0.3(5)
Fe(1)-N(18)-C(58)-C(59)	-179.5(3)

N(19)-N(18)-C(58)-C(57)	-176.1(4)
Fe(1)-N(18)-C(58)-C(57)	4.1(6)
N(17)-C(57)-C(58)-N(18)	1.5(6)
C(56)-C(57)-C(58)-N(18)	-178.3(5)
N(17)-C(57)-C(58)-C(59)	-173.4(6)
C(56)-C(57)-C(58)-C(59)	6.8(10)
N(19)-N(20)-C(59)-C(58)	0.1(6)
C(60)-N(20)-C(59)-C(58)	-179.9(5)
N(18)-C(58)-C(59)-N(20)	-0.2(5)
C(57)-C(58)-C(59)-N(20)	175.0(6)
C(59)-N(20)-C(60)-C(61)	-103.0(6)
N(19)-N(20)-C(60)-C(61)	76.9(6)
N(20)-C(60)-C(61)-C(62)	58.4(7)
N(20)-C(60)-C(61)-C(70)	-124.6(6)
C(70)-C(61)-C(62)-C(63)	1.1(9)
C(60)-C(61)-C(62)-C(63)	178.1(5)
C(61)-C(62)-C(63)-C(68)	-2.6(10)
C(61)-C(62)-C(63)-C(64)	179.2(7)
C(68)-C(63)-C(64)-C(65)	-4.7(12)
C(62)-C(63)-C(64)-C(65)	173.6(7)
C(63)-C(64)-C(65)-C(66)	3.3(13)
C(64)-C(65)-C(66)-C(67)	0.7(11)
C(64)-C(65)-C(66)-C(71)	-179.5(7)
C(65)-C(66)-C(67)-C(68)	-3.3(9)
C(71)-C(66)-C(67)-C(68)	177.0(5)
C(62)-C(63)-C(68)-C(69)	2.7(9)
C(64)-C(63)-C(68)-C(69)	-178.9(7)
C(62)-C(63)-C(68)-C(67)	-176.1(5)
C(64)-C(63)-C(68)-C(67)	2.2(9)
C(66)-C(67)-C(68)-C(63)	1.8(8)
C(66)-C(67)-C(68)-C(69)	-177.0(6)

C(63)-C(68)-C(69)-C(70)	-1.5(10)
C(67)-C(68)-C(69)-C(70)	177.3(6)
C(68)-C(69)-C(70)-C(61)	0.1(11)
C(62)-C(61)-C(70)-C(69)	0.2(10)
C(60)-C(61)-C(70)-C(69)	-176.9(6)
C(72)-N(21)-C(71)-C(66)	-98.3(6)
N(22)-N(21)-C(71)-C(66)	82.7(6)
C(67)-C(66)-C(71)-N(21)	-5.6(8)
C(65)-C(66)-C(71)-N(21)	174.7(6)
N(22)-N(21)-C(72)-C(73)	0.6(6)
C(71)-N(21)-C(72)-C(73)	-178.5(5)
N(22)-N(23)-C(73)-C(72)	-0.4(5)
Fe(2)-N(23)-C(73)-C(72)	176.2(3)
N(22)-N(23)-C(73)-C(74)	-176.0(4)
Fe(2)-N(23)-C(73)-C(74)	0.6(6)
N(21)-C(72)-C(73)-N(23)	-0.1(6)
N(21)-C(72)-C(73)-C(74)	174.2(6)
C(78)-N(24)-C(74)-C(75)	-2.1(7)
Fe(2)-N(24)-C(74)-C(75)	177.8(4)
C(78)-N(24)-C(74)-C(73)	177.8(4)
Fe(2)-N(24)-C(74)-C(73)	-2.3(5)
N(23)-C(73)-C(74)-N(24)	1.2(6)
C(72)-C(73)-C(74)-N(24)	-172.8(6)
N(23)-C(73)-C(74)-C(75)	-179.0(5)
C(72)-C(73)-C(74)-C(75)	7.1(10)
N(24)-C(74)-C(75)-C(76)	1.8(8)
C(73)-C(74)-C(75)-C(76)	-178.0(5)
C(74)-C(75)-C(76)-C(77)	0.0(8)
C(75)-C(76)-C(77)-C(78)	-1.4(9)
C(74)-N(24)-C(78)-C(77)	0.6(8)
Fe(2)-N(24)-C(78)-C(77)	-179.3(4)

C(76)-C(77)-C(78)-N(24)	1.2(9)
F(15A)-B(4A)-F(13)-B(4B)	176(4)
F(14)-B(4A)-F(13)-B(4B)	-53(3)
F(16)-B(4A)-F(13)-B(4B)	63(3)
F(15B)-B(4A)-F(13)-B(4B)	2(4)
F(13)-B(4A)-F(14)-B(4B)	68(4)
F(15A)-B(4A)-F(14)-B(4B)	-166(4)
F(16)-B(4A)-F(14)-B(4B)	-53(4)
F(15B)-B(4A)-F(14)-B(4B)	14(4)
F(13)-B(4A)-F(16)-B(4B)	-76(4)
F(15A)-B(4A)-F(16)-B(4B)	169(4)
F(14)-B(4A)-F(16)-B(4B)	49(4)
F(15B)-B(4A)-F(16)-B(4B)	-18(4)
F(13)-B(4A)-F(15B)-B(4B)	-173(12)
F(15A)-B(4A)-F(15B)-B(4B)	135(16)
F(14)-B(4A)-F(15B)-B(4B)	-43(11)
F(16)-B(4A)-F(15B)-B(4B)	66(11)
F(13)-B(4A)-B(4B)-F(14)	-124.0(19)
F(15A)-B(4A)-B(4B)-F(14)	72(17)
F(16)-B(4A)-B(4B)-F(14)	121(3)
F(15B)-B(4A)-B(4B)-F(14)	-131(12)
F(13)-B(4A)-B(4B)-F(15B)	7(11)
F(15A)-B(4A)-B(4B)-F(15B)	-157(8)
F(14)-B(4A)-B(4B)-F(15B)	131(12)
F(16)-B(4A)-B(4B)-F(15B)	-108(11)
F(13)-B(4A)-B(4B)-F(16)	114.7(14)
F(15A)-B(4A)-B(4B)-F(16)	-49(17)
F(14)-B(4A)-B(4B)-F(16)	-121(3)
F(15B)-B(4A)-B(4B)-F(16)	108(11)
F(15A)-B(4A)-B(4B)-F(13)	-164(16)
F(14)-B(4A)-B(4B)-F(13)	124.0(19)

F(16)-B(4A)-B(4B)-F(13)	-114.7(14)
F(15B)-B(4A)-B(4B)-F(13)	-7(11)
B(4A)-F(14)-B(4B)-F(15B)	-159(6)
B(4A)-F(14)-B(4B)-F(16)	87(5)
B(4A)-F(14)-B(4B)-F(13)	-63(4)
B(4A)-F(15B)-B(4B)-F(14)	129(13)
B(4A)-F(15B)-B(4B)-F(16)	-104(12)
B(4A)-F(15B)-B(4B)-F(13)	6(10)
B(4A)-F(16)-B(4B)-F(14)	-91(5)
B(4A)-F(16)-B(4B)-F(15B)	154(5)
B(4A)-F(16)-B(4B)-F(13)	63(3)
B(4A)-F(13)-B(4B)-F(14)	77(4)
B(4A)-F(13)-B(4B)-F(15B)	-177(5)
B(4A)-F(13)-B(4B)-F(16)	-75(4)

***Note**:* Symmetry transformations were used to generate equivalent atoms.

Table C1.5: Hydrogen coordinates (x 10^4) and isotropic displacement parameters (Å^2 x 10^3) for ap35a.

	x	**y**	**z**	**U(eq)**
H(1A)	610	6538	3783	60
H(2A)	778	5376	3407	66
H(3A)	1245	4979	3774	62
H(4A)	1505	5664	4553	61
H(7A)	1766	6705	5422	55
H(8A)	1793	8586	6330	62
H(8B)	1996	7853	6222	62
H(10A)	2120	6606	6818	59
H(12A)	2281	5382	7490	65
H(13A)	2249	4624	8218	57
H(15A)	1627	6198	8272	66
H(17A)	1447	7365	7567	84

H(18A)	1476	8116	6836	82
H(19A)	1734	4563	8718	63
H(19B)	2057	4383	8891	63
H(20A)	2371	5485	9654	58
H(23A)	2662	6536	10490	64
H(24A)	2840	7450	11219	72
H(25A)	2552	8348	11522	71
H(26A)	2083	8303	11073	59
H(27A)	1044	8152	3873	61
H(28A)	1126	9421	3458	66
H(29A)	1088	10829	3815	69
H(30A)	918	10921	4536	61
H(33A)	724	10730	5402	54
H(34A)	377	9463	6170	58
H(34B)	482	10465	6138	58
H(36A)	922	10924	6735	52
H(38A)	1342	11476	7420	66
H(39A)	1720	11189	8151	65
H(41A)	1458	8669	8244	56
H(43A)	1023	8121	7561	63
H(44A)	673	8380	6772	62
H(45A)	2004	9328	8638	73
H(45B)	1974	10314	8851	73
H(46A)	1691	10426	9569	61
H(49A)	1510	10431	10429	60
H(50A)	1363	10209	11162	70
H(51A)	1361	8741	11486	73
H(52A)	1489	7564	11067	58
H(53A)	432	8579	3762	65
H(54A)	-37	8587	3332	84
H(55A)	-321	7685	3641	86

H(56A)	-133	6839	4400	66
H(59A)	173	5775	5245	63
H(60A)	816	4758	6041	66
H(60B)	498	4687	5979	66
H(62A)	350	6159	6424	82
H(64A)	206	7150	7042	117
H(65A)	268	7595	7903	107
H(67A)	1006	6437	8396	56
H(69A)	1166	5553	7747	88
H(70A)	1084	4989	6913	88
H(71A)	663	8039	8773	66
H(71B)	498	7182	8863	66
H(72A)	793	5989	9556	61
H(75A)	1104	4968	10400	66
H(76A)	1403	4353	11165	76
H(77A)	1841	4997	11534	75
H(78A)	1961	6175	11101	65

Table C1.6: Anisotropic displacement parameters (Å^2 x 10^3)for ap35a. The anisotropic displacement factor exponent takes the form: $-2\pi^2[h^2a^{*2}U^{11} + ... + 2 h k a^* b^* U^{12}]$.

	U^{11}	U^{22}	U^{33}	U^{23}	U^{13}	U^{12}
Fe(1)	34(1)	40(1)	47(1)	-1(1)	17(1)	-2(1)
Fe(2)	29(1)	41(1)	48(1)	0(1)	15(1)	1(1)
N(1)	37(2)	37(2)	46(2)	2(2)	13(2)	-4(2)
N(2)	43(2)	33(2)	46(2)	-4(2)	20(2)	-3(2)
N(3)	41(2)	40(2)	52(3)	2(2)	13(2)	-4(2)
N(4)	38(2)	46(3)	54(3)	1(2)	20(2)	-5(2)
N(5)	38(2)	43(3)	49(2)	0(2)	17(2)	5(2)
N(6)	35(2)	44(3)	50(2)	2(2)	20(2)	-2(2)
N(7)	29(2)	40(2)	43(2)	1(2)	14(2)	2(2)

N(8)	35(2)	38(2)	43(2)	1(2)	16(2)	-3(2)
N(9)	33(2)	40(2)	40(2)	1(2)	11(2)	-2(2)
N(10)	34(2)	36(2)	43(2)	3(2)	9(2)	-3(2)
N(11)	35(2)	49(3)	42(2)	-2(2)	15(2)	0(2)
N(12)	33(2)	41(3)	51(2)	-6(2)	14(2)	-1(2)
N(13)	34(2)	52(3)	50(3)	5(2)	14(2)	-7(2)
N(14)	29(2)	43(3)	54(3)	4(2)	15(2)	0(2)
N(15)	35(2)	35(2)	52(2)	2(2)	16(2)	-1(2)
N(16)	30(2)	40(2)	50(2)	1(2)	16(2)	3(2)
N(17)	40(2)	43(2)	50(2)	-2(2)	20(2)	4(2)
N(18)	35(2)	39(2)	44(2)	-4(2)	16(2)	1(2)
N(19)	41(2)	38(2)	61(3)	-1(2)	25(2)	-5(2)
N(20)	52(3)	45(3)	53(3)	-1(2)	24(2)	-6(2)
N(21)	32(2)	51(3)	56(3)	-10(2)	17(2)	0(2)
N(22)	28(2)	53(3)	58(3)	-8(2)	17(2)	-3(2)
N(23)	33(2)	42(3)	47(2)	-5(2)	17(2)	0(2)
N(24)	49(3)	40(2)	44(2)	-5(2)	19(2)	2(2)
C(1)	45(3)	49(3)	54(3)	5(3)	14(3)	1(3)
C(2)	55(3)	50(3)	62(4)	-9(3)	23(3)	-3(3)
C(3)	52(3)	49(3)	65(4)	-7(3)	34(3)	5(3)
C(4)	40(3)	54(3)	62(4)	0(3)	23(3)	14(3)
C(5)	34(3)	46(3)	48(3)	5(2)	15(2)	0(2)
C(6)	42(3)	51(3)	48(3)	12(3)	19(2)	2(3)
C(7)	32(3)	50(3)	54(3)	4(3)	12(2)	-8(2)
C(8)	44(3)	48(3)	53(3)	5(3)	5(3)	-8(3)
C(9)	43(3)	53(3)	46(3)	-2(3)	11(2)	-6(3)
C(10)	39(3)	60(4)	49(3)	-3(3)	16(2)	-7(3)
C(11)	32(3)	52(3)	43(3)	-3(2)	6(2)	5(2)
C(12)	38(3)	68(4)	56(3)	-3(3)	16(3)	6(3)
C(13)	40(3)	57(3)	45(3)	-7(3)	12(2)	6(3)
C(14)	44(3)	46(3)	53(3)	1(3)	16(3)	7(3)

C(15)	49(3)	56(4)	69(4)	5(3)	29(3)	14(3)
C(16)	40(3)	50(3)	55(3)	-2(3)	19(3)	6(3)
C(17)	76(4)	80(5)	65(4)	17(3)	41(3)	41(4)
C(18)	70(4)	60(4)	79(4)	18(3)	29(4)	31(3)
C(19)	51(3)	43(3)	68(4)	-4(3)	26(3)	2(3)
C(20)	44(3)	46(3)	54(3)	5(3)	14(3)	12(3)
C(21)	34(3)	47(3)	42(3)	2(2)	17(2)	7(2)
C(22)	36(3)	57(3)	53(3)	10(3)	17(2)	5(3)
C(23)	32(3)	65(4)	66(4)	-6(3)	19(3)	4(3)
C(24)	36(3)	73(4)	63(4)	4(3)	6(3)	2(3)
C(25)	45(3)	62(4)	63(4)	2(3)	7(3)	-7(3)
C(26)	35(3)	60(4)	52(3)	-2(3)	13(2)	3(3)
C(27)	51(3)	49(3)	60(3)	-7(3)	29(3)	0(3)
C(28)	53(3)	55(4)	65(4)	4(3)	29(3)	-6(3)
C(29)	51(3)	52(4)	75(4)	14(3)	26(3)	-5(3)
C(30)	43(3)	48(3)	65(3)	9(3)	23(3)	12(3)
C(31)	31(2)	41(3)	48(3)	-2(2)	16(2)	-2(2)
C(32)	25(2)	35(3)	55(3)	0(2)	7(2)	-1(2)
C(33)	42(3)	39(3)	52(3)	-1(2)	13(2)	-1(2)
C(34)	42(3)	56(3)	53(3)	-11(3)	22(3)	0(3)
C(35)	47(3)	38(3)	52(3)	-3(2)	28(3)	-1(2)
C(36)	51(3)	44(3)	43(3)	1(2)	25(3)	-2(3)
C(37)	43(3)	33(3)	48(3)	-3(2)	21(2)	-6(2)
C(38)	69(4)	45(3)	56(3)	2(3)	26(3)	-14(3)
C(39)	55(3)	57(4)	51(3)	-1(3)	17(3)	-20(3)
C(40)	43(3)	46(3)	54(3)	3(3)	21(3)	-4(3)
C(41)	49(3)	42(3)	55(3)	11(3)	24(3)	3(3)
C(42)	40(3)	34(3)	51(3)	-3(2)	24(2)	0(2)
C(43)	59(4)	38(3)	69(4)	2(3)	34(3)	-4(3)
C(44)	43(3)	49(3)	65(4)	-9(3)	19(3)	-8(3)
C(45)	49(3)	70(4)	68(4)	14(3)	26(3)	-1(3)

C(46)	51(3)	43(3)	55(3)	1(3)	11(3)	1(3)
C(47)	41(3)	38(3)	51(3)	2(2)	11(2)	1(2)
C(48)	38(3)	43(3)	41(3)	-3(2)	6(2)	8(2)
C(49)	51(3)	43(3)	53(3)	2(3)	10(3)	4(3)
C(50)	54(3)	61(4)	63(4)	-16(3)	23(3)	2(3)
C(51)	51(3)	66(4)	76(4)	-6(3)	35(3)	4(3)
C(52)	48(3)	42(3)	60(3)	-4(3)	23(3)	-1(3)
C(53)	40(3)	62(4)	65(4)	0(3)	21(3)	-4(3)
C(54)	39(3)	94(5)	70(4)	10(4)	10(3)	0(3)
C(55)	39(3)	91(5)	80(5)	-8(4)	13(3)	4(3)
C(56)	36(3)	57(4)	73(4)	-9(3)	19(3)	-9(3)
C(57)	34(3)	42(3)	61(3)	-8(3)	23(2)	-6(2)
C(58)	41(3)	43(3)	61(3)	-8(3)	25(3)	-9(2)
C(59)	46(3)	50(3)	65(4)	-5(3)	22(3)	-8(3)
C(60)	64(4)	35(3)	75(4)	-3(3)	37(3)	-3(3)
C(61)	61(4)	39(3)	55(3)	0(3)	24(3)	-7(3)
C(62)	47(3)	85(5)	70(4)	-11(4)	13(3)	9(3)
C(63)	42(3)	74(4)	65(4)	-18(3)	15(3)	5(3)
C(64)	55(4)	135(7)	81(5)	-35(5)	-6(4)	41(4)
C(65)	49(4)	122(6)	85(5)	-35(5)	8(4)	23(4)
C(66)	32(3)	49(3)	60(3)	-9(3)	14(2)	0(2)
C(67)	34(3)	43(3)	58(3)	9(3)	6(2)	6(2)
C(68)	37(3)	46(3)	60(3)	9(3)	22(3)	0(2)
C(69)	57(4)	109(6)	46(3)	2(3)	7(3)	31(4)
C(70)	60(4)	96(5)	68(4)	1(4)	27(3)	28(4)
C(71)	32(3)	63(4)	71(4)	-7(3)	18(3)	6(3)
C(72)	37(3)	59(4)	66(4)	-20(3)	29(3)	-11(3)
C(73)	47(3)	58(4)	50(3)	-11(3)	25(3)	-11(3)
C(74)	47(3)	43(3)	56(3)	-17(3)	29(3)	-10(3)
C(75)	64(4)	47(3)	67(4)	-10(3)	37(3)	-11(3)
C(76)	80(5)	45(4)	81(4)	3(3)	47(4)	-4(3)

C(77)	75(4)	48(4)	72(4)	15(3)	34(3)	9(3)
C(78)	51(3)	50(4)	65(4)	6(3)	23(3)	5(3)
B(1)	55(4)	74(5)	67(5)	-2(4)	15(4)	1(4)
F(1)	68(2)	86(2)	98(2)	0(2)	22(2)	9(1)
F(2A)	68(2)	86(2)	98(2)	0(2)	22(2)	9(1)
F(3A)	68(2)	86(2)	98(2)	0(2)	22(2)	9(1)
F(4A)	68(2)	86(2)	98(2)	0(2)	22(2)	9(1)
F(2B)	68(2)	86(2)	98(2)	0(2)	22(2)	9(1)
F(3B)	68(2)	86(2)	98(2)	0(2)	22(2)	9(1)
F(4B)	68(2)	86(2)	98(2)	0(2)	22(2)	9(1)
B(3)	63(5)	51(4)	104(6)	-16(4)	34(5)	5(4)
F(9)	73(3)	91(3)	153(4)	-26(3)	51(3)	-14(2)
F(10)	87(3)	77(3)	168(4)	-10(3)	55(3)	1(2)
F(11)	111(3)	53(2)	129(3)	2(2)	74(3)	-3(2)
F(12)	126(4)	76(3)	136(4)	2(3)	88(3)	-10(3)